Fall 1-31-2010

Synthesis and characterization of metal oxide semiconductors for photoelectrochemical hydrogen production

Sudhakar Shet
New Jersey Institute of Technology

ABSTRACT

SYNTHESIS AND CHARACTERIZATION OF METAL OXIDE SEMICONDUCTORS FOR PHOTOELECTROCHEMICAL HYDROGEN PRODUCTION

by
Sudhakar Shet

The goal of this thesis is to investigate the properties of metal-oxide thin films on fluorine-doped tin oxide (FTO)-coated glass substrates, prepared by using radio-frequency (RF) reactive magnetron sputtering for photoelectrochemical (PEC) applications. Metal-oxide thin films as a photoelectrode are of special interest for PEC systems to produce hydrogen in an aqueous solution by solar energy due to their low cost and potential stability.

The following list represents some of the accomplishments and results of this work:

- Narrowing of N-incorporated ZnO (ZnO:N) was achieved by reactive sputtering in a O_2/N_2 mixture ambient, and ZnO:N films with various bandgaps were realized by varying N concentration, which was controlled successfully by varying the RF powers.

- Nitrogen incorporation narrows the bandgap of ZnO and shifts the optical absorption into the visible-light region. As a result, the ZnO:N films exhibit higher photocurrents than ZnO films.

- *p*-type ZnO thin films with significantly reduced bandgaps were synthesized by heavy Cu incorporation.

- ZnO thin films deposited in pure argon ambient lead to polycrystalline films. However, the presence of N_2 in the deposition chamber ambient promotes the formation of aligned nanorods at temperatures above 300°C and these films exhibit enhanced photocurrents.

- Proper Ar/N_2 ratio in the chamber ambient plays a significant role in the formation of aligned nanorods in ZnO thin films.

- Bandgap-reduced p-type ZnO thin films with various carrier concentrations are realized by Cu and Ga co-doping.

- ZnO thin films co-doped with Ga and N showed significantly enhanced crystallinity and improved N incorporation compared to ZnO doped solely with N and exhibited dramatically improved PEC response.

- Ga and N co-doped ZnO films exhibited enhanced N incorporation and photocurrents as the substrate temperature was increased.

- Controlling O_2/N_2 gas flow rate in the chamber ambient is critical for Ga and N co-doped ZnO thin films; otherwise, it will result in phase separation.

- Synthesized porous ZnO nanocoral structures demonstrated a 10-fold increase in PEC response as compared to compact ZnO films.

- ZnO:N, ZnO:(Ga,N), and ZnO:(Al,N) films deposited under a N_2/O_2 plasma showed n-type behavior due to substitutional N_2 molecules that act as shallow double donors.

- Significantly reduced bandgaps enhanced crystallinity, and PEC responses were observed for Al and N co-doped ZnO thin films.

- N incorporation in the Al and N co-doped ZnO films were successfully controlled by varying the N_2/O_2 gas flow rate and RF powers.

- Bandgap-reduced solid solution of ZnO and GaN (ZnO:GaN) that exhibited improved PEC responses were synthesized.

- It was found that the Al and N co-doped ZnO and ZnO and GaN solid solution deposited under N_2/Ar gas flow failed to incorporate the N in the films; N_2/O_2 gas flow succeeded in incorporating N in the films.

- $CoAl_2O_4$–Fe_2O_3 *p-n* nanocomposite electrodes exhibited much improved photoresponses as compared to *p*-type $CoAl_2O_4$ only.

- Ternary cobalt-based spinal oxides as PEC catalysts are limited by the poor transport properties induced by small polaron mobility.

- *p*-type Cu-Ti-oxide, Cu-W-oxide, and Cu-Sn-oxide films were synthesized.

SYNTHESIS AND CHARACTERIZATION OF METAL OXIDE SEMICONDUCTORS FOR PHOTOELECTROCHEMICAL HYDROGEN PRODUCTION

by
Sudhakar Shet

A Dissertation
Submitted to the Faculty of
New Jersey Institute of Technology
in Partial Fulfillment of the Requirements for the Degree of
Doctor of Philosophy in Materials Science & Engineering

Interdisciplinary Program in Materials Science and Engineering

January 2010

APPROVAL PAGE

SYNTHESIS AND CHARACTERIZATION OF METAL OXIDE SEMICONDUCTORS FOR PHOTOELECTROCHEMICAL HYDROGEN PRODUCTION

Sudhakar Shet

Dr. Nuggehalli M. Ravindra, Dissertation Co-Advisor — Date
Professor and Chair of Physics, NJIT

Dr. Mowafak Al-Jassim, Dissertation Co-Advisor — Date
Group Manager, National Renewable Energy Laboratory, Golden, CO

Dr. Yanfa Yan, Dissertation Co-Advisor — Date
Principal Scientist, National Renewable Energy Laboratory, Golden, CO

Dr. Trevor Tyson, Committee Member — Date
Professor of Physics, NJIT

Dr. Anthony T. Fiory, Committee Member — Date
Research Professor of Physics, NJIT

Dr. Michael R. Booty, Committee Member — Date
Professor of Mathematics, NJIT

Dr. Ken Ahn, Committee Member — Date
Assistant Professor of Physics, NJIT

BIOGRAPHICAL SKETCH

Author: Sudhakar Shet

Degree: Doctor of Philosophy

Date: January 2010

Undergraduate and Graduate Education:

- Doctor of Philosophy in Materials Science & Engineering,
  New Jersey Institute of Technology, Newark, NJ, 2010
- Master of Science in Materials Science & Engineering,
  New Jersey Institute of Technology, Newark, NJ, 2003
- Bachelor of Science in Metallurgy, Materials Science & Engineering,
  National Institute of Technology, Surathkal, India, 1996

Major: Materials Science & Engineering

Presentations and Publications:

S. Shet, K.-S. Ahn, T. Deutsch, H. Wang, N. M. Ravindra, Y. Yan, J. Turner, and M. Al-Jassim, "Synthesis and characterization of bandgap-reduced ZnO:N and ZnO:(Al:N) films for photoelectrochemical water splitting," *Journal of Materials Research (JMR), (accepted).*

S. Shet, K.-S. Ahn, H. Wang, N. M. Ravindra, Y. Yan, J. Turner, and M. Al-Jassim, "Effect of substrate temperature on the photoelectrochemical responses of the Ga and N co-doped ZnO films," *Journal of Electronic Materials (JEM), (submitted).*

S. Shet, K.-S. Ahn, T. Deutsch, H. Wang, N. M. Ravindra, Y. Yan, J. Turner, and M. Al-Jassim, "Influence of gas ambient on the synthesis of co-doped ZnO:(Al,N) filmsfor photoelectrochemical water splitting," *Journal of Electronic Materials (JEM), (submitted).*

K.-S. Ahn, Y. Yan, M.-S. Kang, J.-Y. Kim, S. Shet, H. Wang, J. Turner, and M. Al-Jassim, "$CoAl_2O_4$-Fe_2O_3 p-n nanocomposite electrodes for photoelectrochemical ells," *Applied Physics Letters, (APL)* 95, 022116, (2009).

A. Walsh, K.-S. Ahn, S. Shet, M. N. Huda, T. Deutsch, H. Wang, J. A. Turner, S-H. Wei, Yan and M. Al-Jassim, "Ternary cobalt spinal oxides for solar driven hydrogenproduction: Theory and experiment," (Invited Paper), *Energy & Environmental science*, DOI: 10.1039/b822903a, 2009.

M. Bar, K.-S. Ahn, S. Shet, Y. Yan, L. Weinhardt, O. Fuchs, M. Blum, S. Pookpanratana, K. George, W. Yang, J. D. Denlinger, M. Al-Jassim, C. Heske, "Impact of air-exposure on the chemical and electronic structure of ZnO:Zn_3N_2 thin films," *Applied Physics Letters (APL)*, Vol. 94, issue 1, 012110, 2009.

S. Shet, K.-S. Ahn, Y. Yan, N. M. Ravindra, T. Deutsch, J. Turner, M. Al-Jassim, "Phaseseparation in Ga and N co-incorporated ZnO films and its effect on photo-response in photoelectrochemical water splitting," *Journal of Electronic Materials (JEM), (submitted).*

S. Shet, K.-S. Ahn, Y. Yan, N. M. Ravindra, T. Deutsch, J. Turner, M. Al-Jassim, "Effect of rf power and substrate temperature for the formation of aligned nanorods in ZnO thin films," *Journal of Electronic Materials (JEM), (submitted).*

K.-S. Ahn, S. Shet, T. Deutsch, Y. Yan, J. Turner, M. Al-Jassim, "Mechanism for optimization of photoelectrochemical response in nanoporous nanocrystalline ZnO thin films," *(manuscript under preparation).*

K.-S. Ahn, Y. Yan, S. Shet, K. Jones, T. Deutsch, J. Turner, M. Al-Jassim, "ZnOnanocoral structures for photoelectrochemical cells," Applied Physics Letters (APL), Vol. 93, issue 16, 163117, 2008. [Selected for *Virtual Journal of Nanoscale Science & Technology* Vol.18 (issue 19) (November 10, 2008)].

K.-S. Ahn, S. Shet, T. Deutsch, C.-S. Jiang, Y. Yan, M. Al-Jassim, J. Turner, "Enhancement of photoelectrochemical response by aligned nanorods in ZnO thin films," *Journal of Power Sources (JPS)*, 176, 387-392, 2008.

S. Shet, K.-S. Ahn, Y. Yan, T. Deutsch, K. M. Chrustowski, J. Turner, M. Al-Jassim, Nuggehalli Ravindra, "Carrier concentration tuning of bandgap-reduced p-type ZnO films by co-doping of Cu and Ga for improving photoelectrochemical response," *Journal of Applied Physics (JAP),* 103, 073504, 2008.

R. D. Revero, S. Shet, M. R. Booty, A. T. Fiory, N. M. Ravindra, "Modeling of magneticfield assisted assembly of semiconductor devices," *Journal of Electronic Materials (JEM)*, Vol. 37, No. 4, 374-378, April 2008.

K.-S. Ahn, Y. Yan, S. Shet, T. Deutsch, J. Turner, M. Al-Jassim, "Enhanced photoelectrochemical responses of ZnO films through Ga and N codoping," *Applied Physics Letters (APL)*, Vol. 91, issue 23, 231909, 2007.

N. M. Ravindra, V. R. Mehta, S. Shet, "Silicon nanoelectronics and beyond - An overview and recent developments," *Journal of Materials (JOM)*, 57(6), 16-20, June 2005.

V. R. Mehta, S. Shet, N. M. Ravindra, A. T. Fiory, M. P. Lepselter, "Silicon integrated uncooled infrared detectors: Perspectives on thin films and microstructures," *Journal of Electronic Materials (JEM)*, Vol. 34, No. 5, 484-490, 2005.

S. Shet, V. R. Mehta, A. T. Fiory, M. P. Lepselter, N. M. Ravindra, "The magnetic field-assisted assembly of nanoscale semiconductor devices: A new technique," *Journal of Materials (JOM)*, 56(10), 32-34, October 2004.

S. Shet, et al., "Significantly reduced bandgap and enhanced photoelectrochemical responses of Al and N co-doped ZnO films," *(manuscript under preparation).*

S. Shet, et al., "Influence of gas flow rate for the formation of aligned nanorods in ZnO thin films," *(manuscript under preparation).*

S. Shet, et al., "Effect of gas ambient and varying rf sputtering power for bandgap narrowing of ZnO:GaN solid solution films for photoelectrochemical water splitting," *(manuscript under preparation).*

S. Shet, "Production of $MnSO_4$ from Fe-Mn slag," *(manuscript under preparation).*

S. Shet, et al., "Synthesis and characterization of ZnO:GaN solid solution films for photoelectrochemical water splitting," *(manuscript under preparation).*

S. Shet, K.-S. Ahn, N. M. Ravindra, Y. Yan, T. Deutsch, J. Turner, M. Al-Jassim, "Influence of gas flow rate on the formation of ZnO nanorods and their effect on photoelectrochemical response," Materials Science & technology 2009 conference and exhibition, Pittsburgh, Pennsylvania, USA, October 25-29, 2009. [Invited paper for *ceramic transactions*] – *(submitted).*

S. Shet, K.-S. Ahn, N. M. Ravindra, Y. Yan, T. Deutsch, J. Turner, M. Al-Jassim,"Bandgap reduced p-type ZnO films by co-doping Cu and Ga for improvingphotoelectrochemical response," Materials Science & technology 2009conference and exhibition, Pittsburgh, Pennsylvania, USA, October 25-29, 2009 – *(submitted).*

S. Shet, K.-S. Ahn, N. M. Ravindra, Y. Yan, T. Deutsch, J. Turner, M. Al-Jassim,"Enhanced crystallinity and photoelectrochemical response of the (Ga,N) and (Al,N) co-doped ZnO films," Materials Science & technology 2009 conference and exhibition, Pittsburgh, Pennsylvania, USA, October 25-29, 2009 – *(submitted).*

H. Wang, T. Deutsch, S. Shet, K. Ahn, Y. Yan, M. Al-Jassim and J. Turner,"(Photo)electrochemical Characterization of nanostructured ZnO Electrodes," (Invited paper), *Solar Hydrogen and Nanotechnology IV, SPIE*, Nanoscience + Engineering, pp. 7408-7412, August 2-6, 2009, San Diego, California, USA.

K.-S. Ahn, A. Walsh, S. Shet, M. Huda, T. Deutsch, H. Wang, Y. Yan, S.-H. Wei, J. Turner, M. Al-Jassim, "Understanding the photoelectrochemical properties of spinel-type p-CoM_2O_4 (M: Al, Ga, and In) compounds," (extended abstract) *2009 MRS spring meeting*, April 13-17, San Francisco, California, USA.

H. Wang, T. Deutsch, S. Shet, K. Ahn, Y. Yan, M. Al-Jassim and J. Turner"(Photo)electrochemical Characterization of Doped ZnO Electrodes," (extendedabstract # 526), *215th ECS Meeting*, May 24 - 29, 2009, San Francisco, California, USA.

M. Bär, L. Weinhardt, S. Pookpanratana, K. George, Y. Zhang, C. Heske, K.-S. Ahn, S. Shet, Y. Yan, M. Al-Jassim, O. Fuchs, M. Blum, W. Yang, J.D. Denlinger, and "Impact of air-exposure on the chemical and electronic structure of ZnO:Zn_3N_2 thin films," (extended abstract), *2009 MRS spring meeting*, April 13-17, San Francisco, California, USA.

K.-S. Ahn, Y. Yan, T. Deutsch, S. Shet, K. M. Chrustowski, J. Turner, M. Al-Jassim, "Photoelectrochemical responses of the nanostructured ZnO films synthesized using sputtering system," (extended abstract # 274), *214th ECS Meeting*, October 12-17, 2008, Honolulu, Hawaii, USA.

S. Shet, K.-S. Ahn, T. Deutsch, Y. Yan, J. Turner, M. Al-Jassim, N. M. Ravindra, "Effect of aligned nanorods in ZnO thin films for the enhanced photoelectrochemical response," *Materials Science & Technology 2008 Conference and Exhibition*, pp. 920-935, October 5-9, 2008, Pittsburgh, PA, USA.

K.-S. Ahn, S. Shet, T. Deutsch, Y. Yan, N. M. Ravindra, J. Turner, M. Al-Jassim, "Synthesis and characterization of bandgap reduced p-type Cu incorporated ZnO films," *Materials Science & Technology 2008 Conference and Exhibition*, pp. 901-913,October 5-9, 2008, Pittsburgh, PA, USA.

K.-S. Ahn, S. Shet, T. Deutsch, Y. Yan, N. M. Ravindra, J. Turner, M. Al-Jassim,"Bandgap reduction and photoelectrochemical properties of ZnO:N films deposited by reactive RF magnetron sputtering," *Materials Science & Technology 2008 Conference and Exhibition*, pp 952-961, October 5-9, 2008, Pittsburgh, PA, USA.

Y. Yan, K.-S. Ahn, T. Deutsch, M. Huda, S. Shet, S. H. Wei, J. Turner, M. Al-Jassim,"Application of ZnO for photoelectrochemical water splitting," (extended abstract # 780), *213th ECS Meeting*, May 18-23, 2008, Phoenix, AZ, USA.

K.-S. Ahn, Y. Yan, T. Deutsch, S. Shet, J. Turner, M. Al-Jassim, "Photoelectrochemical responses of the nanostructured ZnO films synthesized using sputtering system," (extended abstract # 67), *213th ECS Meeting*, May 18-23, 2008, Phoenix, AZ, USA.

Y. Yan, K.-S. Ahn, S. Shet, T. Deutsch, M. Huda, S. H. Wei, J. Turner, M. Al-Jassim,"Bandgap reduction of ZnO for photoelectrochemical splitting of water," *Solar hydrogen and nanotechnology II, Proceedings of the SPIE*, Vol. 6650, 66500H (2007).

N. M. Ravindra, B. Sopori, A. T. Fiory, S. Shet, C. Li, R. D. Rivero, V. Agnihotri," Lamp-based processing technologies for silicon solar cell manufacturing," *Proceedings of 16th workshop on crystalline silicon solar cells & modules: Materials and Processes*, pp. 160-167, August 6-9, 2006, Denver, CO, USA.

S. Shet, R. D. Rivero, M. R. Booty, A. T. Fiory, M. P. Lepselter, N. M. Ravindra, "Microassembly techniques: A review," Microstructural and texture requirements for functional materials, *Materials Science & Technology 2006 Conference and Exhibition*, Cincinnati, pp 451-470, OH, USA.

N. M. Ravindra, S. Shet, V. Dhir, V. K. Challa, S. Abedrabbo, A. T. Fiory, "Radiative properties of AlN and Al_2O_3," Glass and optical materials, *Materials Science & Technology 2006 Conference and Exhibition*, pp 575-582, Cincinnati, OH, USA.

N. M. Ravindra, K. Ravindra, M. Rabus, V. R. Mehta, S. E. Rubin, S. Shet, A. T. Fiory, "Application of spectral emissometry," The physics and materials challenges for integrated optics – A step in the future for photonic devices, *Materials Science & Technology 2005 Conference and Exhibition*, pp 49-59,, Pittsburgh, PA, USA.

N. M. Ravindra, M. L. Dattatreya, K. N. Ravindra, S. Shet, M. Rabus, V. R. Mehta, V. E. Venkatesh, H. McCloud, L. Derilhomme, A. C. Culpepper, "Technology based activities in pre-college programs," *Proceedings of the 2005 American society for engineering education annual conference and exposition.*

S. Shet, K.-S. Ahn, H. Wang, T. Deutsch, N. M. Ravindra, Y. Yan, J. Turner, M. Al-Jassim, "Carrier concentration tuning and enhanced photoelectrochemical response of bandgap-reduced Cu and Ga co-doped *p*-type ZnO films," *2010 TMS Annual Meeting & Exhibition*, Seattle, WA, USA, February 14-18, 2010.

S. Shet, K.-S. Ahn, H. Wang, N. M. Ravindra, Y. Yan, J. Turner, M. Al-Jassim, "Experimental study of ternary cobalt spinal oxides for photoelectrochemical hydrogen production," *2010 TMS Annual Meeting & Exhibition*, Seattle, WA, USA, February 14-18, 2010.

S. Shet, K.-S. Ahn, N. M. Ravindra, Y. Yan, T. Deutsch, J. Turner, M. Al-Jassim, "Influence of gas flow rate on the formation of ZnO nanorods and their effect on photoelectrochemical response," *Materials Science & technology 2009 conference and exhibition*, Pittsburgh, Pennsylvania, USA, October 25-29, 2009.

S. Shet, K.-S. Ahn, N. M. Ravindra, Y. Yan, T. Deutsch, J. Turner, M. Al-Jassim, "Bandgap reduced p-type ZnO films by co-doping Cu and Ga for improving photoelectrochemical response," *Materials Science & technology 2009 conference and exhibition*, Pittsburgh, Pennsylvania, USA, October 25-29, 2009.

S. Shet, K.-S. Ahn, N. M. Ravindra, Y. Yan, T. Deutsch, J. Turner, M. Al-Jassim, "Enhanced crystallinity and photoelectrochemical response of the (Ga,N) and (Al,N) co-doped ZnO films," *Materials Science & technology 2009 conference and exhibition*, Pittsburgh, Pennsylvania, USA, October 25-29, 2009.

S. Shet, K.-S. Ahn, N. M. Ravindra, Y. Yan, T. Deutsch, J. Turner, M. Al-Jassim, "Enhanced crystallinity and photoelectrochemical response of the (Ga,N) and (Al,N) co-doped ZnO films," *Materials Science & technology 2009 conference and exhibition*, Pittsburgh, Pennsylvania, USA, October 25-29, 2009.

H. Wang, T. Deutsch, S. Shet, K. Ahn, Y. Yan, M. Al-Jassim and J. Turner "(Photo)electrochemical Characterization of nanostructured ZnO Electrodes," (Invited talk), *Solar Hydrogen and Nanotechnology IV, SPIE*, Nanoscience + Engineering, San Diego, California, USA, August 2-6, 2009.

K.-S. Ahn, A. Walsh, S. Shet, M. Huda, T. Deutsch, H. Wang, Y. Yan, S.-H. Wei, J. Turner, M. Al-Jassim, "Understanding the photoelectrochemical properties of spinel-type p-CoM_2O_4 (M: Al, Ga, and In) compounds," *2009 MRS spring meeting*, San Francisco, California, USA, April 13-17, 2009.

M. Bär, L. Weinhardt, S. Pookpanratana, K. George, Y. Zhang, C. Heske, K.-S. Ahn, S. Shet, Y. Yan, M. Al-Jassim, O. Fuchs, M. Blum, W. Yang, J.D. Denlinger, and "Impact of air-exposure on the chemical and electronic structure of ZnO:Zn_3N_2 thin films," *2009 MRS spring meeting*, San Francisco, California, USA, April 13-17, 2009.

H. Wang, T. Deutsch, S. Shet, K. Ahn, Y. Yan, M. Al-Jassim and J. Turner "(Photo)electrochemical Characterization of Doped ZnO Electrodes," *215th ECS Meeting,* San Francisco, California, USA, May 24 - 29, 2009.

S. Shet, K.-S. Ahn, Y. Yan, N. M. Ravindra, T. Deutsch, J. Turner, M. Al-Jassim, "Effect of gas flow rate on the formation of aligned nanorods in ZnO thin films," *2009 TMS Annual Meeting & Exhibition*, San Francisco, CA, USA, February 15-19, 2009.

S. Shet, K.-S. Ahn, Y. Yan, N. M. Ravindra, T. Deutsch, J. Turner, M. Al-Jassim, "Al and N co-doped ZnO films with significantly reduced bandgap and enhanced photoelectrochemical response," (Invited talk), *2009 TMS Annual Meeting & Exhibition*, San Francisco, CA, USA, February 15-19, 2009.

S. Shet, K.-S. Ahn, Y. Yan, N. M. Ravindra, T. Deutsch, J. Turner, M. Al-Jassim, "Synthesis and characterization of ZnO:GaN thin films for photoelectrochemical water splitting," *2009 TMS Annual Meeting & Exhibition, San Francisco, CA, USA*, February 15-19, 2009.

K.-S. Ahn, Y. Yan, T. Deutsch, S. Shet, K. M. Chrustowski, J. Turner, M. Al-Jassim, "Photoelectrochemical responses of the nanostructured ZnO films synthesized using sputtering system," *214th ECS Meeting*, Honolulu, Hawaii, October 12-17, 2008.

S. Shet, K.-S. Ahn, T. Deutsch, Y. Yan, J. Turner, M. Al-Jassim, N. M. Ravindra, "Effect of aligned nanorods in ZnO thin films for the enhanced photoelectrochemical response," *Materials Science & Technology 2008 Conference and Exhibition*, Pittsburgh, PA, USA, October 5-9, 2008.

S. Shet, K.-S. Ahn, T. Deutsch, Y. Yan, N. M. Ravindra, J. Turner, M. Al-Jassim, "Synthesis and characterization of bandgap reduced p-type Cu incorporated ZnO films," (Invited talk), *Materials Science & Technology 2008 Conference and Exhibition*, Pittsburgh, PA, USA, October 5-9, 2008.

S. Shet, K.-S. Ahn, T. Deutsch, Y. Yan, N. M. Ravindra, J. Turner, M. Al-Jassim, "Bandgap reduction and photoelectrochemical properties of ZnO:N films deposited by reactive RF magnetron sputtering," *Materials Science & Technology 2008 Conference and Exhibition,* Pittsburgh, PA, USA, October 5-9, 2008.

S. Shet, K.-S. Ahn, Y. Yan, T. Deutsch, M. Huda, N. M. Ravindra, M. Al-Jassim, J.Turner, "Synthesis and characterization of Ga and N incorporated ZnO films," *2008 TMS Annual Meeting & Exhibition*, New Orleans, Louisiana, USA. USA, March 9-13, 2008.

S. Shet, K.-S. Ahn, Y. Yan, T. Deutsch, M. Huda, N. M. Ravindra, M. Al-Jassim, J. Turner, "Bandgap narrowing of ZnO films by Cu and In incorporation," *2008 TMS Annual Meeting & Exhibition*, New Orleans, Louisiana, USA, March 9-13, 2008.

R. D. Rivero, V. K. Kasisomayajula, S. Fnu, T. Seman, S. Shet, M. R. Booty, A. T. Fiory, N. M. Ravindra, "Magnetic field assisted assembly-Theory and experiments," *2008 TMS Annual Meeting & Exhibition*, New Orleans, Louisiana, USA, March 9-13, 2008.

G. Devrani, R. D. Rivero, S. Shet, M. R. Booty, A. T. Fiory, N. M. Ravindra, "A two dimensional model for magnetic field assisted assembly," (poster), *4th Annual Provost's Student research Showcase*, Newark, NJ, USA, April 9, 2008.

G. Devrani, R. D. Rivero, S. Shet, M. R. Booty, A. T. Fiory, N. M. Ravindra, "Magnetic field assisted assembly- A two dimensional model," (poster), *11th Annual CUNY Conference in Science & Engineering*, NY, USA, February 25-26, 2008.

K.-S. Ahn, Y. Yan, T. Deutsch, S. Shet, J. Turner, M. Al-Jassim, "Photoelectrochemical responses of the nanostructured ZnO films synthesized using sputtering system," *213th ECS Meeting*, Phoenix, AZ, USA, May 18-23, 2008.

Y. Yan, K.-S. Ahn, T. Deutsch, M. Huda, S. Shet, S. H. Wei, J. Turner, M. Al-Jassim, "Application of ZnO for photoelectrochemical water splitting," *213th ECS Meeting*, Phoenix, AZ, USA, May 18-23, 2008.

Y. Yan, K.-S. Ahn, S. Shet, T. Deutsch, M. Huda, S. H. Wei, J. Turner, M. Al-Jassim, "Bandgap reduction of ZnO for photoelectrochemical splitting of water," Solar hydrogen and nanotechnology II, *Proceedings of the SPIE*, 2007, San Diego, USA, August 27-30, 2007.

S. Shet, K.-S. Ahn, Y. Yan, T. Deutsch, J. Turner, M. Al-Jassim, "Bandgap narrowing and photoelectrochemical properties of N incorporated ZnO films," *2007 Annual Symposium & Equipment Exhibit*, AVS Rocky Mountain chapter, Westminster, CO, USA, September 27, 2007.

S. Shet, "Magnetic field assisted assembly of semiconductor devices," (poster), *3rd Annual Provost's Student research Showcase*, Newark, NJ, USA, April 11, 2007.

S. Shet, R. D. Rivero, M. R. Booty, A. T. Fiory, M. P. Lepselter, N. M. Ravindra, (Invited Talk), "Modeling of magnetic field assisted assembly of semiconductor devices," *2007 TMS Annual Meeting & Exhibition*, Symposium: Recent developments in semiconductor, electro optic and radio frequency materials, Orlando, FL, USA, February 25 – March 1, 2007.

S. Shet, R. D. Rivero, M. R. Booty, A. T. Fiory, M. P. Lepselter, N. M. Ravindra, "Magnetic field assisted assembly of semiconductor devices," (poster), *NJIT Graduate student research day*, Newark, NJ, USA, November 6, 2006.

N. M. Ravindra, B. Sopori, A. T. Fiory, S. Shet, C. Li, R. D. Rivero, V. Agnihotri," Lamp-based processing technologies for silicon solar cell manufacturing," *16th workshop on crystalline silicon solar cells & modules: Materials and Processes*, Denver, CO, USA, August 6-9, 2006.

N. M. Ravindra, B. Sopori, A. T. Fiory, V. R. Mehta, S. Shet, J. Appel, C. Li, "Influence of surface morphology on optical properties of silicon," (Invited Talk), *Materials Science & Technology 2006 Conference and Exhibition*, Cincinnati, OH, USA, October 15-18, 2006.

N. M. Ravindra, S. Shet, V. R. Mehta, A. T. Fiory, "Radiative properties of glassy and crystalline materials," *Materials Science & Technology 2006 Conference and Exhibition*, Cincinnati, OH, USA, October 15-18, 2006.

S. Shet, R. D. Rivero, M. R. Booty, A. T. Fiory, M. P. Lepselter, N. M. Ravindra, "Microassembly techniques: A review," Microstructural and texture requirements for functional materials, *Materials Science & Technology 2006 Conference and Exhibition*, Cincinnati, OH, USA, October 15-18, 2006.

N. M. Ravindra, S. Shet, V. Dhir, V. K. Challa, S. Abedrabbo, A. T. Fiory, "Radiative properties of AlN and Al_2O_3," Glass and optical materials, *Materials Science & Technology 2006 Conference and Exhibition*, Cincinnati, OH, USA, October 15-18, 2006.

S. Shet, D. Boomer, "Flexible thin film sensors," New Jersey commission on science and technology, *NJIT-IP commercialization project (TCAT) meeting*, Newark, NJ, USA, May 1st, 2006.

S. Shet, S. Gopalkrishnan, "Assembling complex structures and circuits using magnetic field assisted assembly (MFAA)," New jersey commission on science and technology, *NJIT-IP commercialization project (TCAT) meeting*, Newark, NJ, USA, December 13, 2005.

N. M. Ravindra, K. Ravindra, M. Rabus, V. R. Mehta, S. E. Rubin, S. Shet, A. T. Fiory, "Application of spectral emissometry," The physics and materials challenges for integrated optics – A step in the future for photonic devices, *Materials Science & Technology 2005 Conference and Exhibition*, Pittsburgh, PA, USA, September 25-28, 2005.

N. M. Ravindra, S. Shet, V. R. Mehta, M. Rabus, A. T. Fiory, "Radiative properties of quartz, erbium oxide and silicon carbide," *Materials Science & Technology 2005 Conference and Exhibition*, Pittsburgh, PA, USA, September 25-28, 2005.

N. M. Ravindra, M. L. Dattatreya, K. N. Ravindra, S. Shet, M. Rabus, V. R. Mehta, V. E. Venkatesh, H. McCloud, L. Derilhomme, A. C. Culpepper, "Technology based activities in pre-college programs," *Proceedings of the 2005 American society for engineering education,* Annual conference and exposition, Portland, OR, June 13-15, 2005.

S. Shet, V. R. Mehta, A. T. Fiory, M. P. Lepselter, N. M. Ravindra, "Macro-Assembly of semiconductor devices," *2005 TMS Annual Meeting & Exhibition*, San Francisco, CA, USA, February 13-17, 2005.

N. M. Ravindra, S. Shet, V. R. Mehta, A. T. Fiory, S. Rubin, M. Rabus, S. Srivatsa, "Temperature dependent infrared properties of InP, AlN, Al_2O_3 and Er_2O_3," *2005 TMS Annual Meeting & Exhibition*, San Francisco, CA, USA, February 13-17, 2005.

N. M. Ravindra, A. T. Fiory, V. R. Mehta, S. Shet, M. P. Lepselter, "Self-Assembly-Review and Applications," *ASM Materials solutions conference & show*, Columbus, OH, USA, October 18-21, 2004.

R. S. Petrova, S. Shet, "Corrosion resistance of coatings containing boron," *Tri-service corrosion conference*, Department of Defense, Las Vegas, NV, USA, November 17-21, 2003.

Patents:

Method of magnetic field assisted self-assembly, N. M. Ravindra, A. T. Fiory, and S. Shet, Patent No. US7217592 B2.

Method of assembling structures using array of electromagnets, N. M. Ravindra, V. Kasisomayajula, S. Shet and A. T. Fiory, Provisional Patent, Final Patent under Review.

Method of fabrication of efficient solar cell, S. Shet and N. M. Ravindra, (Invention disclosure submitted).

Method of fabrication of integrated wind and solar energy, S. Shet and N. M. Ravindra, (patent application in process).

Method of efficient parking system, S. Shet and N. M. Ravindra, (patent application in process).

To my beloved family

ACKNOWLEDGMENTS

The author wishes to express his sincere gratitude to his research advisors, Dr. N. M. Ravindra, Dr. Mowafak Al-Jassim, and Dr. Yanfa Yan for their unwavering guidance, encouragement and support. Without their knowledge and help, this work would not have been possible.

The author would like to thank Dr. Anthony T. Fiory, Dr. Trevor Tyson, Dr. Michael Booty, and Dr. Ken Ahn, for serving as members of the dissertation committee. The author appreciates the financial assistance provided by Dr. N. M. Ravindra, Dr. Mowafak Al-Jassim, Dr. Yanfa Yan, New Jersey Institute of technology, and National Renewable Energy Laboratory.

The author would like to thank all the people, who supported him, at the most needed moments and made his stay at NJIT and NREL more memorable. The author also likes to express his love and gratitude to his family, who kept him focused and encouraged him to do his best. Finally, the author would like to thank God and his generous providence.

TABLE OF CONTENTS

TABLE OF CONTENTS
(Continued)

TABLE OF CONTENTS
(Continued)

TABLE OF CONTENTS
(Continued)

TABLE OF CONTENTS
(Continued)

LIST OF TABLES

LIST OF FIGURES

LIST OF FIGURES
(Continued)

LIST OF FIGURES
(Continued)

LIST OF FIGURES
(Continued)

LIST OF FIGURES
(Continued)

Figure **Page**

LIST OF FIGURES
(Continued)

Figure **Page**

LIST OF FIGURES
(Continued)

Figure **Page**

LIST OF FIGURES
(Continued)

Figure **Page**

LIST OF FIGURES
(Continued)

Figure **Page**

LIST OF FIGURES
(Continued)

Figure **Page**

LIST OF FIGURES
(Continued)

Figure **Page**

LIST OF FIGURES
(Continued)

Figure **Page**

LIST OF FIGURES
(Continued)

LIST OF FIGURES
(Continued)

LIST OF FIGURES
(Continued)

CHAPTER 1

INTRODUCTION

1.1 Objective and Scope of Work

The three main goals of this research, presented in the following dissertation, are the following:

1) Control the process of radio-frequency (RF) reactive magnetron sputtering for the growth of high-quality metal-oxide thin films on fluorine-doped tin oxide (FTO)-coated glass substrates and understand the effect of various parameters of RF reactive magnetron sputtering on the resultant properties of metal-oxide thin films.

2) Understand the metal-oxide thin films as a photoelectrode for photoelectrochemical (PEC) systems for producing hydrogen in an aqueous solution by solar energy.

3) Engineer the bandgap of metal-oxide films to effectively use visible light for solar energy-driven hydrogen production.

Hydrogen is widely considered to be the fuel of the future. It has potential applications for nonpolluting vehicles, domestic heating, and aviation. The use of fuel cells powered by hydrogen generated by solar energy will reduce harmful emissions to nearly zero. Thus, in recent years, hydrogen production through direct water splitting has become a very important research area.

This research was driven by a very specific application to develop photoelectrodes for efficient photoelectrochemical water splitting to produce hydrogen in an aqueous solution by solar energy. Efficient PEC splitting of water to produce hydrogen requires photoelectrodes that (1) are highly stable, (2) have band-edge positions that match the

H_2/H_2O and H_2O/O_2 levels and (3) can absorb most of the photons from the solar spectrum. A concern for direct high-efficient PEC water splitting is the lack of materials that can satisfy all these requirements. Oxides are the most photoelectrochemically stable semiconductors in aqueous solutions.

Transition metal oxides, such as ZnO, TiO_2, WO_3, and Fe_2O_3, also meet the second criterion. PEC systems based on transition metal oxides have received extensive attention due to their potential applications for H_2 production in an aqueous solution by solar energy. However, until now, the demonstrated efficiencies of these oxides have not been satisfactory. The main reason is that these oxides are poor absorbers of photons in the visible region of the solar spectrum because their bandgap is too large. In order to improve the efficiency, the bandgap of these oxides must be narrowed. To date, only TiO_2 has received extensive attention. ZnO has a similar bandgap and band-edge position compared to TiO_2. However, ZnO has a direct bandgap and higher electron mobility compared to TiO_2. Thus, ZnO is expected to be an even better candidate for PEC applications. Like TiO_2, the bandgap of ZnO (~3.3 eV) is too large to use visible light effectively because the solar spectrum has a maximum intensity at ~2.7 eV. Therefore, it is critical to reduce the bandgap of ZnO.

So far, impurity incorporation has been the main method to reduce the bandgap of TiO_2 and WO_3. It has been reported that N, C, and S doping can successfully narrow the bandgap of TiO_2 and WO_3 and improve the photoresponse in the long-wavelength region. Significant amounts of N can only be incorporated into TiO_2 and WO_3 at low temperatures. However, films grown at low temperatures usually exhibited very poor crystallinity, which is extremely detrimental to the PEC performance. Although TiO_2 and

bandgap-reduced TiO_2 have been studied extensively, very limited research exists on using a ZnO photoelectrode for PEC water splitting to produce hydrogen. Thus, there is an immediate need to study extensively ZnO and other metal oxides such as ternary cobalt-based spinal oxides, Cu-Ti-oxide, Cu-W-oxide, Cu-Sn-oxide, doped Cu-Ti-oxide and doped Cu-W-oxide thin films for PEC water-splitting applications.

The research work presented in this dissertation relates to deposition of ZnO, doped and co-doped ZnO thin films, and cobalt-based and copper-based metal-oxide thin films using RF reactive magnetron sputtering system. A series of depositions have been carried out in this system with various sputtering process parameters. The influence of these process parameters on film properties has been investigated. High-purity (99.9999%) argon, oxygen, and nitrogen have been used as sputtering gas ambient for deposition of metal-oxide thin films in some experiments.

ZnO thin films in the form of compact structures and nanostructures were successfully synthesized. Bandgap reduction in ZnO thin films was realized by doping with N and Cu. *p*-type doping in ZnO was achieved by heavy Cu incorporation. Charge-compensated acceptor-donor co-doping in ZnO with enhanced crystallinity and PEC responses were demonstrated. Nanorod and porous ZnO nanocoral structures were synthesized and demonstrated a 10-fold increase in PEC response compared to compact ZnO films. Bandgap-reduced solid solution of ZnO and GaN (ZnO:GaN) thin films that exhibited improved PEC responses were synthesized. Ternary cobalt-based spinal oxides, Cu-Ti-oxide, Cu-W-oxide, Cu-Sn-oxide, doped Cu-Ti-oxide, and doped Cu-W-oxide thin films were successfully deposited and extensively studied for PEC water-splitting applications.

The results obtained in this research were based on the analysis of many experiments for deposition of metal-oxide thin films and their characterization. Characterization techniques included stylus profilometry, X-ray diffraction (XRD), atomic force microscopy (AFM), scanning electron microscopy (SEM), transmission electron microscopy (TEM), X-ray photoelectron spectroscopy (XPS), secondary-ion mass spectroscopy (SIMS), n & k analysis, spectrophotometry and photoelectrochemical measurements.

An effort was made to better understand the deposition process of metal-oxide thin films and the potential applications of PEC water splitting to produce hydrogen in an aqueous solution using solar energy. ZnO thin films with reduced bandgap with enhanced crystallinity and PEC responses were successfully demonstrated. The cobalt- and copper-based metal-oxide thin films were studied extensively. These findings will also have potential applications in other fields of technology and industry.

1.2 Synopsis

This dissertation presents the results of the work on metal-oxide thin-film deposition by RF reactive magnetron sputtering system undertaken at the National Renewable Energy Laboratory (NREL). The presentation of this thesis begins with a background of photoelectrochemical water splitting to produce hydrogen using solar energy, as well as a literature review. A general description of the properties of zinc oxide and cobalt-based ternary oxide is discussed later in Chapter 2. Deposition techniques for thin films with special emphasis on sputtering are discussed in detail in Chapter 3. The details of the system including sample preparation method, substrate mounting, and experimental

parameters are discussed in Chapter 4. The working principles of various characterization techniques used in this work are addressed in Chapter 5. Chapter 6 is dedicated to results and discussion of the research work carried out in this dissertation. Conclusions and recommendations based on this work is presented in the last chapter.

CHAPTER 2

BACKGROUND

2.1 Hydrogen: Future Fuel

Hydrogen is widely considered as a potential alternative to fossil fuels for producing and storing energy. Our current global economy depends heavily on fossil fuels, which are integral to agriculture, industry, transportation, and day-to-day life. Consequently, there have been intense efforts to develop various technologies based on the applications of hydrogen as a fuel, instead of fossil fuels, for the following reasons:

- Deposits of fossil fuels are limited.
- There is a need for a fuel generated from raw materials that are abundantly available.
- The price of fossil fuels is increasing.
- The use of fossil fuels is responsible for climate change [1, 2–6].
- Fossil fuels are not renewable.
- There is a need for a fuel that is environmentally safe.
- Dependence on other countries for fossil fuels is detrimental to the economic security of the nation.

Hydrogen is a versatile energy carrier that has many potential applications, including powering of nonpolluting vehicles and aircrafts, and domestic heating. Therefore, along with photovoltaics, hydrogen is expected to be the foundation of sustainable energy systems [1–3, 7].

Hydrogen is not present in nature in a gaseous form; however, it is abundantly available in water. Therefore, hydrogen must be extracted from the water. To date, steam

reforming has been the principal technique to produce hydrogen [2, 7]. Hydrogen is also produced by water electrolysis using electricity obtained from the combustion of fossil fuels. However, these technologies cannot be considered environmentally friendly because they emit CO_2. On the other hand, a better option to consider is hydrogen obtained using photoelectricity. In addition, such hydrogen represents a storable fuel that is produced from photoelectricity, a nonstorable source of energy [1].

The advantages of hydrogen as a universal energy medium are listed as follows [8]:

- Non-toxic.
- Combustion of hydrogen simply produces liquid water and steam. In this respect, hydrogen use is completely safe from an environmental perspective.
- Easily assimilated into the biosphere: its combustion products are recycled by plants to make carbohydrates.
- Possible to produce hydrogen from the most abundant chemical on earth: water. Hydrogen can be obtained electrolytically, photoelectrochemically, thermochemically, by direct thermal decomposition of water, or biochemically from water.
- The most suitable fuel for use in fuel cells—direct conversion of chemical energy into electricity with an enhanced efficiency.
- Can be used as a feedstock for the chemical industry, enabling the production of an entire gamut of chemicals from hydrogen and conventional petrochemicals.
- Transmission of energy in the form of hydrogen is more economical than through high-voltage alternating-current (AC) lines at large distances.

Hydrogen Generation Using Solar Energy

Unlike fossil fuel reactions—which results in carbon monoxide, carbon dioxide, sulfur dioxide, or particulates—the combustion of hydrogen results in the generation of water, which does not result in air pollution or lead to the emission of greenhouse gases. The

electrolysis of water to produce hydrogen is easily achieved using an electrochemical cell. Water will be split into hydrogen and oxygen gases if a voltage is applied between two electrodes submerged in an acidic or basic aqueous solution. The water-splitting reaction will only occur when external energy is supplied, for example, in the form of electricity. Hydrogen can be produced sustainably—and its generation considered environmentally friendly—if the energy required for splitting water electrochemically is supplied by a renewable energy source, such as solar, wind, hydroelectric, or hydrothermal energy. Solar hydrogen can be produced wherever sunlight and water are available, enabling distributed energy generation and reducing the dependence on countries rich in fossil fuels for energy supplies.

To date, the technologies for hydrogen generation using sources of renewable energy are in the incubation stage. But, there is tremendous growing interest in developing hydrogen technologies that rely on renewable sources of energy. From the literature, the most-promising method of hydrogen production is photoelectrochemical (PEC) water decomposition using a source of renewable energy such as solar energy [1, 9–53]. There have been many papers published on the impact of various structures and materials on the performance of PEC cells since the first reports of this method were published by Honda et al. [9–12] almost 30 years ago [1].

2.2 Photoelectrochemistry of Water Decomposition

2.2.1 Principles

The photoelectrochemical decomposition of water is based on the principle that when two electrodes, at least one of which is a semiconductor, are immersed in an aqueous electrolyte and exposed to light, the absorbed light energy will be converted into electricity. This electricity is then used for water electrolysis [1]. In the PEC process, reactions occurring at the photo-anode and cathode result in the separate evolution of oxygen and hydrogen, respectively.

The photo-electrodes in the assembly can be arranged as follows: (1) photo-anode made of an n-type semiconductor and cathode made of metal or photo-cathode made of a p-type semiconductor, and (2) anode made of metal and photo-cathode made of a p-type semiconductor.

Figure 2.1 shows the PEC cell for the photoelectrolysis of water. In a typical PEC cell, both photo-anode (semiconductor) and cathode (metal) will be immersed in an electrolyte. When light is exposed to the photo-anode, if the energy of the photons ($h\nu$) is equal to or larger than the bandgap of the semiconductor material, intrinsic ionization of the n-type semiconducting materials over the bandgap occurs, leading to the formation of electrons in the conduction band and holes in the valence band.

$$2h\nu \rightarrow 2e^{/} + 2h^{\cdot}, \tag{2.1}$$

where, h is Planck's constant, ν is frequency, $e^{/}$ is the electron, $h^{\cdot}$ is the hole.

The process results in water oxidation into gaseous oxygen and hydrogen ions at the photo-anode/electrolyte interface:

$$2h^{\cdot} + H_2O_{(liquid)} \rightarrow \tfrac{1}{2}\, O_{2(gas)} + 2H^{+}. \tag{2.2}$$

The charge transport involves electron transport in the external circuit and the migration of hydrogen ions in the electrolyte to the cathode, where hydrogen ions are reduced to gaseous hydrogen [1]:

$$2H^{+} + 2e^{/} \rightarrow H_{2(gas)}. \tag{2.3}$$

Accordingly, the overall reaction of the PEC cell may be expressed in the form:

$$2h\nu + H_2O_{(liquid)} \rightarrow O_{2(gas)} + H_{2(gas)}. \tag{2.4}$$

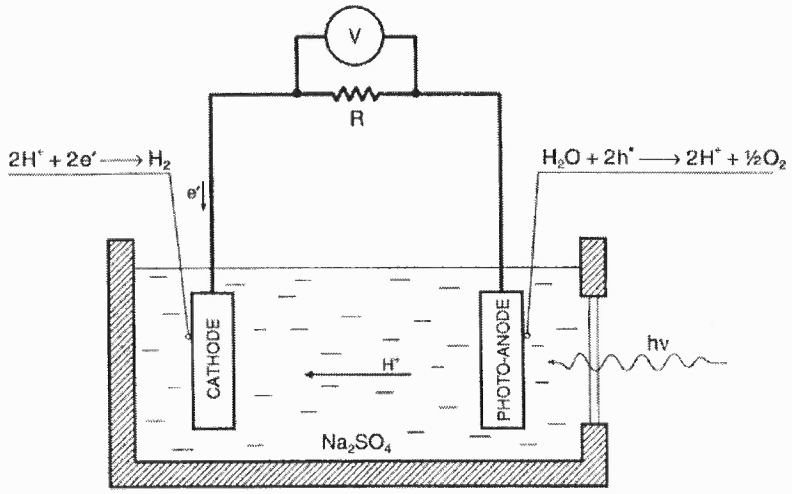

Figure 2.1 Structure of photoelectrochemical cell for water photoelectrolysis [1, 9].

2.2.2 Formation of Electrochemical Chain of PEC

Figure 2.2(a–d) shows a schematic of various stages in the formation of the electrochemical chain of the PEC cell, involving the photo-anode of an n-type semiconductor and metallic cathode. The figure shows the band structure of anode (semiconductor), cathode (metal), and electrolyte under various conditions, such as initial condition when no contact is made, after galvanic contact under dark condition, after light illumination, and after light illumination with applied anodic bias in comparison

with the corresponding H^+/H_2 and O_2/H_2O redox couples. These figures show the various energy quantities, such as: work function, band levels of the electrodes before and after the chains are established, and band bending [1].

Figure 2.2(a) shows the energy diagram before the galvanic contact is made between the two electrodes. The semiconductor has a low work function compared to metal, so when the contact is made between the two electrodes under dark condition, the result is electronic charge transfer from the semiconductor to metal until the work functions of both electrodes assume the same value, as shown in Fig. 2.2(b). This charge transfer results in a region depleted of electrons at the semiconductor surface known as space-charge layer or depletion layer. Negatively charged ions in the electrolyte are attracted toward the positively charged region, resulting in a very thin (< 1 nm) Helmholtz layer. The equilibration of the electrochemical potentials of the electrolyte and the semiconductor leads to band bending of magnitude V_B.. The H^+/H_2 energy level is still above the Fermi energy level of the cathode (metal), which is not favorable for water decomposition. The surface potential of the photo-anode and H^+/H_2 potential are lowered by the illumination of light, as shown in Fig. 2.2(c). To elevate the cathode E_F level above the H^+/H_2 energy level, anodic bias is applied under illumination, thus making the process of water decomposition possible (as shown in Fig. 2.2(d)) [1].

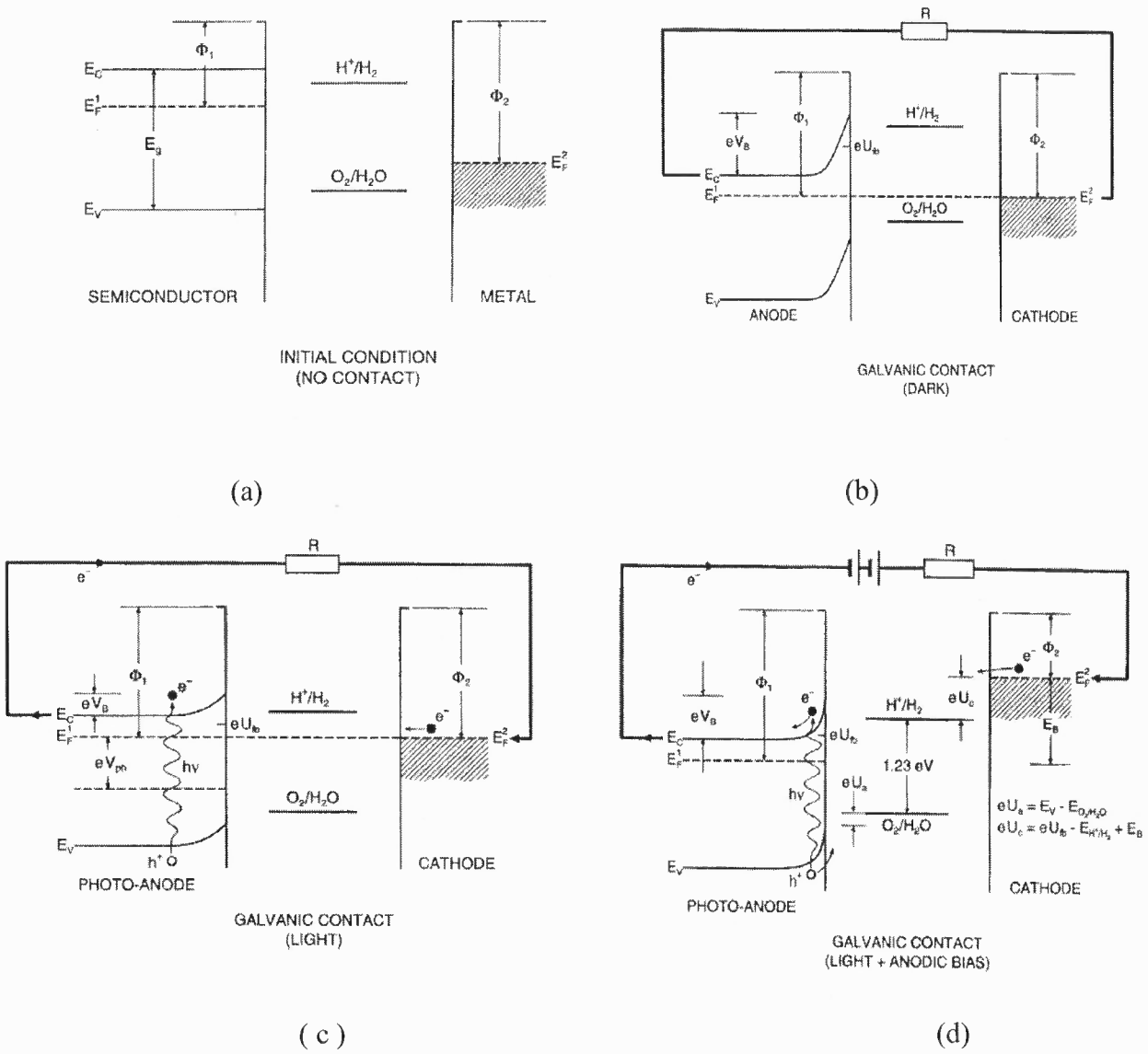

Figure 2.2 Energy diagram of PEC components: Anode (semiconductor), electrolyte, and cathode (metal): (a) before galvanic contact, (b) after galvanic contact between anode and cathode, (c) effect of light on electronic structure of PEC components, and (d) effect of light on the energy diagram of PEC cell with externally applied bias [1].

2.3 Material Aspects of Photoelectrochemical Cells

The photo-electrodes materials used in PEC cells should perform three fundamental functions: (1) optical function required to obtain maximum absorption of solar energy, (2) catalytic function required for water decomposition, and (3) stability in the aqueous

solution. The properties of photo-electrodes should satisfy several specific requirements in terms of semiconducting and electrochemical properties, including [1, 12, 24, 29, 40, 53]:

- Bandgap
- Helmholtz potential
- Schottky barrier
- Flat-band potential
- Electrical resistance
- Corrosion resistance

2.3.1 Bandgap

A semiconducting material is characterized by bandgap E_g. The bandgap is defined as the energy difference between the bottom of the conduction band and top of the valence band. Only that part of incident radiation having energy more than the band gap will be absorbed by the bandgap. This indicates that photons having energy less than E_g, are not available for energy conversion. Therefore, photon-induced ionization through the bandgap is an important quantity for materials that are candidates for photo-electrodes. The optimal bandgap for high-performance photo-electrodes is ~2 eV [1, 12, 24, 29, 53, 54, 55].

2.3.2 Helmholtz Potential Barrier

When a semiconducting photo-electrode material is immersed in a liquid electrolyte, the charge transfer from the semiconductor to the electrolyte leads to the formation of a surface charge of the semiconductor and results in upward band bending, forming a potential barrier similar to that of the solid/solid interface. This surface charge is

compensated by a charge of the opposite sign, which is induced in the electrolyte, which forms a very thin layer (< 1 nm) and is formed of oriented water-molecule dipoles and electrolyte ions adsorbed at the electrode surface known as the Helmholtz layer [1, 53, 56, 57]. The height of this potential barrier is called the Helmholtz barrier. The properties of the photo-electrode surface and nature of the aqueous environment of the electrolyte have a profound influence on the Helmholtz barrier, which, in turn, determines the performance of PEC cells [1, 53].

2.3.3 Schottky Barrier

Because of surface states, concentration gradients, and adsorption states, a potential drop occurs within the interface layer of the solid, called a Schottky barrier. The Schottky barrier plays a crucial role in preventing recombination of the charge formed as a result of photo-ionization [1]. This is because holes, which reside in the valence band, tend to float and move to upper energy levels in the valence band, whereas electrons, which lie in the conduction band, tend to move to lower energy levels in the conduction band. In the case of an n-type semiconductor, the band edges near the interface are curved upward. The absorption of photons can occur at the interface or the bulk of the semiconductor depending on the depth of penetration of light; but the holes produced always move to the interface where they can move to higher energy levels because of the upward curvature. The electrons, on the other hand, move to the bulk of the semiconductor, where they find lower energy than the interface. This effectively separates the electron-hole pairs.

2.3.4 Flat-band Potential

This flat-band potential, U_{fb}, is an important parameter in photo-electrode reactions in PEC cells. To make the bands flat, a potential has to be imposed over the electrode/electrolyte interface, termed as the flat-band potential [24, 53, 54]. When the flat-band potential is higher than the redox potential of the H^+/H_2 couple, water photo-electrolysis may occur [24, 53, 54].

2.3.5 Electrical Resistance

The major source of energy losses from the ohmic resistances of the internal and external circuits of PEC cell constitute electrodes, electrolyte, electrical leads (wires), electrical connections, measurement and control equipment. The electrical resistances of these sources must be minimized to achieve maximum conversion efficiency [1].

2.3.6 Corrosion and Photo-Corrosion Resistance

A very important property desired in the photo-electrodes is very high resistance to electrochemical corrosion and photo-corrosion, from the reactions at the solid/liquid interface, resulting in degradation of its properties. The chemical corrosion occurs when a semiconductor may itself be reactive toward the electrolyte and reacts with it even in the absence of light-generated charge carriers. In contrast, photo-corrosion results when free electrons and holes are generated in the semiconductor, causing a chemical reaction between the semiconductor and electrolyte, and thus altering the chemical nature of the semiconductor and destroying its semiconducting properties. When any form of reactivity occurs, the chemical composition and the related properties of the electrode and photo-electrode change [1, 53, 54]. These changes are not beneficial to the properties of the

photo-electrode, which is essential for photo-conversion. Therefore, the photo-electrodes must be resistant to these types of undesired reactivities [1].

Although valence semiconductors [58, 59] exhibit suitable semiconducting properties such as bandgap width and direct transition, they are not resistant to electrochemical corrosion when exposed to aqueous environments. More suitable candidates for photo-electrodes for electrochemical water decomposition are certain oxide materials, such as TiO_2 and its solid solutions, because they are particularly resistant to these reactivity types [1, 9, 19, 53].

2.4 Impact of Bandgap of Photo-Electrode Material on Solar Energy Spectrum

2.4.1 Solar Energy Spectrum

It is well known that that the maximum amount of energy of the solar spectrum is in the visible region (above ~1.4 eV and below ~3 eV). Hence, to obtain maximum conversion efficiency, an ideal semiconductor should have a bandgap that can absorb the visible region of the solar spectrum [1]. In theory, the minimum energy required to split the water molecule is 1.23 eV. The solar energy spectrum illustrated in Fig. 2.3 depicts segments defining phonon fluxes corresponding to different energy ranges.

In practice, because of various energy losses, the energy that may be used for conversion is smaller than the theoretical energy limit. The estimated value of these combined losses is ~0.8 eV; therefore, the optimal energy range in terms of the photons available for conversion is ~2 eV.

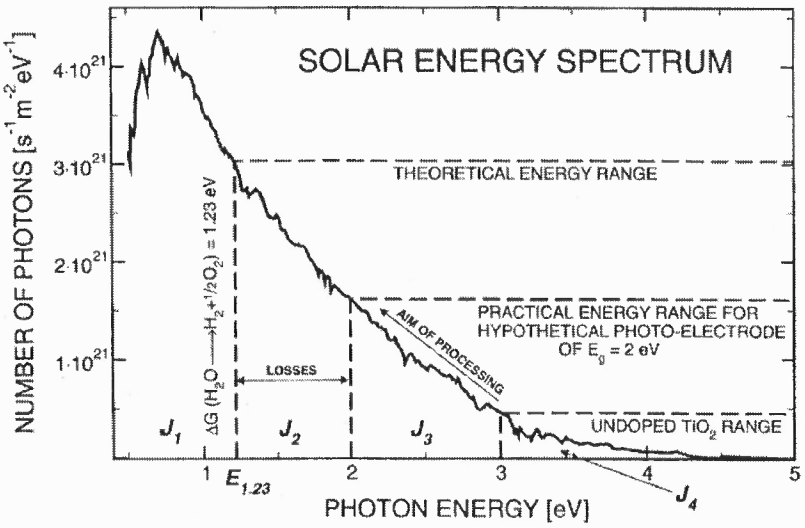

Figure 2.3 Solar energy spectra (AM of 1.5) in terms of number of photons vs. photon energy, showing different flux photon regimes corresponding to specific properties of photoelectrodes [1, 60].

2.5 Literature Review

Various semiconductors have been studied as water-splitting photoelectrodes, but none examined thus far meet all of the requirements to be optimal. Wide-bandgap semiconductors such as TiO_2 and $SrTiO_3$ have the appropriate band-edge energies for water splitting and have good PEC stability, but their bandgaps are too large to absorb a reasonable fraction of the solar spectrum. Valence semiconductors have appropriate bandgaps, but they are not stable in aqueous solutions [1].

The energy conversion efficiency (n_c) of an undoped TiO_2 photo-anode for both thin-film [11] and single-crystal [61] morphologies has been measured to be 0.4% [11, 61]. Cr-doped TiO_2 resulted in a slight increase in n_c to 0.44%, whereas Al doping resulted in 0.6% efficiency increase [61]. Cu, Ta, V, or Y doping did not lead to any substantial changes in the energy conversion efficiency [62]. A substantial increase in

energy conversion efficiency is observed when an external bias (chemical or electrical) is applied. TiO_2 single-crystals studied by Akikusa and Khan [63] reported much larger values (n_c = 1.6%), which were achieved by applying a chemical bias. Nozik reported the total energy conversion efficiency of 10% for TiO_2 single-crystals, with the application of chemical and electrical biases, as well as ultraviolet (UV) light [1, 16]. Quantum energy conversion efficiencies for various TiO_2 specimens, including single-crystals, polycrystals, thin films, and thin TiO_2 layers formed on metallic Ti through oxidation, were reported by Mavroides et al., and from these data, TiO_2 layers formed by oxidation on metallic Ti exhibited the best performance [15].

Significantly high total energy conversion up to 20% [18] or 25% [27] using high-energy light of specific wavelengths was reported for $SrTiO_3$ single-crystals without the application of a bias [18]. At present, only PEC cells based on $SrTiO_3$ as the photo-anode have been shown to exhibit electromotive force (EMF) values that are sufficient for water decomposition without a bias [1].

Photo-electrodes made of non-oxide materials, including GaAs and Al-doped GaAs, exhibited very high total energy conversion efficiencies, in the range of 12%–18%; however, these reports provided no information about the stability of the photo-electrodes [58, 59]. Energy conversion efficiencies up to 4.46% have been reported for photosensitizers of organic compounds, but they exhibit very little stability in aqueous environments [64, 65]. It is clear from the reported data that the energy conversion efficiencies obtained by using specific energy sources whose energy spectrum differs from that of solar energy may be substantially larger than that from solar energy.

Accordingly, the use of UV light resulted in a substantial increase in energy conversion efficiency [1, 28].

The optimal bandgap for high-performance photo-electrodes is ~2 eV. Such a material that satisfies this requirement and is also corrosion resistant is not available commercially. Therefore, there is a need to develop such a material by bandgap engineering. Philips et. al. [66] have reported that, although adding 30 mol% V to single-crystals and polycrystalline specimens of TiO_2 reduces the bandgap to 1.99 eV, the formation of $(Ti_{0.7}V_{0.3})O_2$ had a detrimental effect on the photo-activity due to a substantial increase in the flat-band potential. Zhao et al. [49, 50] observed that increasing the V content resulted in an increase in the energy conversion efficiency. From the above results, it is possible that the effect of V on the photo-electrode is morphological rather than compositional. $V^{4+/5+}$-doped TiO_2 has also been attempted, which forms a solid solution $(Ti_{1-x}V_x)O_2$. N-incorporated bandgap-reduced TiO_2 and WO_3 have been reported by some groups. A significant amount of N can only be incorporated at low temperatures. However, films grown at low temperatures usually exhibited very poor crystallinity, which is extremely detrimental to the PEC cell performance.

2.6 Zinc Oxide

2.6.1 Introduction

Zinc oxide is an inorganic compound with the formula ZnO. It occurs in nature as the mineral zincite. It is usually white in color and nearly insoluble in water. Zinc oxide is an important material for a variety of applications, and because many of our industries rely

critically on this compound, it has been studied intensively since 1935 [67, 68]. There has been development in growth technologies for fabricating high-quality single-crystals, epitaxial layers, quantum wells, nanorods, quantum dots, and related objects of ZnO. Much of the renewed interest in this material has focused on blue/UV lasers, light-emitting diodes (LEDs), and other optoelectronic devices, in addition to (or instead of) the GaN-based structures, transparent thin-film transistors, electronic devices, spintronics, and transparent conducting oxides (TCOs).

ZnO is an II-VI semiconductor with a direct wide-bandgap of around 3.2 eV and a large exciton binding energy of 60 meV at room temperature. ZnO is naturally an n-type semiconductor partially due to its deviation from stoichiometry, i.e., due to the presence of interstitial Zn atoms (Zn_i) in large voids and the presence of oxygen vacancies (V_o) in the crystal and partially due to the presence of background donors such as H and Al. These defects form donor levels at ~0.05 eV [69].

2.6.2 Crystal Structure

Most group II-VI binary compound semiconductors have cubic, zincblende or hexagonal wurtzite structure. The crystal structure of ZnO can be rock salt, zincblende, and wurtzite, as shown in Figs. 2.4 and 2.5. Its ionicity is at the boundary between the covalent and ionic semiconductors.

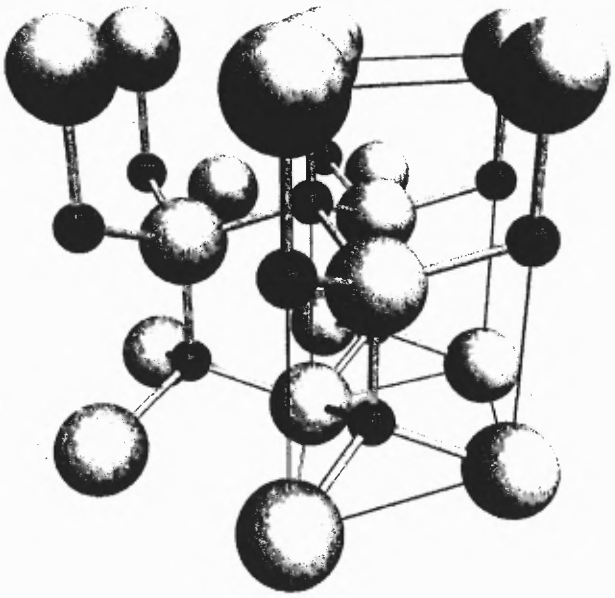

Figure 2.4 The hexagonal wurtzite structure of ZnO. O atoms are shown as large white spheres, Zn atoms as smaller black spheres [67].

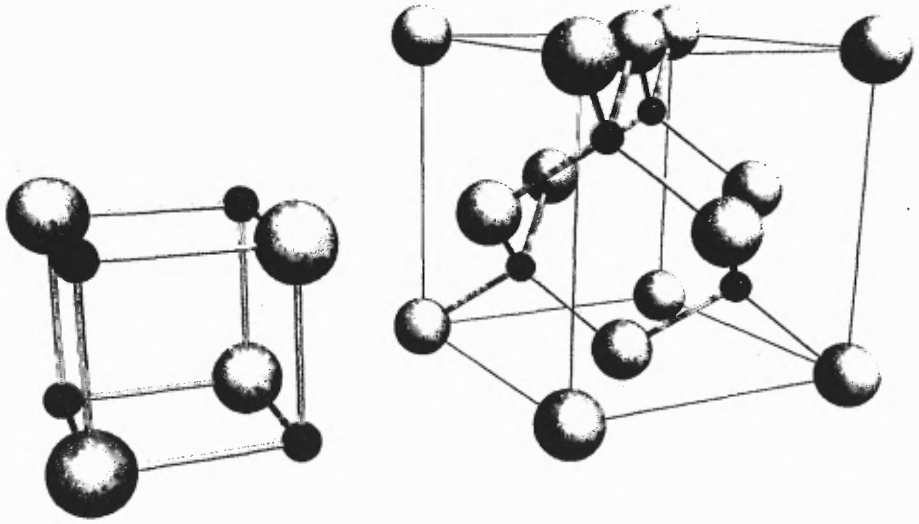

Figure 2.5 The rock salt (left) and zincblende (right) phases of ZnO. O atoms are shown as white spheres, Zn atoms as black spheres [68].

Zinc oxide crystallizes in the wurtzite (B4 type) structure because it is most stable and thus most common at ambient pressure and temperature. This is a hexagonal lattice, belonging to the space group $P6_3mc$, and it is characterized by two interconnecting sub

lattices of Zn^{2+} and O^{2-}, such that each Zn ion is surrounded by a tetrahedron of O ions, and vice versa [67]. Growing ZnO on substrates with cubic lattice structure, the zincblende form can be stabilized. The rock salt NaCl-type structure is only observed at relatively high pressure of ~10 GPa. With ZnO in the wurtzite and zincblende structure, tetrahedral coordination gives rise to polar symmetry along the hexagonal axis. This polarity and other lattice symmetry properties are responsible for a number of the properties of wurtzite ZnO, including its spontaneous polarization and piezoelectricity, and it is also a main factor in etching, defect generation, and crystal growth [67].

2.6.3 Lattice Parameters

Lattice parameters are important to consider when one develops semiconductor devices. There are four main factors that determine the lattice parameters of the semiconductor. The first is free-electron concentration, which affects the potential of the bottom of the conduction band normally occupied by electrons. The second factor is the concentration of impurities and defects and the difference in ionic radii between these defects and impurities and the substituted matrix ions. The third factor is the external strains. The last factor is the temperature-dependence in the semiconductors. The lattice parameters of the hexagonal unit cell are a = 3.2495 Å and c = 5.2069 Å, and the density is 5.605 g cm^{-3} [70]. Table 2.1 shows basic physical parameters of ZnO [67].

Table 2.1 Key Physical Parameters of ZnO [67]

Properties	Value
Stable crystal structure	Wurtzite
Space group	C_{6v}^4 ($C6_3mc$)
E_g (eV)	3.4
m^*_e (m_0)	0.28
m^*_{hh} (m_0)	0.78
a (Å)	3.2
c (Å)	5.2
Density ρ (g cm^{-3})	5.606
Melting point (°C)	1975
Refractive index	2.008 2.029
Thermal conductivity at 300 K (W/(cm.K))	0.6, 1–1.2
Linear thermal expansion (/°C)	*a:* 6.5 x 10^{-6} *c:* 3.0 x 10^{-6}

2.6.4 Electrical Properties and Bandgap

ZnO is considered a good candidate for electronic and optoelectronic devices because it is a direct and wide-bandgap semiconductor with large binding energy (~60 meV). For example, a device made by material with a larger bandgap may have a high breakdown voltage, lower noise, and can operate at higher temperatures with higher power. The performance of electron transport in a semiconductor is different at low and high electrical fields.

The energy distribution of electrons in ZnO does not change much at very low electrical fields, because the electrons cannot get much energy from the applied electrical field, compared with their thermal energy. So, the scattering rate, which determines the electron mobility, does not change much and results in constant electron mobility. At a high electrical field, the energy of the electrons from the applied electrical field is comparable with their thermal energy. The electron distribution function then deviates far away from its equilibrium value. These electrons become hot electrons, whose temperature is higher than the lattice temperature. When the electron drift velocity is higher than its steady-state value, it is possible to make a higher-frequency device.

Due to the large variance of the quality of sample available, the electrical properties of ZnO are very difficult to quantify. Depending on the quality of the layers, the carrier concentration varies considerably, but is typically ~10^{16} cm^{-3}. The largest reported n-type doping is ~10^{20} electrons cm^{-3}, and the largest reported p-type doping is ~10^{19} hole cm^{-3} [67, 71]. The electron effective mass is $0.24m_o$, and the hole effective mass is $0.59m_o$. The corresponding electron Hall mobility at 300 K for low n-type conductivity is μ = 200 $cm^2V^{-1}s^{-1}$ and for low p-type conductivity is 5–50 $cm^2V^{-1}s^{-1}$ [67, 72].

Optical bandgap values from 3.1 to 3.3 eV have been reported for the ZnO single-crystals at room temperature, as well as 3.44 eV at 4 K [73, 74]. The optical bandgap of pure polycrystalline ZnO film is close to 3.28–3.30 eV for various deposition methods [75–77].

All ZnO films exhibit n-type conductivity, made without any intentional doping, caused by a deviation from stoichiometry due to native defects [78]. Traditionally, the

two intrinsic defects most commonly reported in the literature as the dominant background donors in ZnO are the oxygen vacancy (V_o) and interstitial Zn (Zn_i) [79, 80]. It has been demonstrated that Zn_i is a shallow donor, and the donor levels lie in the range of 0.025–0.03 eV below the conduction band [81]. Recent work shows that V_o does not give rise to a shallow donor level [82]. In contrast to the earlier investigations, it was considered to be a deep center about 0.6 or 0.7 eV below the conduction band [83]. In addition, based on first-principles calculations and experimental confirmation, a new source responsible for the observed n-type conductivity has been suggested recently, namely, hydrogen atoms that act as shallow donors [84–86].

Figure 2.6 shows the local-density approximation (LDA) band structure of bulk wurtzite ZnO calculated using dominant atomic self-interaction-corrected pseudopotentials [67, 87]. Both the valence-band maxima and the lowest conduction-band minima occur at the Γ point k = 0, indicating that ZnO is a direct bandgap semiconductor. The bandgap determined from this calculation is 3.77 eV, which matches reasonably well with the reported experimental value of 3.4 eV. Table 2.2 summarizes important electrical parameters of ZnO [67].

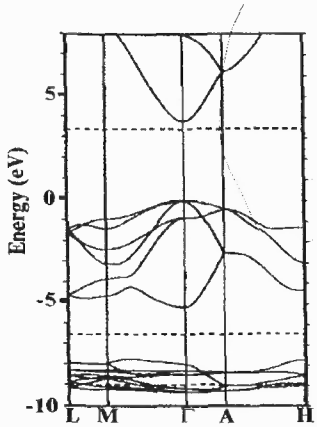

Figure 2.6 The LDA band structure of bulk wurtzite ZnO calculated using dominant atomic self-interaction-corrected pseudopotentials [1, 87].

Table 2.2 Important Electrical Parameters of ZnO [67]

Properties	Value
Bandgap E_g (eV) (300 K)	3.4 direct
Static dielectric constant $\varepsilon_s/\varepsilon_0$	8-8.5
Effective mass of an electron in conduction band, m^*_e	0.28 m_0
Effective mass of an hole in valence band, m^*_h	1.8 m_0
Pressure coefficient dE_g/d_p (meV kbar^{-1})	2.33
Electron affinity (eV)	4.35
Work function (eV)	4.45
Electron mobility at 300 K (cm^2/V-s)	200
Hole mobility at 300 K (cm^2/V-s)	180
Donor level (E_c-E_d) (eV)	0.03

2.6.5 Mechanical Properties

Mechanical properties are also very important in semiconductors, which are related to the following concepts: hardness, piezoelectric constants, bulk modulus, and yield strength. ZnO is a relatively soft material, with a hardness of ~5 GPa at a plastic penetration depth of 3000 nm (for c-axis-oriented bulk ZnO) [67, 88]. There is also some indication that the crystal orientation of ZnO influences the mechanical properties due to the orientation of the basal planes [67, 89, 90]. A-axis-oriented bulk ZnO is significantly softer than c-axis material, with a hardness of ~2 GPa at a plastic penetration depth of 50 nm below contact. Studies show that epitaxial ZnO grown on sapphire is slightly harder than its bulk counterpart, with a hardness of ~5.7 GPa for a c-axis epitaxial layer. Table 2.3 shows key mechanical properties of *c*-axis-oriented wurtzite ZnO, as determined by experiment and theory [67].

Table 2.3 Key Mechanical Properties of *c*-axis-oriented Wurtzite ZnO, as Determined by Experiment and Theory [67]

Parameter	Experimental	Theoretical
Bulk Young's modulus, *E* (GPa)	111.2±4.7	
Bulk hardness, *H* (GPa)	5.0±0.1	
Epitaxial Young's modulus, *E* (GPa)	310±40	
Epitaxial hardness, *H* (GPa)	5.75±0.8	
Bulk modulus, *B* (GPa)	142.4	156.8
dB/dP	3.6	3.6
e_{33} (C m^{-2})	0.96	1.19
e_{31} (C m^{-2})	-0.62	-0.55
e_{15} (C m^{-2})	-0.37	-0.46
Spontaneous polarization (C m^{-2})		-0.047
c_{11} (GPa)	209	246
C_{33} (GPa)	216	246
C_{12} (GPa)	120	127
c_{13} (GPa)	104	105
c_{44} (GPa)	44	56
Born effective charge, Z*		2.1

2.6.6 Thermal Expansion Coefficient, Thermal Conductivity and Specific Heat

The thermal expansion coefficients of ZnO are $\alpha_a = 4.31 \times 10^{-6}$ K^{-1} and $\alpha_c = 2.49 \times 10^{-6}$ K^{-1} at 300 K [91]. Figure 2.7 shows a plot of the ZnO thermal expansion coefficient, α_{th}, as a function of temperature. The highest measured values of thermal conductivity on the polar faces of ZnO [67, 92] gives the value of k = 1.02±0.09 and 0.98±0.08 W $cm^{-1}K^{-1}$. The other values measured from ZnO typically fall in the range of k = 0.6–1 W cm^{-1} K^{-1} [67, 93].

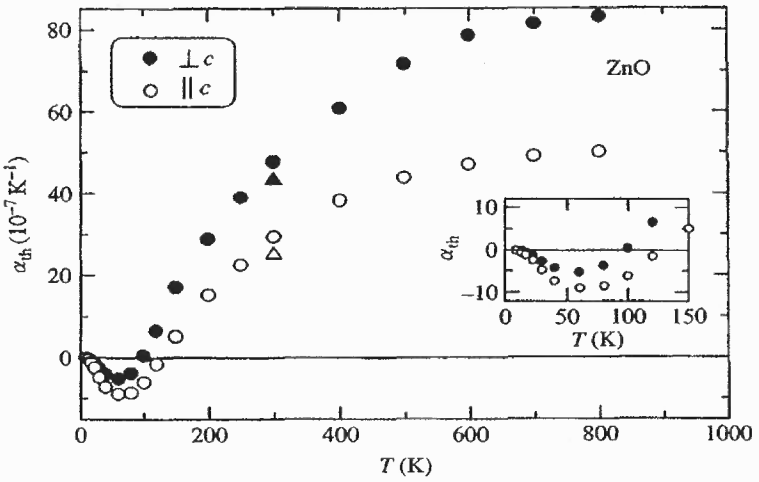

Figure 2.7 Graph of the ZnO thermal expansion coefficient α_{th} as a function of temperature [67, 94].

There are very limited data available in the literature for specific heat measurements in ZnO [67]. The specific heat capacity of ZnO at constant pressure is C_p = 40.3 J mol^{-1}K^{-1} [71]. Figure 2.8 shows the specific heat data for pure (bulk) and varistor ZnO measured between 1.7 and 25 K [95].

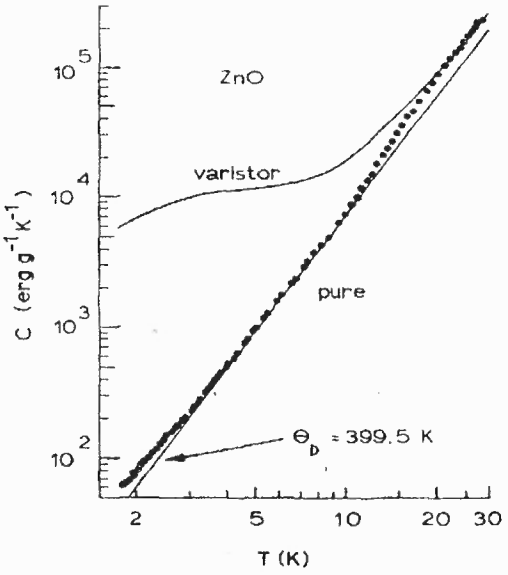

Figure 2.8 The specific heat data for pure (bulk) and varistor ZnO measured between 1.7 and 25 K [67, 95].

sites (see Fig. 2.9) [116–118]. Therefore, isovalent substitution on the spinel cations sites can, in principle, be used to influence both the band-edge character and the magnitude of the electronic bandgaps and optical absorption.

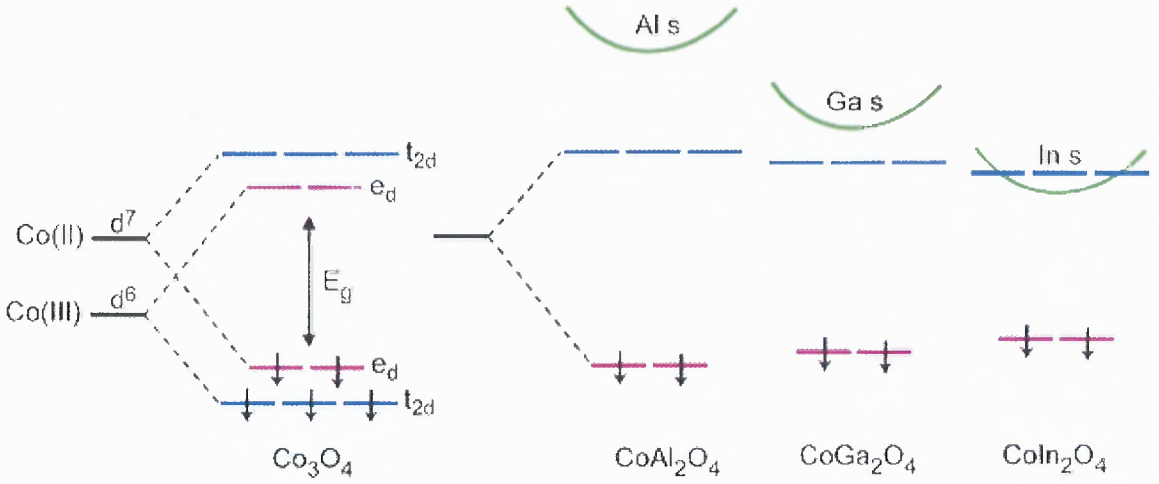

Figure 2.9 Illustration of crystal-field splitting of the minority spin Co 3d states in Co_3O_4 and band-edge electronic structure in the ternary CoX_2O_4 (X = Al, Ga, In) spinels.

The majority of ternary oxides of the form AB_2O_4 adopt the spinel structure, as shown in Figure 2.10. The cubic spinel crystal lattice is based on a face-centered cubic (fcc) packing of oxygen atoms. The A atoms, generally in a +2 oxidation states, occupy 1/8 of the tetrahedral holes, while the B atoms, generally +3, occupy 1/2 of the available octahedral holes. In addition to this "normal" spinel arrangement, it is also possible for the B atoms to occupy tetrahedral sites with a mixture of A and B atoms distributed on the octahedral sites, referred to as the "inverse" spinel structure.

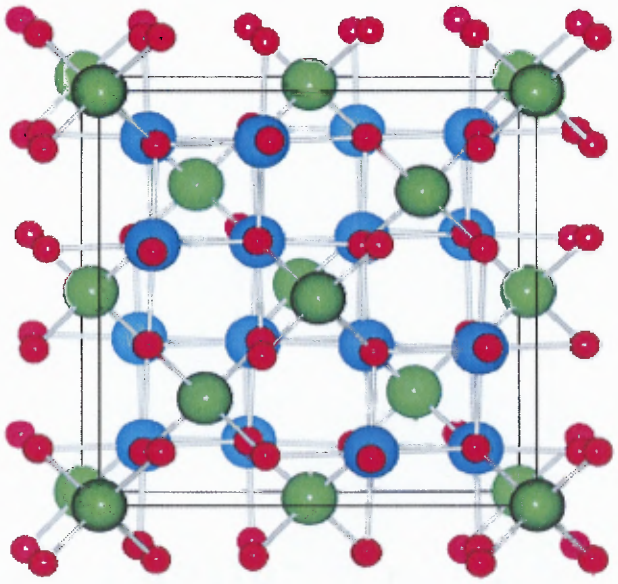

Figure 2.10 Representation of the 56-atom conventional AB_2O_4 spinel unit cell with 8 T_d (A) and 16 O_h (B) cation sites colored green and blue, respectively. The 32 oxygen sites are colored red.

$CoAl_2O_4$ has been used in various applications, such as ceramic pigment (Thénard's blue) [119] and optical coatings, and it is also important as a heterogeneous catalyst in the reformation of methane [120]. The solid-state reaction of Co and Al oxides to form $CoAl_2O_4$ requires a very high temperature of 1200°C [121]. However, $CoAl_2O_4$ is known to exhibit high chemical stability and is insoluble even in acidic solutions, which makes it particularly interesting for PEC applications. $CoAl_2O_4$ exhibits hole-mediated p-type conductivity [122], which is characteristic of oxides formed from transition metals with accessible higher oxidation states.

CHAPTER 3

DEPOSITION TECHNIQUES

3.1 Introduction

The structural, optical, and electrical properties of thin films are of great importance in their device applications. It is demonstrated that the film fabrication techniques play a significant role in governing the properties of films because they depend strongly on the preparation methods and parameters used for a given processing technique. This section, in general, describes the main film growth equipment employed for preparing thin films in this work—a physical vapor deposition (PVD) technique, namely, RF magnetron sputtering.

A variety of deposition techniques, including spray pyrolysis [123-125], sol-gel method [126], chemical vapor deposition (CVD) [127, 128], molecular-beam epitaxy (MBE) [129], pulsed-laser deposition (PLD) [130, 131], and sputtering [132, 133] have been employed to grow ZnO thin films on various substrates. Of special interest is RF magnetron sputtering because it offers safety advantages, avoids the use of toxic gases, has low cost, has high stability in hydrogen plasma and heat cycling, and grows at low temperatures. In addition, sputtering of ZnO has a relatively high deposition rate and hence is well suited for industrial-scale and large-area deposition for applications in PEC devices.

For many decades, thin films have been deposited using physical and chemical vapor deposition techniques. Thin films are of interest not only because they are thin, but also, because the ratio of the surface area to bulk volume is so high that the surface

properties become very important [134]. Physical vapor deposition processes involve controllable transfer of atoms or molecules from a source to a substrate, in which film formation and growth proceeds. Main categories of PVD are vacuum evaporation and sputter deposition. Vacuum evaporation is a process in which atoms or molecules, emitted from a thermal evaporation source, deposit on the substrate with little or no collision with gas molecules in space between the source and the substrate, so that their trajectory is a line of sight. One of the advantages of evaporation can be the high deposition rates [135]. In sputtering, atoms are removed from the solid target (source) surface through impacts of gaseous ions. Chemical vapor deposition is the process of forming stable solids by the decomposition of gaseous chemicals using heat, plasma, ultraviolet, or other energy sources, or a combination of sources [134].

3.1.1 Sputtering

The sputtering phenomenon can be described as follows: when a solid surface (target) is bombarded by accelerated ions (energetic particles), atoms of the solid near the surface can be knocked out due to collisions between the surface atoms and accelerated ions. Sputtering is a process that uses plasma for deposition of films. Plasma is defined as a partially ionized gas (typically 0.001% to 10% of the available atoms and molecules), containing an equal number of positively and negatively charged particles. This allows gas to be conductive by flowing current through the gas medium. At room temperature, a plasma or glow discharge can be initiated and sustained between two electrodes with a sufficiently high voltage difference, and placed in a gaseous environment at a pressure in the medium vacuum range. This condition, often called the fourth state of matter, is characterized by a visible glow and increased electric conductivity. The plasma is caused

by the relaxation of excited gas atoms, in which an electron makes a transition from a higher to a lower energy state, emitting energy in the form of visible light, characteristic of that gas.

In general, the sputtering process consists of four steps: (1) the ions (charged particles) are generated and accelerated toward the target, (2) the ions sputter the target atoms, (3) the ejected (sputtered) atoms are transported to the substrate, where (4) they condense and form a film. The number of sputtered atoms per incident ion is known as the sputtering yield of the target material. Sputtering yields of metals with argon ions with energy below 1 keV are of the order of unity [136]. Sputtering has proven to be a successful method for coating a variety of substrates with thin films of electrically conductive or non-conductive materials. One of the main characteristics of sputtering is its universality. Because the coating material is transferred in the form of atoms or molecules by ion impacts rather than a chemical or thermal process, virtually any material can be deposited. Direct current (DC) is used to sputter conductive materials (DC sputtering) while radio-frequency is used for non-conductive materials (RF sputtering).

3.1.2 Interaction of Ion and Surface of Solid

When an energetic ion approaches the surface of a solid, usually called the target, the following phenomena may occur, as shown in Figure 3.1.

- The impact may cause the target atoms to emit a secondary electron.
- The ion may become implanted.
- The ion may be reflected, probably as a neutral and probably with a large loss of energy.

- The ion impact and the resulting collision cascade may cause some structural reordering in the surface layers of the target.

- The ion impact may set up a series of collisions between atoms of the target, leading to the ejection of one of the target atoms. The ejection process is known as sputtering [137].

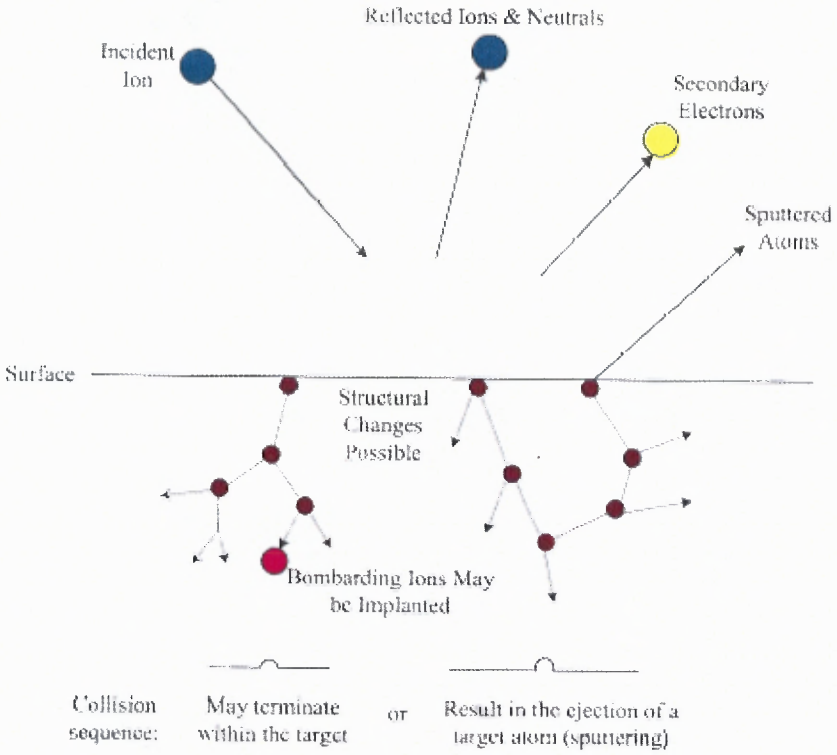

Figure 3.1 Interactions of ions with a surface [137].

3.1.3 Mechanism of Sputtering

Sputtering is a process operating on an atomic or molecular scale whereby an atom or molecule of the surface of a solid (target) is ejected when the surface is struck by fast incident accelerated ions (charged particles). The ejected atoms and/or molecules are deposited on the surface of the substrate and condensed to form solid thin films. Sputtering can be used as a method of film deposition or etching because sputtering removes and transports the target material atoms and/or molecules. The process is often

linked to a game of atomic snooker, as shown in Figure 3.2, because the scattering process employs similar mechanics. In snooker, the cue ball (the bombarding ion) strikes the neatly arranged pack (the atomic array of the target), scattering balls (target atoms) in all directions, including some back toward the player, i.e., away from the target surface [134, 138].

In the energy range most relevant to sputter deposition, the interaction between the impinging ion and target atoms, and the subsequent interactions amongst the latter, can be treated as a series of binary collisions. In the real sputtering process, the interatomic potential function—which is the variation of interatomic repulsion or attraction with separation distance—is rather different from the hard-sphere snooker case; nevertheless, the snooker model is instructive [137].

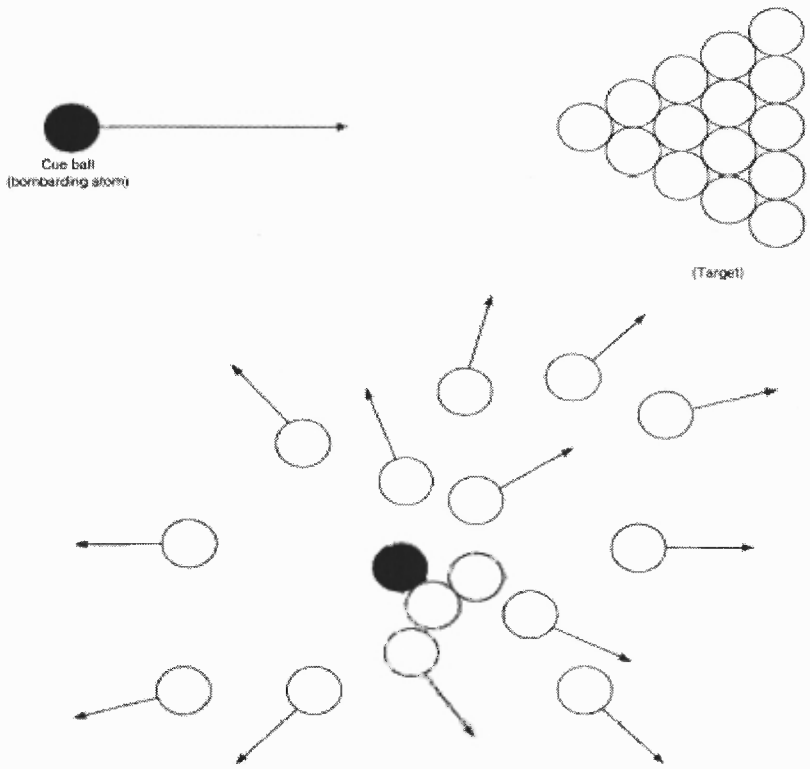

Figure 3.2 Sputtering as an atomic snooker game [137].

3.2 Sputtering Modes

Ultra-thin films to thick coatings of target material can be deposited by sputtering onto the substrate surface. A wide variety of coatings of pure elements, alloys, and compounds can be deposited on a variety of substrates with a reactive or non-reactive sputtering process.

Depending on the various modes to accelerate plasma ions onto the target material, sputtering can be basically classified into four types: (1) DC sputtering, (2) RF sputtering, (3) bias sputtering, and (4) ion-beam sputtering.

3.2.1 DC Sputtering

A DC sputtering system basically consists of two electrodes—a cathode and anode—placed in an evacuated chamber. Figure 3.3 shows the schematic of DC sputtering. A high negative DC voltage is applied to the cathode (sputtering target), whereas the anode (substrate) is grounded, floating electrically, or is biased positively or negatively. Inert gas, generally argon, is introduced in the chamber at some specific pressure. A large potential between the cathode (target) and anode (substrate) with the presence of gas at lower pressure will result in the formation of plasma containing electrons and ions. Positive ions generated in the plasma are accelerated toward the target and impinge on it. During these interactions, momentum transfer from the ions to the target atoms cause the ejection of the latter. They may also liberate secondary electrons from the target and it is these secondary electrons that are responsible for maintaining the electron supply and sustaining the glow discharge. The sputtered atoms from the target fly off in random directions, and some of them land on the substrate, condense there, and form a thin film.

DC sputtering can only be used to deposit coatings that are electrically conductive. This method of deposition cannot be used to deposit insulators because charge will build up on the target surface [137-139]. The DC diode sputtering process cannot be used to sputter insulators because the glow discharge cannot be maintained with a DC voltage if the cathode is not electrically conductive. This can be explained by the fact that when the cathode is bombarded by a positive ion, which is neutralized, an electron is stripped from the cathode surface. Such electrons can be replaced by electrical conduction if the cathode is a conductor; but in case of an insulator, this is not possible. Hence, the front surface of the cathode (insulator) accumulates the positive charge and

the potential difference (between cathode surface and anode surface) decreases. When this value decreases below the value required to sustain the plasma, the plasma extinguishes.

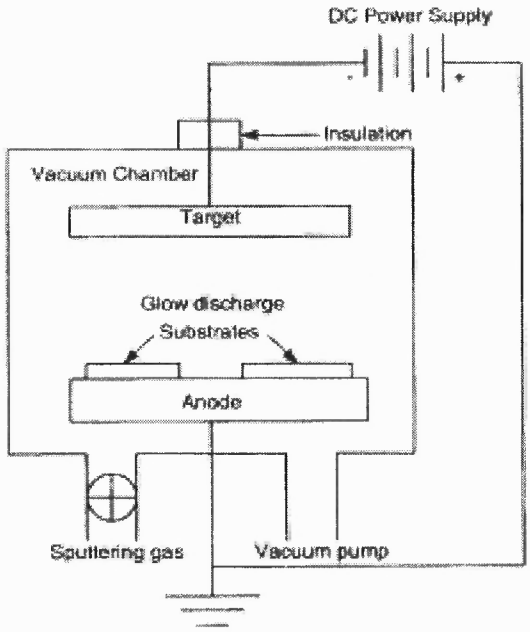

Figure 3.3 Schematic of a DC sputtering system [140].

3.2.2 RF Sputtering

To replenish the lost electrons on surfaces of insulators, a technique was developed that involves the application of an AC voltage instead of DC to the electrode. Radio-frequency sputtering was invented as a means of depositing insulating thin films because they cannot be deposited by DC sputtering technique due to requiring unattainable potential differences between the cathode and anode. The technique of RF sputtering uses an alternating voltage power supply at radio-frequencies above 10 MHz, so that the sputtering target is alternatively bombarded by ions and then electrons to avoid charge built-up. A schematic diagram of an RF sputtering system is shown in Figure 3.4.

RF sputtering can be used to deposit both conductors and insulators. In such a system, the RF power alone is capable of generating the plasma and accelerates ions to the target, followed by electrons, so as to avoid charge build-up, to cause sputtering. However, deposition rate is generally lower than that of DC sputtering. Another advantage of RF sputtering over DC sputtering is less potential for arcing, which is sometimes a problem in DC sputtering systems. Arcing can be due to patches of dirt (with a higher secondary electron coefficient), pockets of outgassing (higher pressure, higher current density locally), or asperities (higher electric field strength). These arcs are less likely to form in RF discharges because the field is maintained in one direction for less than one cycle, and it reduces to zero twice in each cycle, making it more difficult for the arc to be sustained [137].

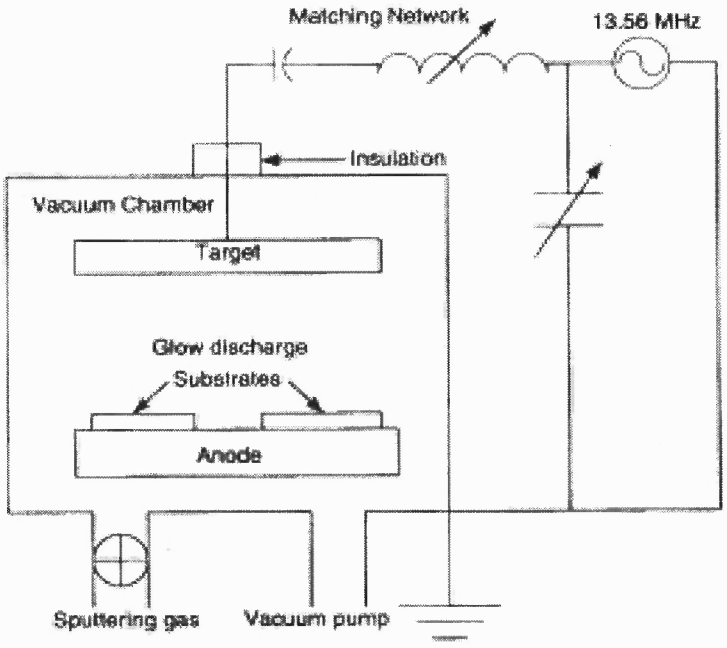

Figure 3.4 Schematic of a simplified RF sputtering system [140].

3.2.3 Ion-Beam Sputtering

In ion-beam sputtering, a high-energy ion beam impacts the sputtering target. With the impact of the high-energy ion beam, material is sputtered off the target and reflected at an oblique angle to the incident ion beam. The material sputtered off the target is reflected toward the sputtering substrate, where it is deposited to form a film.

This technique employs a noble-gas ion beam, extracted from the ion source, to bombard a target, as shown schematically in Figure 3.5. Ions are generated by an external ion-beam source. This means that the substrate can be located in a virtually field-free high-vacuum environment, and this has several implications for the growth of the film. The ion-beam system requires that the ion reach the target without being diverted by collisions with gas atoms. One should have increased control over the energy and the current density of the incident ions on the substrate surface in this type of sputtering technique [134,139]. It can be used to deposit both conductive and non-conductive films [138]. The deposition rate is relatively low.

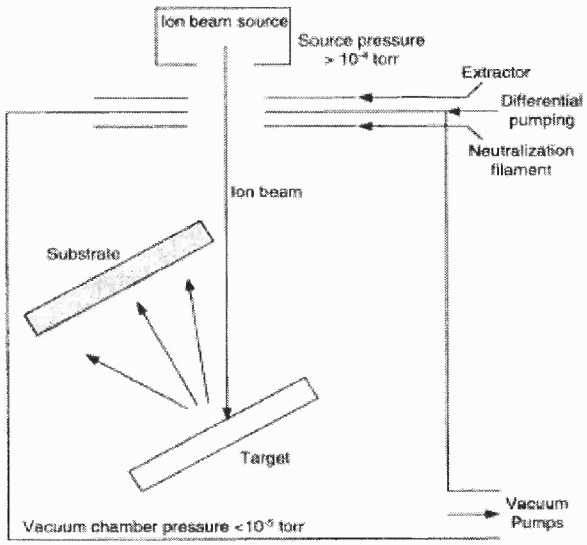

Figure 3.5 Typical configurations for ion-beam sputtering [137].

The advantages of such sputtering are the following [137]:

- Because the substrate is not part of the electrical circuit, it is much easier to incorporate substrate heating, cooling, and process controls.
- Due to isolation of the substrates from the glow-discharge generation process, unwanted heating of the substrates and fast electron bombardment are minimized.
- The low operating pressure reduces energy-attenuating collisions of the sputtered particles en route from target to substrate.
- The low operating pressure in the process chamber minimizes gas contamination of the growing film.

3.2.4 Bias Sputtering

Bias sputtering is the process of negatively charging the substrate with respect to the plasma potential, thus creating an attraction between ions and the substrate. With so many particles bombarding the film, and with the sensitivity of the nucleation and growth processes to this bombardment, changing the flux and energy of incident particles can control the properties of the films. It is difficult to control the behavior of the neutral particles, but the charged particles can be controlled by changing the local electric field, and this is the basis of bias sputtering [137].

In this technique, electric fields near the substrate are modified to vary the flux and energy of incident charged species. Generally, a negative DC or RF bias is applied to the substrate. With target voltages of -1000 to -3000 V, bias voltages of -50 to -300 V are typically used. Due to charge-exchange processes in the anodic dark space, very few discharge ions strike the substrate with full bias voltage. As a result, substrates are not heated substantially [137]. This technique can be applied to any sputtering configurations (DC, RF, magnetron, and reactive). It has also been found that bias sputtering has been effective in altering a broad range of properties in deposited films

such as hardness, resistivity, and residual stress, optical reflectivity, etch rate, dielectric properties, step coverage, film morphology, adhesion, and density [140].

3.2.5 Reactive Sputtering

In reactive sputtering, thin films of compounds are deposited on substrates by sputtering from metallic targets in the presence of a reactive gas, usually mixed with the inert working gas (generally Ar) to obtain chemical compound films. The reaction could take place at any of all or three locations—i.e., at the target, in the gas phase, or at the substrate surface [134]. Reactions can occur on the target surface, following which the reacted material is sputtered. They also occur at the substrate, and in cases of high working pressure, in the gas phase. When sputtering with a reactive gas and argon mixture, the relationship between film properties and the reactive-gas injection rate is generally non-linear. Irrespective of materials considered, during reactive sputtering, the resulting film is either a solid-solution alloy of the target metal doped with the reactive elements, a compound, or some mixture of the two. Reactive sputtering can be applied to any of the sputtering methods. Examples of reactive sputtered films include Zn sputtered in O_2 to form ZnO, Al sputtered in O_2 to form Al_2O_3, Nb and Ti sputtered in N_2 to form NbN, TiN, all in the presence of argon.

The advantages of this method are the following:

- Insulating films can be deposited.
- Compounds can be formed using metallic targets.
- It offers a means for controlling the stoichiometry of the film.
- Films can be of graded composition.

The disadvantages of this method are the following:

- Target poisoning (a compound layer formed on the target due to excess reactive gas), which leads to instabilities such as sparks and plasma extinguishing. By increasing the pumping rate of the chamber and decreasing the concentration of reactive elements in the working-gas atmosphere, the problem can be resolved.

- The gas injection rate affects the film properties in a non-linear fashion that is difficult to predict. The effects are evident in the growth rate, composition, and film structure [139].

3.2.6 Magnetron Sputtering

In diode sputtering, most secondary electrons emitted from the target do not cause ionization events with Ar atoms. They end up being collected by the anode and substrates, where they cause unwanted heating. Because most electrons pass through the discharge region without creating ions, the ionic bombardment and sputtering rate of the target is low because only some electrons are involved in ionizing collisions. Magnetron sputtering is used to increase ionization efficiency and sputtering rate.

Magnetron sputtering dates back to 1936 when Penning [141] proposed applying a perpendicular magnetic field to increase the plasma concentration of glow discharge. If a magnetic field is applied parallel to the surface of a target of a DC sputtering system (perpendicular to the electric field), then, due to Lorentz forces, the secondary electrons that are accelerated from the target to the substrate are forced into a spiral path in the vicinity of the target surface.

3.2.6.1 Principles of Magnetron Sputtering

To understand this effect, consider an electron emitted normally from a surface with velocity v into a region of magnetic field B and zero electric field. The electron will describe a semicircle of radius r, provided it does not collide and it will return to the surface with velocity v. Hence, the effect of the magnetic field is to trap the emitted electron near the surface. To examine a situation that is closer to the magnetic sputtering application, consider a strong electric field that exists in the space above the surface of the sputtering target and also the magnetic field that is parallel to the surface. Let the electric field E decrease linearly with the distance from the target through the dark space (L). The electric field is thus given by:

$$E = E_o(1-y/L) \qquad (3.1)$$

Here, y is the dimension perpendicular to the target with y = 0 at the target surface and the electric field is E_o.

The electrons emitted from the target will be rapidly accelerated vertically—initially away from the target by the strong normal electric fields at the surface, but simultaneously it experiences an increasing force due to magnetic field, F = q(v x B). The presence of an electric field along with the magnetic field changes the electron path from circular to cycloidal (hopping), as shown in Figure 3.6, provided the electron stays in the dark space [137]. This increases the electron path length in the plasma and hence increases the probability of collision with sputtering gas atoms near the target surface. The increase in the production rate of ions that strike the target increases the sputtering rate. The deposition rate enhancement is commonly a factor of 10 over the diode sputtering method. It is also possible to sputter at a lower pressure as compared to DC

diode sputtering process. Sputtering also leads to the heating of the target due to energetic ion bombardment, so the magnetron target mounting incorporates channels for water-cooling during operation to extend the life of the magnet [136, 137]. The system geometry for a simple planar magnetron sputtering system is similar to DC and RF sputtering system, but the applied magnetic field makes the system more effective. Magnetron sputtering is presently the most commonly used sputtering method [142].

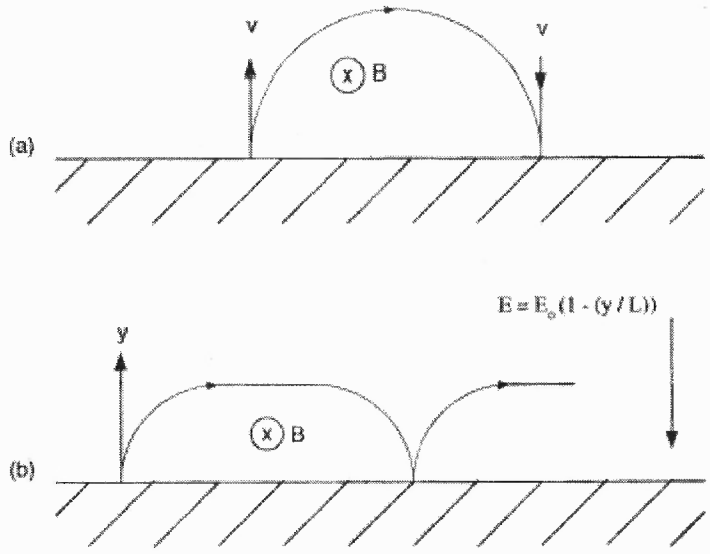

Figure 3.6 Motion of an electron ejected from a surface with velocity v into a region of magnetic field B parallel to the surface: (a) with no electric field, and (b) with a linearly decreasing field [137].

There are many types of magnetrons in practical sputtering systems. The most widely used magnetron electrode configuration in a sputtering system is the circular magnetron [136]. In circular magnetrons, the target surface is planar, and the B-field is created by a permanent magnet behind the target. A schematic of the target arrangement and magnets for a circular magnetron is shown in Figure 3.7. The plasma is most intense where the magnetic field is parallel to the target surface and this is where maximum ejection of target atoms is expected. This result in the target erosion pattern is called the

racetrack. A schematic of a detailed cross-section view of a circular magnetron sputtering source is shown in Figure 3.7.

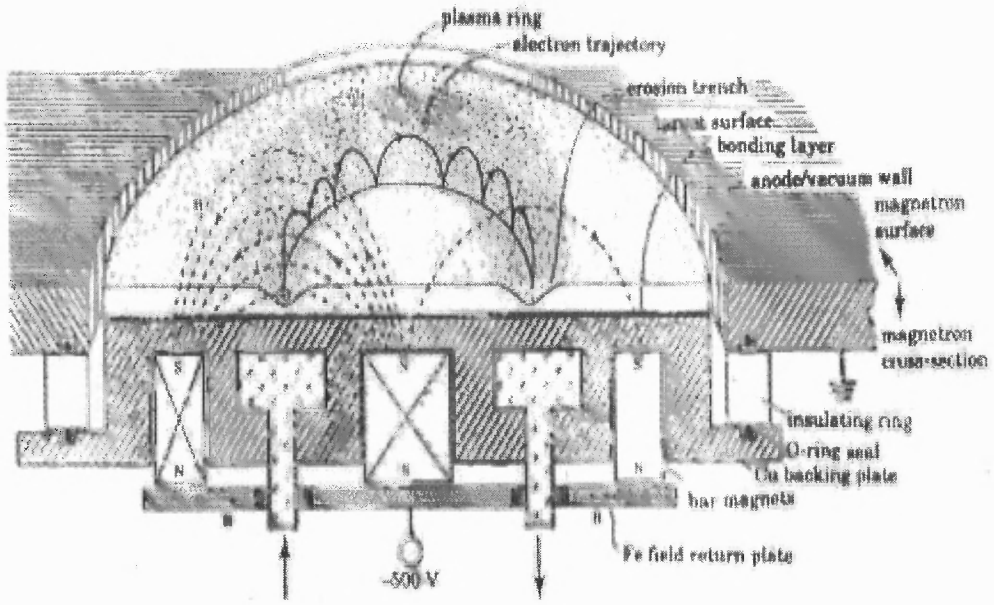

Figure 3.7 Cross section of a circular magnetron source, showing the magnetic field, racetrack, and electron orbits [136].

The disadvantage of magnetron sputtering is the localized erosion of the target, which gives low target material utilization, non-uniform deposition pattern, and requires frequent replacement of the target. Uniformity improves as the target-to-substrate spacing is increased, but this causes a decrease in the deposition rate. Thus, a tradeoff is often made between deposition rate and thickness uniformity. Magnetron sputtering is a powerful and flexible technique that can be used to coat virtually any substrate with a wide range of materials—any metal or alloy and a variety of compounds.

CHAPTER 4

EXPERIMENTAL METHODOLOGY

4.1 RF Magnetron Sputtering System

In this research work, an RF magnetron sputtering system was used to deposit thin films. Figures 4.1 and 4.2 show photographs of the RF magnetron sputtering system used in this work. Figure 4.1 shows the Edwards 306 auto sputtering system, and Figure 4.2 shows the AJA sputtering system. The working principle of both systems is the same; the only difference is that the AJA sputtering system is an advanced version of the Edwards sputtering system, with additional features such as computer control, large chamber size, and multiple guns.

Figure 4.1 RF reactive magnetron sputtering system (Edwards Auto 306) at National Renewable Energy Laboratory.

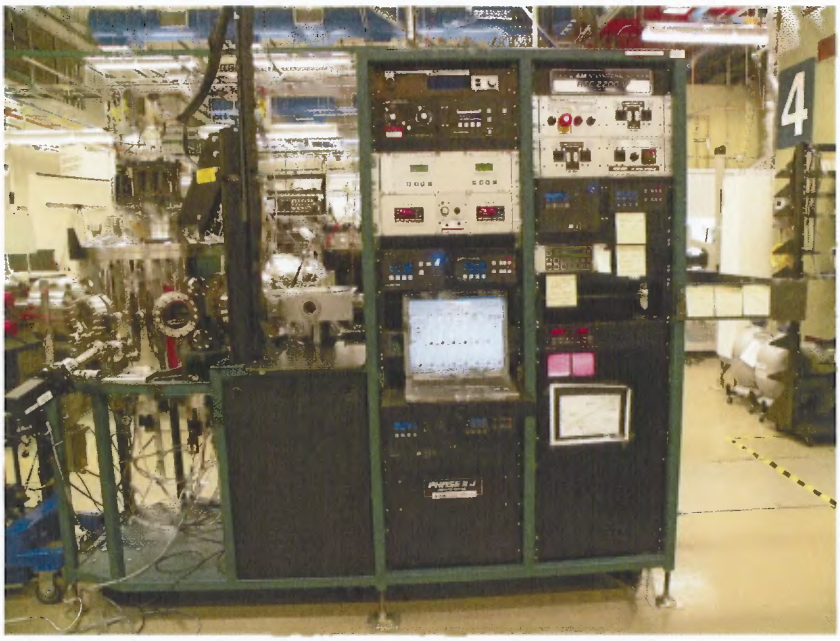

Figure 4.2 RF reactive magnetron sputtering system (AJA) at National Renewable Energy Laboratory.

The system consists of a sputter chamber, vacuum pumping system, and gas-delivery system. The sputter chamber is cylindrical in shape, with an inside diameter of 36 inches and an inside height of 14 inches. The chamber has numerous ports that allow flexibility in attaching various accessories, gauges, and vacuum feedthroughs. The front of the chamber has a view port to allow viewing of the process. Inside the chamber, two sputter guns, working with two different targets, can allow simultaneous sputtering from both the targets. In the sputter chamber, a target (Zn metal or ZnO or ZnO-2 wt% Al, or any other metal oxide or metal) that is 3 inches in diameter is clamped to a copper base plate on the water-cooled cathode, which houses permanent magnets for directing charged particles. The RF power is supplied by a RF generator operating at a frequency of 13.56 MHz, which is connected to the cathode through an impedance-matching network with variable capacitors. The RF power for the sputtering process can be

selected by using the knob in the control panel of RF power supply. The RF power has a maximum of 400 W.

Figure 4.3 is a photograph of the sputtering chamber (Edwards Auto 306) with the top lid lifted, showing the platter with the substrate holder. A stainless-steel shield is mounted below the substrate platter on the top lid of the chamber. This stainless-steel shield prevents deposition on the chamber top lid. A motorized hoist lifts the heavy top lid of the chamber. The top lid has many ports, one of which has the carrousel substrate platter attached to it. Other ports on the top lid of the chamber have feedthroughs for the substrate rotator, thermocouples, and cables for cooling water and heating lamps.

An inner view of the sputtering chamber (Edwards Auto 306) is shown in Figure 4.4. The chamber has two sputtering guns, to which a target of 3-inch diameter and 0.125-inch thickness is clamped to the water-cooled copper base plate. A shutter is placed above the target, which can be closed and opened. Stainless-steel foil is covered inside the chamber to avoid cross-contaminants.

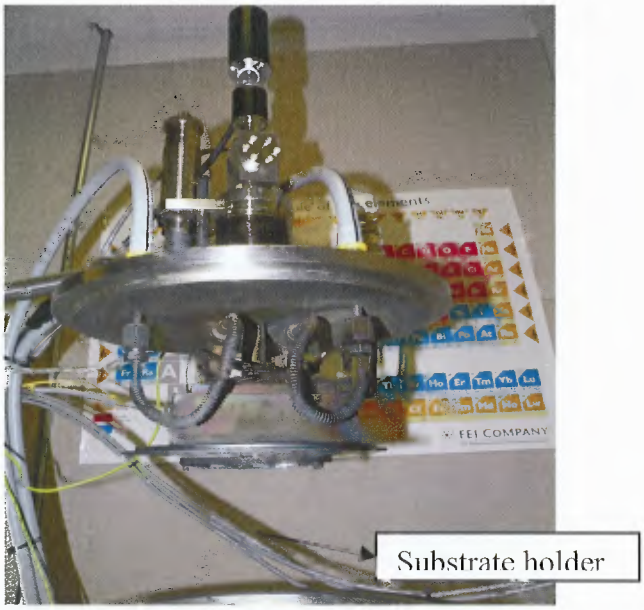

Figure 4.3 A view of the sputtering chamber (Edwards Auto 306) with the top lid lifted, showing the platter with the substrate holder.

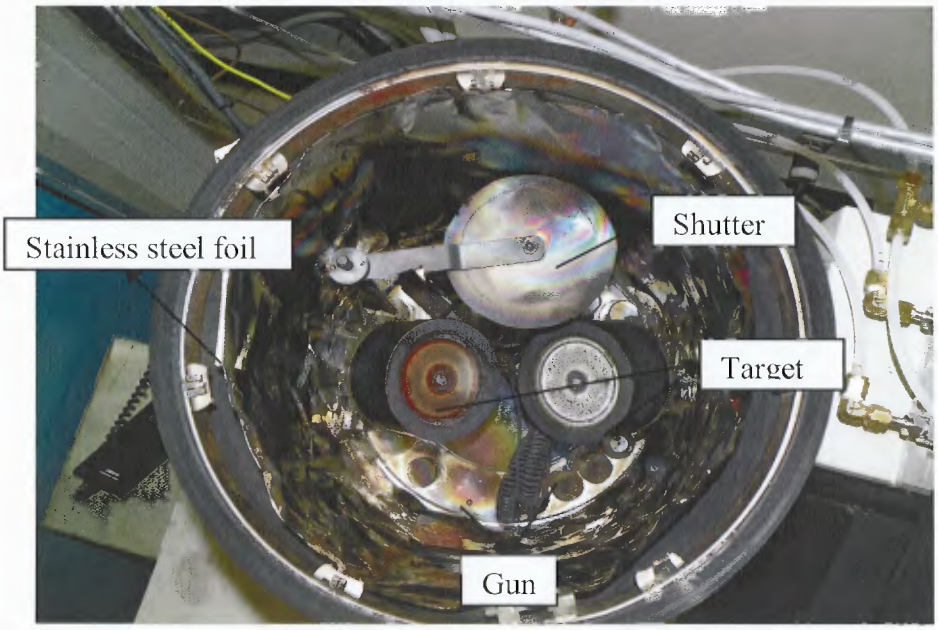

Figure 4.4 An inner view of the sputtering chamber (Edwards Auto 306), showing the two guns with shutter.

The sputtering system set up with the configuration of substrate is placed above the target facing the target. The distance between the target and substrate is 8 cm and can be varied. A shutter is placed between the target and substrate, which can be closed and

opened using the knob placed outside the chamber during the pre-sputtering and sputtering process. The substrates are placed onto the substrate holder (anode), which can heat substrates via the temperature controller. The substrate holder is heated from the back by irradiative mercury (Hg) lamp and the temperature measured indirectly by a thermocouple located below the substrate holder. The substrate can be rotated at different RPMs by using the substrate rotator knob, thus allowing for uniform films. A motorized hoist lifts the heavy top lid of the chamber. The top lid has many ports, one of which has the substrate platter attached to it. Other ports on top have feedthroughs for thermocouples, cables for heating lamps, and the substrate rotator. High-purity (99.9999%) gases, such as argon, oxygen, and nitrogen, are delivered from the high-pressure gas cylinders via Rota meters, mass flow meters, and a control system into the chamber. The high vacuum in the chamber is established by using a rotary pump and turbo molecular pump, which reaches a minimum pressure of 1×10^{-7} torr.

4.2 Substrate Preparation

Substrate surface preparation is an important step in thin-film deposition because it ensures good bonding between the thin film and substrate. Substrate preparation can also influence other characteristics of the thin films. In the present study, a substrate of FTO that is 12 inch x 12 inch and 0.1 inch thickness was cut using a 2.25 inch x 1.5 inch diamond-tip indenter.

The substrate was cleaned ultrasonically, using high-intensity sound waves that generate pressure fluctuations that produce microscopic bubbles in the liquid medium. These bubbles produce the shockwaves, which impinge on the sample surface and

remove dirt from the surface of the substrate. This cleaning process involves three steps. During the first step, the substrates were ultrasonically cleaned with acetone for 30 minutes, and during the second step with methanol for 30 minutes. In the final step, substrates were cleaned with deionized water for 60 minutes and finally dried using N_2 gas. The samples were then kept in desiccators to prevent any contamination before loading them in the sputtering chamber.

4.2.1 Substrate Mounting

Substrates of FTO (2.25 inch x 1.5 inch) are mounted on steel holders using four screws that hold the substrate that is attached to the substrate holder and prevent any movement. Figures 4.5 and 4.6 are photographs of the mounted FTO substrate for the Edwards Auto 306 and AJA sputtering systems, respectively. After the film-deposition step, FTO substrates are cut into five equally sized pieces for various sample characterization. Substrates are mounted in the holders outside the chamber and the holders are then inserted into the slots in the platter.

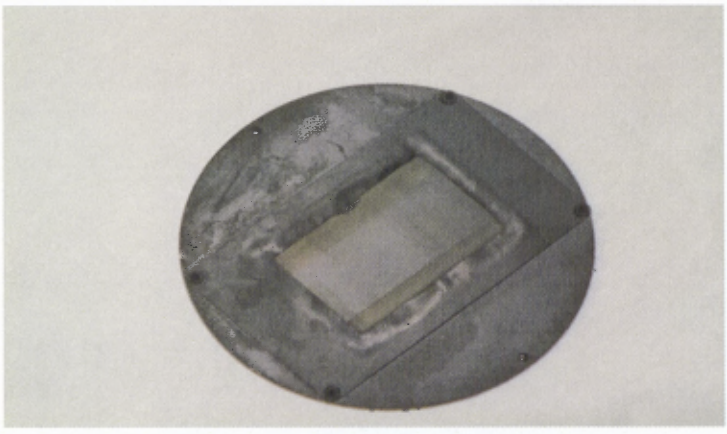

Figure 4.5 Fluorine-doped tin oxide (FTO)-coated glass substrate mounted on the substrate holder for the Edwards Auto 306 sputtering system.

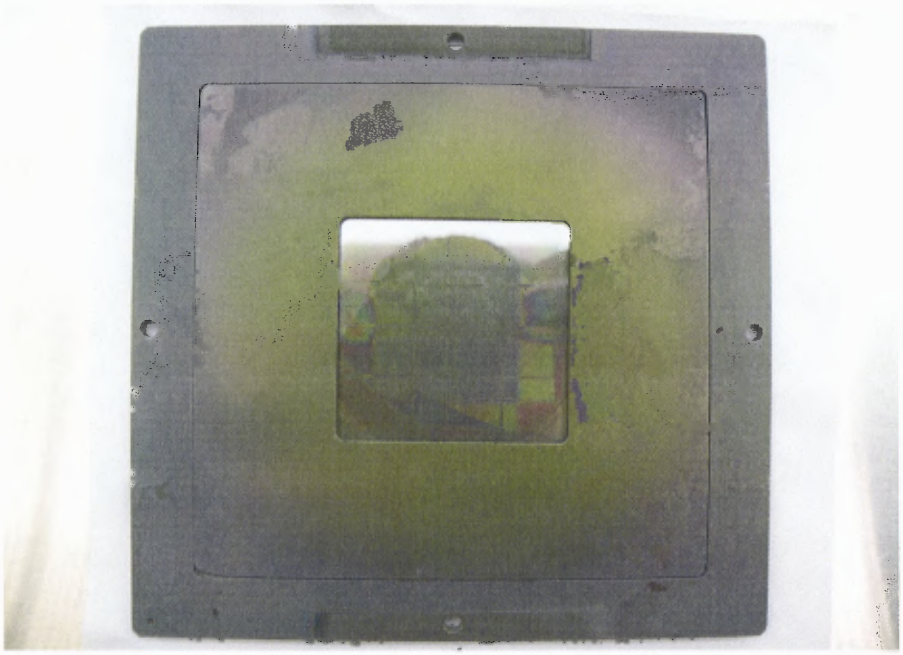

Figure 4.6 Fluorine-doped tin oxide (FTO)-coated glass substrate mounted on the substrate holder for the AJA sputtering system.

4.2.2 Deposition Parameters

A series of depositions were carried out on the FTO substrate by changing the sputtering parameters. The magnetron source was energized by a RF power supply. Targets used include metal, oxide, and nitride targets (3 inches in diameter and 0.125 inch thick) for different sputtering conditions. The metal targets were Zn, Ti, W, or Cu; the oxide targets were ZnO, ZnO-2 wt% Al, CuO, Ga_2O_3, Al_2O_3, or Co_3O_4; and the nitride target was GaN. Gallium oxide powder and Cu metal chips (area: 2 x 5 mm^2) were used as a co-dopant for co-doped ZnO films.

In some cases, metal-oxide powders were used as co-dopants for co-doped metal-oxide thin films. The distance between the target and substrate was maintained at 8 cm in most of the experiments. The distance was chosen to generate the conditions for the proper deposition rate. The base pressure was kept below 5 x 10^{-6} torr and the working

pressure was below 5 x 10^{-3} torr. The chamber ambient was either pure argon, oxygen, mixed argon and oxygen, or mixed oxygen and nitrogen with different gas flow rate ratios. Argon (99.999%) was used as the sputtering gas and oxygen (99.99%), nitrogen (99.999%) was also used for some of the experiments. During the deposition of the N-doped ZnO films, Zn metal and ZnO were reactively sputtered with an oxygen and nitrogen mixture. For metal-oxide thin-film deposition, a mixture of argon and oxygen gas was used.

During experiments in which substrate heating was required, the substrate holder was heated from the back by an irradiative Hg lamp and indirectly measured by a thermocouple located below the substrate holder. For most of the experiments, substrates were rotated at 30 RPM to enhance deposition uniformity. A pre-sputtering cleaning was performed for 30 minutes to eliminate possible contaminants from the target. This can increase the temperature of the substrate up to 800°C. Post-deposition annealing was carried out for most of the deposited samples at 500°C in air for 2 hours, and in some case, oxygen or ammonia gas was used.

The following procedure was followed for the process:

1. Samples were prepared as explained in the previous section and loaded into the sputtering chamber.
2. The sputtering system was pumped down until the base pressure was below 5 x 10^{-6} torr.
3. Depending on the experiment, appropriate gas and flow rate is selected and the gas flow valve is opened.
4. RF power is selected depending on the experiment.
5. Pre-sputtering was carried out for about 20 to 30 minutes with the shutter closed.
6. Depending on the experiment, the substrate is heated until the temperature stabilizes.

7. Substrate is rotated at 30 RPM.

8. Thin film was deposited.

At the completion of the deposition run, the system was allowed to cool down before venting with nitrogen and removing the substrate with the deposited thin film.

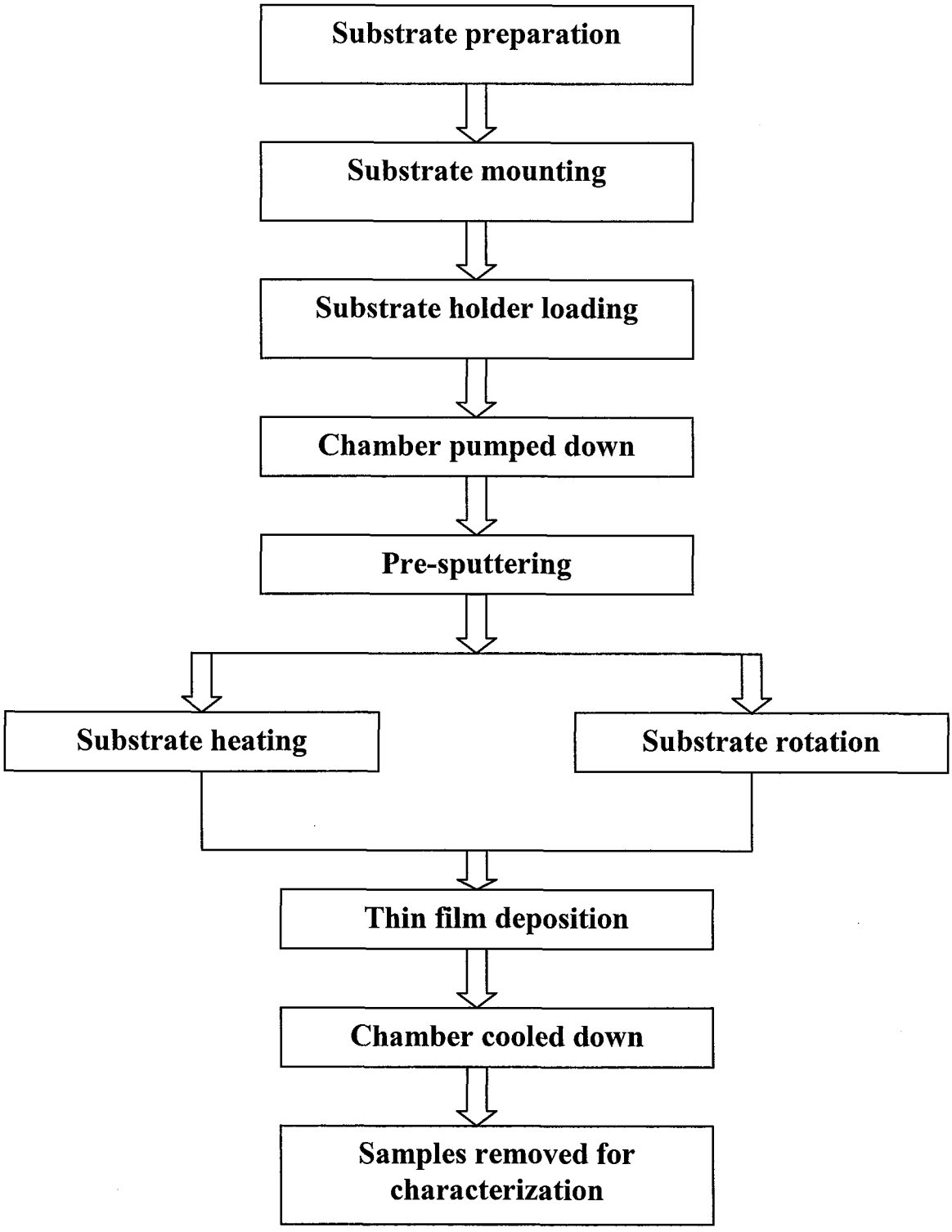

Figure 4.7 Chart summarizing steps followed during deposition process.

CHAPTER 5

CHARACTERIZATION TECHNIQUES

5.1 Surface Profilometry

Many direct and indirect techniques exist for measuring the thickness of a deposited thin film. The most generally used technique is the surface profilometer. The stylus profilometer uses a diamond-tipped stylus with a tip radius of 12.5 μm to scan across the sample surface, and it measures the surface topography of thin and thick films. The stylus force is adjustable from 1 to 40 mg, and vertical magnification of a few thousand up to a million times is possible. The instrument has vertical resolution in nanometers and horizontal resolution as small as 20 nm and measures film thicknesses from 5 nm and over 500 μm. The step height is measured by electromechanically tracking the motion of the mechanical stylus as it sweeps across the step. Figure 5.1 shows a Dektak profilometer setup. The measurement functions and leveling are computer controlled in this equipment. Its output is a graph of stylus height versus position, from which step height, surface roughness, and other features can be determined. The deposition rate was calculated by dividing the total thickness of the film by the total time of deposition.

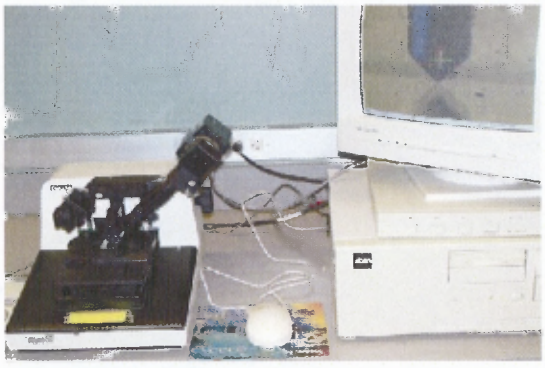

Figure 5.1 Dektak Profilometer [143].

5.2 Scanning Electron Microscopy

Scanning electron microscopy (SEM) is the most widely used technique to characterize very small features of surfaces with a resolution of micrometer or even less. SEM provides information related to morphology, topography, composition, and crystallography. In this technique, the area to be examined or the microvolume to be analyzed is irradiated with a finely focused electron beam. Figure 5.2 shows a schematic of a combination instrument, which can be operated as an electron microprobe and as an SEM.

An SEM consists of an electron accelerator that focuses the electron beam from a tungsten or lanthanum hexaboride (LaB_6) cathode filament onto the specimen using electromagnetic lenses. Pairs of scanning coils located at the objective lens deflect the beam either linearly or in raster fashion over a rectangular area of the specimen surface. Electrons that have energies ranging from a few keV to 50 keV are used. When they impinge on the specimen, the primary electrons are scattered elastically and some loose energy inelastically to other atomic electrons and/or to the lattice. The types of signals produced when the electron beam impinges on a specimen surface include secondary electrons, characteristic X-rays, Auger electrons, backscattered electrons, and photons of various energies. A detection system measures the intensity of electrons scattered by the specimen and forms the image. These signals are obtained from specific emission volumes within the sample and can be used to examine many characteristics of the sample [144, 145]. Insulating specimens cannot be analyzed directly in the SEM, because they accumulate the absorbed electrons on the surface. The accumulated electrons eventually build up a charge region, which can deflect the beam in an irregular manner

and lead to severe image distortion. Insulating samples can often be coated with a thin conducting layer such as Ag paste or Al for subsequent examination.

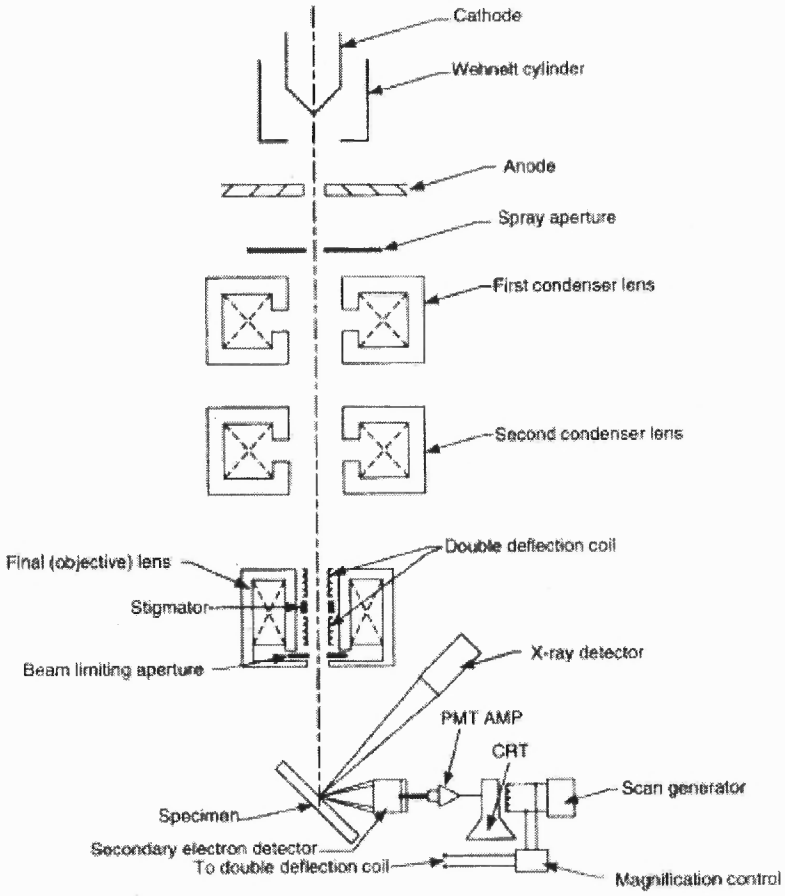

Figure 5.2 Schematic of a scanning electron microscope [145].

In X-ray energy dispersive analysis (EDX), frequently referred to as electron microprobe analysis, the primary radiation of interest is the characteristic X-rays emitted as a result of the electron bombardment. The analysis of the characteristic X-rays can yield both qualitative identification and quantitative compositional information from the region of a specimen as small as a micrometer in diameter.

5.3 X-Ray Diffraction

X-ray diffraction (XRD) provides a unique technique for obtaining crystallographic information such as lattice constant, identification of crystalline materials, orientation of single crystals, preferred orientation of polycrystals, phases, and even composition (determined by comparison with standard data).

X-rays are form of electromagnetic radiation. A diffraction beam may be defined as a beam composed of a large number of scattered rays mutually reinforcing one another [145]. A parallel beam (1 and 2) of X-rays of wavelength λ is incident on parallel planes (A-A1 and B-B1) at an angle θ, as shown in Figure 5.3. When a beam of X-rays impinges, a portion of this beam (labeled 1 and 2) will be scattered in all directions by the electrons associated with each atom (P and Q). If the path-length difference between diffracted beams (1-P-1a) and (2-Q-2a) is equal to a whole number, n, of wavelength λ, the condition of diffraction is satisfied. This condition is given by Bragg's law:

$$n\lambda = 2d\sin\theta\,, \tag{5.1}$$

Where:

n = integral number describing the order of reflection,

λ = wavelength of the X-rays,

d = interplanar spacing for the reflected plane,

θ = Bragg angle where a maximum in the diffracted intensity occurs.

The XRD instrument consists of three basic parts: (1) a source of radiation, consisting of an X-ray tube and a high-voltage generator, (2) the detector and counting instrument, and (3) the diffractometer. The X-ray diffractometer works as shown in Figure 5.4.

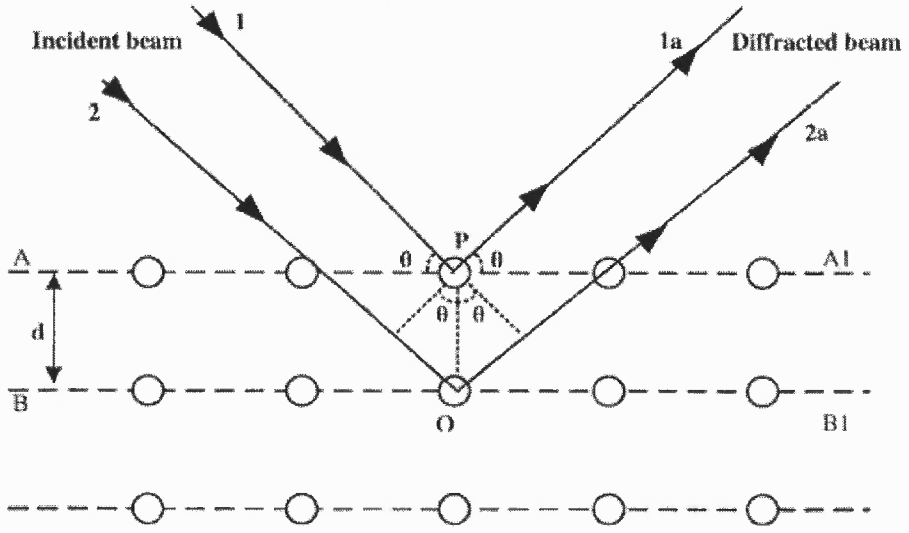

Figure 5.3 Diffraction of X-rays by planes of atoms (A-A1 and B-B1) [146].

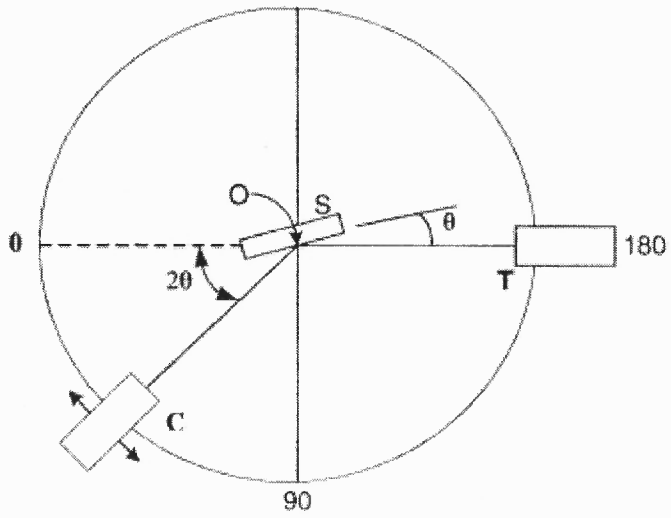

Figure 5.4 Schematic diagram of an X-ray diffractometer [146].

A specimen S in the form of a flat plate is supported so that rotation about the axis labeled O is possible. The X-ray beam is generated at source (point T), and intensities of diffracted beams from the sample are detected by a counter at point C. As the counter moves at constant velocity, a recorder automatically plots the diffracted beam intensity as

a function of diffraction angle 2θ and peaks are obtained [146]. The powder diffraction pattern of a material is characteristic of that substance, so the diffraction data obtained from an unknown material can be compared with the standard Powder Diffraction Files (PDF) of many known materials compiled by the Joint Committee on Powder Diffraction Standards (JCPDS) to determine its crystallinity, chemical composition, and other important properties of materials of interest. The three most-intense diffraction lines form the basis of data on each powder diffraction file.

Advantages of XRD are that it is a non-destructive technique and does not require any sample preparation or removal of the film from substrate. The disadvantages of XRD relates to studying very thin films of light elements. The great penetrating power of X-ray means that with typical incident angles, their path length through such films is too short to produce diffraction beams of sufficient intensity. Under such conditions, the substrate, rather than the film, dominates the diffracted X-ray signal.

5.4 Atomic Force Microscopy

Atomic force microscopy (AFM) is one of the most commonly used characterization techniques for surface study. This technique is a very attractive method for measuring surface topography on a scale from angstroms to 100 microns. AFM is a type of scanning probe microscopy (SPM). Figure 5.5 shows the schematic of a generalized SPM.

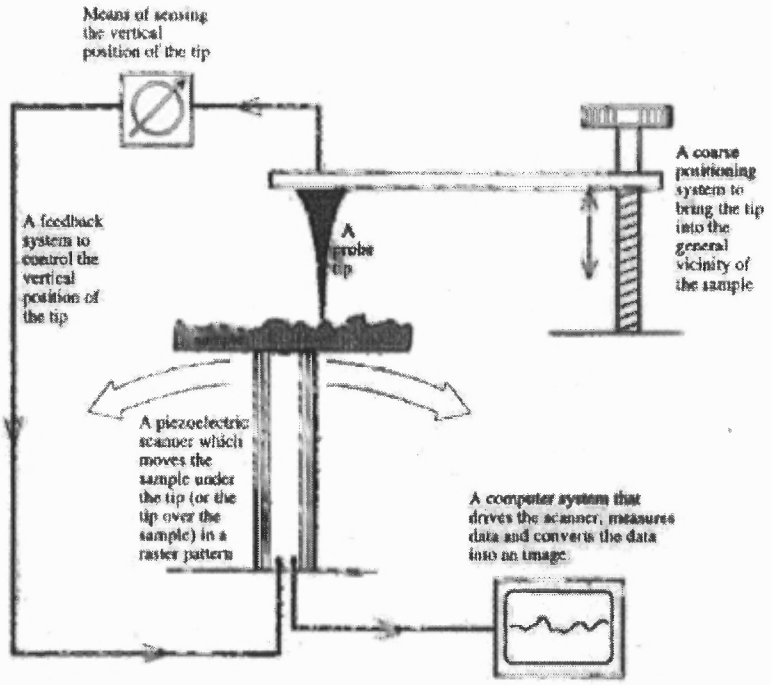

Figure 5.5 Schematic of a generalized scanning probe microscope [147].

5.4.1 Principle of Operation of Atomic Force Microscopy

An atomically sharp tip is scanned over a surface with feedback mechanisms that enable the piezoelectric scanners to maintain the tip at a constant force (to obtain height information) or height (to obtain force information) above the sample surface. Tips are typically made from Si_3N_4 or Si and are extended down from the end of a cantilever. The nanoscope AFM head employs an optical detection system in which the tip is attached to the underside of a reflective cantilever. A diode laser is focused onto the back of a reflective cantilever.

As the tip scans the surface of the sample, moving up and down with the contour of the surface, the laser beam is deflected off the attached cantilever into a dual-element photodiode. Several forces typically contribute to the deflection of an AFM cantilever.

The force most commonly associated with AFM is an inter-atomic force called van der Waals force. The photodetector measures the difference in light intensities between the upper and lower photodetectors, and then converts it to voltage. Feedback from the photodiode difference signal, through software control from the computer, enables the tip to maintain either a constant force or constant height above the sample. In the constant-force mode, the piezoelectric transducer monitors real-time height deviation. In the constant-height mode, the deflection force on the sample is recorded. AFM can be operated in mainly two modes: (1) contact mode and (2) tapping mode.

In the contact regime, the tip is held less than a few angstroms from the sample surface, and the inter-atomic force between the tip and sample is repulsive. In the non-contact regime, the tip is held on the order of tens to hundreds of angstrom from the sample surface, and the inter-atomic force between the tip and sample is attractive. A schematic arrangement of major components for tapping-mode operation of AFM is shown in Figure 5.6. Tapping mode in AFM operates by scanning a tip attached to the end of an oscillating cantilever across the sample. The cantilever is oscillating at or near its resonant frequency with amplitude typically ranging from 20 to 100 nm. The frequency of oscillation can be at or on either side of the resonant frequency. During scanning, the tip lightly "taps" on the sample surface, contacting the surface at the bottom of the swing. The feedback loop maintains constant oscillation amplitude by adjusting the distance between the tip and sample surface and maintains a constant root mean square (RMS) of the oscillation signal acquired by the split photodiode detector.

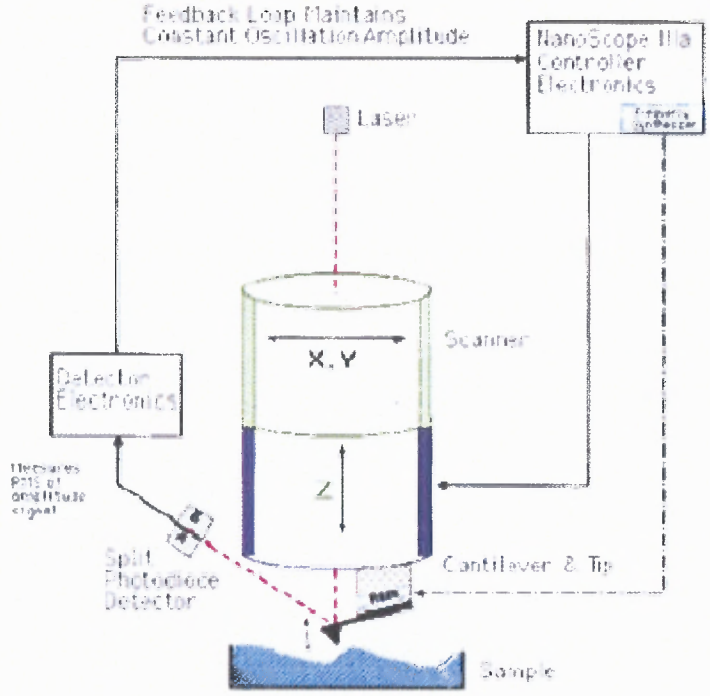

Figure 5.6 Schematic arrangements of AFM showing the feedback loop for tapping-mode operation [147].

The laser deflection detects the RMS amplitude of the cantilever oscillation. Topographical image will be formed by recording the vertical movement of the cantilever at every x,y data point. Compared to contact mode, the main advantage of tapping mode is that lateral shear forces are eliminated, which are present in the contact mode.

5.5 Secondary-Ion Mass Spectroscopy

Secondary-ion mass spectroscopy (SIMS) is a failure-analysis technique used in the compositional analysis of a sample. SIMS operates on the principle of bombarding a material with a beam of ions (incident ions) with high energy (1-30 keV) onto the surface, thereby transferring some of the energies into the lattice atoms. These incident ions are also called primary ions and they interact with the sample or surface that is to be

measured. Initially, the upper layer of the sample gets amorphized and some of the ions get implanted due to atomic collisions within the solid, resulting in the ejection or sputtering of atoms from the material. A small percentage of these ejected atoms leave as either positively or negatively charged ions, which are referred to as "secondary ions," which can be analyzed via mass spectrometry. Figure 5.7 represents the basic principle of the SIMS technique. The secondary ions are characteristic functions of the composition of the surface. This method is a highly sensitive surface analytical technique and the typical detection limits range from 10^{14} to 10^{15} cm^{-3}. The range of lateral resolution is from 1 to 100 μm and the depth resolution ranges from 50 to 100 Å [149, 150].

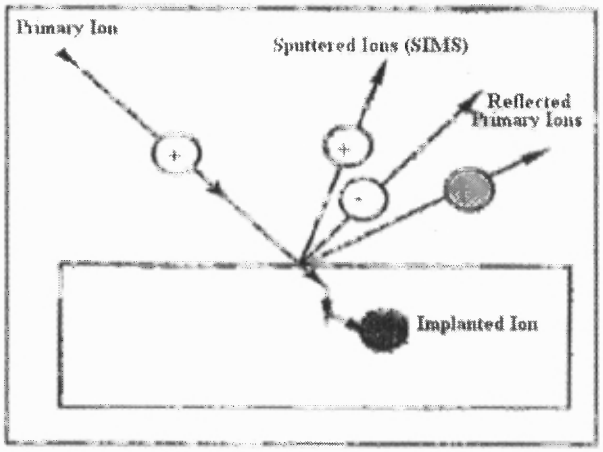

Figure 5.7 Principle of operation of SIMS [150].

Figure 5.8 shows the detailed flowchart of SIMS operation. SIMS can be used for almost any element in the Periodic Table except for noble gases because of the difficulty in ionization. SIMS has its own advantages and disadvantages. Advantages of SIMS are the following: (1) It can be used for a wide range of materials, including organic, inorganic compounds, polymers, ceramics, solid-state materials, and biological samples; (2) It has high spatial resolution; (3) The sensitivity of this analysis is very high and

ranges from ppm to ppb; and (4) It is able to distinguish isotopes. Disadvantages are that it is a destructive technique and the equipment is highly complex.

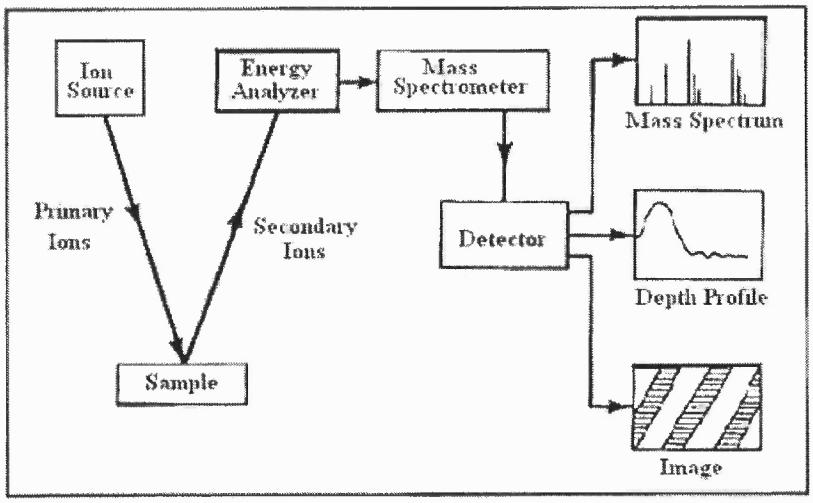

Figure 5.8 Flowchart explaining the SIMS technique [150].

5.6 X-Ray Photoelectron Spectroscopy

X-ray photoelectron spectroscopy (XPS), also known as electron spectroscopy for chemical analysis (ESCA), is a very powerful tool for obtaining chemical compound information on the sample surface, and it can be combined with ion-beam etching equipment to measure depth profiles of XPS spectra.

XPS operation involves irradiating a sample surface with mono-energetic X-rays, and then measuring the states of electrons that are ejected from the sample surface by means of an energy analyzer. The energy analyzer acts as a band-pass filter, allowing only electrons with a particular kinetic energy to the electron detector. Figure 5.9 shows a schematic of an XPS setup. The main components of an XPS system include: (1) source of X-rays, (2) ultra-high-vacuum (UHV) stainless-steel chamber with UHV pumps, (3) electron collection lens, (4) electron energy analyzer, (5) (Mu-metal) magnetic field

shielding, (6) electron detector system, (7) moderate-vacuum sample introduction chamber, (8) sample mounts, (9) sample stage, and (10) set of stage manipulators. The X-ray is irradiated on the sample surface, which has sufficient energy to ionize an atom and emit a free electron from either the core or valence levels. The emitted electron is usually called the "photoelectron." The binding energy E_B of electrons in the sample can be determined by the following equation:

$$E_{kin} = h\nu - E_B - \Phi, \tag{5.2}$$

where, E_{kin} is the kinetic energy of the emitted photoelectron, $h\nu$ is the photon energy, E_B is the electron binding energy, and Φ is the work function of the material. This equation forms the basis of photoelectron spectroscopy. The binding energy of an electron depends on the sub-shell from which it originated. The characteristic energies at which electrons are emitted from the various sub-shells allow the atom to be identified. The above equation shows that the kinetic energy of a photoelectron changes with the photon energy, but the electron binding energy is independent of photon energy. XPS spectra are therefore usually plotted in terms of binding energy.

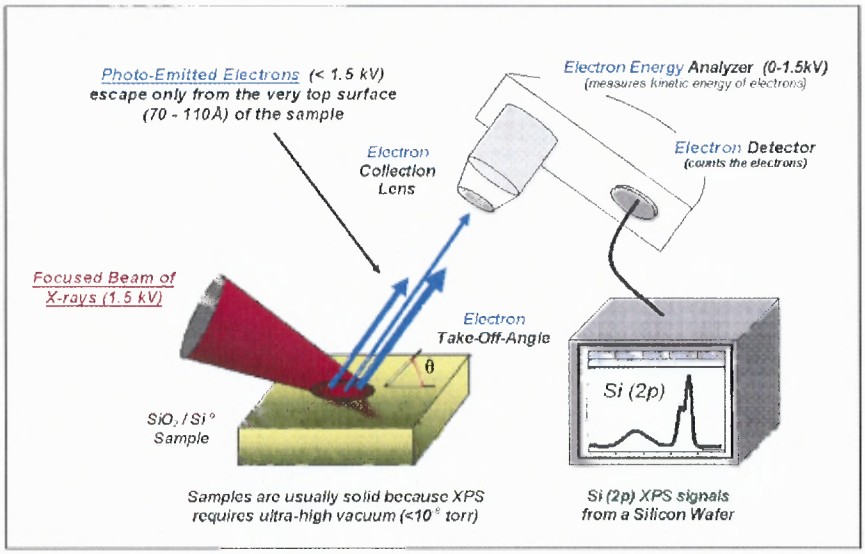

Figure 5.9 X-ray photoelectron spectroscopy [151].

XPS can also be used to identify chemical state, because the chemical bonding of an atom has an influence on the binding energy of all electrons. Shifts in binding energy make XPS a useful tool in chemical-state analysis. The advantages of XPS are the following: (1) chemical-state identification on surfaces, (2) identification of all elements except for H and He, (3) quantitative analysis, including chemical-state differences between samples, (4) applicable for a wide variety of materials, including insulating samples (e.g., paper, plastics, and glass), (5) depth profiling with matrix-level concentrations, and (6) thickness measurements. Disadvantages include: (1) detection limits typically ~0.1 at%, (2) smallest analytical area ~10 μm, (3) limited specific organic information, and (4) sample compatibility with a UHV environment [152].

5.7 Transmission Electron Microscopy

Transmission electron microscopy (TEM) is the most powerful tool for studying the full range of structural properties of interfaces, crystals, and thin films. It can also provide high spatial resolution information on composition, chemistry, and electrical properties.

The high spatial resolution of TEM is achieved by focusing the charged electron beam. Generally, higher the operating energy of the TEM, greater will be the lateral spatial resolution. TEM offers two mechanisms for observing the sample: sample and diffraction. The image mode produces a representation of the entire sample depth, as well as contrast results from several mechanisms, including mass contrast, phase contrast, thickness contrast, and diffraction contrast. Each of these modes provides specific information about a selected sample area. In the diffraction mode, the image of the diffracted electrons is obtained from the electron-illuminated sample, which provides information on crystallinity and crystal orientation.

Figure 5.10 shows a schematic diagram of the TEM setup. A light source at the top of the microscope emits the electrons that travel through the vacuum in the column of the microscope. Instead of glass lenses focusing the light in the light microscope, the TEM uses electromagnetic lenses to focus the electrons into a very thin beam. The electron beam then travels through the specimen of interest. Depending on the density of the material present, some of the electrons are scattered and disappear from the beam. At the bottom of the microscope, the unscattered electrons are incident on a fluorescent screen, which gives rise to a shadow image of the specimen with its different parts displayed in varied darkness according to their density.

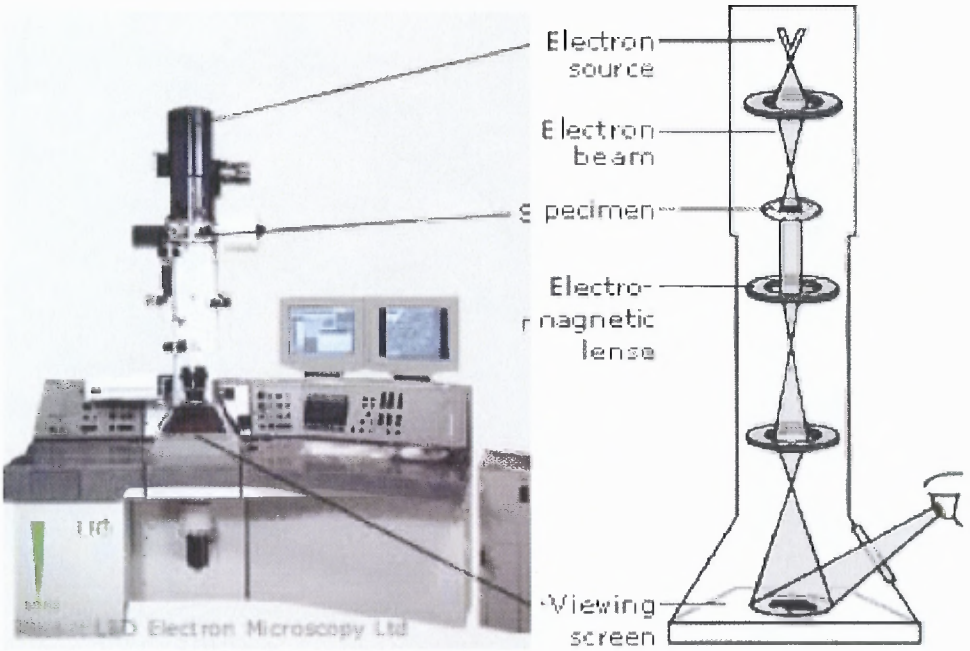

Figure 5.10 Transmission electron microscope [153].

TEM has its advantages and disadvantages. The advantages of TEM are the following: (1) the ultimate elemental mapping resolution of any analytical technique, (2) sub-0.5-nm image resolution, and (3) small-area crystallographic information. The disadvantages of TEM are the following: (1) significant sample preparation time, (2) samples are often prepared that are <100 nm, and (3) some materials are not stable in an electron beam environment.

5.8 Focused Ion Beam Microscope

Focused ion beam microscopy (FIB) is a widely used technique to characterize very small features of surfaces. FIB operates in a similar fashion to a scanning electron microscope, except for using a beam of ions instead of electrons used in SEM. Generally, a FIB microscope uses a finely focused beam of gallium ions of spot size < 10 nm, which is ejected from a liquid gallium ion source, to scan across the sample. The imaging of a

FIB microscope, using secondary electrons, provides surface information with similar resolution to that obtainable from an SEM. Figure 5.11 shows a schematic diagram of FIB setup.

Figure 5.11 Focused ion beam microscope [154].

A major difference between FIB and SEM is that FIB can directly etch material in selected regions for in-situ sectioning and imaging. The FIB microscope operates in two modes: (1) In high-magnification microscopy mode, only a low-beam current (< 100 pA) operation must be employed. This mode is used to take images of samples; (2) In the high-beam current (>1000 pA) operation mode, a large amount of material can be removed by sputtering, allowing precision milling of the specimen down to a submicron scale.

5.9 Spectrophotometer

Spectrophotometry is one of the most important tools for investigating the optical properties of the films. Figure 5.12 shows the Varian Cary 5G optical layout, which is based on two monochromators with a sampling and reference beam. The principle advantage of a double-beam spectrophotometer is that fluctuations in lamp intensity do not affect measurement results, because a reference signal is constantly taken throughout the scan, and the final measured value does not rely on a previously measured reference scan as is the case for a single-beam spectrophotometer.

Figure 5.12 Spectrophotometer [155].

The Cary 5G system uses a tungsten halogen lamp as the visible and near-infrared (NIR) source and a deuterium lamp as the ultraviolet (UV) source. An automated carousal swaps the lamps at a specified wavelength of 300 nm. The light beam passing through the sample or along the reference-beam path is detected by a photomultiplier tube (PMT) in the UV-Vis region and a lead sulfide (PbS) detector in the NIR region.

5.10 n & k analyzer

The n & k analyzer is an important technique for measuring the optical properties of the films. The n & k 1280 Analyzer uses broadband spectrophotometry over a wavelength range of 190 to 1000 nm, with innovative optics in conjunction with the Forouhi-Bloomer dispersion equations and other proprietary algorithms.

Figure 5.13 n & k analyzer [156].

Figure 5.13 shows the n & k analyzer 1280. These n & k analyzers determine film thickness, the spectra of refractive index (n), and extinction coefficient (k), as well as energy bandgap, interface roughness, and other optical properties. The spectra on n and k can be correlated to various other physical parameters, such as composition, resistivity, and degree of crystallinity. A wide variety of materials can be characterized including dielectrics, semiconductors, polymers, transparent conductors, and metals. Optical properties of structures such as thin films (less than 20 angstroms), thick films (up to 300 microns), and multi-layer stacks, deposited on transparent, opaque, or rough substrates,

can be measured using n & k 1280 Analyzer. Furthermore, an n & k analyzer is non-destructive and fast, providing results within seconds [156,157].

5.11 Photoelectrochemical Cell

A photoelectrochemical cell is the same as an electrochemical cell, except that it must allow for the easy illumination of the photoelectrode. A typical cell has three electrodes: the working electrode, reference electrode, and counter electrode. The cell consists of these three electrodes immersed in an aqueous solution held in a container. This is shown in Figure 5.14. For example, the container is a glass beaker, and it should be transparent to light. The glass container should be large enough to allow easy placement of the electrodes without being so large as to waste aqueous solution. They are also convenient for doing repeated measurements in many solutions. The electrolyte can be acidic or basic aqueous solution with different pH buffers. The working electrode is the semiconductor under examination, which generally has an exposed area of less than 0.25 cm^2. The counter electrode is a platinum sheet with an exposed area of about 2 cm^2. The reference electrode is a standard Ag/AgCl electrode filled with a saturated KCl solution. The working electrode is located right in front of the reference electrode. There is no ohmic loss associated with the reference electrode, because it does not pass any current. The counter electrode should be kept next to the reference electrode to minimize the ohmic loss.

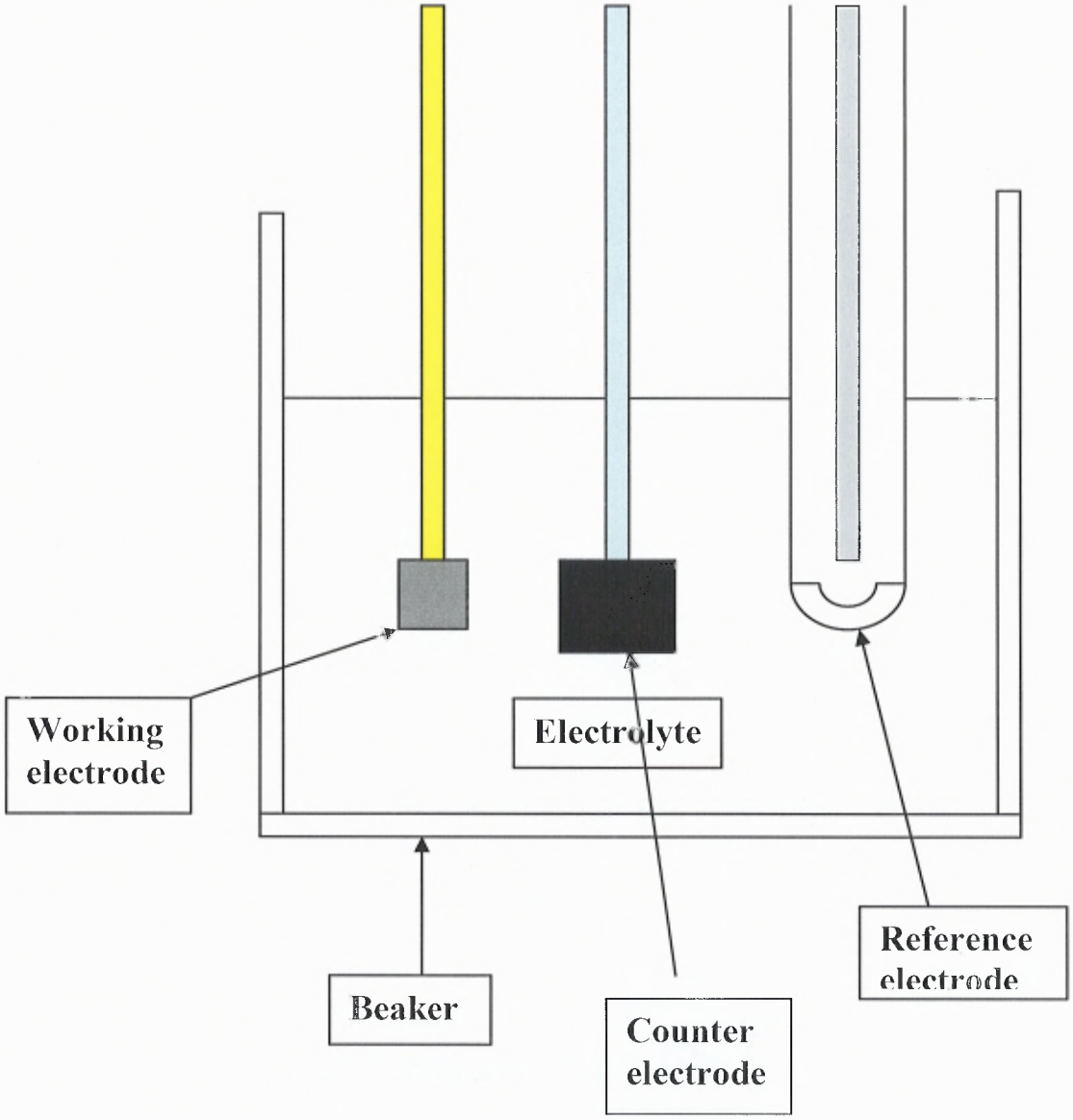

Figure 5.14 A schematic diagram of the photoelectrochemical cell.

Generally, a platinum sheet is used as the counter electrode, because it is chemically and electrochemically inert in many aqueous solutions. This removes the possibility that the dissolution products from the counter electrode will contaminate the

solution or the counter electrode will fail because of the buildup of an insulating corrosion product. In general, the counter electrode should have a much larger active area than the working electrode so that charge transfer at its surface is not hampered by high current densities.

A saturated Ag/AgCl reference electrode is usually selected because it is rugged, easy to maintain, and relatively inexpensive. Proper regular maintenance of a calomel electrode consists of keeping it filled with saturated KCl solution and storing it in saturated KCl solution when it is not being used. Less often, the electrode needs to be flushed with deionized water to remove large deposits of the KCl crystals that inevitably precipitate in it as the solution evaporates.

CHAPTER 6

RESULTS AND DISCUSSION

The research aimed to investigate high-quality metal-oxide thin films on fluorine-doped tin oxide (FTO)-coated glass for photoelectrochemical water splitting using solar energy. This chapter presents the results and discussions of the work carried out in this thesis.

6.1 Bandgap Narrowing of ZnO:N Films by Varying RF Sputtering Power in O_2/N_2 Mixtures

In this part of the research, bandgap narrowing of ZnO:N films by varying RF sputtering power in O_2/N_2 mixtures were investigated. ZnO:N thin films were synthesized by reactive RF magnetron sputtering using a Zn metal target in mixed N_2 and O_2 ambient with low O_2 mass flow rate [$(O_2/N_2+O_2)) = 5\%$].

To synthesize ZnO:N films with similar thickness, deposition rates for different RF powers were determined. The deposition rate increased linearly with the increase of RF power. The rates were 9, 17.5, 27.5, 40, and 73 nm/min for the ZnO:N films grown at 80, 100, 120, 150, and 200 W, respectively. The deposition rates were 3.7 and 74.2 nm/min for pure ZnO and Zn_3N_2 films, respectively. The gas ambient has a big impact on the deposition rate. The deposition rate of ZnO:N film grown in mixed N_2 and O_2 ambient is much higher than that of ZnO films grown in pure O_2 ambient, even though the same RF power was used. On the other hand, the deposition rate of the ZnO:N film grown in mixed N_2 and O_2 ambient at 200 W is similar to that of the Zn_3N_2 film grown at 200 W. The enhancement of deposition rate in N_2-containing ambient could be due to the

nitridation of the Zn metal target surface, because the Zn nitride is more conductive than the ZnO, leading to much higher sputtering yield [158, 159]. The ZnO:N film grown at 70 W had reproducibility problems, whereas those grown at RF powers of 80 W or higher were reproducible. This indicates that an RF power of at least 80 W is required to activate the N source for reproducible ZnO:N films in our sputtering system [160-163].

Figure 6.1 shows the XRD curves of ZnO, Zn_3N_2, and ZnO:N grown at different RF powers. It is seen that the ZnO film exhibits poor crystallinity due to the room-temperature sputtering process. The ZnO:N film grown at 80 W shows better crystallinity than the pure ZnO film, despite a faster deposition rate. For pure ZnO growth, the ambient is pure O_2 gas. For ZnO:N growth, the ambient is mainly N_2 with only 5% O_2. The substrate temperature was indirectly measured by a thermocouple (TC), which was placed next to the substrate. The TC indicated that the substrate temperature was about 41°C during the sputtering process for pure ZnO films. The substrate temperature during the sputtering process is affected by the bombardment of the sputtered ions and, therefore, the substrate temperature increases with increase in sputtering yield (or deposition rate) and sputtering time. Higher sputtering yield enhances the ion bombardment, accelerating the increase in substrate temperature. However, it also simultaneously reduces the sputtering process time for the same thickness of the film, limiting the increase of the substrate temperature. It is also seen that the temperature measured by the TC did not increase above 44°C for any of the ZnO:N films [160-163].

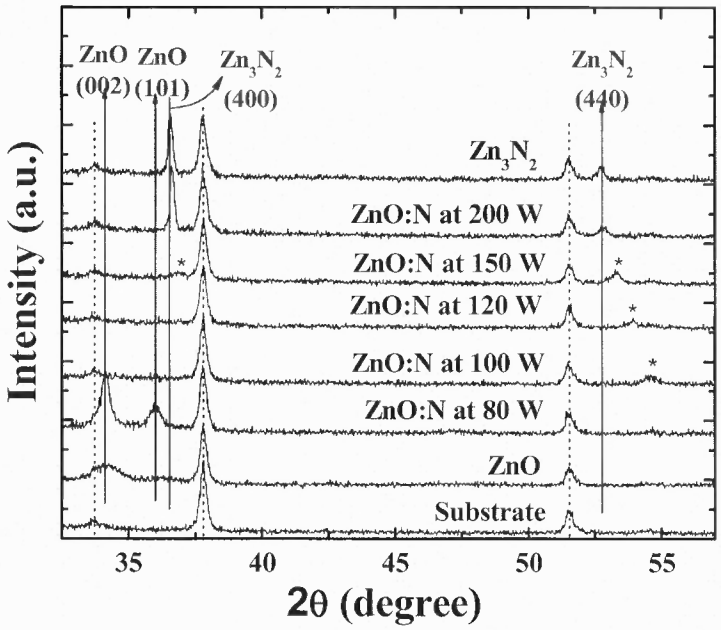

Figure 6.1 X-ray diffraction curves of pure ZnO, Zn_3N_2, and ZnO:N films grown at various RF powers [160-163].

When the RF power was increased to 100 W, the crystallinity again became poor. The peaks belonging to ZnO, seen in the XRD curve of the ZnO:N grown at 80 W, disappeared. The ZnO:N film at 100 W grew at almost twice the deposition rate observed during 80 W deposition. In addition, the concentrations of N in 80 W and 100 W samples were about 2 at% and 20 at%, respectively, as determined by XPS. It is known that a high concentration of dopant can deteriorate crystal structure. Therefore, poor crystallinity of the ZnO:N film grown at 100 W may be caused mainly by the high concentration of N, as well as by the high deposition rate. Crystallite sizes were 9.4 and 24.4 nm for the pure ZnO and the ZnO:N grown at 80 W, respectively, which were estimated by applying the Debye-Scherrer equation to the XRD data. The ZnO:N film grown at 100 W exhibited only weak diffraction near 35°, indicating that it had a short-range order, amorphous-like structure. When the RF power was further increased to 200 W, the film became Zn_3N_2-

like. It is also noted that when the growth ambient was changed into mixed N_2 and O_2, a small peak appeared, as indicated by *. This peak shifted to a lower angle as the RF power increased, indicating increased N concentration. These peaks indicate the formation of zinc oxynitride films. The XRD data reveal that the sample grown at 200 W became polycrystalline Zn_3N_2-like [160-163].

The microstructure of the zinc oxynitride films was investigated by TEM. We found that the zinc oxynitride films have an intermediate ordering structure. Figure 6.2(a) shows a high-resolution TEM image obtained from a ZnO:N film grown at an RF power at 120 W. The grain sizes are very small, in the range of a few nanometers. Nanoprobe X-ray energy-dispersive spectroscopy (EDS) [Fig. 6.2(b)] revealed that these small grains are indeed zinc oxynitrides, with about 20 at% of N [160-163].

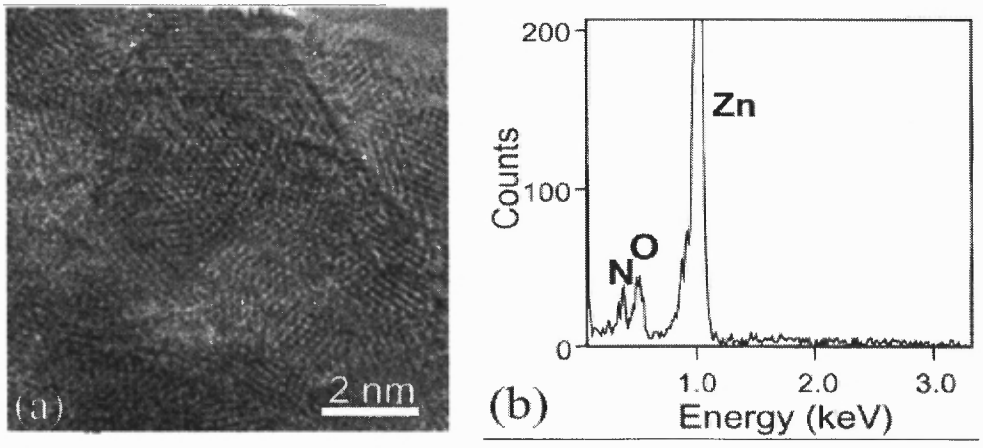

Figure 6.2 (a) High-resolution TEM images of a zinc oxynitride film deposited at an RF power of 120 W. (b) Nanoprobe X-ray dispersive spectroscopy obtained from the zinc oxynitride grains [160-163].

Figure 6.3(a) shows the relative absorption coefficients for the ZnO:N films grown at different RF powers. The absorption coefficient was assumed in order to evaluate the bandgap energies of the films [164]. The direct electron transition from

valence to conduction bands was also assumed for the absorption coefficient curves, because both ZnO and Zn_3N_2 films are direct-bandgap materials [159, 165]. The optical bandgap for the direct electron transition is described by the following equation [159]:

$$(\alpha h\nu)^2 = \beta(h\nu - E_g)\,, \tag{6.1}$$

where, $h\nu$ is the photon energy, E_g is an optical bandgap, and β is the edge width. In accordance with this equation, $[(-\ln T)(h\nu)]^2$ was plotted against the photon energy $h\nu$, as shown in Fig. 6.3(a). The optical bandgaps of the films were also determined by extrapolating the linear portion of each curve in Fig. 6.3(a) to $[(-\ln T)(h\nu)]^2 = 0$. They are about 2.9 eV (RF power = 80 W), 2.31 eV (RF power = 100 W), 2.15 eV (RF power = 120 W), 1.76 eV (RF power = 150 W), and 1.55 eV (RF power = 200 W). The bandgaps are 3.28 and 1.52 eV for pure ZnO and Zn_3N_2, respectively. It shows clearly that the bandgap decreased with the increase in RF power.

Figure 6.3(b) shows the absorption spectra of ZnO:N films grown at various RF powers. In order to eliminate the effect of the substrate, the absorbance was calculated by the following equation [166]:

$$A=1-R(ZnO)-T(ZnO)/T(substrate), \tag{6.2}$$

where, R and T are the measured reflectance and transmittance, respectively. The absorption spectra show that the light absorptions are successfully shifted into visible regions with the increase in RF power. Therefore, it demonstrates that RF power can be used effectively to control the N concentration in ZnO:N thin films.

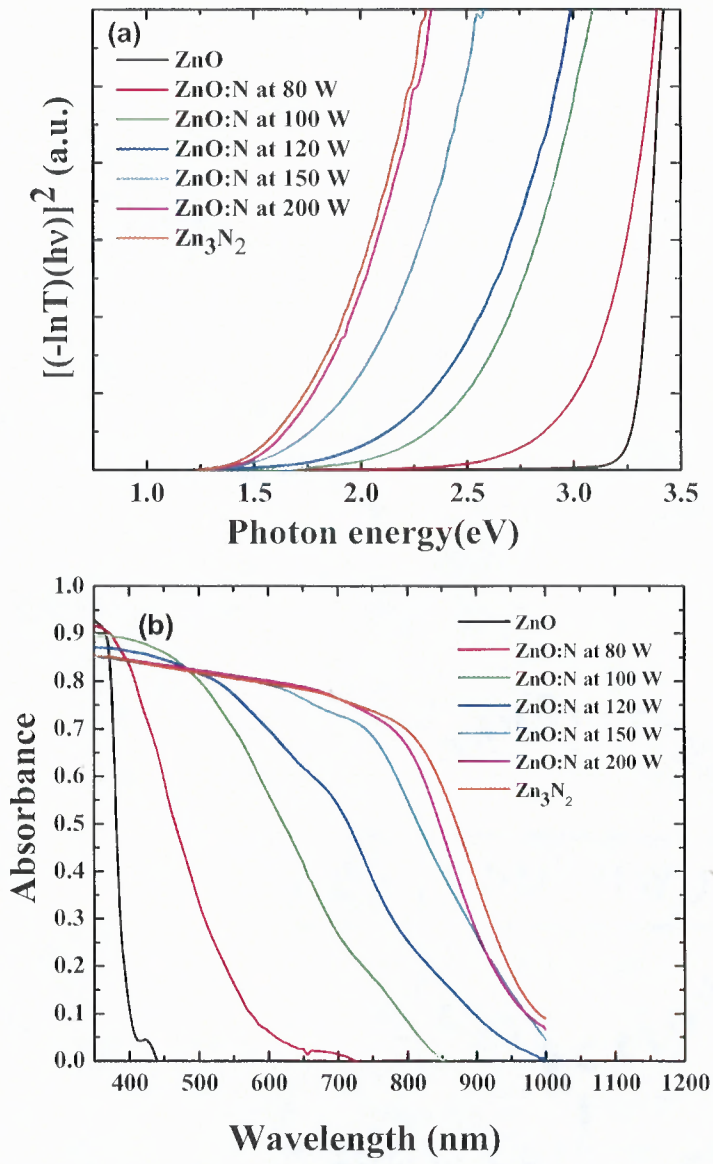

Figure 6.3 (a) Relative absorption coefficients of pure ZnO, Zn_3N_2, and ZnO:N films grown at various RF powers. (b) Optical absorption spectra of the ZnO:N films grown at various RF powers [160-163].

To understand the effects of N incorporation on the optical properties of ZnO:N, we calculated the electronic structure of N-incorporated ZnO by first-principles density-functional theory using the super-cell approach [167, 168]. The host supercell contains 128 atoms. Figure 6.4 shows the calculated density of states (DOS) of ZnO and ZnO:N.

The red curve indicates the calculated total DOS of the supercell containing pure ZnO (marked by ZnO). The blue curve is the calculated total DOS of the super-cell containing one substitutional N atom (marked by ZnO:N). The dark-yellow curve indicates the calculated partial DOS of the N atom [marked by N(x4)], which is scaled up by 4 times. The valence band of ZnO is mainly derived from O *2p* orbitals. The N *2p* orbitals are much shallower than the O *2p* orbitals. When N atoms are incorporated in ZnO, they introduce an impurity band above the valence band of ZnO. As a result, the valence-band maximum (VBM) of ZnO:N becomes shallower due to the mixing between O*2p* and N *2p* states. In the mean time, the conduction band remains unchanged, as is seen in Figure 6.4. Therefore, the bandgap is reduced. The position of the VBM depends on the concentration of N atoms. A higher N concentration leads to a shallower VBM, and therefore, a smaller bandgap. Thus, the bandgap of ZnO:N can be controlled by the concentration of N in ZnO:N [160-163].

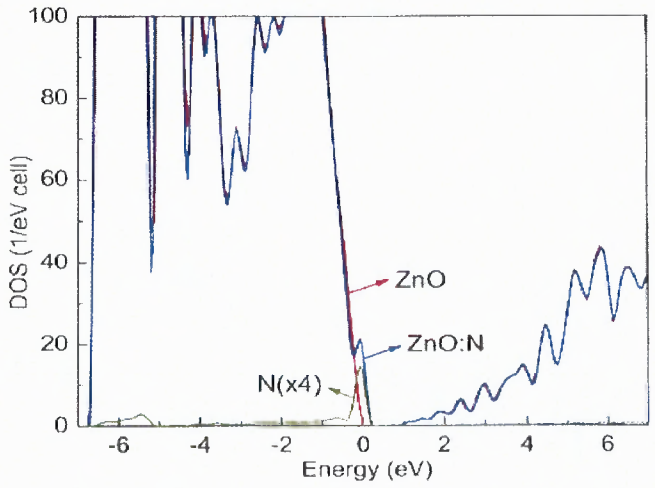

Figure 6.4 Calculated total DOS of pure ZnO (red curve indicated by ZnO) and ZnO:N (blue curve indicated by ZnO:N), and partial DOS of the N atom (dark-yellow curve indicated by N) in supercell [160-163].

6.2 Photoelectrochemical Properties of N-Incorporated ZnO Films

The photoelectrochemical properties of ZnO:N thin films prepared by reactive RF magnetron sputtering in mixed N_2 and O_2 gas ambient and comparison of those as-grown and annealed pure ZnO films are presented in this part of the research.

Figure 6.5 shows XRD curves of the as-grown and annealed ZnO and ZnO:N films. The as-grown ZnO film exhibits nanocrystalline features with crystallite sizes below 10 nm, as estimated according to the Scherrer equation. However, the as-grown ZnO:N films showed a sharper peak, indicating larger crystallite sizes of about 24 nm. Deposition rate analyses show that the growth rate was 9 nm/min for ZnO:N film deposition, but 3.7 nm/min for pure ZnO. A higher deposition rate is known to result in increased crystallinity. Because the crystallinity of the film is closely related to its PEC property, the pure ZnO film was annealed for 1 h at 500°C in air ambient to achieve similar crystallinity to that of ZnO:N. After annealing, the crystallite sizes were shown to have increased to about 22 nm, close to that of ZnO:N film, as shown in Figure 6.5 [161-163, 169].

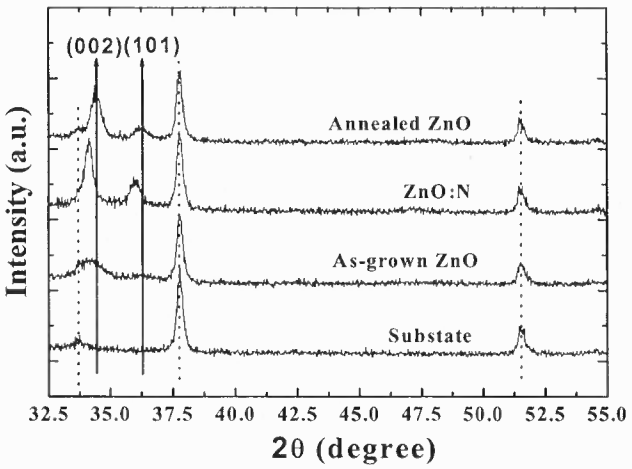

Figure 6.5 X-ray diffraction curves of the as-grown ZnO, ZnO:N, and annealed ZnO films [161-163, 169].

Figure 6.6 shows optical absorption spectra of the as-grown and annealed ZnO films and the as-grown ZnO:N films. The as-grown and annealed ZnO films showed similar optical absorption spectra and could only absorb light with wavelengths below 450 nm, due to their wide bandgap. However, the ZnO:N films could absorb lower-energy photons, up to 700 nm, indicating that the bandgap was narrowed by N incorporation in ZnO [159, 170].

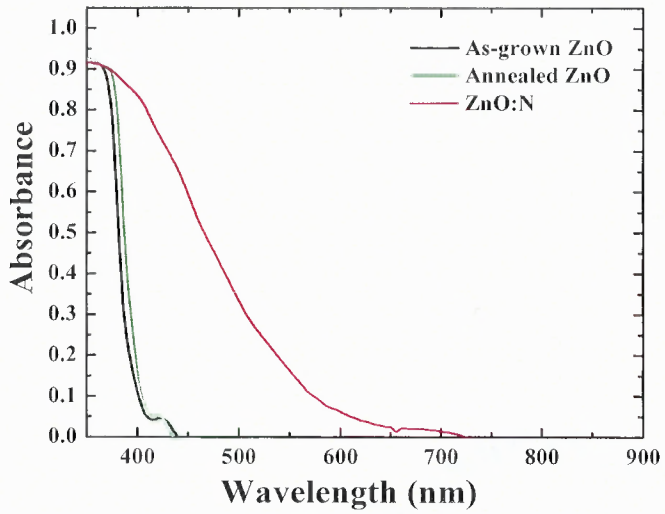

Figure 6.6 UV-Vis optical absorption spectra of the as-grown and annealed ZnO and ZnO:N films [161-163, 169].

Figure 6.7 shows Mott-Schottky plots of the as-grown and annealed ZnO films and the ZnO:N films. The positive slopes indicate that all of the samples are n-type semiconductors. The origins of the n-type conductivity in the as-grown and annealed ZnO films are likely due to native defects such as Zn interstitials or/and oxygen vacancies (V_o) [171]. It is known that an N occupying an O site (N_o) is an acceptor, which should result in p-type ZnO:N [172]. However, Figure 6.7 shows that the ZnO:N film was actually n-type. It was reported that the ZnO films deposited in N_2 plasma are usually n-

type, due to substitutional N_2 molecules at an O site that act as shallow double-donors [173, 174]. Perkins *et al.* [173] reported recently that a N_2/O_2 plasma can contain a substantial fraction of N_2^+ molecules that can become incorporated into the ZnO films, leading to the n-type behavior. Theoretical study [174] has also shown that the dissociation energy for N_2 molecules is very high (9.9 eV).

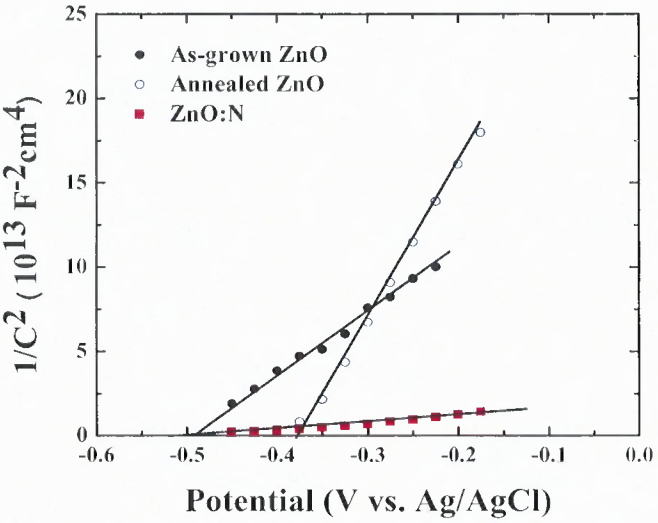

Figure 6.7 Mott-Schottky plots of the as-grown and annealed ZnO and ZnO:N films [161-163, 169].

To confirm the presence of N states in the ZnO:N films, XPS measurements were employed. Figure 6.8 shows the XPS spectra of the N 1s region of the annealed ZnO film and the ZnO:N film. The annealed ZnO film exhibits no N 1s peak, whereas the ZnO:N film shows three N 1s-related components. The N 1s peak around 404.2 eV corresponds to the substitutional N_2 at the O site [173]. The peaks around 396.4 and 398.5 eV (the shoulder part of the peak) correspond to substitutional N and carbon/hydrogen-related nitrogen, respectively [173]. These data indicate that the ZnO:N film contains substantial

amounts of substitutional N, as well as substitutional N_2, at O sites. The calculated total N concentration is about 2 at.%.

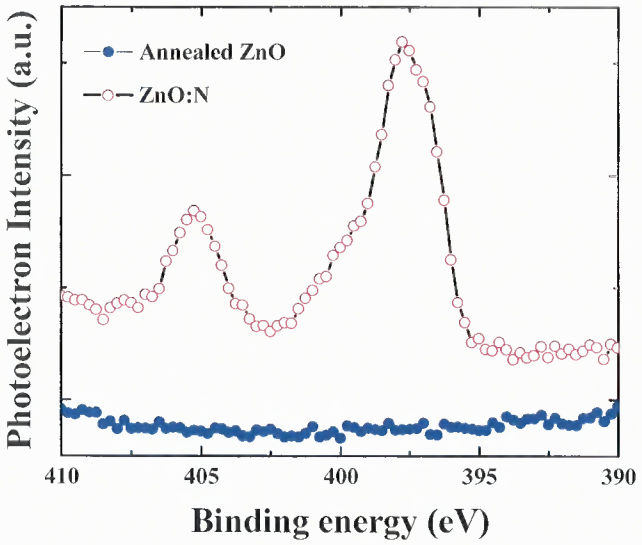

Figure 6.8 XPS spectra of the N 1s region for the annealed ZnO and ZnO:N films [161-163, 169].

From the slopes of the Mott-Schottky plots, the donor densities in the films were evaluated according to the following equation [175]:

$$\frac{1}{C^2} = \left(\frac{2}{e_o \varepsilon \varepsilon_o N_d}\right)\left[(E - E_{fb}) - \frac{kT}{e_o}\right], \tag{6.4}$$

where, N_d is the donor density, ε_o is the permittivity of vacuum, ε is the dielectric constant of the semiconductor, E is the electrode potential, E_{fb} is flat-band potential, and kT/e_o is the temperature-dependent term in the Mott-Schottky equation. Assuming the dielectric constant of the samples to be about 8.5 [176], the donor densities of the as-grown and annealed ZnO films and the ZnO:N film are calculated to be 4.6×10^{16}, 1.8×10^{16}, and $3.8\times10^{17}/cm^3$, respectively. The annealed ZnO film exhibits lower donor

density than the as-grown ZnO films. This may be due to the annealing being conducted in air, which can reduce the amount of Zn interstitials and O vacancies. ZnO:N films exhibit a higher donor density than the as-grown ZnO films due to N_2 incorporation and/or native defects such as Zn interstitials and O vacancies [161-163, 169].

The flat-band potentials (E_{fb}) of these films are obtained by the x-intercept of their Mott-Schottky plots. The as-grown ZnO films and the ZnO:N films have similar E_{fb} (≈ -0.49 V vs. Ag/AgCl). However, the annealed ZnO films have an E_{fb} value of -0.38 V, which is about 0.1 V higher than that of the as-grown ZnO films [161-163, 169].

Figure 6.9 shows photocurrent-voltage curves for the as-grown and annealed ZnO films and the ZnO:N films under illumination with the ultraviolet/infrared (UV/IR) filter and dark currents. The anodic photocurrents of all the samples increase with increasing potentials, which is again indicative of n-type semiconductor (as corroborated in Figure 6.7). The photocurrent onset potentials of the samples were about 0.2 to 0.4 V anodic from their Mott-Schottky-determined flat-band potentials. This overpotential is due to slow charge transfer and surface recombination at the semiconductor/solution interface [177, 178]. Figure 6.10 shows photocurrent behavior with time for the annealed ZnO under light on/off illumination at 1.0 V. It shows that initial photocurrent decay appeared with light on illumination, despite a high potential of 1.0 V. The photocurrent decay indicates recombination of photogenerated charge carriers through the surface states. In addition, crystallite size was small, as shown in Figure 6.5, leading to a large number of surface recombination centers. Therefore, this overpotential is due to the surface recombination. Because the dark anodic currents begin to appear around 1.1 V, the maximum photocurrents of the three samples are compared at this potential. No limiting

photocurrents are observed before the appearance of the dark anodic currents at 1.1 V [161-163, 169].

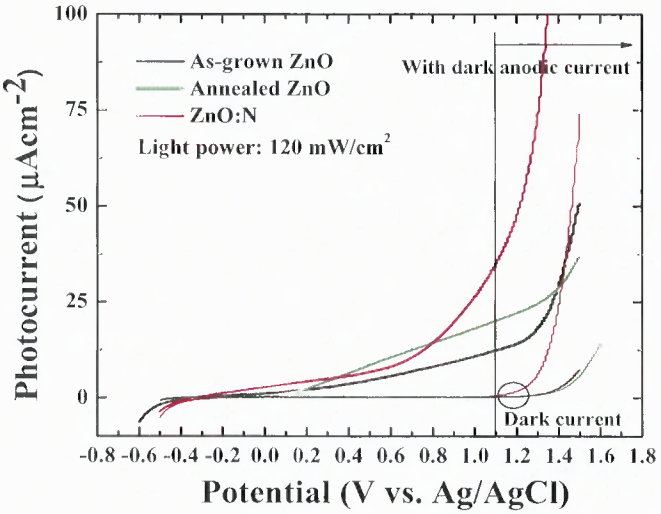

Figure 6.9 Photocurrent-voltage curves for the as-grown and annealed ZnO and the ZnO:N films under light illumination (intensity 120 mW/cm^2) with the UV/IR filter and under dark condition, indicated by the circle. (0.5 M Na_2SO_4 aqueous solution and scan rate of 5 mV/s were used.) [161-163, 169].

This phenomenon appears to be related to the small width of the space-charge layer of these samples. A photocurrent normally increases with the increase in the width of the space-charge layer if the width is shorter than the film thickness [179]. If the width of the space-charge layer is larger than the film thickness, a limiting photocurrent should be observed. Assuming a Schottky approach for the semiconductor/solution interface, the width of the space-charge layer, W, can be expressed as [180]:

$$W = \left[\frac{2\varepsilon\varepsilon_o (E - E_{fb})}{qN_D} \right]^{1/2} . \tag{6.5}$$

From the data of the Mott-Schottky plots in Figure 6.7, the W values of the samples are calculated. At a potential of 1.1 V, the W values are about 181, 281, and 62 nm for the as-grown and annealed ZnO films and the ZnO:N films, respectively. These W

values at 1.1 V are much smaller than that for the film thickness of 500 nm, resulting in no limiting photocurrents. The photocurrent of the annealed ZnO films at 1.1 V is larger than that of the as-grown ZnO films, most likely due to both better crystallinity and larger value of W of the annealed ZnO films. It should be noted that the photocurrent of the ZnO:N films at 1.1 V is larger than of the annealed ZnO films, despite its much smaller W value. Even with similar crystallinity (as shown in Figure 6.5) and smaller W value, the larger photocurrent of the ZnO:N films indicates that the photocurrent is affected more significantly by the optical properties of the ZnO and ZnO:N films [161-163, 169].

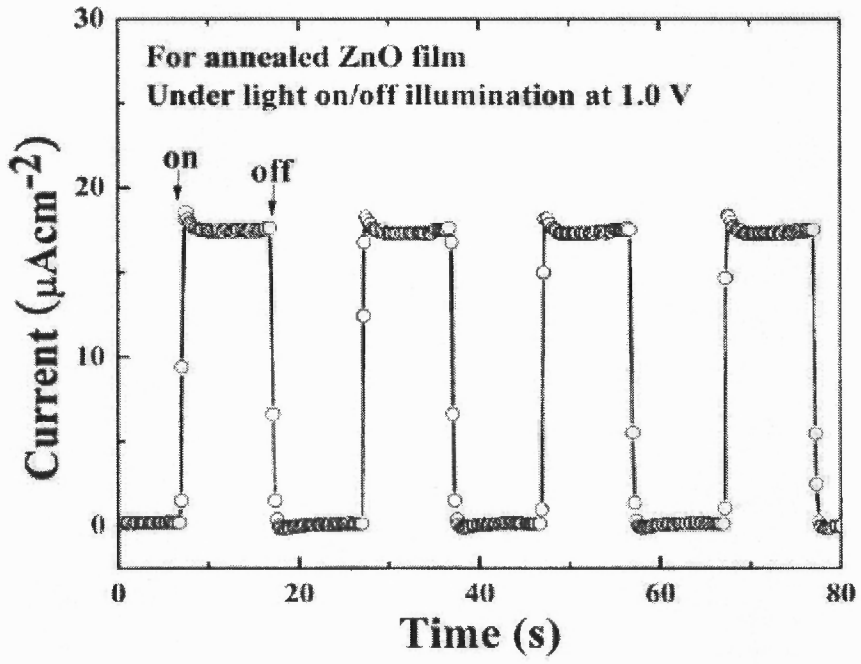

Figure 6.10 Photocurrent behavior with time for the annealed ZnO films performed under light on/off illumination with the UV/IR filter at 1.0 V. (Light intensity of 120 mW/cm^2 and 0.5 M Na_2SO_4 aqueous solution were used) [161-163, 169].

To investigate in more detail these two competing factors (i.e., the width of the space-charge layer and inherent optical property), we measured photoresponses with color-filtered illumination. Figure 6.11 shows the photocurrent-voltage curves of the samples under illumination with UV/IR filter in combination with a blue filter (a), yellow

filter (b), and red filter (c) that correspond to wavelength ranges of 350-475, 505-800, and 580-800 nm, respectively. The insets show the optical spectra of the filters. The photocurrents of the as-grown and annealed ZnO films in Figure 6.11(a) are almost the same as in Figure 6.9. Because ZnO films have large bandgaps and can only absorb light in the short-wavelength region below 450 nm (Figure. 6.6), the blue filter should pass all above-gap photons, leaving photocurrents unaltered. However, data indicate that with blue filtering, the photocurrent of the ZnO:N films is smaller than that of the ZnO films at potentials below 1.1 V. In the long-wavelength regions, the ZnO:N films exhibit photoresponse, but the pure ZnO films do not, due to their large bandgap. Figures 6.11(b) and (c) show that both the as-grown and annealed pure ZnO films do not demonstrate any photoresponse in the long-wavelength region. Figure 6.11(c) using the red and UV/IR filter shows no discernable difference with Fig. 6.11(b) and corroborates the visible light absorption of the ZnO:N films. Note that ZnO:N films are not optimized and the photocurrents generated by ZnO:N films are not high. These results demonstrate that N incorporation in ZnO can shift the photoresponse of ZnO films into the visible-light region, which is the main component of sunlight [161-163, 169].

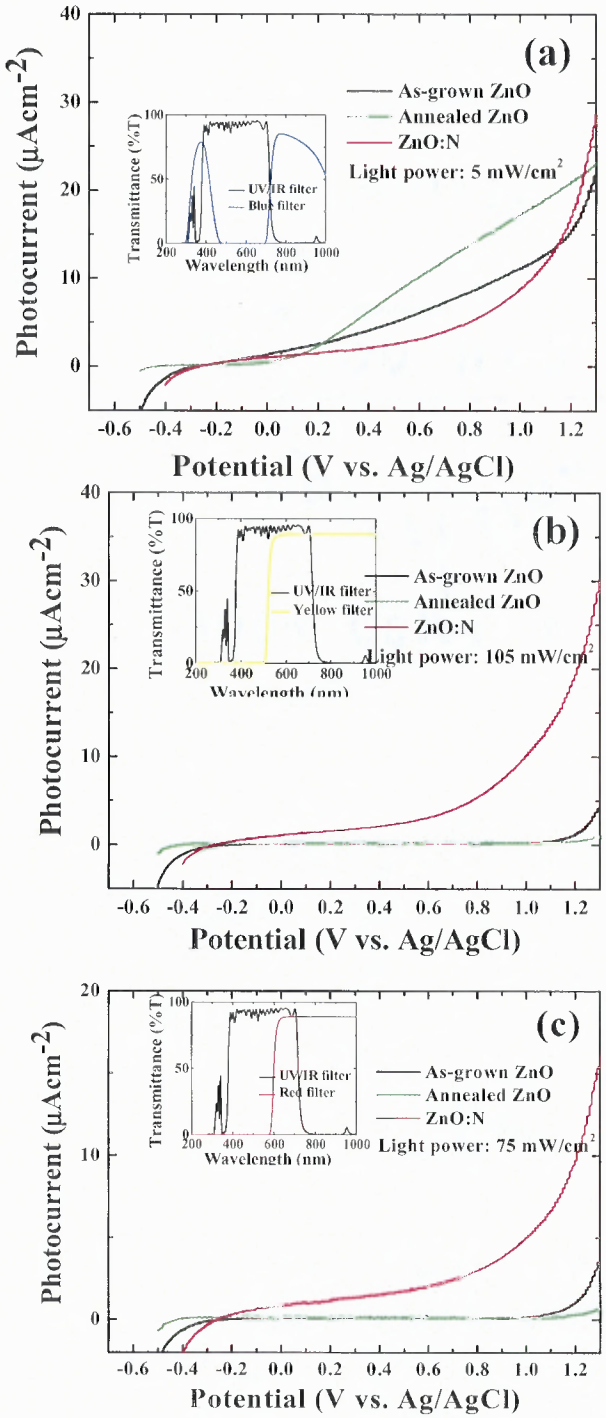

Figure 6.11 Photocurrent-voltage curves of the samples under light illumination with the UV/IR filter and (a) blue, (b) yellow, and (c) red filters, whose light intensities are 5, 105, and 75 mW/cm^2, respectively. The insets show the transmittance profiles of the filters [161-163, 169].

6.3 Synthesis of Bandgap-Reduced *p*-type ZnO Films by Cu Incorporation

In this part of the research, synthesis of both p-type and significantly reduced-bandgap ZnO thin film by heavy Cu-incorporation is reported.

The density-functional theory calculations were performed using the VASP code, with local density approximation [167], and ultrasoft pseudopotentials [168]. Zn 3*d*, Cu 3*d*, Ag 4*d*, and Au 5*d* were treated as valence states. The energy cutoff for the plane-wave expansion was 380 eV. The impurities in ZnO were modeled by the supercell approach. A 128-atom host supercell is used for all defect calculations. In all the calculations, the supercell size was keep the same, but all the atoms are allowed to relax until the Hellmann-Feynman forces acting on them become less than 0.01 eV/Å [162].

The large bandgap of ZnO is attributed to the fact that both the O 2*p* orbital and the Zn 3*d* orbital are too deep. As a result, the valance-band maximum (VBM) of ZnO is too deep. The position of conduction-band minimum (CBM) is appropriate for PEC water splitting. Therefore, it is desirable to up-shift the VBM to reduce the bandgap of ZnO. Accordingly, there are two methods to reduce the bandgap: (1) generating impurity bands above the O 2*p* orbital; and (2) up-shift the O 2p orbital by introducing cations with *d* orbitals shallower than Zn 3*d*. For the first method, the impurity bands can be generated by incorporating impurities such as N, C, and S [162].

For the second method, Group-Ib elements are potential candidates, because their *d* orbitals are shallower than the 3*d* orbital of Zn. The coupling between the Group-Ib *d* orbital and O 2*p* orbital is expected to push the valence band of ZnO upward, but the conduction band should remain unchanged. In addition, the shallow *d* orbital would produce impurity bands. Thus, the VBM will be up-shifted and the bandgap of ZnO will

be narrowed. Figure 6.12 shows calculated PDOS of the first (red), second (blue), and third (green) nearest-neighboring O atoms of an impurity and the PDOS of the impurity (dotted black), which is (a) Cu, (b) Ag, and (c) Au. It is seen that the *d* bands of Cu, Ag, and Au are all mixed with the 2*p* band of the O, ensuring strong *d*-*p* coupling with the first nearest-neighboring O atom. As a result, the *p* band of the first nearest-neighboring O atoms of the impurity is pushed to higher energy. The CBM is not affected significantly by these impurities. It is thus expected that the VBM will be shifted to higher energy after doping with Cu, Ag, or Au, resulting in preferred bandgap narrowing. Calculations also showed that the solubility of Cu in ZnO should be higher than that of Ag and Au, because the size mismatch between Cu and Zn is smaller than that between Ag or Au and Zn. Calculations further revealed that Group-Ib elements are potential dopants to produce p-type ZnO. However, because of their high ionization energies, high concentrations of these impurities are needed to produce p-type conductivity. According to calculated impurity formation energies [181], Cu incorporation may be the most possible candidate that can lead to both p-type and bandgap-reduced ZnO [162].

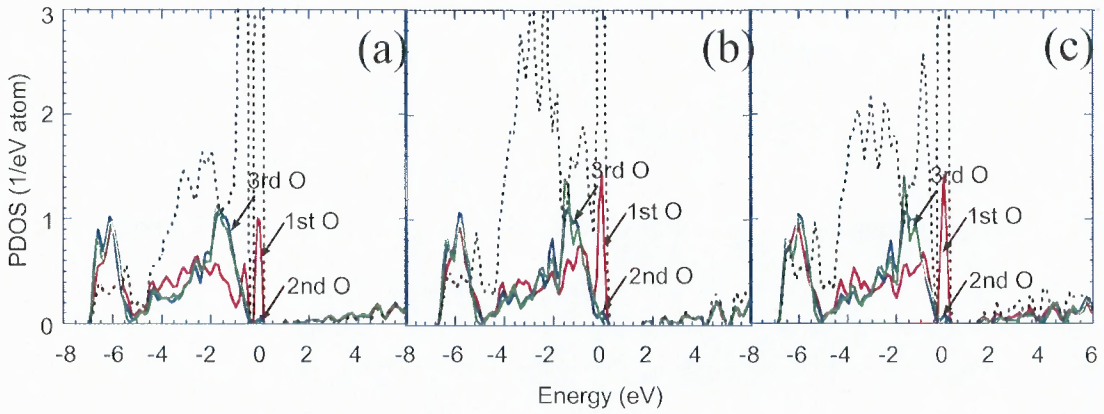

Figure 6.12 Calculated PDOS of ZnO with a substitutional Group-Ib element, (a) substitutional Cu, (b) a substitutional Ag, and (c) a substituional Au [162].

Figures 6.13(a) and 6.13(b) show X-ray diffraction curves for as-grown and 500°C-annealed ZnO:Cu films, respectively. The number n of ZnO:Cu(n) indicates the number of Cu chips dispersed on the Zn target for the depositions. All the as-grown films had a short-range ordered, amorphous-like structure. After post-deposition annealing, the films exhibited a polycrystalline structure, with a main peak at 34.4° corresponding to the (002) plane. There are no peaks corresponding to metallic Cu or its compounds, indicating no obvious phase separation in as-grown and 500°C-annealed ZnO:Cu films. However, it was found that a CuO phase begins to form when ZnO:Cu films were annealed at 600°C. Figure 6.13(c) shows a comparison of XRD curves obtained from ZnO:Cu(10) films annealed at 500° and 600°C. The diffraction peaks at 35.58° and 38.63°, corresponding to $(\bar{1}11)$ and (111) of the CuO phase, are only seen in ZnO:Cu(10) films annealed at 600°C [162, 182-184].

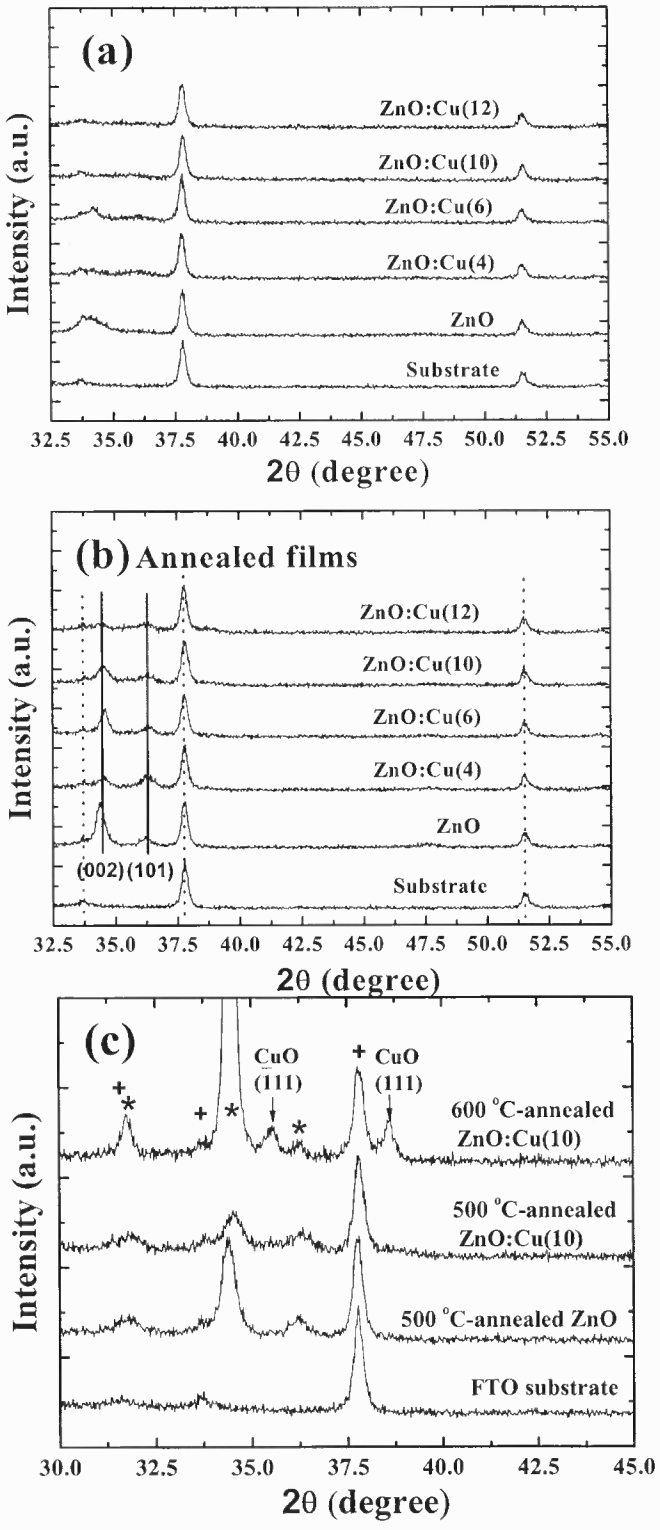

Figure 6.13 X-ray diffraction curves of (a) as-grown, (b) 500°C-annealed ZnO:Cu films with varying number of Cu chips (4, 6, 10, and 12), respectively, and (c) ZnO:Cu(10) films annealed at 500° and 600°C. * and + indicate the peaks related to ZnO and FTO substrate, respectively [162, 182-184].

It is known that the Zn-O bonding energy is rather low, only about 159 kJ/mol [171,185]. Annealing at high temperature can dramatically enhance the formation of O vacancies in ZnO. To reveal the annealing effects, we measured the optical absorption of pure ZnO films annealed at various temperatures. Figure 6.14 shows the optical absorption of an as-grown ZnO film and ZnO films annealed at 500° and 600°C. It is seen that the optical absorption of the film annealed at 600°C exhibits a dramatic change: its absorption extends into regions with much longer wavelength, due to the formation of a high concentration of O vacancies. This significant structural change at this annealing temperature should help the formation of the CuO phase. These results suggest that the annealing temperature should be lower than 600°C to avoid the formation of the CuO phase [162, 182-184].

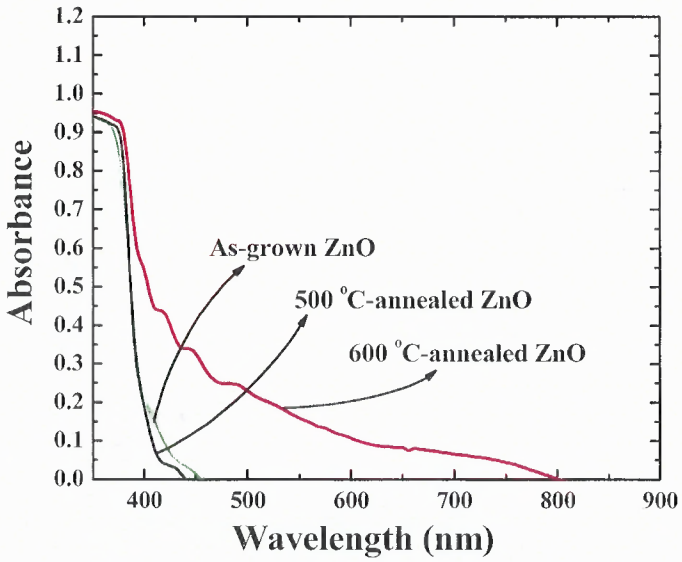

Figure 6.14 Optical absorption curves of the as-grown, 500°C-annealed, and 600°C-annealed pure ZnO films [162, 182-184].

Figures 6.15(a)–(c) show AFM surface morphology (1×1 μm^2, height: 251 nm) of the 500°C-annealed ZnO, ZnO:Cu(4), and ZnO:Cu(12) films, respectively. The grain size of the annealed pure ZnO film is much larger than that of the annealed ZnO:Cu films.

Figure 6.15(d) shows grain size and root-mean-square (RMS) surface roughness of the annealed films as a function of the number of Cu chips. The surface roughness decreased slightly from 20 to 15.5 nm with the increase of Cu chips.

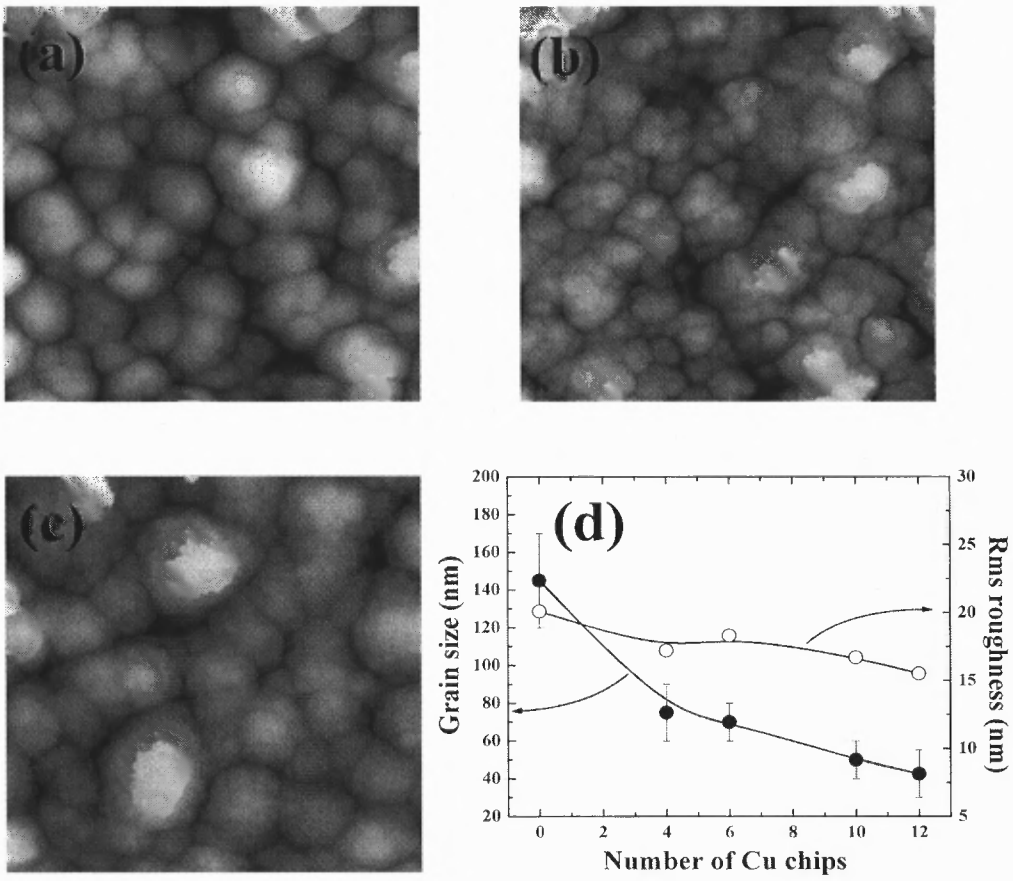

Figure 6.15 [(a)-(c)] AFM surface morphologies (1 x 1 μm^2, height: 251 nm) of the 500°C-annealed pure ZnO, ZnO:Cu(4), and ZnO:Cu(12). (d) Grain size and root-mean-square (RMS) surface roughness of the 500°C-annealed films as a function of the number of Cu chips [162, 182-184].

The Cu concentrations in ZnO:Cu films were measured by XPS, which increased from 3.0 to 9.8 at% with the increase in Cu chips from 4 to 12. Cu can have various bonding states, such as Cu°, Cu^{1+}, and Cu^{2+} [186]. Figure 6.13 showed that there are no CuO peaks for the 500°C-annealed ZnO:Cu films, indicating that Cu atoms exist in either

the Cu° or Cu^{1+} states. The Cu^{1+} state in ZnO acts as an acceptor state [181]. Unfortunately, the Cu° and Cu^{1+} states have very similar $3p_{3/2}$ values of 932.7 and 932.5 eV, respectively, which make it very difficult to distinguish them by XPS [186].

Figures 6.16(a) and 6.16(b) show the optical-absorption spectra of as-grown and 500°C-annealed pure ZnO and ZnO:Cu films, respectively. The as-grown and 500°C-annealed pure ZnO films showed similar optical-absorption spectra and could absorb only light of wavelengths below 450 nm, due to its wide-bandgap nature. Figure 6.16(a) shows that the absorption of the as-grown ZnO:Cu films extend into the infrared region. These absorptions may only be explained by the metallic Cu states. Because the depositions were carried out at room temperature, the ZnO:Cu films were not fully crystallized, as shown by the XRD curves. It is very likely that Cu atoms may not be fully oxidized, leaving metallic Cu in the as-grown films. Such metallic Cu atoms are responsible for the absorption in the infrared region. However, the 500°C-annealed ZnO:Cu films did not absorb the photons in the infrared region. XRD revealed that recrystallization occurred during the annealing process. It is very likely that the metallic Cu atoms were activated to occupy Zn sites during this process and the metallic Cu atoms changed their states from Cu° to Cu^{1+}. As a result, the optical absorption moved to the shorter-wavelength region, because there is no more metallic Cu-induced absorption in the infrared region [162, 182-184].

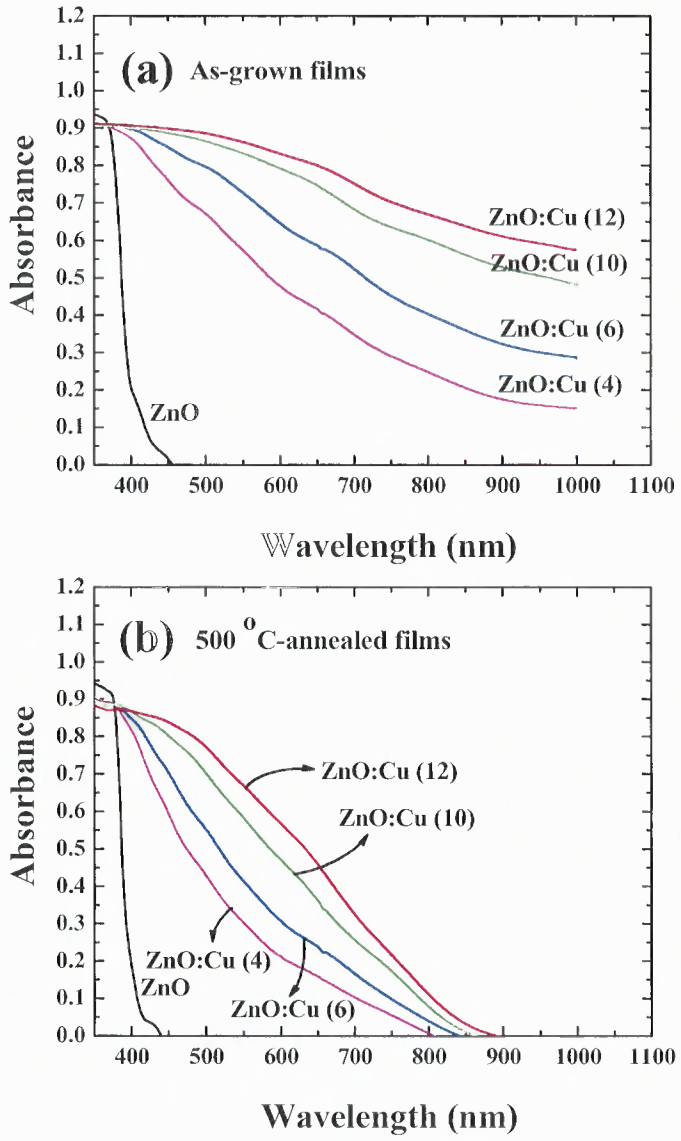

Figure 6.16 Optical absorption spectra of (a) as-grown and (b) 500°C-annealed ZnO:Cu films with varying number of Cu chips [162, 182-184].

Figure 6.17(a) shows absorption coefficients of the 500°C-annealed pure ZnO and ZnO:Cu films derived from Figure 6.16(b). The optical bandgap cannot be modeled by a simple direct or indirect transition. Theoretical study [24] has shown that the Cu 3d orbital is much shallower that the Zn 3d orbital. When a Cu atom occupies a Zn site in ZnO, it introduces two main effects: (1) The strong d-p coupling between Cu and O

moves O 2p up, which narrows the direct fundamental bandgap; and (2) The Cu 3d orbital creates impurity bands above the ZnO valance band. The transitions from the impurity bands to conduction bands are usually a mixture of direct and indirect. Thus, for heavily doped ZnO:Cu thin films, their optical bandgap contains two parts—the direct fundamental bandgap and the mixed impurity bandgap. The direct optical bandgaps of the films were determined by extrapolating the linear portion of each curve in Figure 6.17(a) to $(\alpha h\nu)^2 = 0$. The measured optical bandgap for pure ZnO films annealed at 500°C was 3.26 eV, which is consistent with the results reported elsewhere [187]. The direct optical bandgaps measured for ZnO:Cu films annealed 500°C gradually decreased from 3.16 to 3.05 eV with the increase in the Cu concentration, as shown in Figure 6.17(b) [162, 182-184].

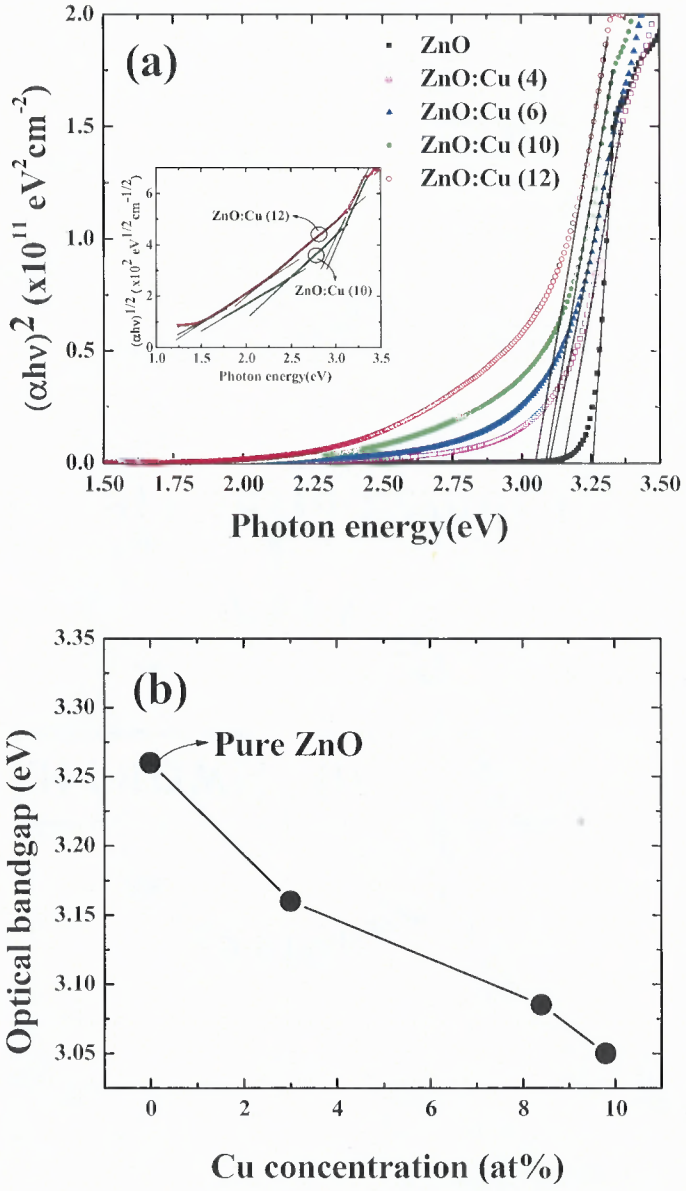

Figure 6.17 Direct transition-optical-absorption coefficients of the 500°C-annealed ZnO:Cu films with different number of Cu chips. Inset shows indirect transition-optical-absorption coefficients of the 500°C-annealed ZnO:Cu(10 and 12) films. (b) Energy bandgaps with the increase of the Cu concentration for the annealed pure ZnO and ZnO:Cu films [162, 182-184].

Figure 6.18 shows an XPS spectrum of the valence band of the 500°C-annealed ZnO:Cu(10) films. Zero binding energy corresponds to the Fermi energy (E_F). For pure ZnO, the VBM is ~3.2 eV below E_F. However, Figure 6.18 shows that the annealed ZnO:Cu(10) film has a VBM value located 1.2 eV below the E_F, indicating that these bandgap reductions are caused by the moving up of the valance band. Furthermore, the impurity bands cause additional bandgap reduction, as shown by the absorption tails below 3.0 eV. In these cases, it is difficult to give defined bandgaps, as shown in the inset of Figure 6.17(a).

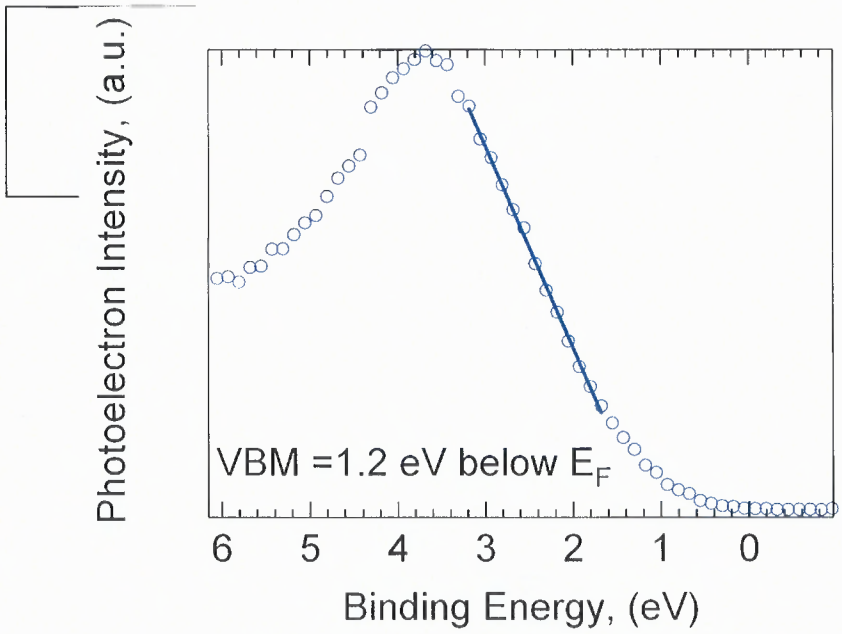

Figure 6.18 X-ray-excited valence band of the 500°C-annealed ZnO:Cu(10) film. Zero binding energy corresponds to the E_F [162, 182-184].

The Cu^{1+} states indicate that annealed ZnO:Cu thin films should be p-type. To confirm the p-type conductivity, Mott-Schottky plots are measured and shown in Figure 6.19. Mott-Schottky relationships on n-type and p-type semiconductors are expressed according to the following equations [175, 188]:

$$\frac{1}{C^2} = \left(\frac{2}{e_o \varepsilon \varepsilon_o N_d}\right)\left((E - E_{fb}) - \frac{kT}{e_o}\right) \quad \text{for n-type} \tag{6.6}$$

$$\frac{1}{C^2} = \left(\frac{2}{e_o \varepsilon \varepsilon_o N_a}\right)\left((-E + E_{fb}) - \frac{kT}{e_o}\right) \quad \text{for p-type,} \tag{6.7}$$

where, C is the depletion-layer capacitance per unit surface area, N_d and N_a is the donor and acceptor densities, respectively; ε_o is the permittivity of vacuum, ε is the dielectric constant of the semiconductor, E is the electrode potential, E_{fb} is the flat-band potential, and kT/e_o is the temperature-dependent term in the Mott-Schottky equation. The diffuse charge in the depletion layer in the semiconductor, together with its compact countercharge in the Helmholtz plane, can be conceived as a series connection of two capacitances (C_{sc} of depletion layer and C_H of Helmholtz layer). In series, the smallest capacitance dominates. Helmholtz capacitance of the semiconductor is ignored because it is much larger than the C_{SC} value associated with the depletion layer. Surface area of the counter electrode is much higher than that of the working electrodes, leading to the enhanced C_H value of the counter electrode. Therefore, the measured differential capacitance of the cell corresponds to the differential capacitance of the semiconductor depletion layer [189].

Figure 6.19(a) shows the Mott-Schottky plot of the 500°C-annealed pure ZnO film. It has a positive slope in the linear region of the plot, indicating an n-type semiconductor according to Eq. 4(a). Assuming the dielectric constant of the samples as about 8.5 [176], the donor concentration of the annealed ZnO film could be evaluated from the slope of the linear part, which was 2.3×10^{16} cm^{-3}. Figure 6.19(b) shows the Mott-Schottky plot of the 500°C-annealed ZnO:Cu(12) film, which had a negative slope indicating p-type behavior. It indicates that the Cu° metallic states were activated into the

form of Cu^{1+} substitutional acceptor states by the post-deposition annealing process at 500°C, because the Cu° metallic states cannot result in a p-type semiconductor [181]. In a similar manner, all other 500°C-annealed ZnO:Cu films in this experiment showed negative slopes. To confirm p-type conductivity, open-circuit voltage (V_{oc}), and photoelectrochemical (PEC) characteristics for the 500°C-annealed pure ZnO and ZnO:Cu films were also investigated. The V_{oc} value of the ZnO:Cu films moved anodic with illumination, whereas the V_{oc} value of the pure ZnO shifted cathodic with illumination. Moreover, the PEC characteristics of the ZnO:Cu films under chopped illumination showed cathodic photoresponses (indicative of p-type semiconductor), whereas the pure ZnO film exhibited anodic photoresponses (n-type semiconductor). These investigations confirm that the 500°C-annealed ZnO:Cu films are p-type semiconductors.

The hole concentrations of the films were evaluated from the slope of the linear part in Figure 6.19(b) with Eq. 4(b). Figure 6.19(c) shows the carrier concentrations of the 500°C-annealed ZnO and ZnO:Cu films. The hole concentrations of the 500°C-annealed ZnO:Cu films were increased from 1.8×10^{19} to 2.8×10^{20} cm^{-3} with the increase of the Cu concentration. It should be noted that the hole concentrations are significantly lower than the Cu concentrations. Theoretical study [181] showed that the activation energy of the Cu acceptors in the ZnO:Cu film is very high (0.7 eV above the VBM). This indicates that only a small fraction of the incorporated Cu is activated to donate holes, resulting in the discrepancy between the hole concentrations and Cu concentrations. These results demonstrate that *p*-type ZnO thin films with significantly

reduced bandgaps can be synthesized for PEC water-splitting applications [162, 182-184].

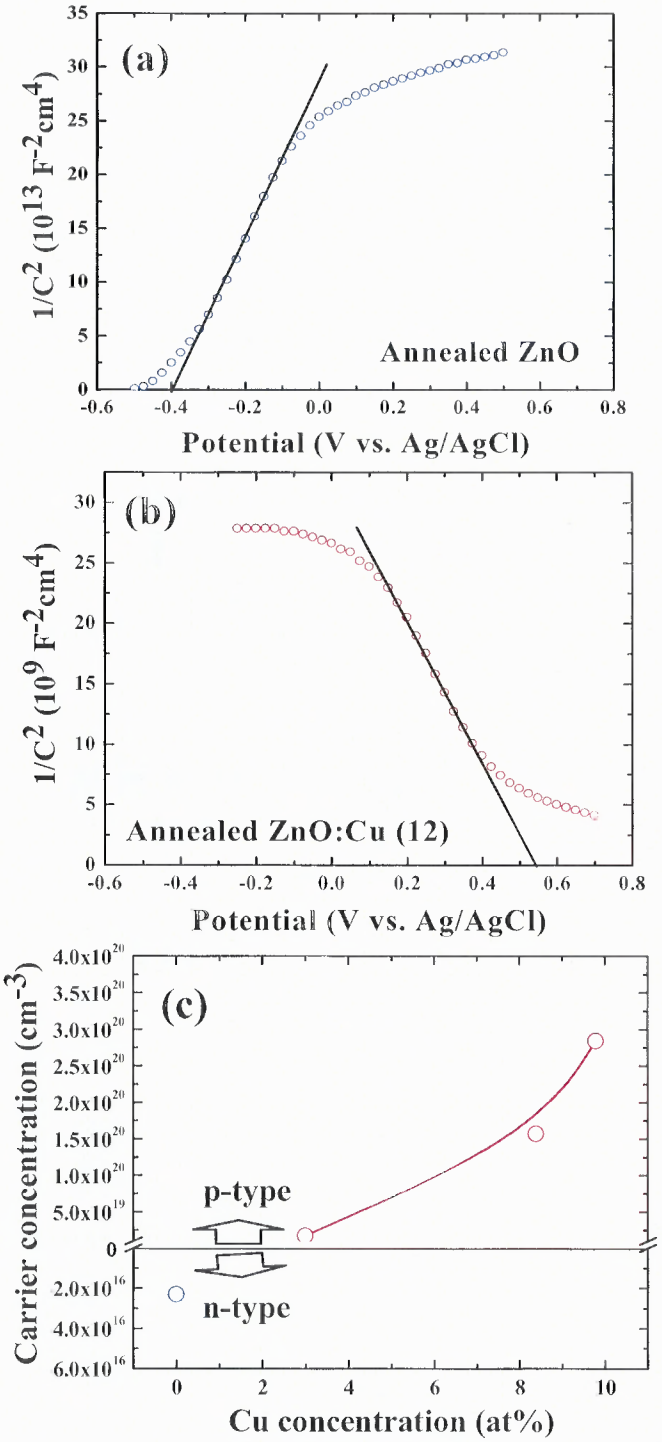

Figure 6.19 Mott-Schottky plots of 500°C-annealed (a) pure ZnO and (b) ZnO:Cu(12) films. (c) Carrier concentrations of the 500°C-annealed films as a function of Cu concentration [162, 182-184].

6.4 Carrier Concentration Tuning of Bandgap-Reduced *p*-type ZnO Films by Co-Doping of Cu and Ga

In this part of the study, the synthesis of *p*-type ZnO films with similar bandgaps but varying carrier concentrations through co-doping of Cu and Ga is reported. The ZnO:(Cu,Ga) films are synthesized by RF magnetron sputtering in O_2 gas ambient at room temperature, followed by post-deposition annealing at 500°C in air for 2 hours.

Two sets of samples were deposited, which exhibited different PEC behaviors. Figure 6.20 shows XRD curves for the first set of samples. For comparison, XRD curves of a pure ZnO sample and a ZnO:Cu sample with similar thickness are also shown. The location of the (111) peak of Ga_2O_3 is indicated by the red line. It is seen that the incorporation of Cu leads to decreased crystallinity as compared to pure ZnO films. The incorporation of additional Ga showed similar crystallinity as compared to ZnO:Cu films.

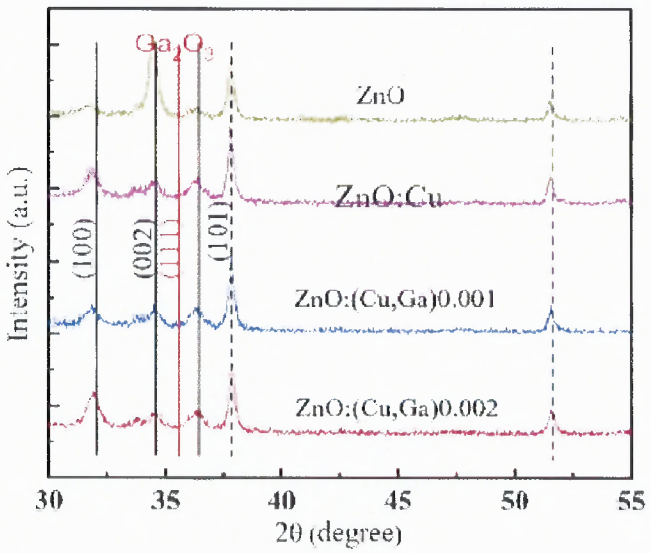

Figure 6.20 XRD curves of ZnO:(Cu,Ga)0.001, ZnO:(Cu,Ga)0.002, ZnO:Cu, and ZnO samples with similar thickness of about 0.5 μm. The dotted line indicates the peaks from FTO substrate [190].

The XRD curves showed no Cu oxides and Ga oxides, thus indicating no phase separation. However, the incorporation of Cu and Ga changed the preferred orientation of the films. For example, with the dopants, the (002) peak was suppressed and the (100) and (101) peaks were enhanced. AFM images also confirmed that the ZnO:Cu and ZnO:(Cu,Ga) films have similar grain sizes. Figures 6.21(a), 6.21(b), and 6.21(c) show AFM images from the ZnO:Cu, ZnO:(Cu,Ga)0.001, and ZnO:(Cu,Ga)0.002 samples, respectively. The images clearly show that the incorporation of a low concentration of Ga did not significantly change the morphology and average crystallite sizes [190].

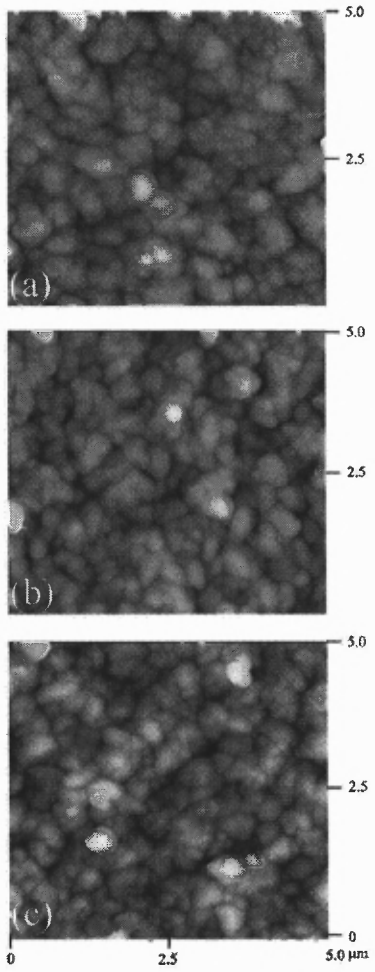

Figure 6.21 AFM images taken from (a) ZnO:Cu, (b) ZnO:(Cu,Ga)0.001, and (c) ZnO:(Cu,Ga)0.002 samples [190].

Figures 6.22(a) and 6.22(b) show the optical-absorption spectra and absorption coefficients of the first set of samples, pure ZnO, and ZnO:Cu samples with similar thickness. The ZnO:Cu sample exhibits absorption in the visible region due to two main effects: (1) The strong d-p coupling between Cu and O upshifts the O 2p orbital, which narrows the fundamental bandgap; and (2) The Cu 3d orbital creates impurity bands above the ZnO valance band. The bandgap for the ZnO:Cu sample is calculated to be about 3.05 eV. Based on previous compositional study, this bandgap corresponds to about 10 at.% Cu in the film. The incorporation of Ga does not significantly change the absorption spectrum as compared to that of ZnO:Cu due to low Ga concentration. This ensures that the effect of Ga incorporation is mainly to tune the carrier concentration of Zn:Cu films. However, small blue shifts are observed for the sample co-doped with Ga as compared to the ZnO:Cu sample. The measured bandgaps are about 3.12 eV for ZnO:(Cu,Ga)0.001 and ZnO:(Cu,Ga)0.002 samples. The blue shift can be understood as follows. The impurity band generated by Cu in ZnO is partially occupied. When Ga is incorporated, the Ga $4s^2 4p^1$ electrons will fill some of the unoccupied states in the Cu-induced impurity band. Such filling will lower the energy of the system through a downward shift of the Cu-induced impurity band. This downward shift, therefore, leads to the observed blue shift in the optical absorption spectra [190].

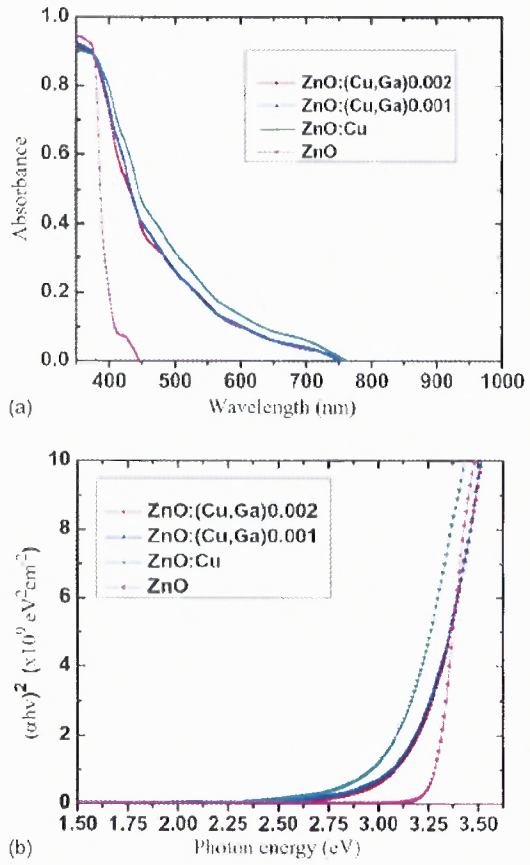

Figure 6.22 (a) Optical absorption curves and (b) absorption coefficients of ZnO, ZnO:Cu, ZnO:(Cu,Ga)0.001, and ZnO:(Cu,Ga)0.002 samples [190].

The conductivity of ZnO films is *n*-type, whereas it is *p*-type for ZnO:Cu with ten Cu chips. The different type of conductivity was confirmed by photocurrent-voltage curves. Figures 6.23(a) and 6.23(b) show measured photocurrent-voltage curves under illumination with the UV/IR filter and dark currents for a pure ZnO film and ZnO:Cu, respectively. Figure 6.23(a) shows that the photocurrent increases with an increase in applied potential, which is characteristic of *n*-type conductivity. Figure 6.23(b) shows that the photocurrent increases with a decrease in applied potential, which is characteristic of *p*-type conductivity. Thus, the ZnO film is *n*-type and the ZnO:Cu film is *p*-type. However, the photocurrent of the ZnO:Cu film is very low. The poor PEC

performance can be attributed to the high concentration of Cu, which is necessary for sufficient bandgap reduction. The high concentration of Cu results in very high carrier concentration and, therefore, very small depletion width [179, 191]. In addition, the high concentration of Cu also introduces a large number of charged defects, which can act as recombination centers. These two effects are probably the main reasons for poor PEC performance. These two undesired effects can be overcome by co-doping of Ga, which is a shallow donor in ZnO [190].

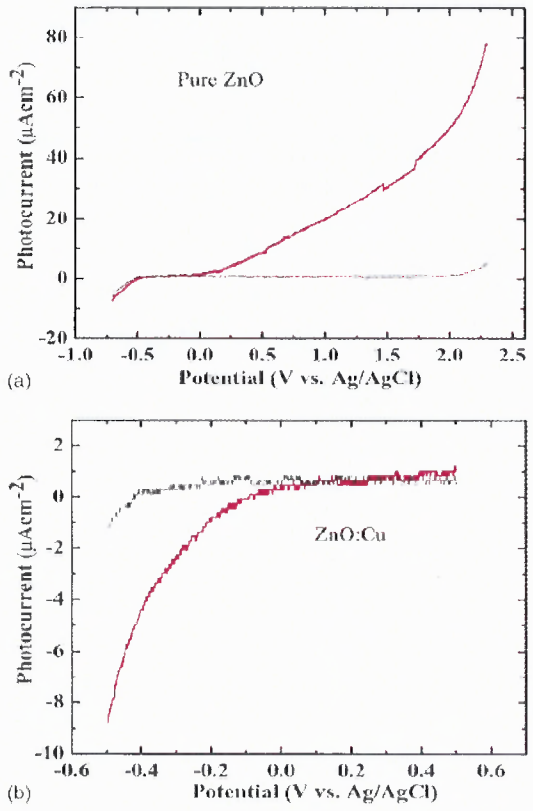

Figure 6.23 Photocurrent-voltage curves under (red) continuous illumination, (black curve) dark conditions, with an UV/IR filter measured from (a) ZnO:Cu and (b) ZnO:Cu films [190].

Figure 6.24 shows the measured photocurrent-voltage curves under illumination with the UV/IR filter and dark currents for ZnO:Cu, ZnO:(Cu,Ga)0.001, and ZnO:(Cu,Ga)0.002. Both ZnO:(Cu,Ga)0.001 and ZnO:(Cu,Ga)0.002 films showed *p*-

type conductivities, indicating that the role of Ga in these films is to reduce the hole concentration that is generated by Cu incorporation. The reduction in hole concentration increases the depletion width so that more photon-generated electron-hole pairs can be collected. Furthermore, the incorporation of Ga will neutralize charged Cu ions, so that recombination will also be suppressed. Thus, ZnO:(Cu,Ga)0.001 and ZnO:(Cu,Ga)0.002 films showed significantly increased photocurrents as compared to the ZnO:Cu film. The photocurrent at a potential of -0.5 V for the ZnO:(Cu,Ga)0.001 sample improved by almost one order of magnitude. The ZnO:(Cu,Ga)0.002 sample showed lower photocurrents than the ZnO:(Cu,Ga)0.001 sample, indicating that an optimum carrier concentration exists. If the carrier concentration of a film is very low, the film will become very resistive and the photocurrent will begin to decrease. The incorporation of more than a certain level of Ga may even cause *p*-type ZnO:Cu film to become *n*-type [190].

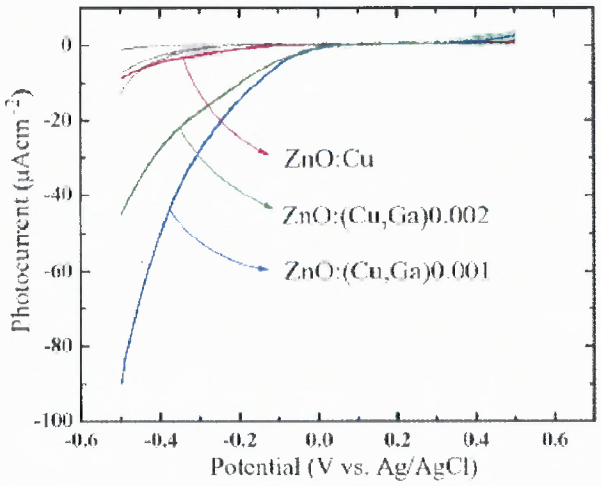

Figure 6.24 Photocurrent-voltage curves under continuous illumination, (black curve) dark conditions, with an UV/IR filter measured from ZnO:Cu, ZnO:(Cu,Ga)0.001, and ZnO:(Cu,Ga)0.002 samples [190].

Figure 6.25 shows XRD curves for the second set of samples. For comparison, XRD curves of a pure ZnO sample and a ZnO:Cu sample with similar thickness are also shown. All the peaks have higher intensities than that of the first set of samples due to larger thickness. Similar to the first set of samples, the incorporation of Cu changes the preferred orientation as compared to ZnO. The incorporation of additional Ga did not significantly change the crystallinity as compared to ZnO:Cu films. AFM images also confirmed this conclusion. The XRD curves showed no Cu oxides or Ga oxides, thus indicating no phase separation. However, the incorporation of Cu and Ga changed the preferred orientation of the films [190].

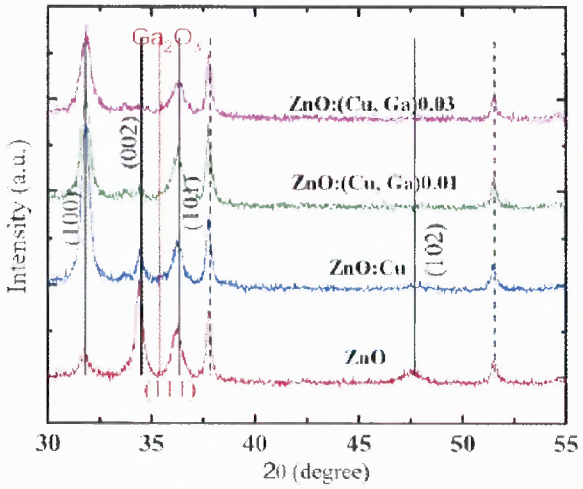

Figure 6.25 XRD curves of ZnO:(Cu,Ga)0.01, ZnO:(Cu,Ga)0.03, ZnO:Cu, and ZnO samples with similar thickness of about 1 μm. The dotted line indicates the peaks from FTO substrate [190].

Figures 6.26(a) and 6.26(b) show the optical-absorption spectra and absorption coefficients of the second set of samples and ZnO:Cu samples with similar thickness. The bandgap for the ZnO:Cu sample is calculated to be about 3.0 eV, which corresponds to about 11 at.% Cu in the film. As in the first set of samples, blue shifts are also observed for the second set of samples; however, the shift is much more significant. The

measured bandgaps are very similar for ZnO:(Cu,Ga)0.01 and ZnO:(Cu,Ga)0.03 samples, (about 3.15 eV). This indicates that more unoccupied states are now filled by the electrons from Ga, as more Ga_2O_3 powders were dispersed on the target.

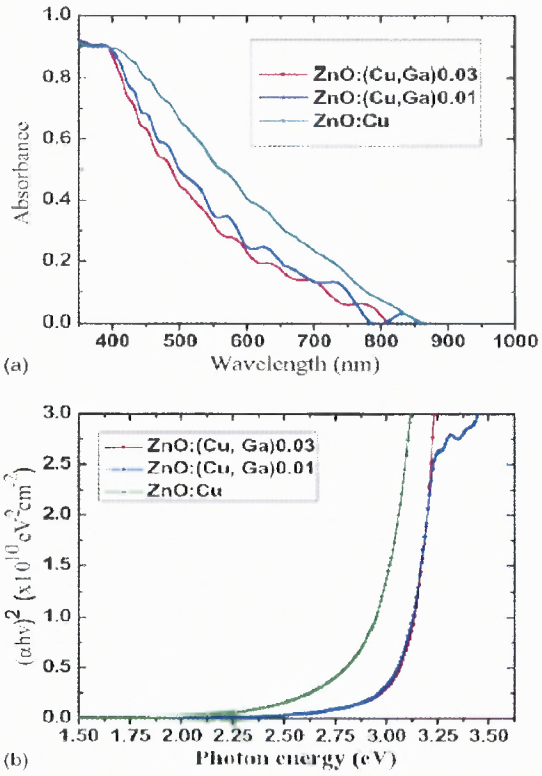

Figure 6.26 Optical absorption curves and (b) absorption coefficients of ZnO:Cu, ZnO:(Cu,Ga)0.01, and ZnO:(Cu,Ga)0.03 samples [190].

Figures 6.27(a) and 6.27(b) show measured photocurrent-voltage curves under illumination with the UV/IR filter and dark currents for ZnO:(Cu,Ga)0.01 and ZnO:(Cu,Ga)0.03, respectively. It can be clearly seen that both ZnO:(Cu,Ga)0.01 and ZnO:(Cu,Ga)0.03 films are no longer *p*-type, but are *n*-type. Thus, the Ga concentration is so high in these samples that holes are completely compensated and the films become *n*-type. Both ZnO:(Cu,Ga)0.01 and ZnO:(Cu,Ga)0.03 films showed very high dark currents indicating poor quality, which may be the result of incorporation of too much Ga. Because the photocurrent-voltage curves indicate that both ZnO:(Cu,Ga)0.01 and

ZnO:(Cu,Ga)0.03 are *n*-type, the bottom of the conduction bands in these materials may be filled with electrons, which partially contribute to the large blue shift seen in Figure 6.26 [190].

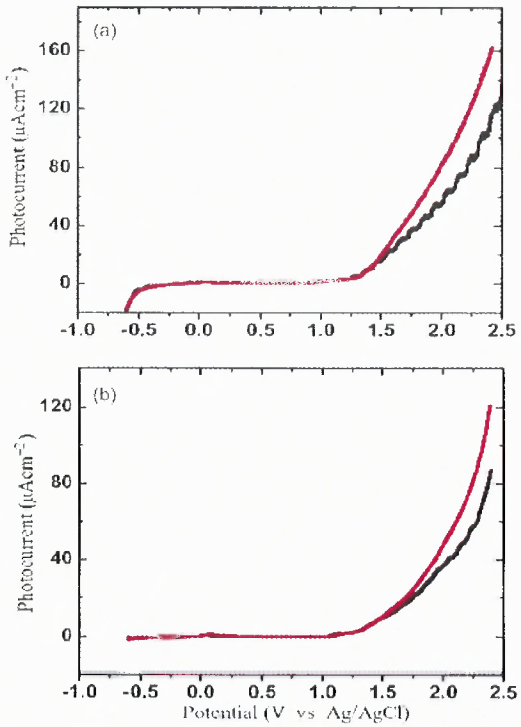

Figure 6.27 Photocurrent-voltage curves under (red curve) continuous illumination, (black curve) dark condition, with an UV/IR filter measured from (a) ZnO:(Cu,Ga)0.01 and (b) ZnO:(Cu,Ga)0.03 films [190].

6.5 Enhanced Photoelectrochemical Responses of ZnO Films through Ga and N Co-Doping

The crystallinity and PEC responses of ZnO thin films co-doped by Ga and N are reported in this part of the research. Ga and N co-doped ZnO [ZnO:(Ga,N)] and N-doped ZnO (ZnO:N) films were grown by reactive RF magnetron sputtering for the same growth conditions and annealed at 500°C in air for 2 hours. For comparison, ZnO:N films were also grown at 500°C.

Figure 6.28 shows the XRD curves for ZnO:N(1), ZnO:N(2), and ZnO:(Ga,N) films. The ZnO:N(1) film exhibited the * peak around 55°, which is in between the peak positions of the Zn_3N_2 and ZnO. From a previous study, it corresponds to the peak of the Zn oxynitride, indicating that a high concentration of N has been incorporated into ZnO. However, its crystallinity was inferior due to the incorporation of the nitrogen. The crystalline quality was characterized from the full width at half maximum (FWHM) of the XRD curve instead of the peak intensity, because the FWHM is an intrinsic property [192]. The crystallite size, estimated according to the Scherrer equation with the FWHM, is about 16 nm. The ZnO:N(2) films exhibited much better crystallinity (crystallite size: 29 nm). However, all the peaks correspond to pure ZnO without any indication of oxynitride structure as seen in the ZnO:N(1) film.

X-ray photoelectron spectroscopy (XPS) results confirmed that no nitrogen is present in the ZnO:N(2) films grown at 500°C. However, the ZnO:N(1) film showed a nitrogen concentration of 22 at%. These results indicate that a high concentration of N can be incorporated into ZnO at low substrate temperatures, but these films have very poor crystallinity. ZnO films with high crystallinity can be synthesized at high temperatures; but at these substrate temperatures, it is very difficult to incorporate a significant amount of nitrogen into the films. Surprisingly, however, the co-doped ZnO:(Ga,N) films exhibited significantly enhanced crystallinity, yet with the incorporation of N. From the XRD curve shown in Figure 6.28, the crystallite size of ZnO:(Ga,N) films is estimated to be around 40 nm, which is even better than the ZnO:N(2) films grown at 500°C. Such significantly enhanced crystallinity can be attributed to the Ga source used (i.e., Ga_2O_3). Because the ionic radius of substitutional

Ga^{3+} is close to that of Zn^{2+}, the size mismatch is very small. Furthermore, the Ga_2O_3 source provides more oxygen during the sputtering process [193], leading to decreased oxygen vacancies and enhanced crystallinity. A similar effect of the Ga oxide source on ZnO crystallinity has also been reported [36]. The nitrogen concentration in the ZnO:(Ga,N) films was estimated to be about 2 at%, which is much lower than that of the ZnO:N(1) film. This is because the additional oxygen, with its high chemical activity, generated from the Ga_2O_3 source limited the N incorporation [194, 195].

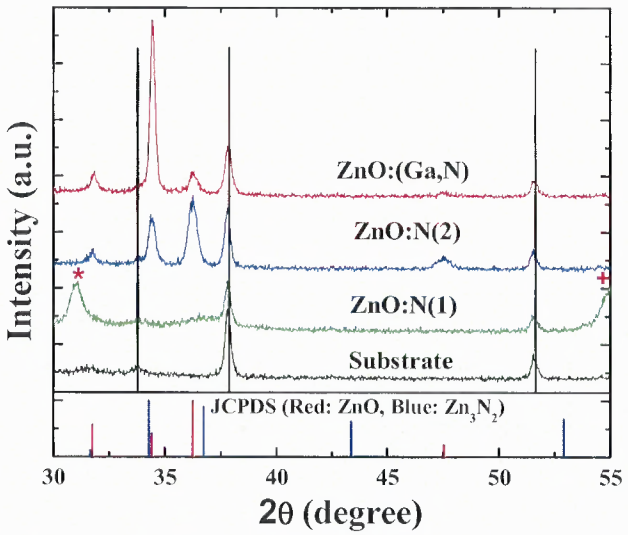

Figure 6.28 XRD curves for a ZnO:N(1), ZnO:N(2), and ZnO:(Ga,N) films, respectively [194, 195].

Figure 6.29 shows the optical absorption coefficients for the samples used in this experiment. The direct electron transition from valence to conduction bands was assumed to calculate the bandgap from the absorption coefficient curves, because both of the ZnO and Zn nitride films are known to be direct-bandgap materials. The optical bandgaps of the films were determined by extrapolating the linear portion of each curve. The bandgap of the ZnO:N(2) film grown at 500°C is 3.27 eV, which corresponds well to the bandgap of the pure ZnO. The ZnO:N(1) film exhibited a significantly decreased bandgap of 1.75

eV, due to the high concentration of N. The co-doped ZnO:(Ga,N) film exhibited a bandgap of 3.19 eV, which is slightly lower than the ZnO:N(2) film grown at 500°C. This small reduction in bandgap is due to N-induced upshifting of the valance band. It is shown theoretically that the incorporated N would generate an impurity band above the valance band. The absorption from this impurity band cannot be characterized by direct band transitions and typically results in an absorption tail in the measured optical absorption curve. Such an absorption tail is clearly evident in Figure 6.29 for the co-doped ZnO:(Ga,N) film. This tail can be considered to lead to further bandgap reduction, which enables light harvesting in the much longer wavelength regions as compared to the ZnO:N(2) film [194, 195].

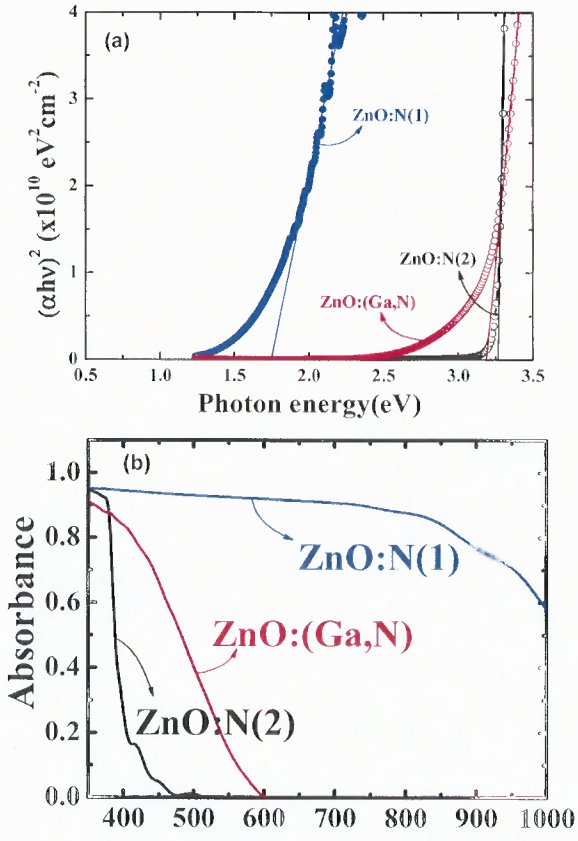

Figure 6.29 (a) Direct transition-optical-absorption coefficients (b) Optical absorption curves of a ZnO:N(1), ZnO:N(2), and ZnO:(Ga,N) films, respectively [194, 195].

Figure 6.30(a) shows Mott-Schottky plots of ZnO:N(1), ZnO:N(2), and the co-doped ZnO:(Ga,N) films. All the samples exhibited positive slopes, indicating *n*-type semiconductors. From previous study, it is known that ZnO:N films deposited under a N_2/O_2 plasma showed *n*-type behavior, due to substitutional N_2 molecules that act as shallow double-donors. The donor concentrations of the films were calculated from the slopes of the Mott-Schottky plots, which were about 9.93, 2.1, and 2.43×10^{17} cm^{-3} for ZnO:N(1), ZnO:N(2), and ZnO:(Ga,N), respectively. The co-doped ZnO:(Ga,N) film exhibited similar donor concentration compared to the ZnO:N(2) film grown at 500°C, indicating that the co-doped film is a highly compensated system [194, 195].

Because the major contribution to PEC response is from the collection of carriers photogenerated in the built-in electrical field near surface regions, the depletion width is an important factor for PEC application of semiconductors. In general, a larger depletion layer *(W)* is preferred to suppress the recombination rate. Figure 6.30(b) shows the *W* values with the potential for the samples, which were calculated from the results of the Figure 6.30(a). It shows that the co-doped ZnO:(Ga,N) and the ZnO:N(2) film grown at 500°C exhibited much wider *W* values, compared to the ZnO:N(1) film, owing to lower donor concentration [194, 195].

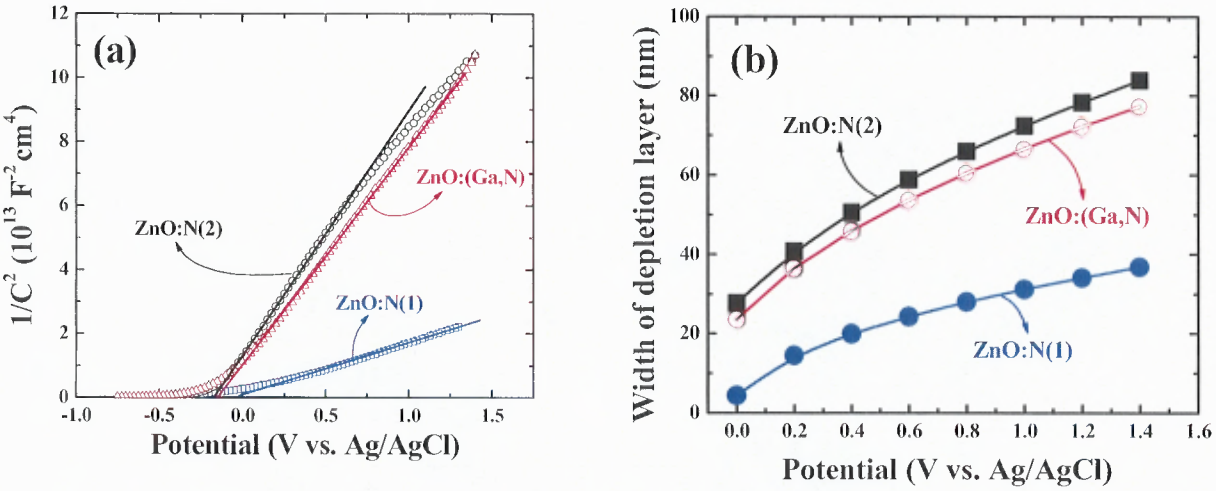

Figure 6.30 (a) Mott-Schottky plots of a ZnO:N(1), ZnO:N(2), and ZnO:(Ga,N) films, respectively. (b) *W* values with the potential, estimated from (a) [194, 195].

Figure 6.31(a) shows the photocurrent-voltage curves of ZnO:N(1), ZnO:N(2), and ZnO:(Ga,N) films under illumination with the UV/IR filter. The inset in Figure 6.31(a) shows the enlarged photocurrent-voltage curves. It showed clearly that the ZnO:(Ga,N) film exhibited significantly increased photocurrents, compared to the other films. At the potential of 1.2 V, the photocurrents were 484, 55, and 38 μAcm^{-2} for the co-doped ZnO:(Ga,N), ZnO:N(1), and ZnO:N(2) films, respectively. To investigate the photoresponses in the long-wavelength region, a green color filter (wavelength: 538.33 nm; FWHM: 77.478 nm) was used in combination with the UV/IR filter, as shown in Figure 6.31(b). The ZnO:N(2) film grown at 500°C exhibited no clear photoresponse, due to its wide bandgap. The ZnO:(Ga,N) film exhibited much higher photocurrent than the ZnO:N(1) film, despite much less light absorption. It indicates that a very high recombination rate of the photogenerated electrons and holes is present in the ZnO:N(1) film, due to its inferior crystallinity and small *W* value. On the other hand, the co-doped

ZnO:(Ga,N) exhibited remarkably increased crystallinity and good *W* value, which led to greatly enhanced photocurrent than the ZnO:N(1) film. The results demonstrate clearly that photocurrents can be obtained from the impurity-band-induced absorption tail. We expect that further enhanced photocurrents should be possible with higher N incorporation in ZnO facilitated by the co-doping approach [194, 195].

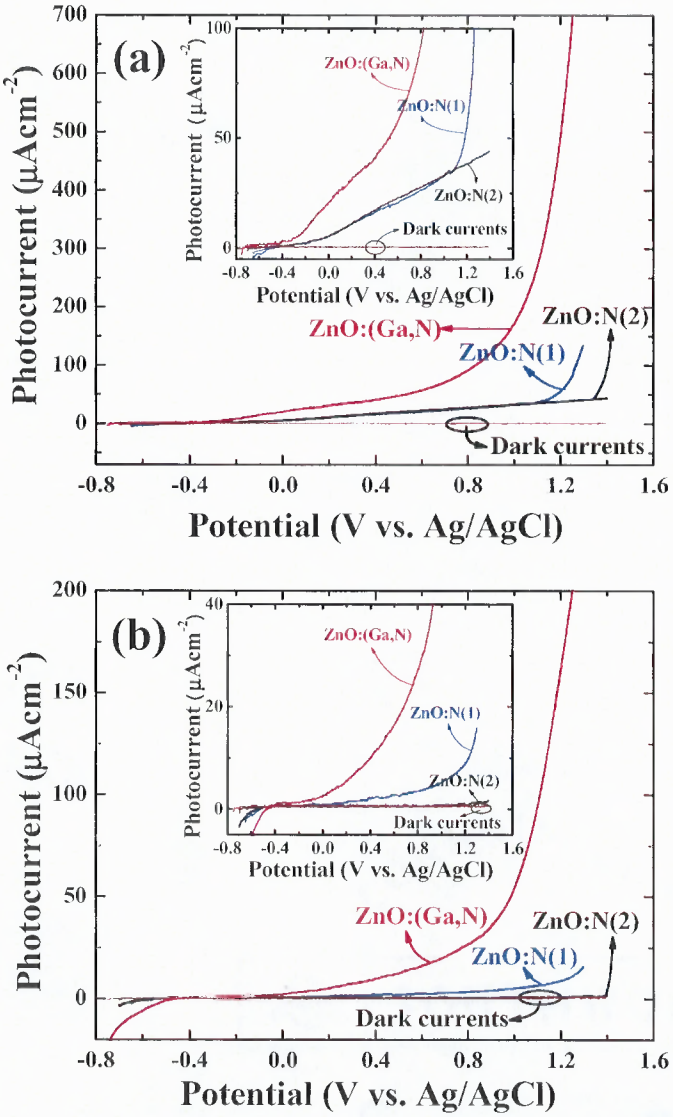

Figure 6.31 (a) Photocurrent-voltage curves of a ZnO:N(1), ZnO:N(2), and ZnO:(Ga,N) films, respectively, under the illumination (a) with an UV/IR filter and (b) with the combined green and UV/IR filter. The inset shows the enlarged photocurrent-voltage curves. Scan rate of 5 mV/s was used [194, 195].

6.6 Effect of Substrate Temperature on Photoelectrochemical Responses of ZnO Films Co-Doped by Ga and N

In this part of the research, effect of substrate temperature on the crystallinity and PEC responses of ZnO thin films co-doped by Ga and N are reported. Ga and N co-doped ZnO [ZnO:(Ga,N)] films were grown by reactive RF magnetron sputtering at various substrate temperatures.

Figure 6.32 shows the X-ray diffraction curves for ZnO and Ga-N co-doped ZnO films deposited at substrate temperatures of 100°, 300°, and 500°C. The ZnO films exhibited poor crystallinity due to deposition at low temperatures. However, Ga-N co-doped ZnO film deposited at 100°C showed sharper peaks. As the substrate temperature is increased to 300° and 500°C, the peak intensities are decreased, indicating the incorporation of more N in the films. It is known from recent reports that incorporated N atoms can deteriorate the crystal structure and modify the growth mode [196-198]. The crystallite size of the ZnO films, estimated according to the Scherrer equation, is about 21 nm. The Ga-N co-doped ZnO films deposited at 100°C exhibited much better crystallinity (crystallite size: 44 nm). This is because the deposition is carried out at the increased substrate temperature of 100°C, and very low concentration of N incorporated in the film, whereas ZnO film was deposited at room temperature. Such significantly enhanced crystallinity may be because Ga_2O_3 powders were used as the Ga source. The ionic radius of substitutional Ga^{3+} is close to that of Zn^{2+}. The size mismatch between them is very small. Furthermore, the Ga_2O_3 source provides more oxygen during the sputtering process [193], leading to decreased oxygen vacancies and enhanced crystallinity. A similar effect of the Ga oxide source on ZnO crystallinity has also been reported by other groups [193]. The crystallite size of Ga-N co-doped ZnO films deposited at a substrate

temperature of 300° and 500°C is 35 and 24 nm, respectively, indicating that more N is incorporated in these films.

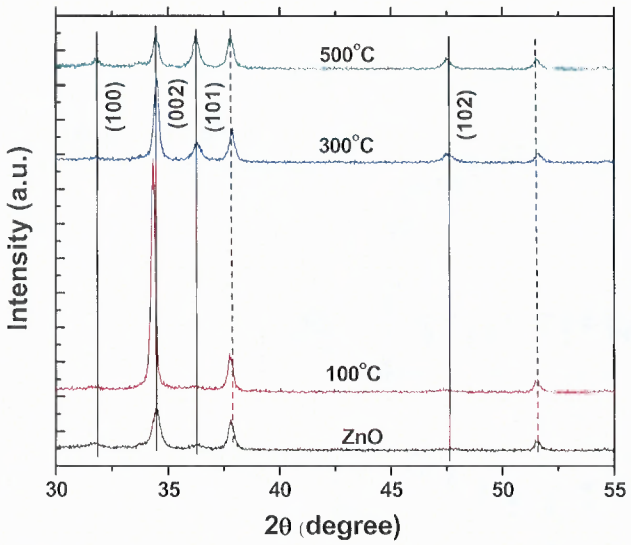

Figure 6.32 XRD curves for ZnO, and ZnO:N:Ga films deposited at a substrate temperature of 100°, 300°, and 500°C [199].

XPS results confirmed that a very low concentration of nitrogen (0.19 at.%) is present in the Ga-N co-doped ZnO films grown at 100°C, whereas films deposited at 300° and 500°C contain 0.8 and 1.4 at.% N, respectively. ZnO films with high crystallinity can be synthesized at high temperatures, but a significant amount of nitrogen is very difficult to be incorporated into ZnO films at these substrate temperatures. However, with Ga-N co-doping, a significant amount of N can be incorporated into ZnO even at higher substrate temperatures [199].

Figure 6.33 shows optical absorption spectra of ZnO films and Ga-N co-doped ZnO films deposited at a substrate temperature of 100° to 500°C. The ZnO films showed optical absorption due to light with wavelengths below 450 nm because of their wide bandgap. However, Ga-N co-doped ZnO film can absorb lower-energy photons, up to

750 nm as the substrate temperature increased from 100° to 500°C, indicating that the bandgap was narrowed by Ga-N incorporation in ZnO [159, 170].

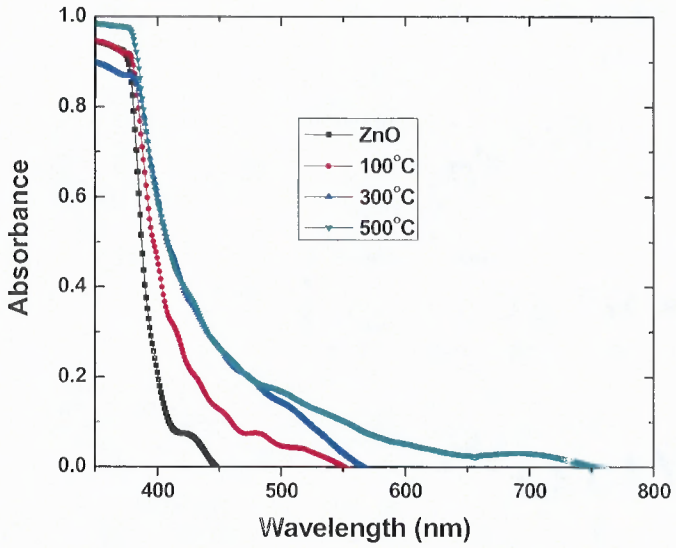

Figure 6.33 Optical absorption curves of a ZnO, and ZnO:N:Ga films deposited at substrate temperature of 100°, 300°, and 500°C [199].

Figure 6.34 shows the optical absorption coefficients for the samples used in this experiment. The direct electron transition from valence to conduction bands was assumed for the absorption coefficient curves, because ZnO films are known to be direct-bandgap materials. The optical bandgap of the films was determined by extrapolating the linear portion of each curve. The bandgap of the ZnO film is 3.26 eV, which is consistent with the results reported elsewhere. The direct optical bandgaps measured for Ga-N co-doped ZnO films deposited at a substrate temperature of 100° to 500°C gradually decreased from 3.25 to 3.22 eV. This small bandgap reduction is due to N-induced upshifting of the VBM. It is shown theoretically that the incorporated N would generate an impurity band above the valence band. The absorption from this impurity band cannot be characterized by direct band transitions and typically results in an absorption tail in the measured

optical absorption coefficients curve. Such an absorption tail is clearly evident in Figure 6.34 for the Ga-N co-doped ZnO film. This tail can be considered to lead to further bandgap reduction, which enables light harvesting in the much longer-wavelength regions as compared to that of the ZnO film [199].

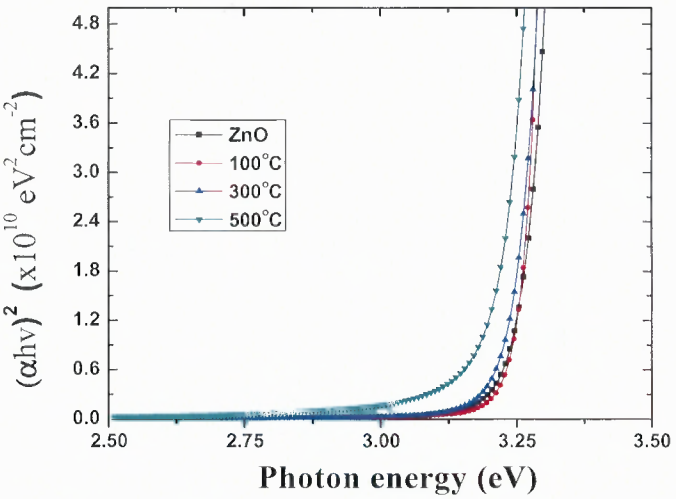

Figure 6.34 Direct transition-optical absorption coefficients of a ZnO, and ZnO:N:Ga films deposited at substrate temperature of 100°, 300°, and 500° C [199].

Figure 6.35 shows Mott-Schottky plots of ZnO, and Ga-N co-doped ZnO films grown at substrate temperatures of 100°, 300°, and 500°C. All the samples exhibited positive slopes, indicating n-type semiconductor behavior. Previous studies reported that ZnO:N films deposited under a N_2/O_2 plasma showed n-type behavior, due to substitutional N_2 molecules that act as shallow double-donors. For Ga-N co-doped samples, Ga atoms are shallow donors. The Ga concentration in the films tunes the donor (free electron) concentration. The donor concentrations of the films, calculated from the slopes of the Mott-Schottky plots [191, 200], were about 8.6×10^{16}, 2.85×10^{17}, 2.74×10^{17}, and 2.52×10^{17} /cm^3 for ZnO, and Ga-N co-doped ZnO films deposited at 100°, 300°, and 500°C, respectively. The Ga-N co-doped ZnO film exhibited nearly similar

donor concentration as compared to ZnO:N film grown at 500°C [194, 195], indicating that the co-doped film is a highly compensated system.

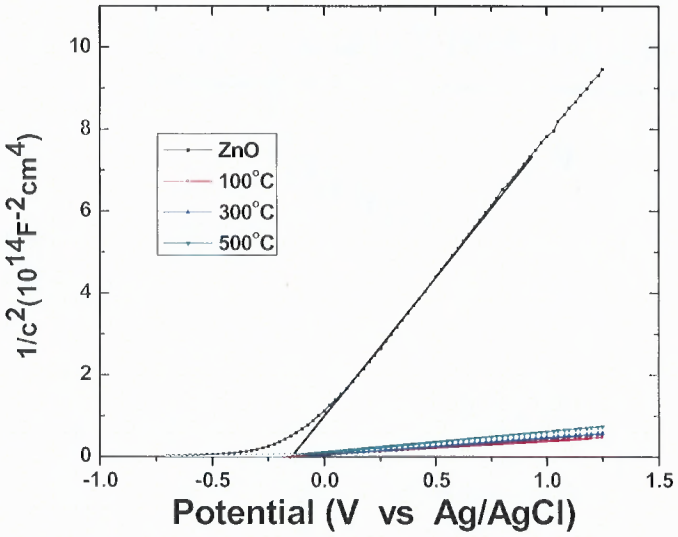

Figure 6.35 Mott-Schottky plots of a ZnO, and ZnO:N:Ga films deposited at substrate temperature of 100°, 300°, and 500°C [199].

The depletion width is an important factor for the PEC application of semiconductors. In general, a larger depletion layer, *W*, is preferred to promote photo-generated carrier separation. Figure 6.36 shows the *W* values with the potential for the samples, which were calculated from the results of Figure 6.35. It shows that ZnO showed much wider *W* compared to the Ga-N co-doped ZnO films. The Ga-N co-doped ZnO film exhibited increased *W* values as the substrate temperature is increased, due to lower donor concentration [199].

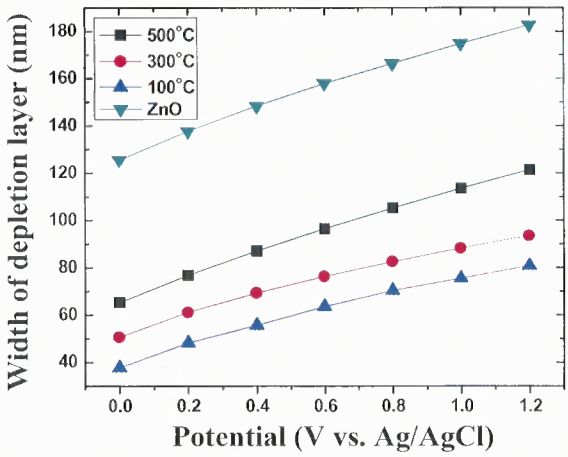

Figure 6.36 Depletion layer width (*W*) values with the potential, estimated from 6.35 (above graph) [199].

Figure 6.37 shows the photocurrent-voltage curves of ZnO and Ga-N co-doped ZnO films under illumination with an UV/IR filter. It shows clearly that the Ga-N co-doped ZnO films exhibited increased photocurrents, as compared to the ZnO film. Furthermore, as the substrate temperature is increased for Ga-N co-doped ZnO film, the photocurrents increased accordingly [199].

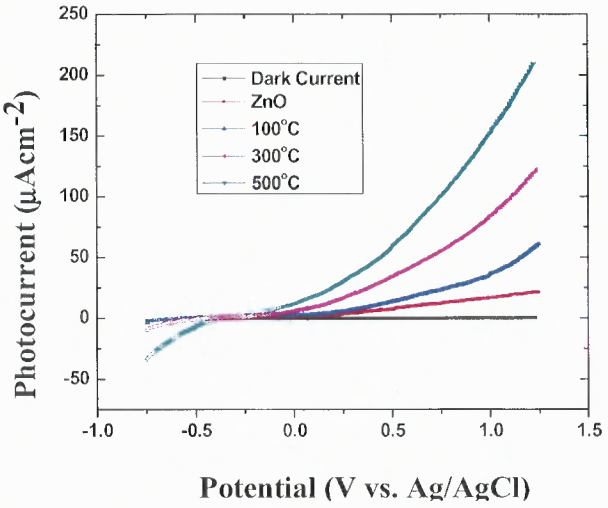

Figure 6.37 Photocurrent-voltage curves of a ZnO, and ZnO:N:Ga films deposited at substrate temperature of 100°, 300°, and 500°C, under the illumination with a UV/IR filter [199].

At the potential of 1.25 V, the photocurrents were 20, 56, 115, and 203 μAcm^{-2} for the ZnO, Ga-N co-doped ZnO films deposited at 100°, 300°, and 500°C, respectively. This indicates that a very high recombination rate of the photogenerated electrons and holes is present in the ZnO film, despite its wider *W* value; this may be due to its inferior crystallinity combined with wider bandgap. To investigate the photoresponses in the long-wavelength region, a green-color filter was used in combination with the UV/IR filter, as shown in Figure 6.38. The ZnO film exhibited no clear photoresponse, due to its wide bandgap. The Ga-N co-doped ZnO films exhibited photocurrent, despite much less light absorption. It is evident that the Ga-N co-doped ZnO films exhibited increased crystallinity, good *W* value, reduced bandgap, and compensated charge, which led to an enhanced photocurrent compared to the ZnO film [199].

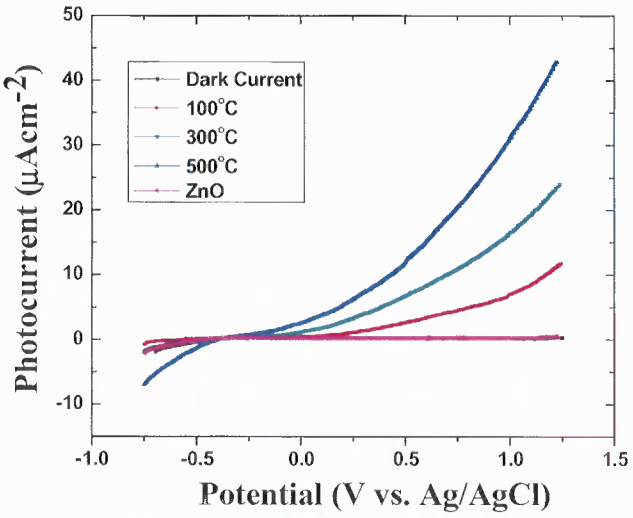

Figure 6.38 Photocurrent-voltage curves of a ZnO, and ZnO:N:Ga films deposited at substrate temperature of 100°, 300°, and 500°, under the illumination with the combined green and UV/IR filters [199].

The results demonstrate clearly that photocurrents can be obtained from the impurity-band-induced absorption tail. The co-doping of Ga and N in ZnO can shift photoresponse of ZnO into the visible-light region, which is the main component of

sunlight. It is expected that further enhanced photocurrents should be possible when more N is incorporated in ZnO by the co-doping approach [199].

6.7 Phase Separation of Ga and N Co-Incorporated ZnO Films and Its Effect on Photo-Response

In this part of the research, phase separation of Ga and N co-incorporated ZnO films and its effect on photoresponse are reported. Ga and N co-doped ZnO [ZnO:(Ga,N)] films were grown by reactive RF magnetron sputtering at various substrate temperatures.

Figure 6.39 shows the XRD curves for ZnO, ZnO:N, and ZnO:(Ga:N) films deposited in mixed N_2 and O_2 with an oxygen gas ratio $[O_2/(N_2+O_2)]$ = 1.2% and 2.5%. The ZnO film exhibited poor crystallinity due to deposition at room temperature. The ZnO:N film also showed poor crystallinity, due to the deposition at low temperature, along with the heavy incorporation of nitrogen. According to the previous study, the ZnO:N film exhibited the * peak around 31°, which corresponds to zinc oxynitride, indicating that a high concentration of nitrogen was incorporated in ZnO. The ZnO:N film showed a nitrogen concentration of 22 at.% as determined from XPS results. However, charge-compensated co-incorporated ZnO:(Ga:N) films exhibited significantly enhanced crystallinity, with the incorporation of nitrogen. The crystallite sizes were estimated according to the Scherrer equation using the FWHM of specific peaks. The (002) peak was used for ZnO and ZnO:(Ga:N) films, while * peak was used for ZnO:N film. The crystallite size was estimated to be about 21, 29, 34, 44, and 40 nm for ZnO, ZnO:N, ZnO:(Ga:N)(1), ZnO:(Ga:N)(2), and ZnO:(Ga:N)(3) films, respectively [201].

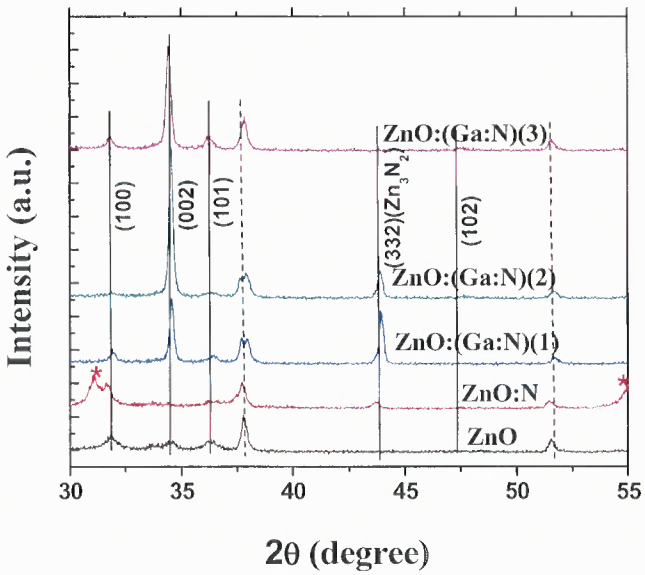

Figure 6.39 Optical absorption coefficients of a ZnO, ZnO:N, and ZnO:Ga:N films deposited in mixed N_2 and O_2 with an oxygen gas ratio $O_2/(N_2+O_2)$ = 1.2% and 2.5% [201].

Figure 6.40 shows AFM surface morphologies of the ZnO, ZnO:N, ZnO:(Ga:N)(1), and ZnO:(Ga:N)(3) samples, respectively. It clearly shows that the ZnO:(Ga:N) films have slightly larger grain size, as compared to ZnO and ZnO:N films.

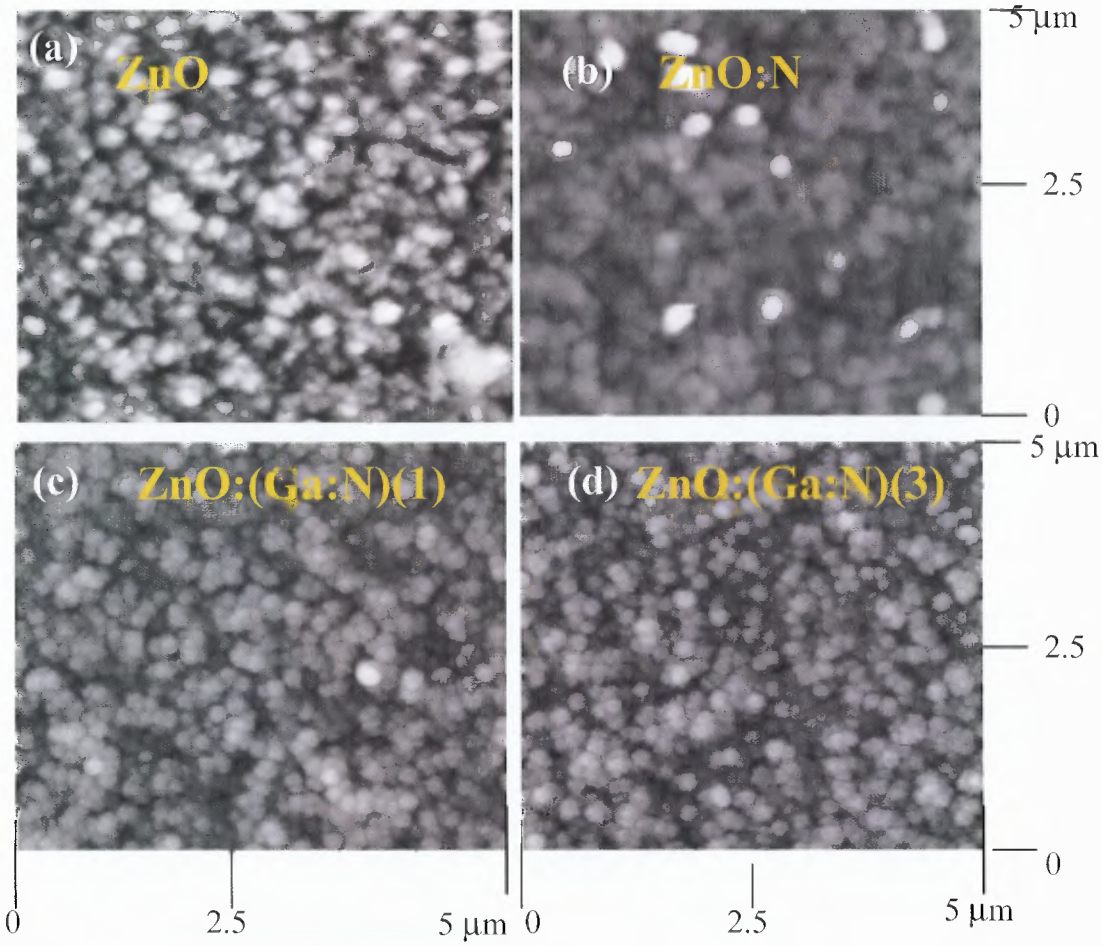

Figure 6.40 AFM images taken from (a) ZnO, (b) ZnO:N, (c) ZnO:Ga:N(1), and (d) ZnO:Ga:N(3) samples [201].

Significantly enhanced crystallinity of co-incorporated ZnO:(Ga:N) films can be attributed to the Ga source used (i.e., Ga_2O_3 powder): the Ga_2O_3 source provides more oxygen during the sputtering process, leading to decreased oxygen vacancies and enhanced crystallinity. The nitrogen concentration in ZnO:(Ga:N)(1, 2), and ZnO:(Ga:N)(3) films was estimated to be about 6 and 2 at.%, respectively. This low incorporation of N in co-doped ZnO:(Ga:N) films, as compared to ZnO:N film, is partially due to the additional oxygen generated from the Ga_2O_3 source. The ZnO:(Ga:N)(1, 2) films showed higher concentration of N incorporation than that of

ZnO:(Ga:N)(3) film. This is due to the decreased oxygen gas ratio in mixed N_2 and O_2 ambient from 2.5% to 1.2%. However, ZnO:(Ga:N)(1) and ZnO:(Ga:N)(2) films deposited in an oxygen gas ratio 1.2% showed a (332) Zn_3N_2 peak, indicating a phase segregation in the films. In contrast, ZnO:(Ga:N)(3) film grown in mixed N_2 and O_2 with an oxygen gas ratio 2.5% did not show any phase separation, indicating that the phase separation is very sensitive to the gas flow ratio in mixed gas ambient [201].

Figure 6.41 shows optical absorption spectra of the ZnO, ZnO:N, and ZnO:(Ga:N) films deposited in mixed N_2 and O_2. The ZnO films showed optical absorption spectra and could only absorb light with wavelengths below 450 nm, due to their wide bandgap. However, the ZnO:N film could absorb lower-energy photons due to the very high concentration of N. The ZnO:(Ga:N) films also showed light absorption into the visible-light region due to the N incorporation in the films.

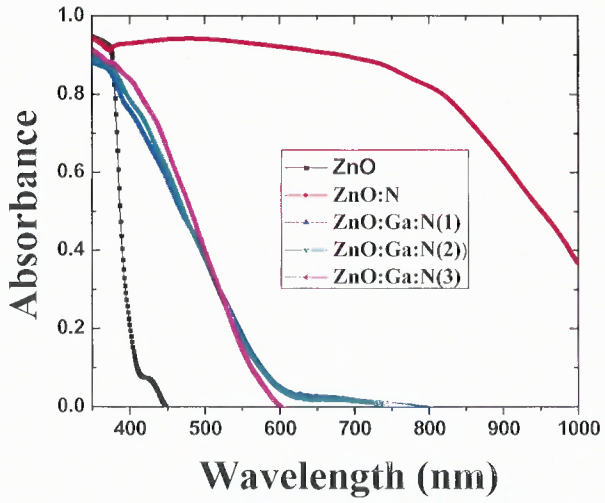

Figure 6.41 Optical absorption curves of ZnO, ZnO:N, and ZnO:Ga:N films deposited in mixed N_2 and O_2 with an oxygen gas ratio $O_2/(N_2+O_2)$ = 1.2% and 2.5% [201].

The optical absorption coefficients for the samples are shown in Figure 6.42. The direct electron transition from valence to conduction bands was assumed for the absorption coefficient curves of Figure 6.42 (a), because ZnO films are known as direct-

bandgap materials. The bandgap of the ZnO film is 3.26 eV, which is consistent with the results reported elsewhere. The direct optical bandgap measured for ZnO:N film is 1.75 eV, due to the high concentration of N. The co-doped ZnO:(Ga:N)(1) and ZnO:(Ga:N)(2) films exhibited a direct bandgap of 3.23 eV. The co-doped ZnO:(Ga:N)(3) film exhibited a bandgap of 3.19 eV, which is slightly lower than the ZnO film. The ZnO:Ga,N (1, 2) films also exhibited long absorption tails and it may be related to the indirect electron transition. To confirm this, the indirect transition absorption coefficients were plotted in Figures 6.42(b) and 6.42(c) for ZnO:(Ga,N)(1 and 2) and ZnO:(Ga,N)(3), respectively. Figures 6.42(a) and 6.42(b) clearly show that the ZnO:(Ga,N)(1 and 2) have both direct and indirect transitions for high-energy and low-energy regions, respectively. It indicates that these films were phase-separated into the mixed form of the ZnO and Zn_3N_2, which is in good agreement with XRD data.

However, Figure 6.42(c) clearly shows that ZnO:(Ga,N)(3) is not according to the indirect transition, indicating no existence of the Zn_3N_2. Rather, it can be due to the N-induced impurity bands mixed with the Ga. The absorption of the films with the impurity band cannot be characterized only by direct band transition, and it typically results in an additional absorption tail together with reduced bandgap, due to the VBM moved up by the N impurity band. We should also note that although the ZnO:Ga,N (1 and 2) films had more N incorporation than the ZnO:Ga,N(3); they exhibited higher direct absorption coefficients of ZnO:(Ga:N)(3) films deposited in 2.5% N_2 gas flow rate mixed N_2 and O_2 gas ambient [201].

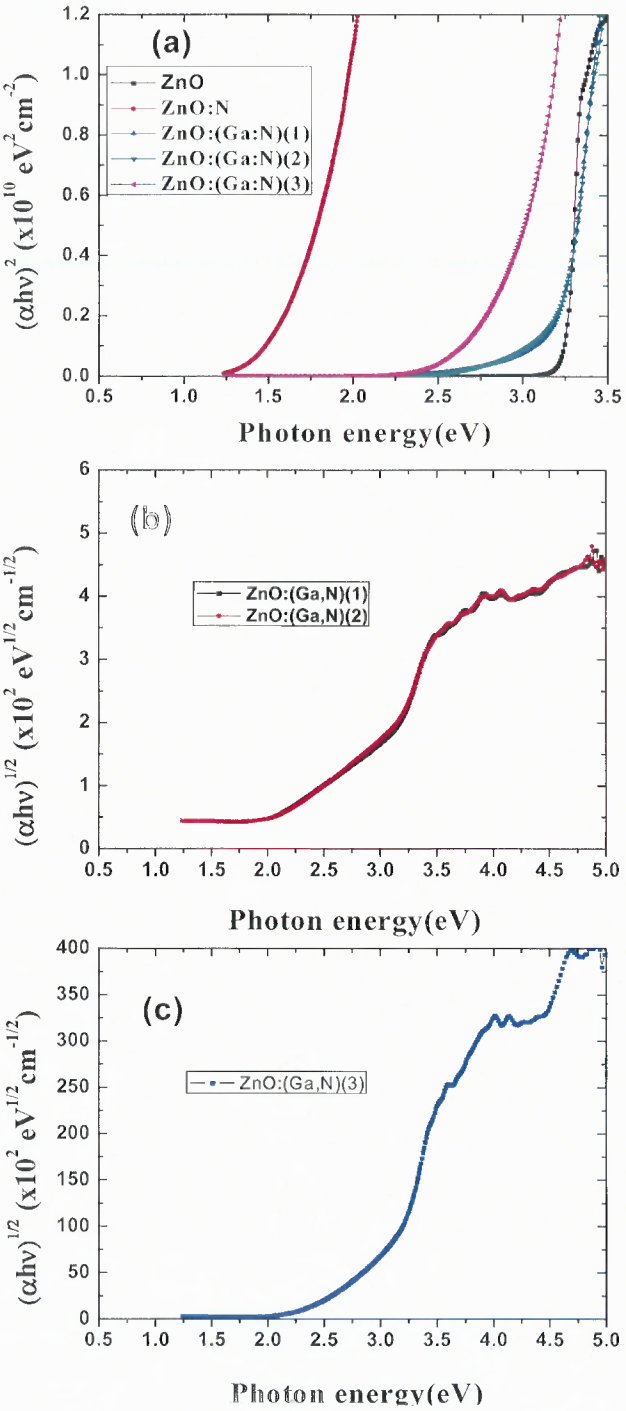

Figure 6.42 (a) Direct-transition optical-absorption coefficients of ZnO, ZnO:N, and ZnO:(Ga:N) films deposited in mixed N_2 and O_2 gas ambient. (b) Indirect-transition optical-absorption coefficients of ZnO:(Ga:N)(1) and ZnO:(Ga:N)(2) films deposited in 1.2% N_2 gas flow rate mixed N_2 and O_2 gas ambient. (c) Indirect-transition optical-bandgap in Figure 6.42(a). It is because the nitrogen of ZnO:Ga,N (1 and 2) films has mixed phases of ZnO and Zn_3N_2 [201].

Figure 6.43(a) shows Mott-Schottky plots of ZnO, ZnO:N, and ZnO:(Ga:N) films deposited in mixed ambient. All the samples exhibited positive slopes, indicating *n*-type semiconductors. Previous studies reported that ZnO:N films deposited in a N_2/O_2 plasma showed *n*-type behavior, due to substitutional N_2 molecules that act as shallow double-donors. The donor concentrations of the films were calculated from the slopes of the Mott-Schottky plots, which were about 6.2 x 10^{16}, 9.9 x 10^{17}, 2.7 x 10^{17}, 2.9 x 10^{17}, and 2.4 x 10^{17} cm^{-3} for ZnO, ZnO:N, ZnO:(Ga:N)(1), ZnO:(Ga:N)(2), and ZnO:(Ga:N)(3) films, respectively. The ZnO:N film exhibits a higher donor density compared to ZnO film due to high concentration of N_2 incorporation and/or native defects such as Zn interstitials and O vacancies. The incorporated ZnO:(Ga:N) films exhibited lower donor concentration than the ZnO:N film but higher than that of ZnO film. The donor concentration of ZnO:(Ga:N) films with or without phase separation of Zn_3N_2 are similar. The major contribution to PEC response comes from the carriers photogenerated in the built-in electrical field near surface regions, so the depletion width is an important factor for PEC application of semiconductors. In general, a larger depletion layer (*W*) is preferred to increase the harvesting efficiency of the photogenerated electron-hole pairs without the recombination.

Figure 6.43(b) shows the *W* values with the potential for the samples, which were calculated from the results of the Figure 6.43(a). It shows that ZnO showed much wider *W* compared to the ZnO:N and ZnO:(Ga:N) films. Co-doped ZnO:(Ga:N) films exhibited increased *W* values compared to ZnO:N film, due to lower donor concentration [201].

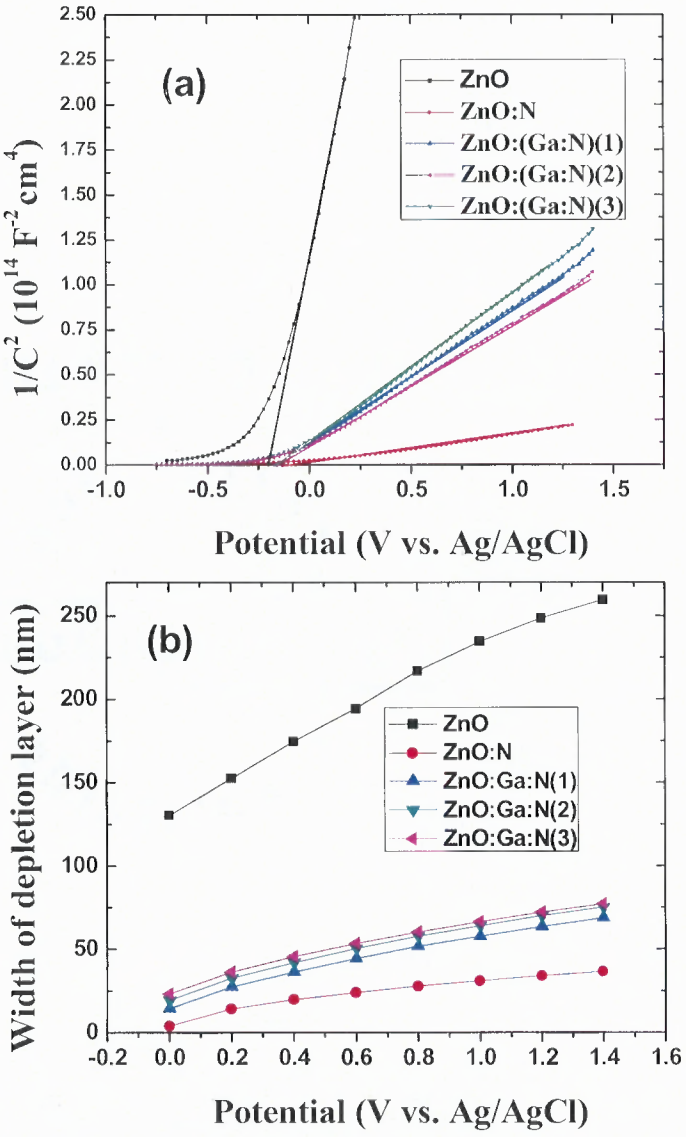

Figure 6.43 (a) Mott-Schottky plots of ZnO, ZnO:N, and ZnO:Ga:N films, respectively. (b) W values with the potential, estimated from (a) [201].

Figure 6.44 shows the photocurrent-voltage curves of ZnO, ZnO:N, and ZnO:(Ga:N) films deposited in mixed N_2 and O_2 gas ambient, under illumination with an UV/IR filter. It clearly showed that the ZnO:(Ga:N)(3) film exhibited significantly increased photocurrents, as compared to the other films. Even though the ZnO:Ga, N (1 and 2) films had better crystallinity than the pure ZnO, their PEC properties were lower

than that of the pure ZnO at the low potential region below 0.8 V. It indicates that a high recombination rate between the photogenerated electrons and holes exists in the films. Their inferior photocurrents are attributed to the phase segregation of Zn_3N_2, which is photo-inactive [201].

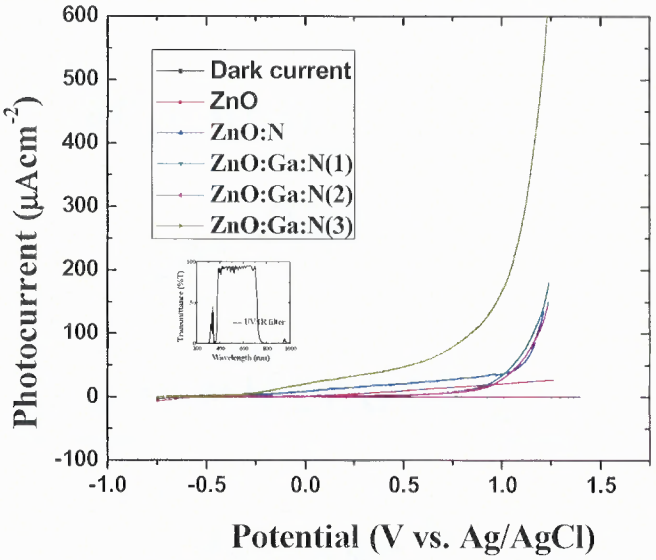

Figure 6.44 Photocurrent-voltage curves of ZnO, ZnO:N, and ZnO:Ga:N films, respectively, under the illumination with an UV/IR filter [201].

To investigate the photoresponses in the long-wavelength region, a green-color filter was used in combination with the UV/IR filter, as shown in Figure 6.45.

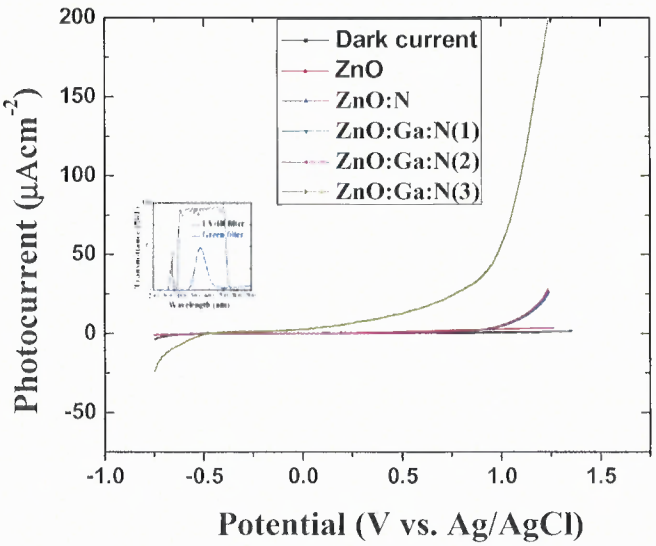

Figure 6.45 Photocurrent-voltage curves of ZnO, ZnO:N, and ZnO:Ga:N films, under illumination with the combined green and UV/IR filter [201].

The ZnO film exhibited no clear photoresponse due to its wide bandgap. The ZnO:(Ga:N)(3) film exhibited much higher photocurrent than the other films, due to the improved crystallinity, reduced bandgap, proper *W* value, and N-incorporated single phase without the phase separation. On the contrary, the ZnO:(Ga:N)(1 and 2) films exhibited no photoresponses. It indicates that the Zn_3N_2 phase in these films is photo-inactive, even though it had a very low bandgap below 2 eV. Therefore, the formation of the Zn_3N_2 in the co-doped ZnO:(Ga:N) films is very detrimental to obtaining an enhanced PEC response. Encountered instability issues when the film is in contact with electrolytes. Nonetheless, these results demonstrate clearly that growth conditions must be controlled carefully to avoid the formation of Zn_3N_2 in Ga and N co-incorporated ZnO thin films to improve PEC response [201].

6.8 Enhancement of Photoelectrochemical Response by Aligned Nanorods in ZnO Thin Films

In this part of the research, deposition in pure Ar ambient leads to polycrystalline ZnO thin films. However, the presence of N_2 in the deposition ambient promotes the formation of aligned nanorods above 300°C. ZnO thin films are deposited in pure Ar and mixed Ar and N_2 gas ambient at various substrate temperatures by RF sputtering ZnO targets.

Figures 6.46(a)–(d) show XRD curves for the ZnO(Ar) films and ZnO(Ar:N_2) films deposited at various substrate temperatures for 100, 200 and 300 W RF power, respectively. The crystallinity of ZnO films increases gradually with the increase in substrate temperatures in both cases. For both cases, films have random orientation at low substrate temperature. With the increase in substrate temperature to 500°C, the (002) peak of the film was greatly enhanced, as shown in Figure 6.46. The measured FWHM values of (002) peaks are shown in Figure 6.47(a). The FWHM of ZnO(Ar) was slightly decreased with the increase in the substrate temperature. ZnO(Ar:N_2)(100W) films grown at temperatures below 200°C and ZnO(Ar:N_2)(300W) films grown at temperatures below 300°C exhibited random orientation and larger FWHM values than the ZnO(Ar) films grown at the same temperatures. This is because a high concentration of the N is incorporated in ZnO(Ar:N_2) films at these temperatures. However, ZnO(Ar:N_2)(100W) films exhibited smaller FWHM values than the ZnO(Ar) films. The reason for these low FWHM values for ZnO(Ar:N_2)(100W) films is the very low incorporation of the N in the film because the RF power was comparatively low to dissociate enough N. It is known from recent reports that incorporated N atoms can deteriorate the crystal structure and modify growth mode [196-198].

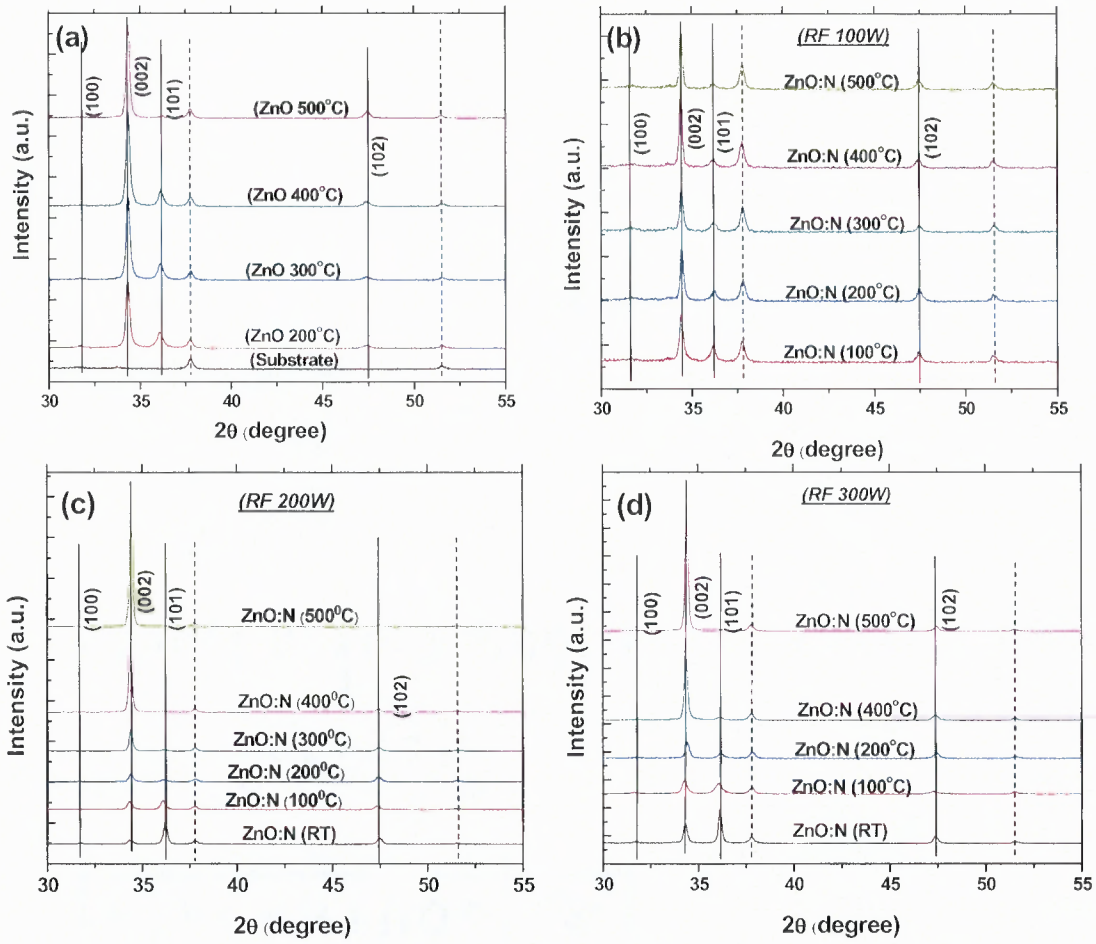

Figure 6.46 XRD curves for the ZnO(Ar) and ZnO(Ar:N_2) films deposited at different substrate temperatures for 100, 200 and 300 W RF power [202-204].

However, the FWHM values of ZnO(Ar:N_2)(200W) and ZnO(Ar:N_2)(300W) films increase rapidly when the substrate temperatures are above 300°C because no significant N can be incorporated at these temperatures. At a substrate temperature above 300°C, ZnO(Ar:N_2) films exhibit much smaller FWHM values than the ZnO(Ar) films. The rapid growth of the FWHM values indicates either increased crystallinity or formation of nanorods or nanowires along the c-axis [202-204].

The N concentrations (at.%) for the ZnO(Ar:N_2) films measured by XPS are shown in Figure 6.47(b). With the increase in substrate temperature, the N concentration decreased rapidly and disappeared at temperatures above 300°C. Also, it is clearly evident from Figure 6.47(b) that, as the RF power increases, there is more N incorporation in the film [202-204].

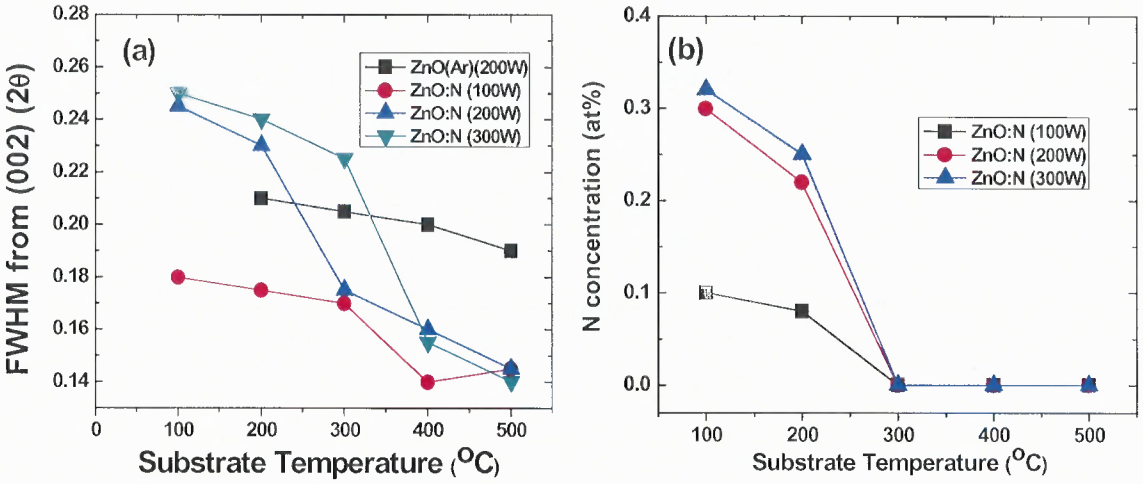

Figure 6.47 (a) FWHM values estimated from (002) peak for the ZnO(Ar) and ZnO(Ar:N_2) films. (b) The N concentrations for the ZnO(Ar:N_2) films as a function of the substrate temperature [202-204].

Figure 6.48(a) shows XRD curves for the ZnO(Ar:N_2) films deposited at a substrate temperature of 100°C at varying RF power from 100 to 500 W. The crystallinity of ZnO films decreases gradually with the increase in RF power. The measured FWHM values of (002) peaks are shown in Figure 6.48(b). The FWHM of ZnO(Ar:N_2) was slightly increased with the increase in the RF power, indicating gradual increase in N concentration in the film. Figure 6.48(c) shows the N concentrations (at.%) for the ZnO(Ar:N_2) films. With the increase in RF power, the N concentration increased gradually [202-204].

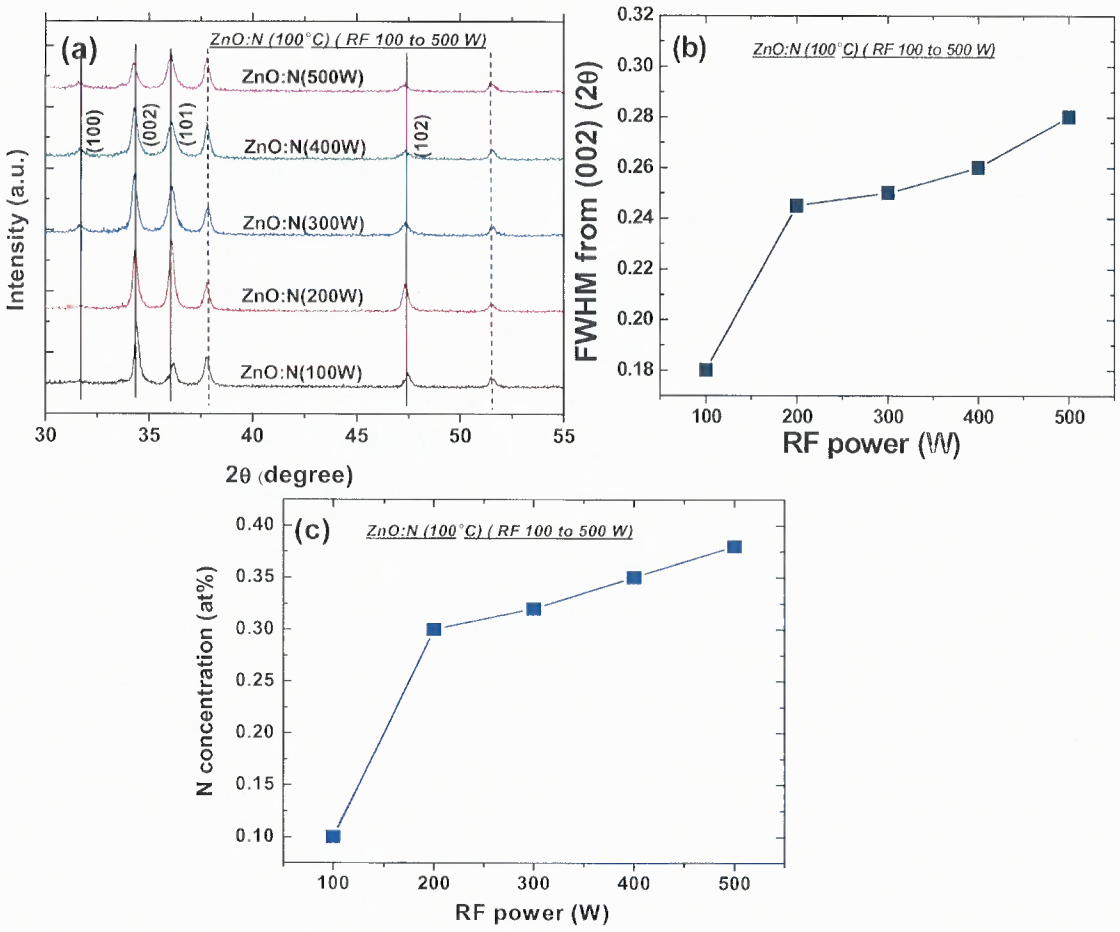

Figure 6.48 (a) FWHM values estimated from (002) peak for the ZnO(Ar) and ZnO(Ar:N_2) films. (b) The N concentrations for the ZnO(Ar:N_2) films as a function of the substrate temperature [202-204].

AFM images reveal that the significantly increased (002) peak in the XRD curve obtained in ZnO(Ar:N_2) at different RF power is largely due to the formation of aligned nanorods along the c-axis. Figures 6.49, 6.50, 6.51, and 6.52 show AFM surface morphology (5×5 μm^2) of ZnO(Ar), ZnO(Ar:N_2)(100W), ZnO(Ar:N_2)(200W), and ZnO(Ar:N_2)(300W) films deposited for varying substrate temperatures, respectively. It shows clearly that the ZnO(Ar:N_2) deposited at 100°C has a random orientation. As substrate temperature increases, aligned nanorods along the c-axis were promoted to

form. At 500°C, the ZnO(Ar:N_2) film deposited at 200 and 300 W and at 400°C for 100 W reveals growth of hexagonal-like nanorods. However, the ZnO(Ar) film deposited at the same temperature is polycrystalline, as shown in Figure 6.49. It should be noted that diameters of the nanorods are smaller than that of the grains in polycrystalline ZnO film. The smaller FWHM value for the ZnO(Ar:N_2) film is attributed to the nanorod feature [205-207].

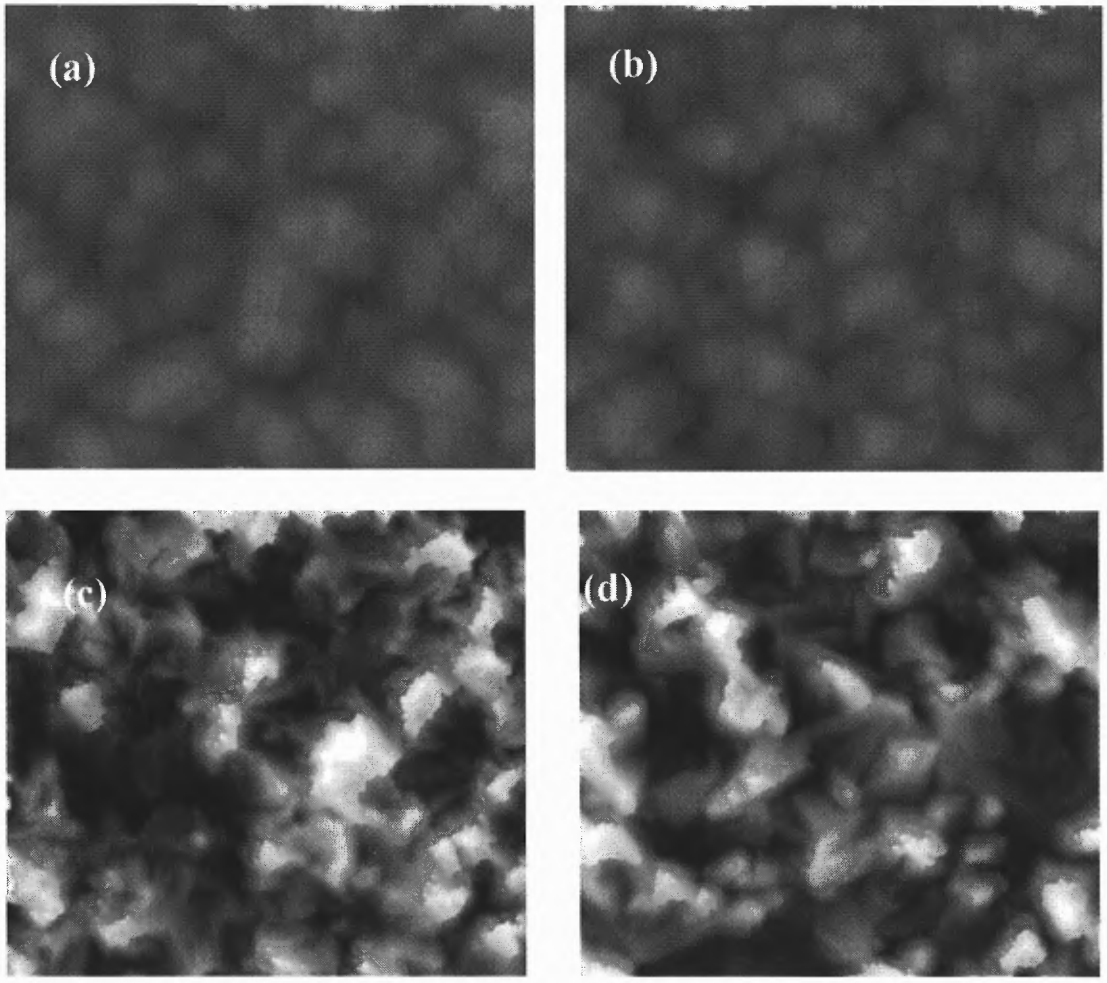

Figure 6.49 AFM surface morphology (5×5 μm^2) of (a-d) the ZnO(Ar)(200W) films deposited at the substrate temperatures of 100°, 200°, 400°, and 500°C, respectively [202-204].

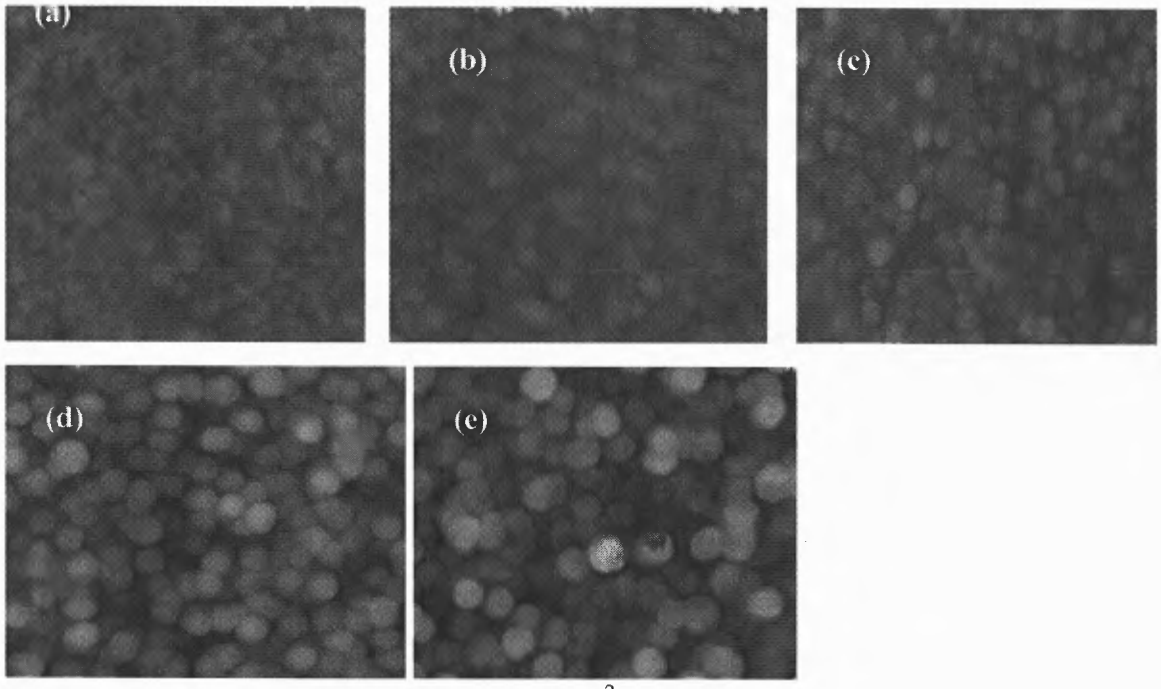

Figure 6.50 AFM surface morphology (5×5 μm^2) of (a-e) the ZnO(Ar:N_2)(100W) films deposited at the substrate temperatures of 100°, 200°, 300°, 400°, and 500°C, respectively [202-204].

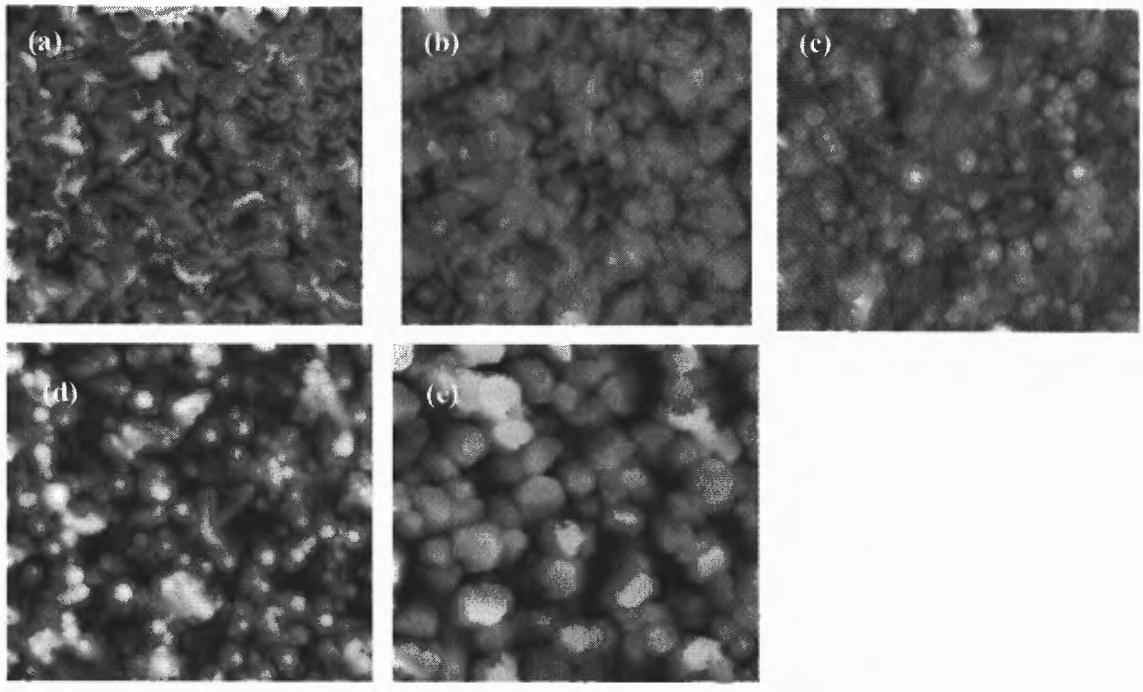

Figure 6.51 AFM surface morphology (5×5 μm^2) of (a-e) the ZnO(Ar:N_2)(200W) films deposited at the substrate temperatures of 100°, 200°, 300°, 400°, and 500°C, respectively [202-204].

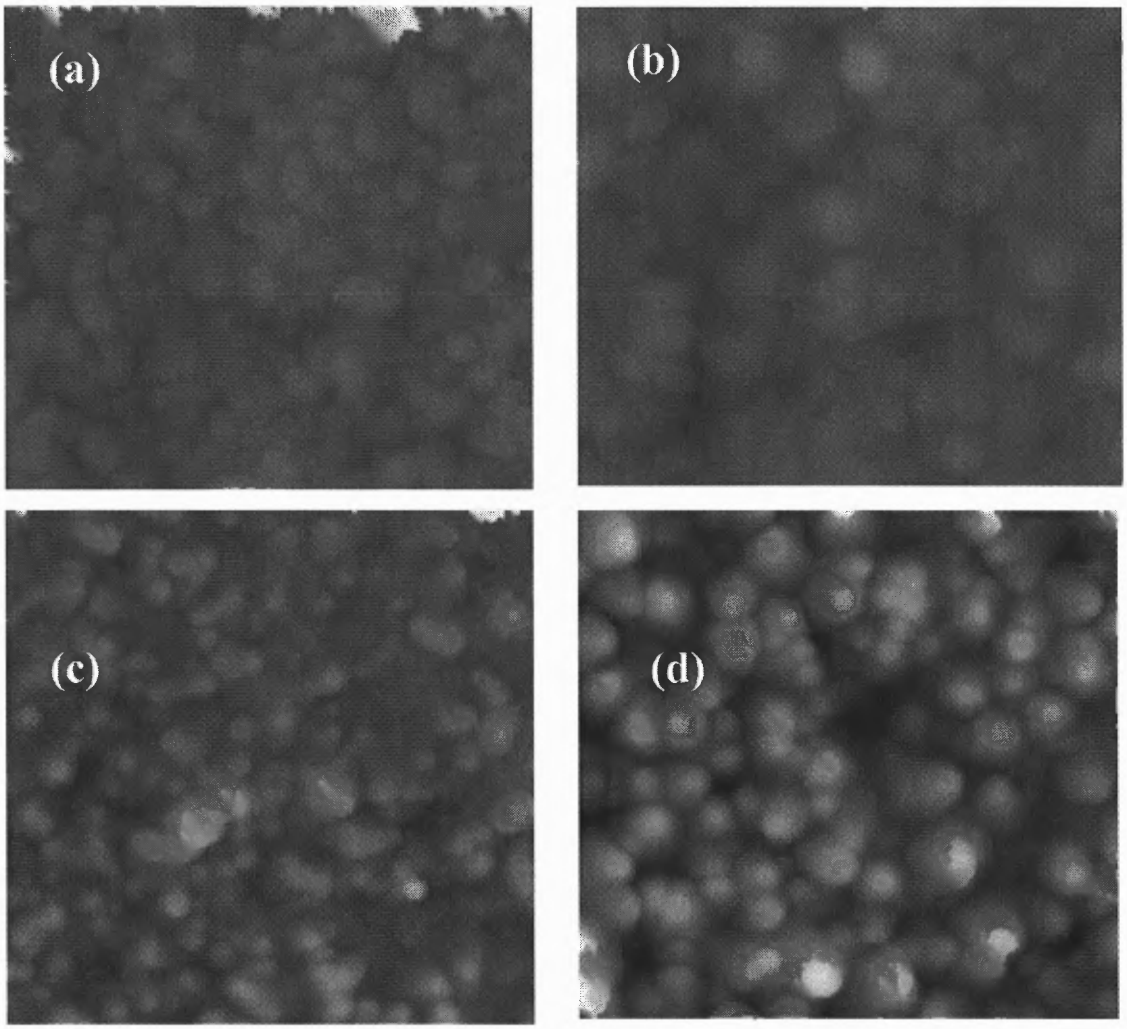

Figure 6.52 AFM surface morphology (5×5 μm^2) of (a-e) the ZnO(Ar:N_2)(300W) films deposited at the substrate temperatures of 100°, 200°, 300°, and 500°C, respectively [202-204].

Figures 6.53(a-d) show FE-SEM top-views of the ZnO(Ar) and ZnO(Ar:N_2) films, respectively, deposited at a substrate temperature of 500°C. It clearly shows that the nanorod structure was not present in the ZnO(Ar), whereas Figures 6.53(b), 6.53(c), and 6.53(d) exhibited vertically aligned, single-crystal hexagonal-like nanorods with flat (0002) surfaces for the ZnO(Ar:N_2) films at 400°C (100W), 500°C for 200 and 300 W. No metal clusters were found at the end of the nanorods, indicating that the growth mechanism is not catalyst-assisted, vapor-liquid-solid (VLS) growth [206-208].

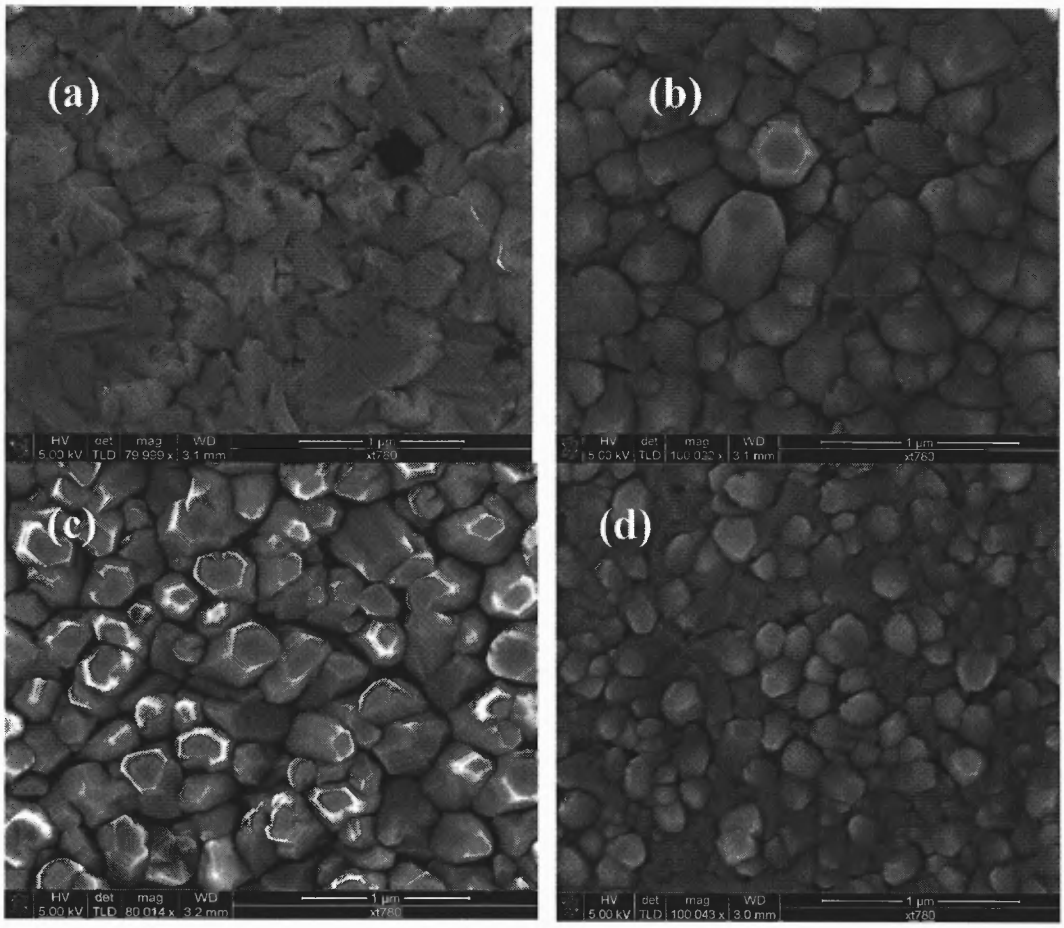

Figure 6.53 FE-SEM top-views of (a) ZnO(Ar)(200W), (b) ZnO(Ar:N_2)(100W), (c) ZnO(Ar:N_2)(200W), (d) ZnO(Ar:N_2)(300W) deposited at 500°C [202-204].

Recently, catalyst-free ZnO nanorods/nanowires have been synthesized by various chemical and physical techniques such as metal-organic vapor-phase epitaxy, plasma-enhanced chemical vapor deposition, and pulse-laser deposition [206-209]. The nanorod structures provide high surface areas and superior carrier transport (or conductivity) along the c-axis, which may lead to increased interfacial reaction sites and reduced recombination rate [210, 211]. Therefore, the aligned nanorod films should lead to enhanced PEC response [202-204].

Figure 6.54 (a-d) shows absorption coefficients for the ZnO(Ar)(200W), ZnO(Ar:N_2)(100W), ZnO(Ar:N_2)(200W), and ZnO(Ar:N_2)(300W) films deposited at various substrate temperatures, respectively [202-204].

Figure 6.55(a) shows optical bandgaps of the ZnO(Ar) and ZnO(Ar:N_2) films deposited at different substrate temperatures by varying the RF power from 100 to 300 W. The measured optical bandgaps for ZnO(Ar) films deposited at 200° to 500°C increased very slightly (from 3.235 to 3.26 eV). The bandgap of the ZnO(Ar:N_2)(100W), (200W) and (300W) film deposited at 100° and 200°C is lower than that of the ZnO(Ar) films.

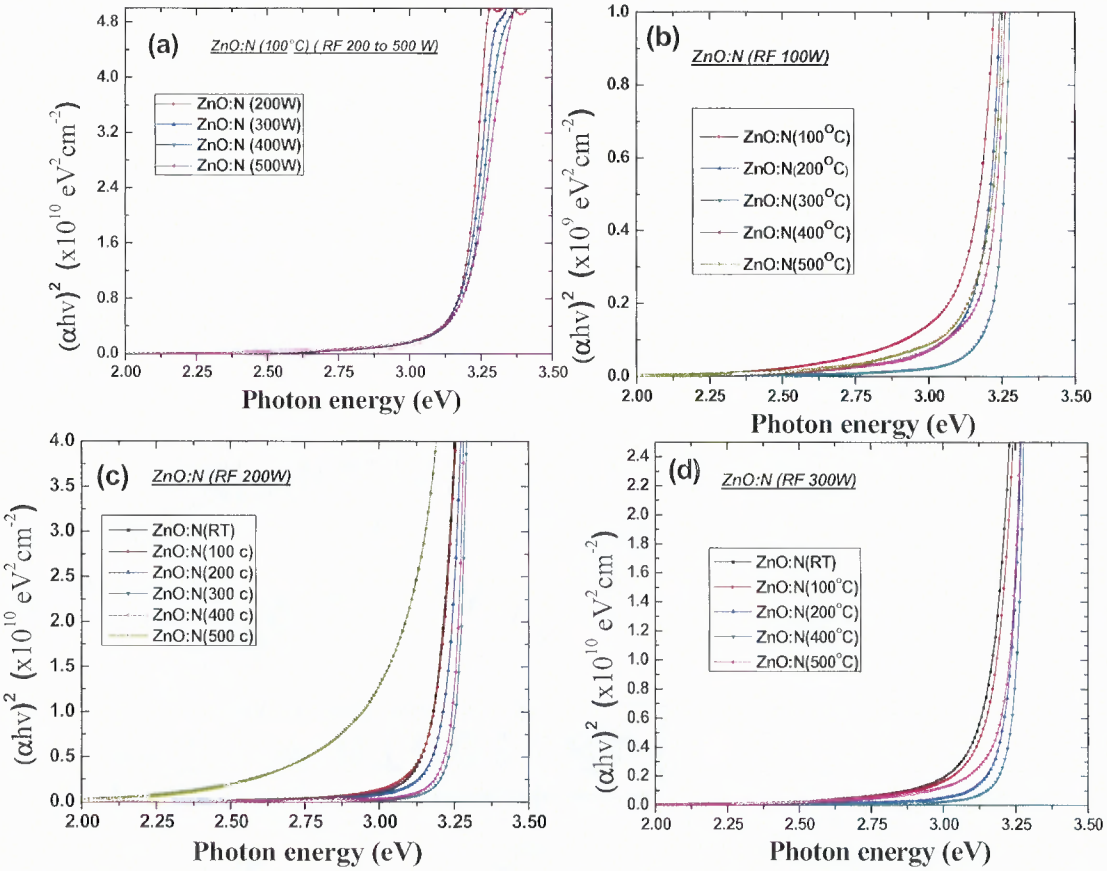

Figure 6.54 Optical absorption coefficients of (a) ZnO(Ar)(200W), (b) ZnO(Ar:N_2)(100W), (c) ZnO(Ar:N_2)(200W), and (d) ZnO(Ar:N_2)(300W) films [202-204].

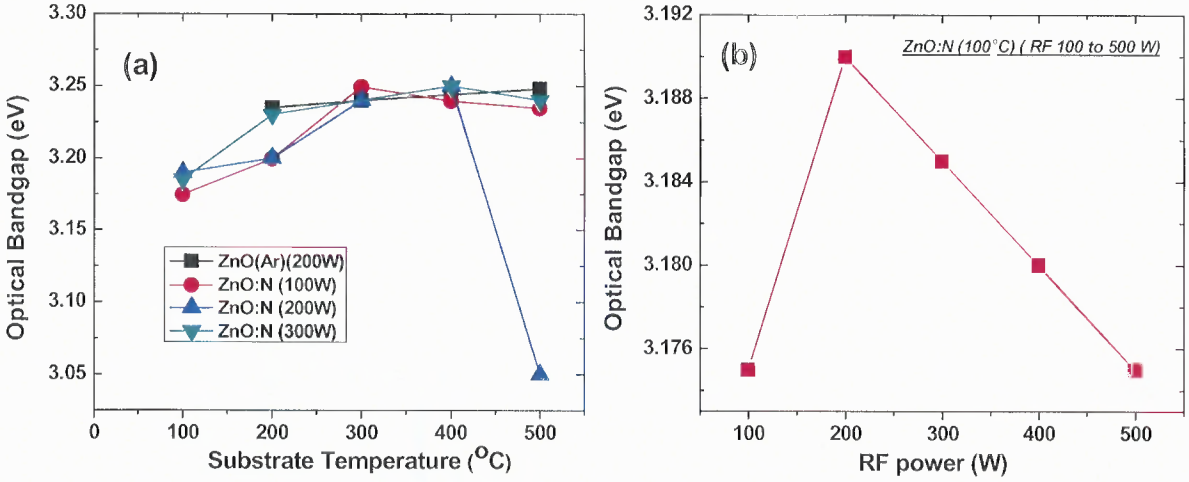

Figure 6.55 Estimated optical bandgaps of (a) ZnO(Ar:N_2) films deposited at varying RF power from 100 to 300 W as a function of the substrate temperature, and (b) ZnO(Ar:N_2) films deposited at varying RF power from 100 to 500 W at a substrate temperature of 100°C [202-204].

This bandgap reduction is due to the incorporation of N, which generates an impurity band above the valence band of ZnO [212]. However, when substrate temperatures are increased to 300° and 400°C for 100 and 200 W, the bandgap reduction disappears. The reason is because, at these temperatures, N incorporation is suppressed, as confirmed by XPS composition measurements. Thus, the bandgaps of ZnO(Ar:N_2) grown at these temperatures should have similar bandgaps as the ZnO(Ar) films. It is interesting to note, however, that the ZnO(Ar:N_2) films with aligned nanorods deposited at 500°C for 200 W and 300 W exhibited a much lower bandgap than the ZnO(Ar) film grown at the same temperature. Because XPS indicates no detectable N incorporated in the ZnO(Ar:N_2) nanorod film, the bandgap reduction must be induced by intrinsic defects, likely oxygen vacancies [213], which could explain the absorption tail below 3 eV. The impurity band can enable light absorption in the long-wavelength regions. In the case of ZnO(Ar:N_2)(100W), when substrate temperatures are increased above 300°C, the film showed lower bandgap than the ZnO(Ar) film grown at the same temperature. The

bandgap reduction can be attributed to intrinsic defects, likely oxygen vacancies. Figure 6.55(b) shows optical bandgaps of the ZnO(Ar:N_2) films deposited at substrate temperature of 100°C by varying the RF power from 100 to 500 W. The measured optical bandgaps for ZnO(Ar:N_2) films increased as RF power increased from 100 W to 200 W and then started to decrease as RF power is increased above 200 W. The bandgap reduction can be attributed to N concentration incorporated in the film as the RF power is increased [202-204].

Figures 6.56(a) and 6.56(b) show photocurrent-voltage curves of the ZnO(Ar:N_2) and ZnO(Ar) films deposited at 400°C, respectively, under continuous illumination (red curve) and dark condition (black curve), with an UV/IR filter. Both ZnO films show very small dark currents up to a potential of 1.4 V. The photocurrents under light-on and light-off conditions are the same as those under illumination and dark currents, respectively, because of the small dark currents. The ZnO(Ar:N_2) nanorod film deposited at 400°C exhibits much higher photocurrents than the ZnO(Ar) film deposited at the same substrate temperature [202-204].

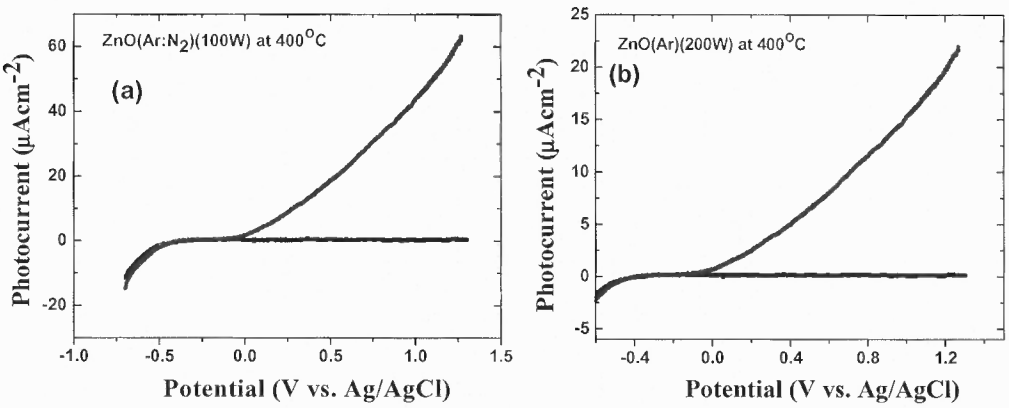

Figure 6.56 Photocurrent-voltage curves of (a) ZnO(Ar:N_2)(100W) nanorod and (b) ZnO(Ar)(100W) films, deposited at 400°C under (red curve) continuous illumination, (black curve) dark condition, with an UV/IR filter. Electrolyte and scan rate were 0.5 M Na_2SO_4 mild aqueous solution and 5 mV/s, respectively [202-204].

To see the effects of substrate temperature at varying RF power on PEC response, photocurrents were measured at 1.2 V potential for ZnO(Ar:N_2) and ZnO(Ar) films under continuous illumination with UV/IR filter. Figure 6.57(a) shows the measured photocurrents as a function of the substrate temperature for the ZnO(Ar:N_2) and ZnO(Ar) films in different ambient at varying substrate temperature and RF power. At low substrate temperatures (below 300°C), the photocurrent of ZnO(Ar:N_2) films are slightly higher than that of ZnO(Ar) films, because these ZnO(Ar:N_2) films have smaller bandgaps than ZnO(Ar) films. For these ZnO(Ar/N_2) films, the low crystallinity should be responsible for the small increase in photocurrents. However, the photocurrent increases for ZnO(Ar:N_2) films as the substrate temperature increases. The ZnO(Ar:N_2) film deposited at 500°C for 200 and 300 W exhibits the best PEC response—more than two times higher than the ZnO(Ar) films deposited at the same temperature. The ZnO(Ar:N_2) film deposited at 400°C for 100 W exhibits a better PEC response than the ZnO(Ar) films deposited at the same temperature. The enhancement can be attributed to

the aligned nanorod structure along the c-axis and additional light absorption in the long-wavelength regions. Figure 6.57(b) shows the measured photocurrents as a function of the RF power for the ZnO(Ar:N_2) films deposited at a substrate temperature of 100°C. The decrease in photocurrent as the RF power is increased from 100 to 500 W can be attributed to a decrease in crystallinity [202-204].

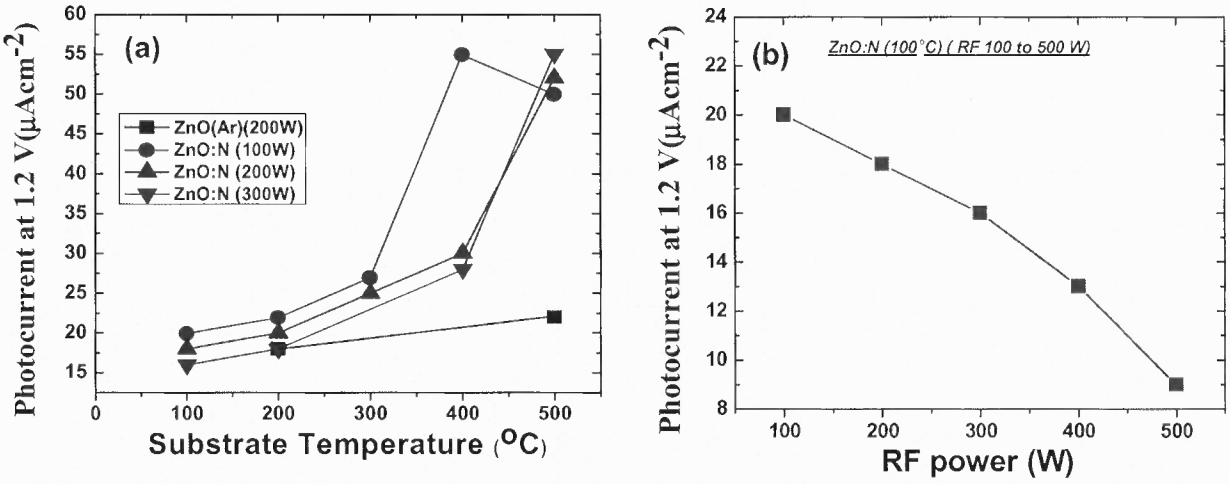

Figure 6.57 (a) Photocurrents measured at 1.2 V as a function of the substrate temperature for the ZnO(Ar:N_2) and ZnO(Ar) films deposited at different RF power. (b) Photocurrents measured at 1.2 V as a function of the RF power for the ZnO(Ar:N_2) deposited at a substrate temperature of 100°C [202-204].

These currents can only result from the photon absorption by the defect bands. Thus, these results indicate that the formation of impurity bands do not necessarily significantly increase the recombination rate and can be used to provide additional photon absorption in the long-wavelength regions. However, it should be noted that the concentration of point defects should be optimized. If the concentration is too high, the point defects may significantly increase the electron-hole recombination rate and act as dominant recombination centers, resulting in decreased photoresponse. This has been observed in the low-crystallinity ZnO(Ar:N_2) films deposited below 300°C. Nevertheless,

these results show that sputter-deposited ZnO films at a substrate temperature of 500°C for 200 and 300 W and 400°C for 100 W in mixed Ar:N_2 gas ambient exhibited aligned nanorods along the c-axis and a slightly reduced bandgap, leading to greatly enhanced PEC response [202-204].

6.9 Effect of Gas Flow Rate for Forming Aligned Nanorods in ZnO Thin Films

In this part of the research, effect of gas flow rate in forming aligned nanorods in ZnO thin films is summarized.

Figures 6.58 shows XRD curves for the ZnO thin films deposited at different nitrogen-to-argon ratios at a substrate temperature of 500°C. From the results reported in the previous section, aligned nanorod can be formed in mixed N_2 to Ar chamber ambient at a substrate temperature of 500°C. The crystallinity of ZnO thin films increases gradually with the increase in nitrogen percentage in the chamber ambient up to 25%. Above 25% nitrogen, the crystallinity begins decreasing. Of all these chamber ambients, ZnO thin film deposited at 25% nitrogen showed greatly enhanced (002) peak. The ZnO thin film grown at 75% nitrogen showed the least crystallinity. The FWHM of the (002) peak of ZnO thin films decreased as the N_2 percentage in the chamber ambient increased from 0% to 25%, and FWHM started increasing again as the N_2 gas flow rate increased above 25%. The ZnO thin film deposited at 75% nitrogen ambient showed the maximum FWHM value. It is known from recent reports that incorporated N atoms can deteriorate the crystal structure and modify the growth mode. However, when the substrate temperatures are above 300°C, no significant N can be incorporated at these temperatures. The rapid decrease of the FWHM values as the N_2 percentage in the

chamber ambient increased from 0% to 25% indicates either increased crystallinity or the formation of nanorods or nanowires along the c-axis. No significant N concentrations (at.%) were found for the ZnO thin films measured by XPS [214-215].

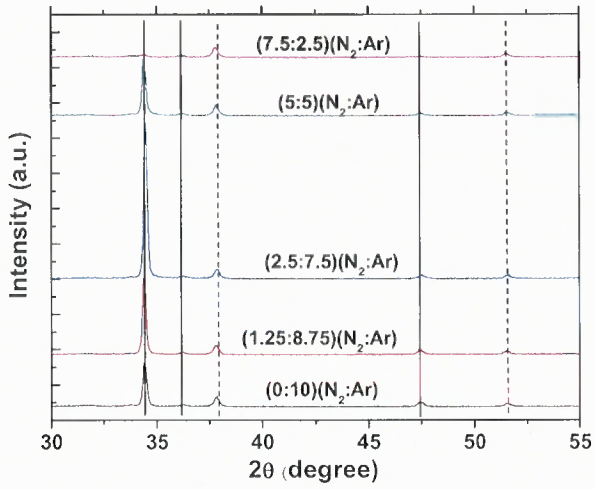

Figure 6.58 X-ray diffraction curves for ZnO thin films deposited at different nitrogen-to-argon ratios [214-215].

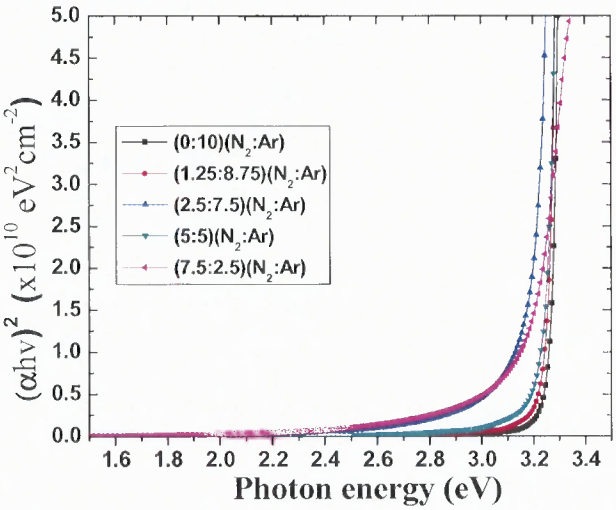

Figure 6.59 Absorption coefficients for the ZnO thin films deposited at different nitrogen-to-argon ratios [214-215].

Figure 6.59 shows absorption coefficients of the ZnO thin films deposited at different N_2-to-Ar gas flow rate ratios in the chamber ambient. The direct optical bandgaps of the films were determined by extrapolating the linear portion of each curve in Figure 4 to $(\alpha hv^2) = 0$. The measured optical bandgaps for ZnO thin films deposited at different N_2-to-Ar ratios are almost identical (~3.25 eV). It should be noted that when films were deposited at a substrate temperature of 500°C, no significant amount of nitrogen is incorporated in the film, as confirmed by XPS. However, ZnO thin films deposited at 25% nitrogen in the chamber ambient showed little reduction in the bandgap. Because there is no detectable N incorporated in the ZnO (25%N_2) nanorod film, bandgap reduction may be caused by intrinsic defects, likely oxygen vacancies, which are responsible for the absorption tail below 3 eV [214, 215].

AFM images reveal that the significantly increased (002) peak in the XRD curve obtained in ZnO thin films is largely due to the formation of aligned nanorods along the c-axis. Figure 6.60 shows AFM surface morphology (5×5 μm^2) of ZnO thin films deposited at 0%, 75%, and 25% nitrogen. It clearly shows that the ZnO thin film deposited at 0% N_2 has a random orientation. In comparison, ZnO thin film grown at a chamber ambient of 25% N_2 reveals the growth of hexagonal-like nanorods. It should be noted that the diameters of the nanorods are smaller than those of the grains in polycrystalline ZnO thin film. The smaller FWHM value for the ZnO thin film is attributed to the nanorod feature. ZnO thin film grown at 75% nitrogen chamber ambient is polycrystalline [214, 215].

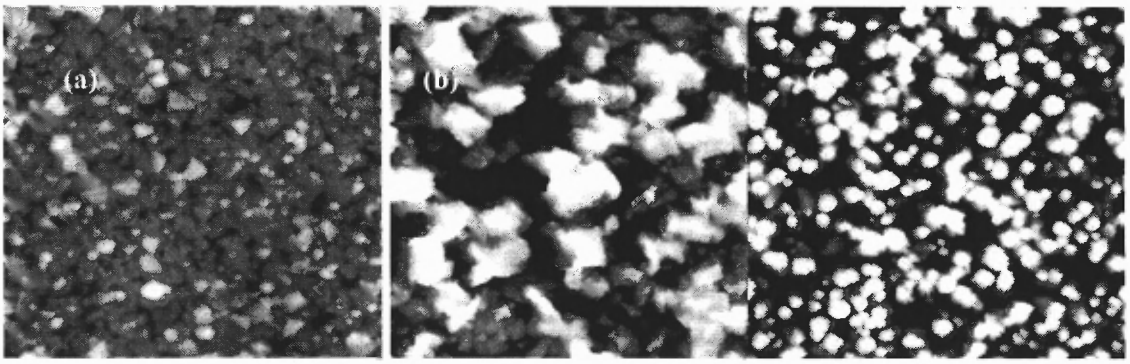

Figure 6.60 AFM surface morphology (5×5 μm^2) of (a-c) the ZnO thin films deposited at the nitrogen-to-argon ratio of 0%, 25%, and 75%, respectively [214-215].

Figures 6.61 shows FE-SEM top-views of the ZnO thin films deposited at 0%, 75%, and 25% nitrogen. It clearly shows that the nanorod structure was not present in the ZnO thin film grown at 0% and 75% N_2 chamber ambient, whereas ZnO(25%N_2) film exhibited vertically aligned, single-crystal hexagonal-like nanorods with a flat (0002) surface. The nanorod structures provide high surface areas and superior carrier transport (or conductivity) along the c-axis, which may lead to increased interfacial reaction sites and reduced recombination rate. Therefore, the aligned nanorod films should lead to enhanced PEC response [214, 215].

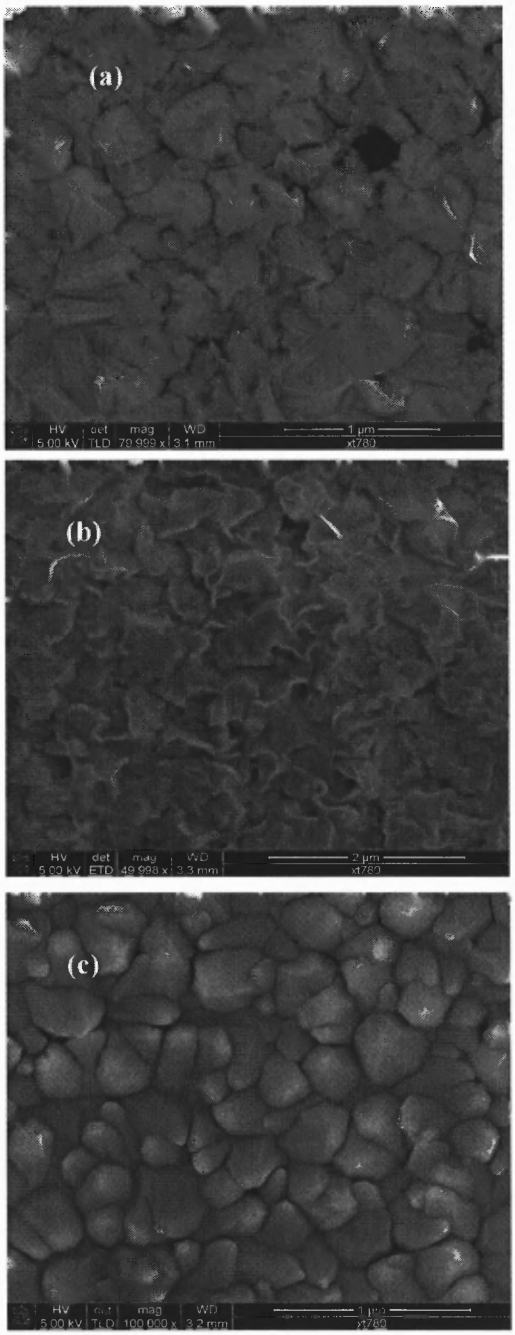

Figure 6.61 FE-SEM top-views of (a-c) the ZnO thin films deposited at the nitrogen-to-argon ratio of 0%, 25%, and 75%, respectively [214-215].

Figures 6.62(a) and 6.62(b) show photocurrent-voltage curves of the ZnO (0% N_2) and ZnO (25% N_2) thin films deposited at 500°C, respectively, under dark condition (black curve) and continuous illumination (red curve), with an UV/IR filter. A very small

dark current up to a potential of 1.2 V is shown by both the films. The ZnO (25% N_2) thin film exhibited much higher photocurrent than the ZnO (0% N_2) film due to the aligned nanorod formed along the c-axis [214-215].

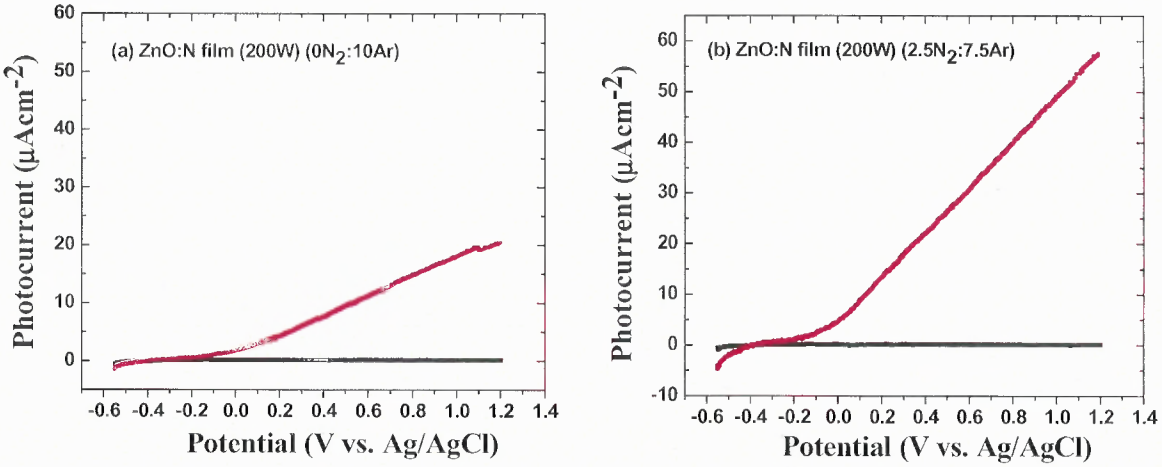

Figure 6.62 Photocurrent-voltage curves of (a) ZnO(0%N_2) and (b) ZnO(25%N_2) films, deposited at 500°C under (red curve) continuous illumination, (black curve) dark condition, with an UV/IR filter. Electrolyte and scan rate were 0.5 M Na_2SO_4 mild aqueous solution and 5 mV/s, respectively [214-215].

Figure 6.63 shows the measured photocurrents as a function of the nitrogen-to-argon gas flow rate ratio in the chamber ambient for the ZnO thin films. To see the effects of N percentage in the chamber ambient on PEC response, we measured photocurrent at 1.2 V potential for ZnO thin films under continuous illumination with UV/IR filter. At 0% nitrogen, the photocurrent of the ZnO thin film is lower than that of the films deposited at 12.5% nitrogen chamber ambient because of the low crystallinity. However, the photocurrent increases for ZnO thin films as the nitrogen percentage increased in the chamber ambient up to 25%, and it begins decreasing again as the nitrogen percentage is further increased above 25%. The ZnO thin film deposited at 25% nitrogen exhibited the best PEC response. The enhancement can be attributed to the

aligned nanorod structure along the c-axis. The decrease in photocurrent above 25% nitrogen in the chamber ambient is due to no more nanorod structure in the films; rather, there is a random orientation of grains. These results show that an optimum chamber ambient must be present to form nanorods along the c-axis in sputter-deposited ZnO thin films, which leads to greatly enhanced PEC response [214-215].

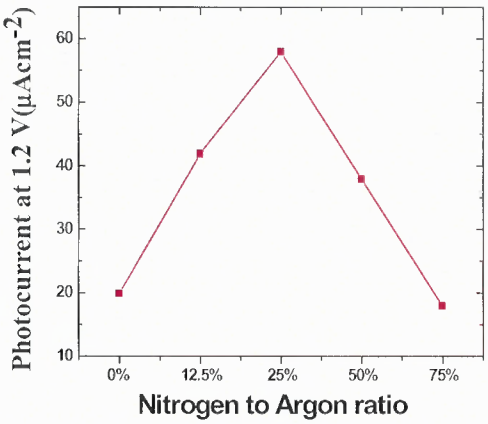

Figure 6.63 Photocurrents measured at 1.2 V as a function of the nitrogen-to-argon ratio for the ZnO thin films deposited at a substrate temperature of 500°C [214-215].

6.10 Synthesis of Nanocoral Structure in ZnO films and Their Impact on Photoelectrochemical Response

In this part of the research, the synthesis and characterization of ZnO nanocoral structures is presented. Porous ZnO nanocoral structures on FTO substrates are synthesized using a two-step process: sputter-deposition of the Zn films with different RF powers, followed by thermal annealing at 500°C in flowing O_2.

The effect of RF power on the grain size and orientation of the synthesized Zn films is shown in Figure 6.64(a), which shows the XRD curves for the substrate and the Zn metal films deposited at different RF powers. The sputtering was performed under Ar

ambient, so all samples exhibited pure Zn metal phases. The peak intensity and the FWHM show that the grain size increases with increasing RF power. This is due to the increased energy of the sputtered Zn ions [216]. It is evident that the intensity of the (0002) peak increases with increasing RF power. Figure 6.64(b) shows the intensity ratio between the (0002) and the (101) peaks for the Zn films as a function of the RF power. The intensity ratio is 0.53 for Zn powder samples. It is seen that the Zn films deposited at RF powers greater than 150 W exhibited a higher peak intensity ratio, indicating that high RF power promotes (0002) orientation. Figures 6.64(c) and 6.64(d) show the SEM images for the Zn films deposited at 50 and 200 W, respectively. It clearly shows that the Zn film deposited at 50 W has randomly oriented small grains, whereas the 200-W Zn films exhibited large hexagon-like grains. This is in a good agreement with the XRD results [217].

The Zn films were then annealed at 500°C in the O_2 environment for at least 8 hours to ensure full oxidization. XRD revealed that the annealed films contain only the ZnO phase. Annealed samples are referred to as 35-W ZnO, 50-W ZnO, 100-W ZnO, 150-W ZnO, and 200-W ZnO. It is found that the orientation and grain size of the initial Zn films can dramatically affect the microstructure of the thermally oxidized ZnO films [217].

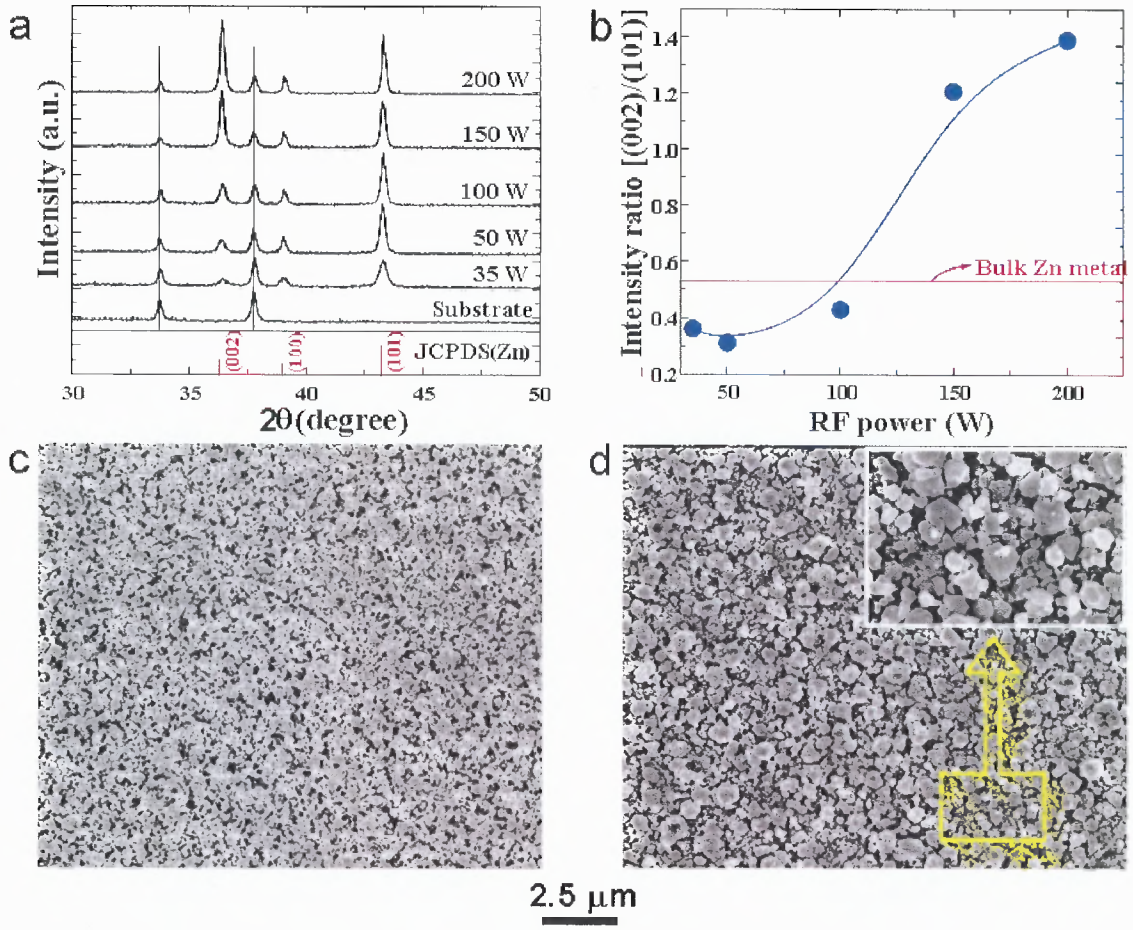

Figure 6.64 Structure of as-deposited Zn films. (a) XRD curves of the substrate and the Zn metal films deposited at RF powers of 35, 50, 100, 150, and 200 W. (b) XRD peak intensity ratio of (0002)/(101) estimated from (a). (c and d) SEM images of 50-W and 200-W Zn films, respectively [217].

Figure 6.65 shows the SEM images taken from the annealed samples of 35-W ZnO, 50-W ZnO, 100-W ZnO, and 150-W ZnO. Clearly, the 50-W ZnO (Fig. 6.63(b)) and the 100-W ZnO (Fig. 6.63(c)) samples exhibit a nanocoral structure. The average size of the nanocorals for the 50-W ZnO is significantly smaller than that of the 100-W ZnO samples, indicating that the size of the nanocorals can be tuned by the RF power. The 35-W ZnO consists of nanoparticles, as seen in Figure 6.65(a). The 150-W ZnO and the 200-W ZnO are simply nanocrystalline ZnO films, as seen in Figure 6.65(d). These

nanoparticle and nanocrystalline films are not as compact as films deposited directly as ZnO. The SEM images reveal two unique features for the nanocoral structures. First, because the nanocorals are composed of nanosheets, the structure is very porous, producing a large surface area. Second, the nanosheets grow together smoothly, providing an excellent electrical pathway for carrier collection. These two unique features are very favorable for PEC applications [210, 218-220].

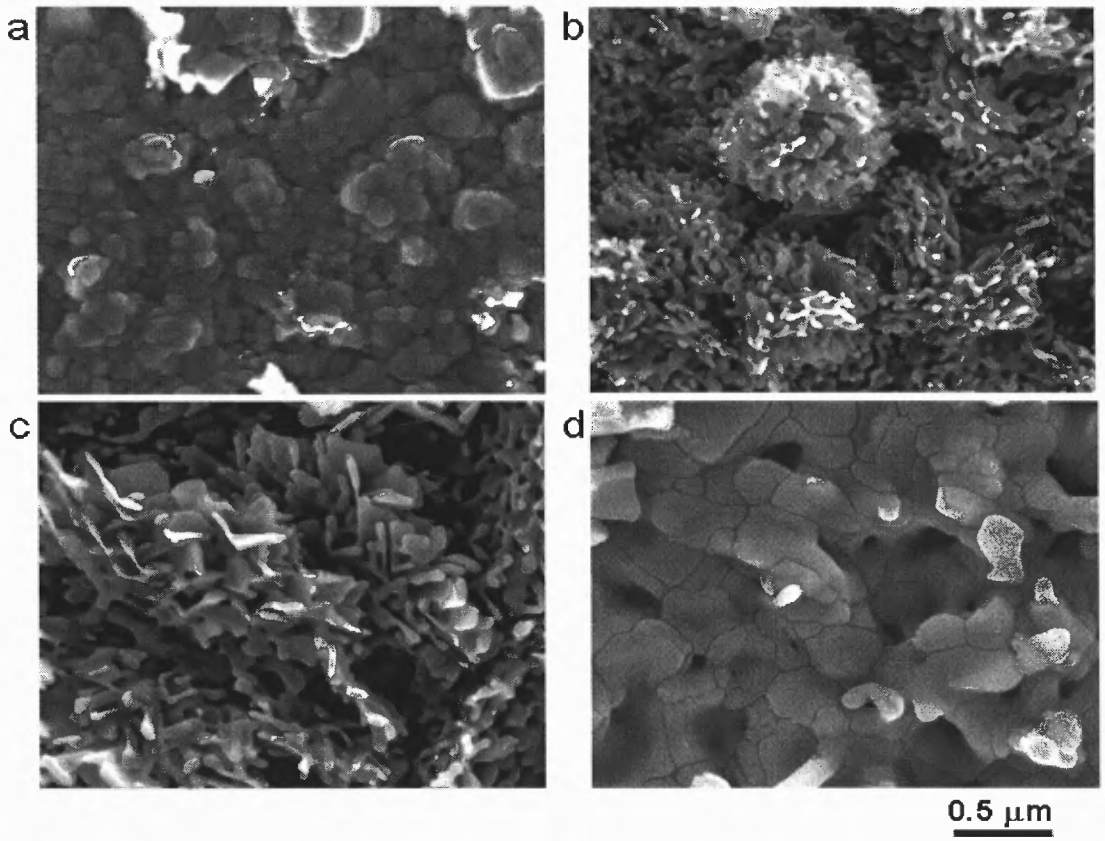

Figure 6.65 Microstructures of thermal oxidized ZnO films. (a, b, c, and d) SEM images of 35-W, 50-W, 100-W, and 150-W ZnO films, respectively. The 35-W ZnO sample shows nanoparticles. The 50-W ZnO and 100-W ZnO samples show nanocoral structures. The 150-W ZnO sample is a nanocrystalline film. The 200-W ZnO sample has a similar nanocrystalline feature [217].

The nanosheet features in the nanocoral nanostructures were further examined by TEM. Figures 6.66(a) and 6.66(b) show bright-field (BF) TEM images taken from 50-W ZnO and 100-W ZnO samples, respectively. The nanosheet features are clearly evident. It was found that the sizes of nanosheets in the 50-W ZnO sample are more uniform than those in the 100-W ZnO sample. The nanosheets in the 50-W ZnO sample are typically similar to those shown in Figure 6.66(a). However, in the 100-W ZnO sample, it was often observed additional nanosheets with much larger sizes than those seen in Figure 6.66(b). Figure 6.66(c) shows an example of a large nanosheet seen in the 100-W ZnO sample. Thus, both the 50-W ZnO and 100-W ZnO samples have similar features, but the average size of nanosheets for 100-W ZnO is much larger than 50-W ZnO, consistent with the results obtained from the SEM images.

From the diffraction contrast, we also observed that the nanosheets are typically single crystals. The nanosheets with small sizes are usually free from lattice defects and strains, whereas the nanosheets with large sizes usually contain defects and strains, marked by the white arrows in Figure 6.66(c). The growth direction of the nanosheets was also determined. ZnO has polar surfaces, such as ±(0001) and ±(101), and non-polar surfaces, such as ±(100) and ±(110). In catalytic growth, the growth directions can be along the polar and non-polar surfaces. For the 50-W ZnO and 100-W ZnO samples, the surface of most of the nanosheets is the non-polar surface (110). Figure 6.66(d) shows a high-resolution TEM image (HRTEM) taken from a nanosheet. The inset is a convergent-beam electron diffraction (CBED) pattern taken from the same area. Both the CBED pattern and HRTEM image indicate that the surface is the (110) non-polar surface.

Cross-sectional TEM samples also revealed that the 50-W ZnO and 100-W ZnO samples are porous [217].

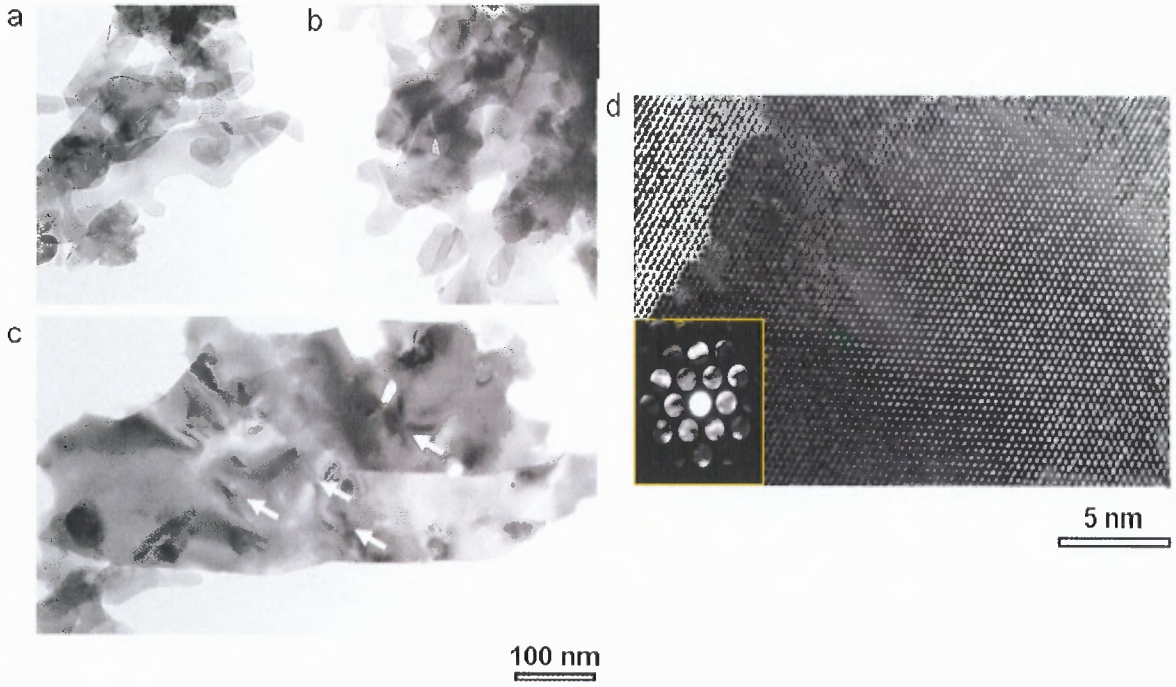

Figure 6.66 TEM images of the nanocoral structures. (a and b) Typical TEM BF images taken from 50-W ZnO and 100-W ZnO, showing nanosheets or nanoleaves. (c) Typical large-size nanosheets or nanoleaves, (d) HRTEM image from a nanosheet in 100-W ZnO. The inset is a CBED pattern taken from the same area. These images indicate that the surface of the nanosheet is a non-polar (110) surface [217].

The above SEM and TEM images show that 50-W ZnO and 100-W ZnO samples both have nanocoral structures. These samples should exhibit enhanced PEC performance as compared to the normal compact ZnO thin films. The 50-W ZnO sample has smaller nanosheets, larger surface area, and better crystallinity than the 100-W ZnO sample. Thus, the 50-W ZnO sample is expected to exhibit better PEC performance than 100-W ZnO. These expectations have been confirmed by PEC response tests on various ZnO film morphologies. Figures 6.67(a)-6.67(c) show the photocurrent-voltage curves for the 50-W, 100-W, and 150-W ZnO films, respectively, under chopped light illumination with

an UV/IR filter (see Methods). A 0.5-M Na_2SO_4 aqueous solution with a pH of 6.8 was used as the electrolyte. All of the samples showed very small dark currents up to a potential of 1.3 V, indicating that the photocurrents under light-on conditions are generated only by absorbed photons without a dark-current contribution.

To compare the PEC responses, the photocurrents for all samples at 1.2 V were plotted, as in Figure 6.67(d). For comparison, the PEC responses of compact ZnO films are also plotted in the figure. Because all the films have similar thicknesses, the photocurrents can be compared. Clearly, the nanoparticle film (35-W ZnO) and the nanocoral films (50-W ZnO and 100-W ZnO) exhibited higher PEC responses than compact ZnO films. Among them, the 50-W ZnO nanocoral film exhibited the best PEC response and its photocurrent at 1.2 V is ten times higher than that of the compact ZnO films. On the other hand, the 150-W and 200-W ZnO films showed much lower PEC responses than the ZnO coral nanostructures. The insets in Figures 6.67(a)-6.67(c) show the current transients, performed at constant 1.2 V under light on/off illumination. The photocurrents of the ZnO nanocoral structures decay very sharply without exhibiting photocurrent tails under light-off conditions.

However, the photocurrents for the nanocrystalline ZnO structures (150-W ZnO) decays slowly, showing photocurrent tails, which indicates a trap-related carrier transport process [211, 220-222]. This suggests that the ZnO nanocoral films have much better carrier transport than the nanocrystalline structures. This can be attributed to the deformation-free nature and smooth electrical pathway as shown in the SEM and TEM results. The 35-W ZnO nanocoral structure exhibited a lower PEC response than the other nanocoral structures, indicating that the surface area of the nanoparticle films is not as

large as the nanocoral films. The comparative PEC performance tests have been repeated over many runs, and the results are reproducible. The greatly enhanced PEC response of the 50-W ZnO nanocoral film suggests that the nanocoral structure has advantages for PEC applications such as water splitting by sunlight, dye-sensitized solar cells, and Li batteries [217].

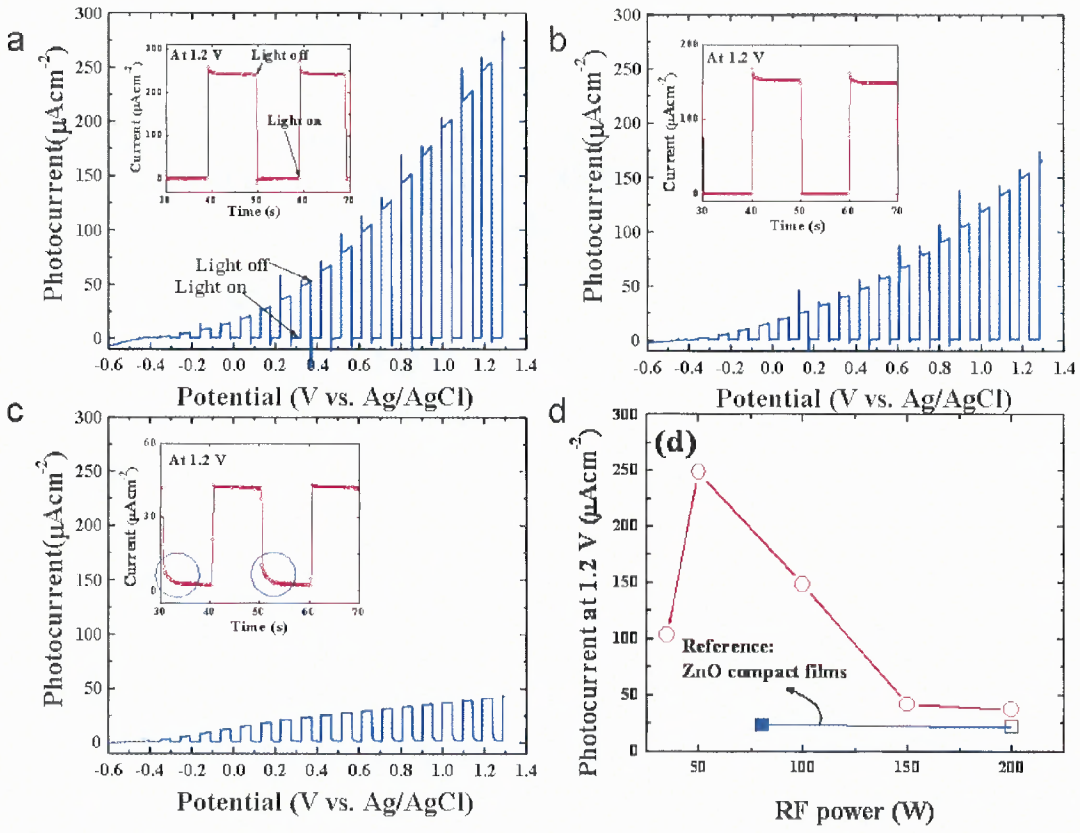

Figure 6.67 PEC performances of various ZnO films. (a, b, and c) Photocurrent-voltage curves of the 50-W, 100-W, and 150-W ZnO nanostructural films, respectively, measured under chopped light illumination with an UV/IR cut-off filter. Insets are the current transient with time performed at 1.2 V under the light on/off illumination. (d) Photocurrents of different ZnO films measured at 1.2 V. Ten times increase on the photocurrent at this potential is demonstrated for the 50-W ZnO nanocoral structure as compared to the conventional compact ZnO films [217].

6.11 Synthesis and Characterization of ZnO:N Films Using ZnO Target

Synthesis and characterization of ZnO:N films sputtered using ZnO target is the subject of this part of the research. ZnO:N thin films were synthesized using a ZnO target by reactive RF magnetron sputtering in mixed N_2 and O_2 ambient with low O_2 mass flow rate [$(O_2/(N_2+O_2)) = 10\%$].

Figure 6.68 shows the XRD curves of ZnO, and ZnO:N films grown at different RF powers in mixed N_2 and O_2 ambient with O_2 mass flow rate of 10%. It is seen that the ZnO film exhibits poor crystallinity due to the low-temperature sputtering process. The ZnO:N film grown at 100 W showed better crystallinity than the pure ZnO film, despite a faster deposition rate. For ZnO growth, the ambient is pure Ar gas. For ZnO:N growth, the ambient is mainly N_2 with only 10% O_2. When the RF power was increased to 200 and 300 W, the crystallinity again became poor. The ZnO:N films deposited at higher RF power grew faster compared to the deposition rate observed during 100-W deposition. The concentrations of N in 100, 200, and 300 W samples were about 1, 1, and 2 at.%, respectively, as determined by XPS. It is known that a high concentration of dopant can deteriorate crystal structure. However, poor crystallinity of the ZnO:N film grown at 200 and 300 W may be caused mainly by the high deposition rate. Crystallite sizes were about 21, 42, 34, and 35 nm for the ZnO, ZnO:N(100W), ZnO:N(200W), and ZnO:N(300W) samples, respectively, which were estimated by applying the Debye-Scherrer equation to XRD data [223].

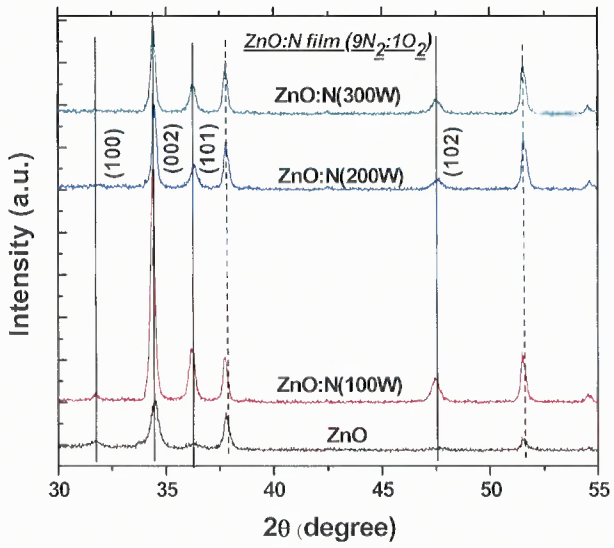

Figure 6.68 X-ray diffraction curves of ZnO, and ZnO:N films grown at different RF powers in mixed N_2 and O_2 ambient with O_2 mass flow rate of 10% [223].

Figure 6.69(a) shows the optical absorption spectra of the ZnO and ZnO:N films grown at different RF powers. The ZnO films showed optical absorption spectra and could only absorb light with wavelengths below 450 nm, due to their wide bandgap. However, the ZnO:N film could absorb lower-energy photons, up to 1000 nm, indicating the N incorporation in ZnO. Figure 6.69(b) shows the optical absorption coefficients of the ZnO and ZnO:N films grown at different RF powers. The direct electron transition from valence to conduction bands was assumed for the absorption coefficient curves, because ZnO films are known to be direct-bandgap materials. The optical bandgaps of the films were determined by extrapolating the linear portion of each curve. The bandgap of the ZnO film is 3.26 eV. The direct optical bandgaps measured for ZnO:N films deposited at a substrate temperature of 100°C, for 100 to 300 W, gradually decreased from 3.2 to 3.15 eV. This small bandgap reduction is due to N-induced upshifting of the valance band. It is shown theoretically that the incorporated N would generate an impurity band above the valance band [223].

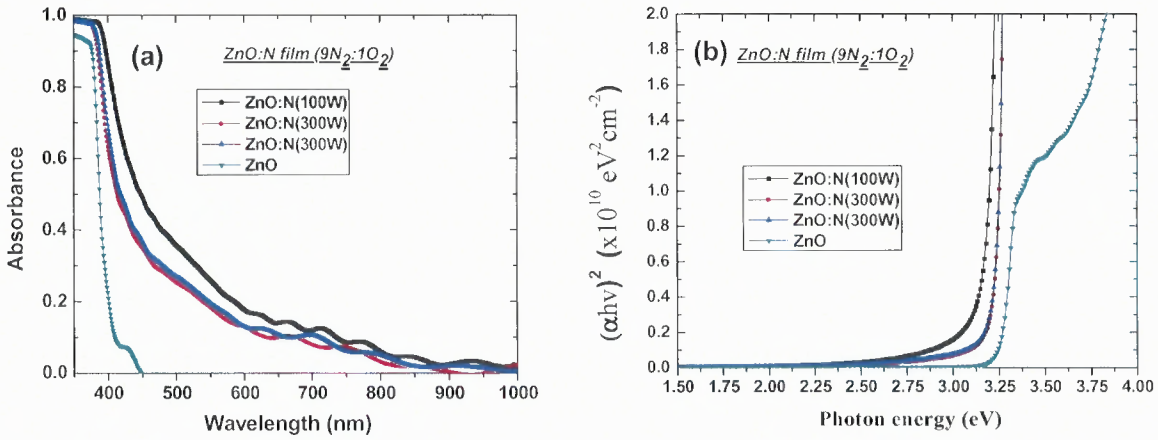

Figure 6.69 (a) Optical absorption spectra of the ZnO and ZnO:N films grown at different RF powers. (b) Optical absorption coefficients of the ZnO and ZnO:N films grown at different RF powers [223].

Figure 6.70 shows Mott-Schottky plots of ZnO:N thin films. All the samples exhibited positive slopes, indicating n-type semiconductors. As reported in earlier sections, ZnO:N films deposited under a N_2/O_2 plasma showed n-type behaviors due to substitutional N_2 molecules, which act as shallow double-donors [223].

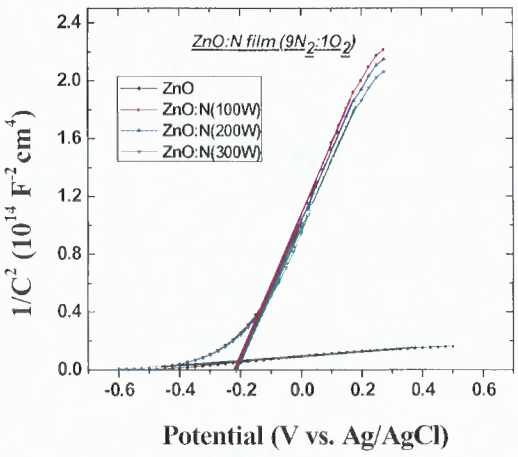

Figure 6.70 Mott-Schottky plots of ZnO:N [223].

Figure 6.71(a) shows the photocurrent-voltage curves of ZnO:N thin films under illumination with the UV/IR filter. It clearly showed that the ZnO:N films exhibited very small photocurrents. At the potential of 1.2 V, the photocurrents were 11.6, 15.14, 13.09, and 12.1 μAcm^{-2} for the ZnO, 100-W, 200-W, and 300-W ZnO:N films, respectively. To investigate the photoresponses in the long-wavelength region, a green-color filter (wavelength: 538.33 nm; FWHM: 77.478 nm) was used in combination with the UV/IR filter, as shown in Figure 6.71(b). The ZnO and ZnO:N films exhibited no clear photoresponse, due to the wide bandgap and very low concentration of N incorporation. This indicates that a very high recombination rate of the photogenerated electrons and holes is present in the ZnO:N film because of its inferior crystallinity and uncompensated charges [223].

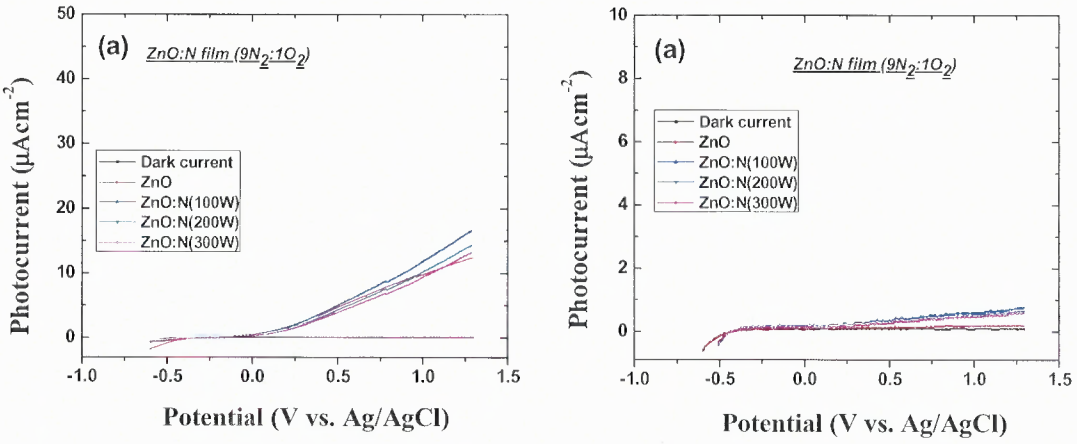

Figure 6.71 (a) The photocurrent-voltage curves of ZnO:N thin films, under illumination with the UV/IR filter. (b) The photocurrent-voltage curves of ZnO:N thin films, under illumination with the combined green and UV/IR filters [223].

6.12 Synthesis and Characterization of Al and N Co-Doped ZnO Films

Synthesis and characterization of ZnO:(Al,N) films is the subject of this part of the research. ZnO:(Al,N) thin films were synthesized using a ZnO target by reactive RF magnetron sputtering in mixed N_2 and O_2 ambient with low O_2 mass flow rate [$(O_2/(N_2+O_2))$ = 10% and 25%].

Figure 6.72 shows the XRD curves of ZnO, ZnO:Al deposited at 300 W and ZnO:(Al,N)(2) films grown at different RF powers in mixed N_2 and O_2 ambient with O_2 mass flow rate of 10%. It is seen that the ZnO:Al film exhibits poor crystallinity, which may be due to the low-temperature and high-RF sputtering process combined with pure Ar gas ambient. The ZnO:(Al,N)(2) film grown at 100 W shows better crystallinity than the ZnO, and ZnO:Al films, despite faster deposition rate. For pure ZnO growth, the ambient is Ar gas. For ZnO:(Al,N)(2) growth, the ambient is mainly N_2 with only 10% O_2. When the RF power was increased to 200 and 300W, the crystallinity surprisingly increased, yet with significant incorporation of N. Such significantly enhanced crystallinity is attributed to the charge-compensated donor-acceptor co-doping, because co-doping reduces the formation energy, which enhances the N incorporation in the film. As the RF power is increased from 100 to 300 W, N incorporation in the film is increased. The concentrations of N in 100-W, 200-W, and 300-W samples were about 2, 4, and 5 at.%, respectively, as determined by XPS. Applying the Debye-Scherrer equation to XRD data, crystallite sizes were 21, 24, 32, 35, and 39 nm for the ZnO, ZnO:Al, ZnO:(Al,N)(2)(100W), ZnO:(Al,N)(2) (200W), and ZnO:(Al,N)(2) (300W) samples, respectively [223].

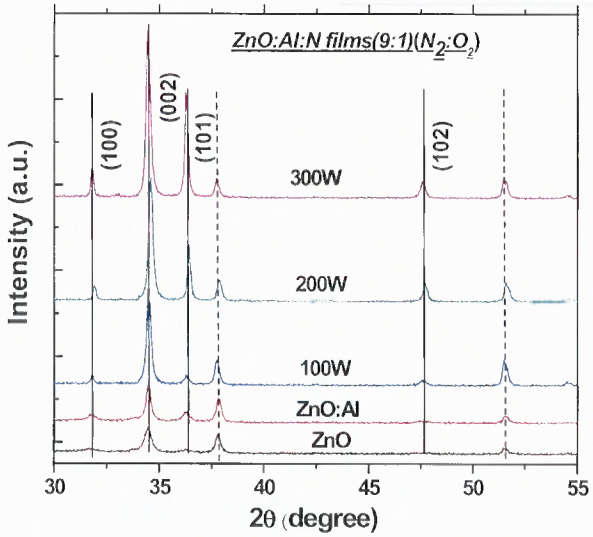

Figure 6.72 X-ray diffraction curves of ZnO, ZnO:Al deposited at 300 W, and ZnO:(Al,N)(2) films grown at different RF powers in mixed N_2 and O_2 ambient with O_2 mass flow rate of 10% [223].

Figure 6.73(a) shows the optical absorption spectra of the ZnO, ZnO:Al, and ZnO:(Al,N)(2) films grown at different RF powers. The ZnO and ZnO:Al films showed optical absorption spectra and could absorb only light with wavelengths below 450 nm, due to their wide bandgap. However, the ZnO:(Al,N)(2) films showed optical absorption that moved to the shorter-wavelength region, indicating a significant amount of N incorporation in the films. The optical absorption coefficients of the ZnO, ZnO:Al, and ZnO:(Al,N)(2) films grown at different RF powers are shown in Figure 6.76(b). The bandgap of the ZnO:Al film is 3.35 eV. The direct optical bandgaps measured for ZnO:(Al,N)(2) films at 100 to 300 W reduced drastically from 3.13 to 2.02 eV. This significant bandgap reduction is due to enhanced N incorporated in the films [223].

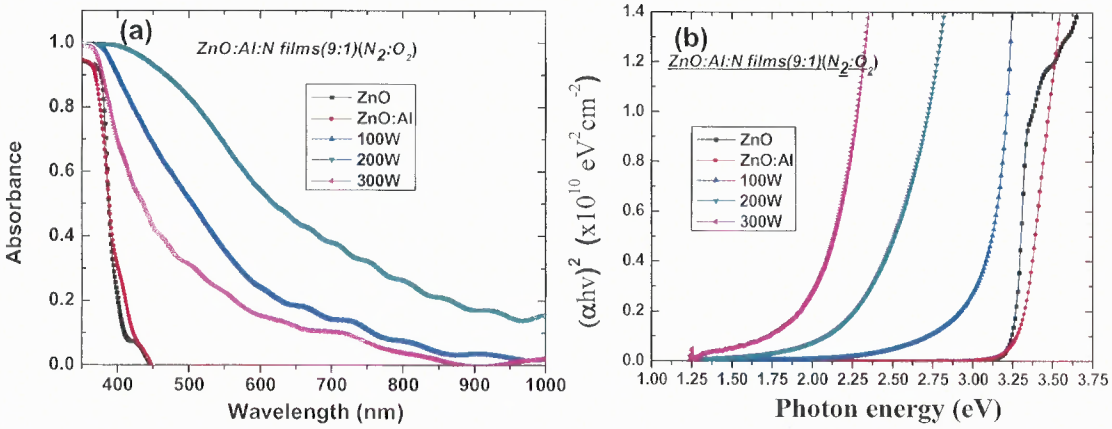

Figure 6.73 (a) Optical absorption spectra of the ZnO, Zno:Al and ZnO:(Al,N)(2) films grown at different RF powers. (b) The optical absorption coefficients of the ZnO, ZnO:Al, and ZnO:(Al,N)(2) films grown at different RF powers [223].

Figure 6.74 shows the XRD curves of ZnO, ZnO:Al deposited at 300 W, and ZnO:(Al,N)(3) films grown at different RF powers in mixed N_2 and O_2 ambient with O_2 mass flow rate of 25%. Clearly, as the RF power is increased from 100 to 300 W, crystallinity is greatly enhanced. Applying the Debye-Scherrer equation to our XRD data, crystallite sizes were 21, 24, 28, 35, and 44 nm for the ZnO, ZnO:Al, ZnO:(Al,N)(2)(100W), ZnO:(Al,N)(2) (200W), and ZnO:(Al,N)(2) (300W) samples, respectively. However, an insignificant amount of N is incorporated in the ZnO:(Al,N)(3) film grown at 100 W, confirmed by XPS, indicating that RF power was not enough to activate the N source. As the RF power is increased to 200 and 300 W, incorporation of N is increased, indicating that there should be minimum RF power needed to dissociate the N_2 molecules. The concentrations of N in 100-W, 200-W, and 300-W samples were about 1, 2, and 3 at.%, respectively, as determined by XPS. Compared to ZnO:(Al,N)(2) films grown in mixed N_2 and O_2 ambient with O_2 mass flow rate of 10% , ZnO:(Al,N)(3) thin films deposited in mixed N_2 and O_2 ambient with O_2 mass flow rate of 25% showed

comparatively less N incorporation at respective RF power. These results make it clear that with limited oxygen pressure, N incorporation in ZnO thin films can be controlled by varying the RF power during sputtering and charge-compensated donor-acceptor doping [223].

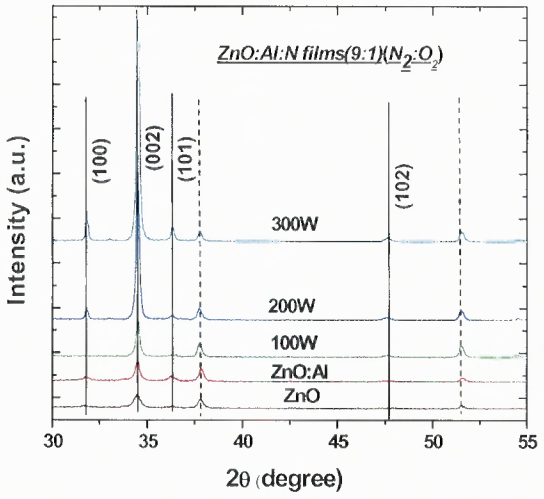

Figure 6.74 X-ray diffraction curves of ZnO, ZnO:Al deposited at 300 W and ZnO:(Al,N)(3) films grown at different RF powers in mixed N_2 and O_2 ambient with O_2 mass flow rate of 25% [223].

Figure 6.75 shows the optical absorption coefficient of the ZnO, ZnO:Al, and ZnO:(Al,N)(3) films grown at different RF powers. The direct optical bandgaps measured for ZnO:(Al,N)(3) films at 200 and 300 W are 3.13 and 2.9 eV, respectively [223].

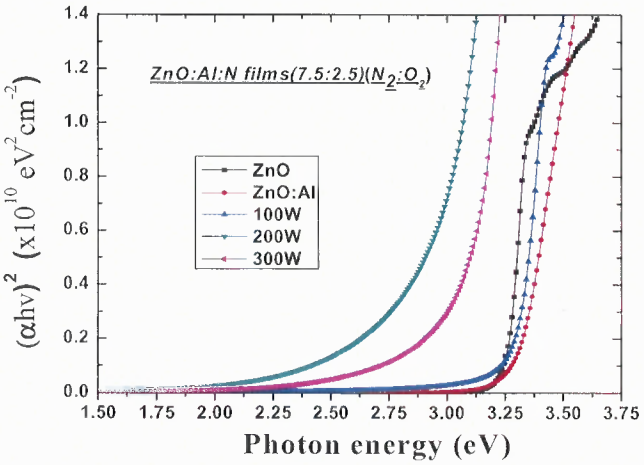

Figure 6.75 The optical absorption coefficient of the ZnO, ZnO:Al, and ZnO:(Al,N)(3) films grown at different RF powers [223].

Figures 6.76(a) and 6.76(b) show Mott-Schottky plots of ZnO:(Al,N)(2) and ZnO:(Al,N)(3) thin films, respectively. All the samples exhibited positive slopes, indicating n-type semiconductors. As reported in earlier sections, ZnO:N films deposited under a N_2/O_2 plasma showed n-type behavior due to substitutional N_2 molecules, which act as shallow double-donors [223].

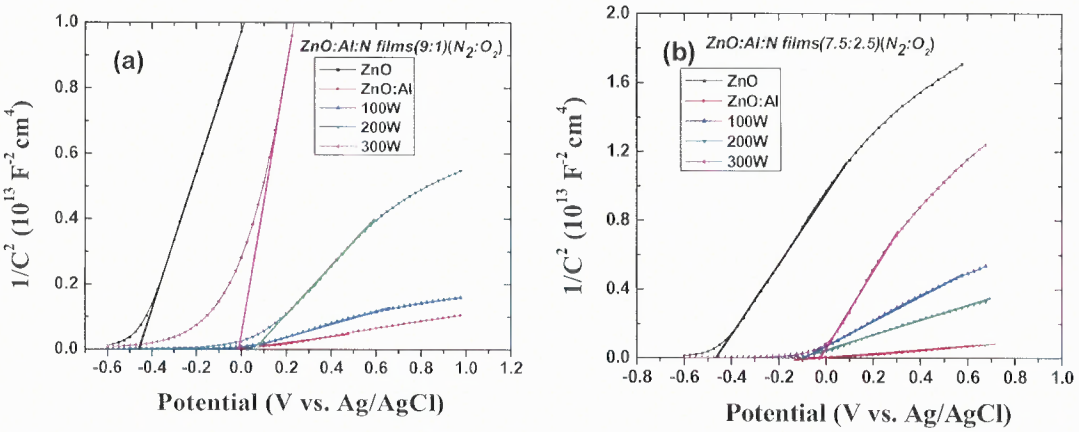

Figure 6.76 (a) Mott-Schottky plots of (a) ZnO:(Al,N)(2) and (b) ZnO:(Al,N)(3) thin films [223].

Figures 6.77(a) and 6.77(b) show the photocurrent-voltage curves of ZnO:(Al,N)(2) and ZnO:(Al,N)(3) thin films, respectively, under illumination with the UV/IR filter. Clearly, the ZnO:Al:N(2) films exhibited enhanced photocurrents compared to the ZnO:(Al,N)(3) films. At a potential of 1.2 V, the photocurrents were 14.6, 29.2, 40.1, and 54.3 μAcm^{-2} for the ZnO:Al, 100-W, 200-W, and 300-W ZnO:(Al,N)(2) films, respectively. At a potential of 1.2 V, the photocurrents were 23.77, 33.64, and 35.66 μAcm^{-2} for the 100-W, 200-W, and 300-W ZnO:(Al,N)(3) films, respectively [223].

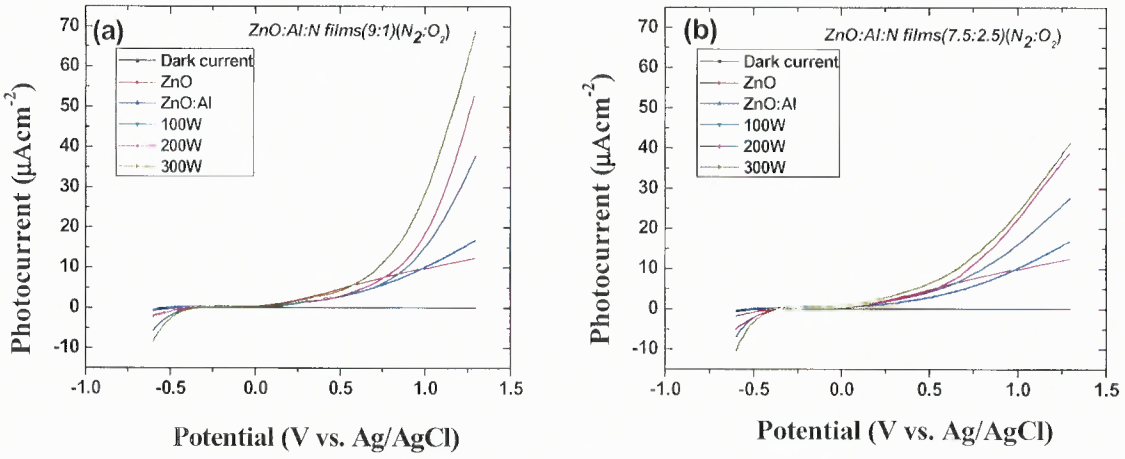

Figure 6.77 (a) The photocurrent-voltage curves of (a) ZnO:(Al,N)(2), and (b) ZnO:(Al,N)(3) thin films, under illumination with the UV/IR filter [223].

To investigate the photoresponse in the long-wavelength region, a green-color filter (wavelength: 538.33 nm; FWHM: 77.478 nm) was used with the UV/IR filter, as shown in Figures 6.78(a) and 6.78(b). The ZnO and ZnO:Al films exhibited no clear photoresponse, due to its wide bandgap. The co-doped ZnO:(Al,N) films exhibited much higher photocurrent than the ZnO and ZnO:Al films, despite much less light absorption. This indicates that a very high recombination rate of the photogenerated electrons and holes is present in the ZnO and ZnO:Al films, due to inferior crystallinity and

uncompensated charges. On the other hand, the co-doped ZnO:(Al,N) film exhibited remarkably increased crystallinity and charge compensation, which led to enhanced photocurrent compared to the ZnO and ZnO:Al films. The results clearly demonstrate that significantly reduced bandgap and enhanced photocurrents can be obtained with low O pressure by varying the RF power during sputtering and charge-compensated donor-acceptor doping approach [223].

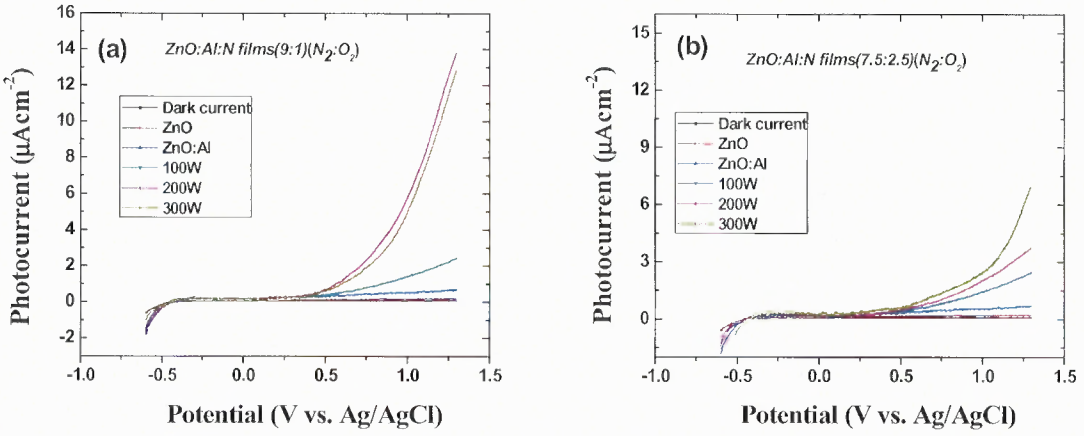

Figure 6.78 The photocurrent-voltage curves of (a) ZnO:(Al,N)(2), and (b) ZnO:(Al,N)(3) thin films, under illumination with the combined green and UV/IR filters [223].

6.13 Effect of Gas Ambient on Synthesis of Al and N Co-Doped ZnO Films

In this part of the research, effects of gas ambient on the synthesis of Al and N co-doped ZnO films are presented. The co-doped ZnO:(Al,N) thin films are synthesized by RF magnetron sputtering in mixed Ar and N_2 and mixed O_2 and N_2 gas ambient at 100°C, followed by post-annealing at 500°C in air for 2 hours.

Figure 6.79 shows the XRD curves of ZnO grown in Ar ambient and ZnO:(Al,N)(Ar/N_2) grown in mixed Ar and N_2 gas ambient with N_2 mass flow rate of

25% to 75%. Dotted lines in the XRD plots indicate substrate peaks. The ZnO film exhibits poor crystallinity because of the low-temperature sputtering process. The ZnO:(Al,N)(Ar/N_2) films showed better crystallinity than the ZnO film. The mixed N_2 and Ar gas ambient should be the reason for enhanced crystallinity [224].

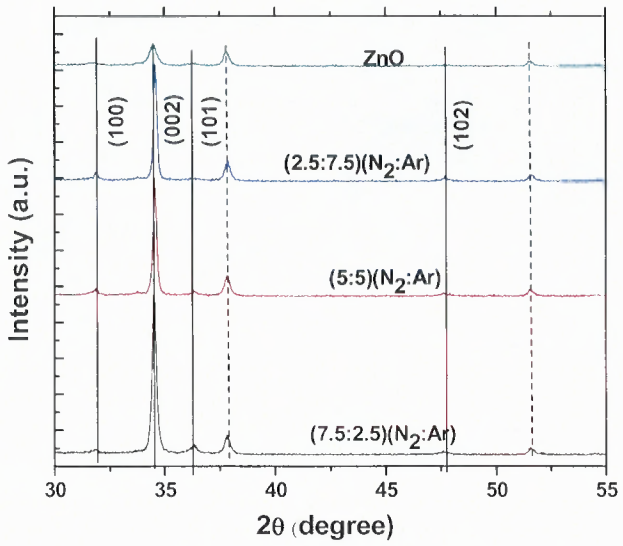

Figure 6.79 X-ray diffraction curves of ZnO, and ZnO:(Al,N)(Ar/N_2) films grown at 200 W in Ar and mixed Ar and N_2 gas ambient with N_2 mass flow rate of 25% to 75%, respectively [224].

No significant change in crystallinity is observed by varying the N_2 mass flow rate from 25% to 75%. One would expect that the incorporated N concentration should increase as the N_2 mass flow rate increases. This may be because no significant N concentration is incorporated in the film. It is known that a high concentration of dopant can deteriorate crystal structure. However, applying the Debye-Scherrer equation to our XRD data, crystallite sizes were 21, 30, 32, and 37 nm for the ZnO, ZnO:(Al,N)(Ar/N_2) films for 25%, 50%, and 75% N_2 mass flow rate, respectively. These indicate that N may not be incorporated in ZnO even when the samples were deposited in mixed Ar and N gas

ambient. Indeed, XPS measurements confirmed that no detectable N concentrations were found in these ZnO:(Al,N)(Ar/N_2) films [224].

Figure 6.80 shows the optical absorption coefficients of the ZnO and ZnO:(Al,N)(Ar/N_2) films. The direct electron transition from valence to conduction bands was assumed for the absorption coefficient curves because ZnO has a direct bandgap [24, 25]. The optical bandgaps of the films were determined by extrapolating the linear portion of each curve. The bandgap of the ZnO film is 3.25 eV, which is consistent with the results reported elsewhere. The direct optical bandgaps measured for ZnO:(Al,N)(Ar/N_2) films with N_2 mass flow rate of 25%, 50%, and 75% are about 3.28, 3.32, and 3.35 eV, respectively, which, surprisingly, are larger than that of ZnO. These bandgap differences can be understood by the crystallinity of the samples. ZnO has the lowest crystallinity, meaning that it has point defects, such as oxygen vacancies. The presence of these defects introduces impurity bands and leads to a reduced bandgap compared to high-purity ZnO. When the N_2 mass flow rate increased from 25% to 50% to 75%, the crystallinity of ZnO:(Al,N)(Ar/N_2) films increased, as indicated by XRD curves; this means decreased defect concentration. Furthermore, no N was incorporated. Thus, the bandgaps of ZnO:(Al,N)(Ar/N_2) films are generally larger than that of the ZnO grown in pure Ar ambient and the bandgap increased as the N_2 mass flow rate increased [224].

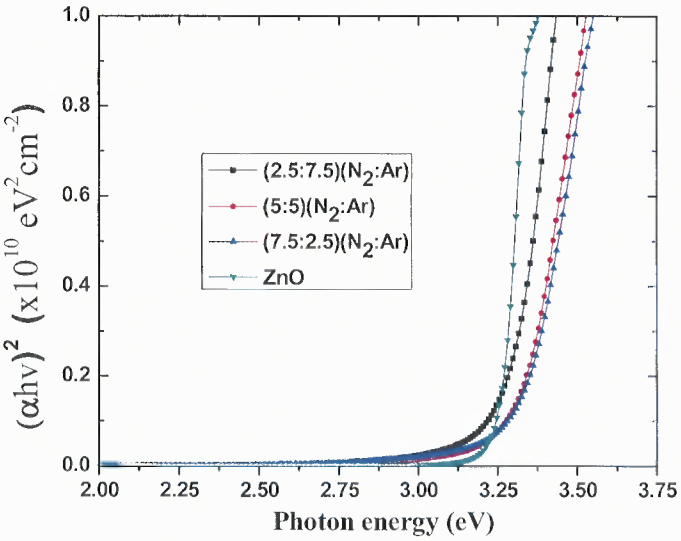

Figure 6.80 The optical absorption coefficients of the ZnO and ZnO:(Al,N)(Ar/N_2) films grown at 200 W in Ar and mixed Ar and N_2 gas ambient with N_2 mass flow rate of 25% to 75% [224].

Figure 6.81(a) shows Mott-Schottky plots of the ZnO and ZnO:(Al,N)(Ar/N_2) films. All the samples exhibited positive slopes, indicating n-type behaviors. It is known from earlier reports that ZnO and Al-doped ZnO films are n-type semiconductors. The photocurrent-voltage curves of the ZnO and ZnO:(Al,N)(Ar/N_2) films, under illumination with the UV/IR filter, are shown in Figure 6.81(b). It showed clearly that the ZnO:(Al,N)(Ar/N_2) films exhibited enhanced photocurrents, as compared to the ZnO film. The enhanced photocurrent should be due to the increased crystallinity of ZnO:(Al,N)(Ar/N_2) films. At a potential of 1.2 V, the photocurrents were 3.5, 8.5, 14.56, and 18.7 μAcm^{-2} for the ZnO, ZnO:(Al,N)(Ar/N_2) films with 25%, 50%, and 75% N_2 mass flow rates, respectively. To investigate the photoresponses in the long-wavelength region, a green-color filter (wavelength: 538.33 nm; FWHM: 77.478 nm) was used with the UV/IR filter.

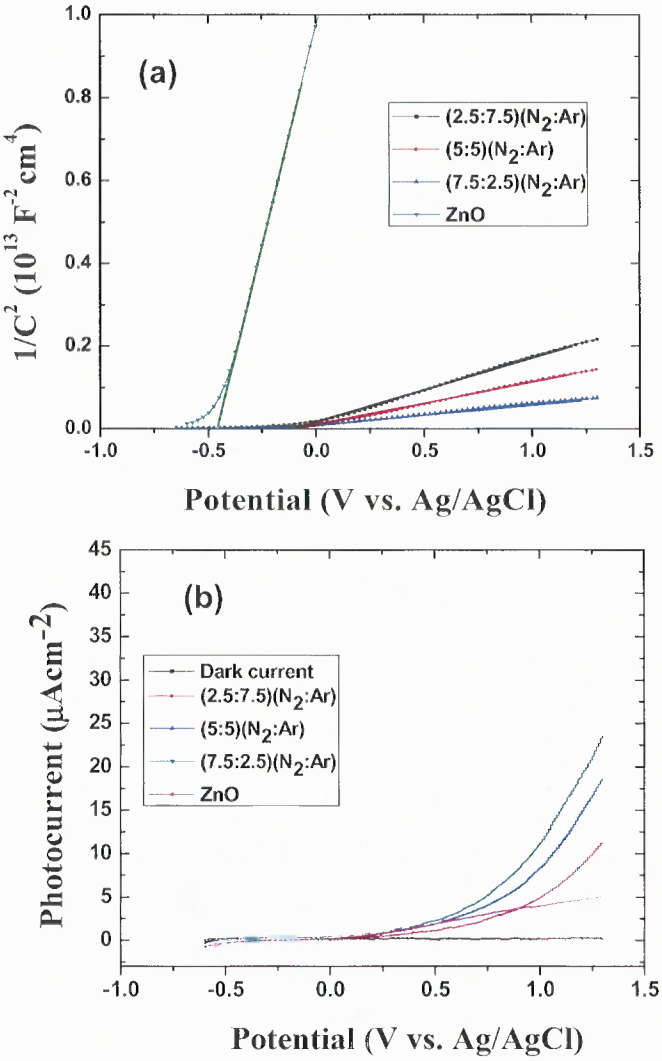

Figure 6.81 (a) Mott-Schottky plots of the ZnO and ZnO:(Al,N)(Ar/N_2) films grown at 200 W in Ar and mixed Ar and N_2 gas ambient with N_2 mass flow rate of 25% to 75%. (b) Photocurrent-voltage curves of the ZnO and ZnO:(Al,N)(Ar/N_2) films under illumination with the UV/IR filter [224].

The ZnO and ZnO:(Al,N)(Ar/N_2) films exhibited no clear photoresponse, as shown in Figure 6.82, confirming that no detectable N was incorporated. The modest photocurrents achieved in ZnO and ZnO:(Al,N)(Ar/N_2) films are because of its wide

bandgap, which limits absorption to UV light only. It is clear that the mixed Ar and N_2 gas ambient did not promote N incorporation [224].

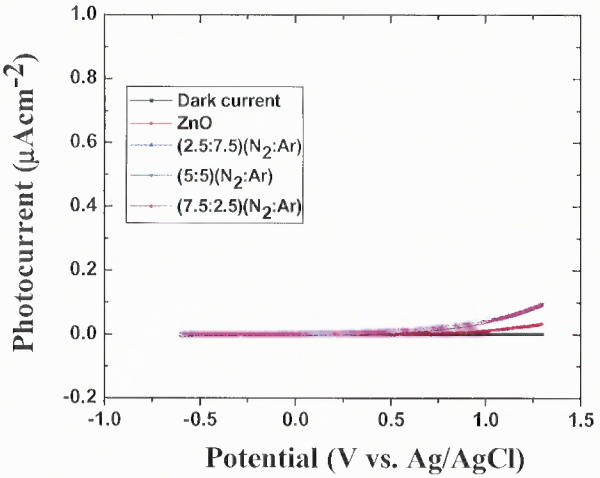

Figure 6.82 Photocurrent-voltage curves of the ZnO, ZnO:Al, and ZnO:(Al,N)(Ar/N_2) films under the illumination with the combined green and UV/IR filters [224].

However, when the growth ambient was changed to mixed O_2 and N_2 (second set of samples), N incorporation was observed. Figure 6.83 shows the XRD curves of ZnO:Al, grown in Ar ambient and ZnO:(Al,N)(O_2/N_2) films in mixed O_2 and N_2 gas ambient with N_2 mass flow rate of 25%, 50%, and 75%. Dotted lines in the XRD plots indicate substrate peaks. It is seen that the ZnO:Al film exhibits poor crystallinity because of the low temperature and pure Ar gas ambient. The ZnO:(Al,N)(O_2/N_2) films show better crystallinity than that of ZnO and ZnO:Al films. The enhancement of crystallinity is attributed to both charge-compensated donor-acceptor co-doping and the mixed O_2 and N_2 gas ambient. We found that the co-doping enhanced the N incorporation in the ZnO:(Al,N)(O_2/N_2) film. The concentrations of N in ZnO:(Al,N)(O_2/N_2) films for 25%, 50%, and 75% N_2 mass flow rate were about 1, 1.6, and 3 at.%, respectively, as determined by XPS. Applying the Debye-Scherrer equation to our XRD data, crystallite

sizes were 21, 24, 33, 35, and 40 nm for the ZnO, ZnO:Al, ZnO:(Al,N)(O_2/N_2) films for 25%, 50%, and 75% N_2 mass flow rate, respectively [224].

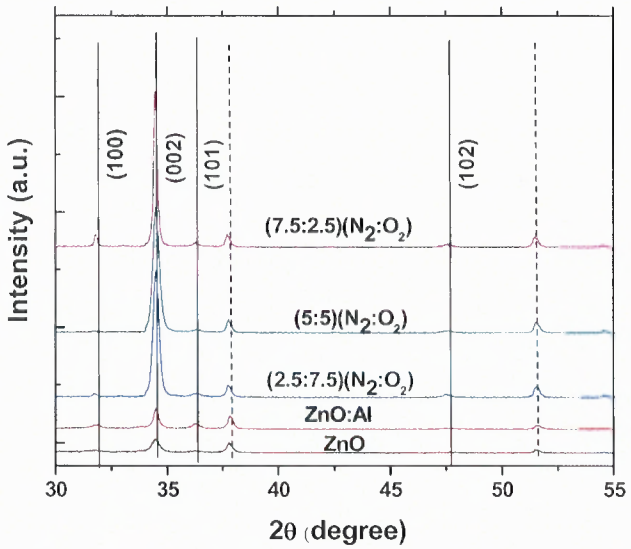

Figure 6.83 X-ray diffraction curves of X-ray diffraction curves of ZnO, ZnO:Al, and ZnO:(Al,N)(O_2/N_2) films grown at 200 W in O_2 and mixed O_2 and N_2 gas ambient with N_2 mass flow rate of 25% to 75%, respectively [224].

Figure 6.84(a) shows the optical absorption spectra of the ZnO, ZnO:Al, and ZnO:(Al,N)(O_2/N_2) films. The ZnO and ZnO:Al films showed optical absorption spectra and could only absorb light with wavelengths below 450 nm, due to their wide bandgap. However, the ZnO:(Al,N)(O_2/N_2) films showed optical absorption in the longer-wavelength region, indicating that a significant amount of N has been incorporated into these samples. The optical absorption coefficients of the ZnO, ZnO:Al, and ZnO:(Al,N)(O_2/N_2) films are shown in Figure 6(b). The bandgap of the ZnO:Al film is 3.35 eV, which is consistent with the results reported elsewhere. The direct optical bandgaps measured for ZnO:(Al,N)(O_2/N_2) films for N_2 mass flow rate from 25% to 75% gradually decreased from 3.13 to 2.85 eV. This reduction in bandgap is due to N-induced

upshifting of the VBM. It is shown theoretically that the incorporated N would generate an impurity band above the VBM.

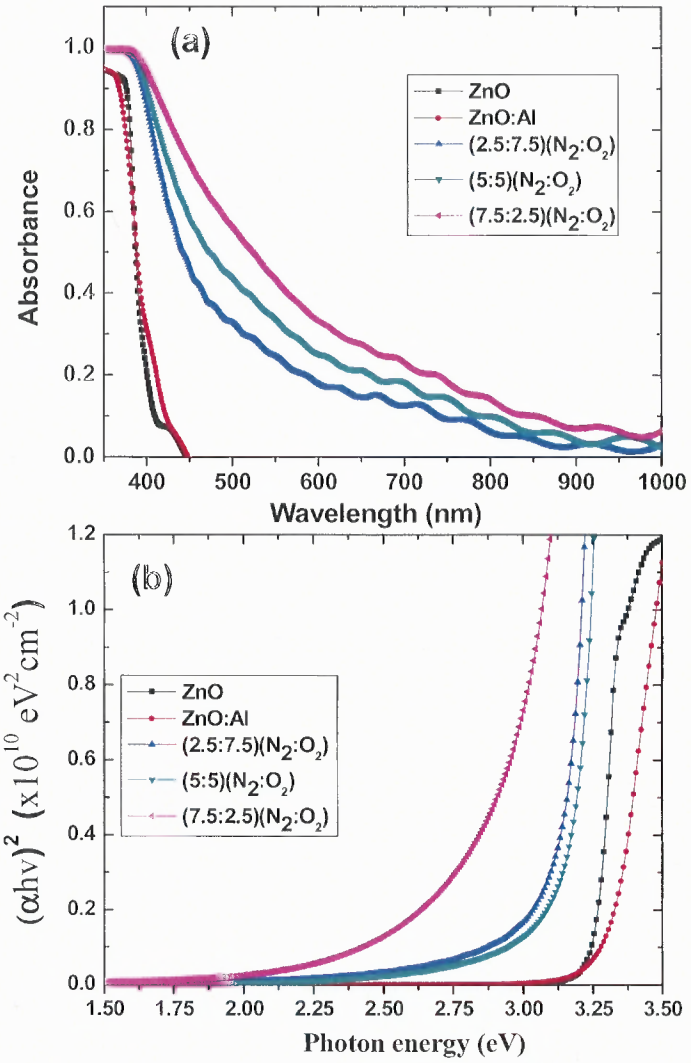

Figure 6.84 (a) Optical absorption curves of ZnO, ZnO:Al, and ZnO:(Al,N)(O_2/N_2) films grown at 200 W in O_2 and mixed O_2 and N_2 gas ambient with N_2 mass flow rate of 25% to 75%, respectively. (b) The optical absorption coefficients of the ZnO, ZnO:Al, and ZnO:(Al,N)(O_2/N_2) films grown at 200 W in O_2 and mixed O_2 and N_2 gas ambient with N_2 mass flow rate of 25% to 75% [224].

The absorption from this impurity band cannot be characterized by direct band transitions, and it typically results in an absorption tail in the measured optical absorption curve. Such an absorption tail is clearly evident in Figure 6.84(b) for the co-doped

ZnO:(Al,N)(O_2/N_2) films. This tail can be considered as further bandgap reduction, which enables light-harvesting in the much longer-wavelength regions as compared to the ZnO, ZnO:Al, and ZnO:(Al,N)(Ar/N_2) films [224].

Figure 6.85(a) shows Mott-Schottky plots of the ZnO:Al and ZnO:(Al,N)(O_2/N_2) films. All the samples exhibited positive slopes, indicating n-type semiconductors. Previous studies report that ZnO:N films deposited under a N_2/O_2 plasma had *n*-type behavior due to substitutional N_2 molecules that act as shallow double-donors. In ZnO:(Al,N)(O_2/N_2) films, excess Al can also be the source of donors. The photocurrent-voltage curves of the ZnO, ZnO:Al, and ZnO:(Al,N)(O_2/N_2) films, under illumination with the UV/IR filter, are shown in Figure 6.85(b). It clearly shows that the ZnO:(Al,N)(O_2/N_2) films exhibited enhanced photocurrents, compared to the ZnO, ZnO:Al, and ZnO:(Al,N)(Ar/N_2) films. The enhanced photocurrent can be attributed to the increased crystallinity, enhanced N incorporation, and compensated-charge defects in ZnO:(Al,N)(O_2/N_2) films. At a potential of 1.2 V, the photocurrents were 3.5, 13.24, 21.69, 33.12, and 34.18 μAcm^{-2} for the ZnO, ZnO:Al, and ZnO:(Al,N)(O_2/N_2) films with 25%, 50%, and 75% N_2 mass flow rate, respectively [224]. To investigate the photoresponses in the long-wavelength region, a green-color filter was used in combination with the UV/IR filter, as shown in Figure 6.86.

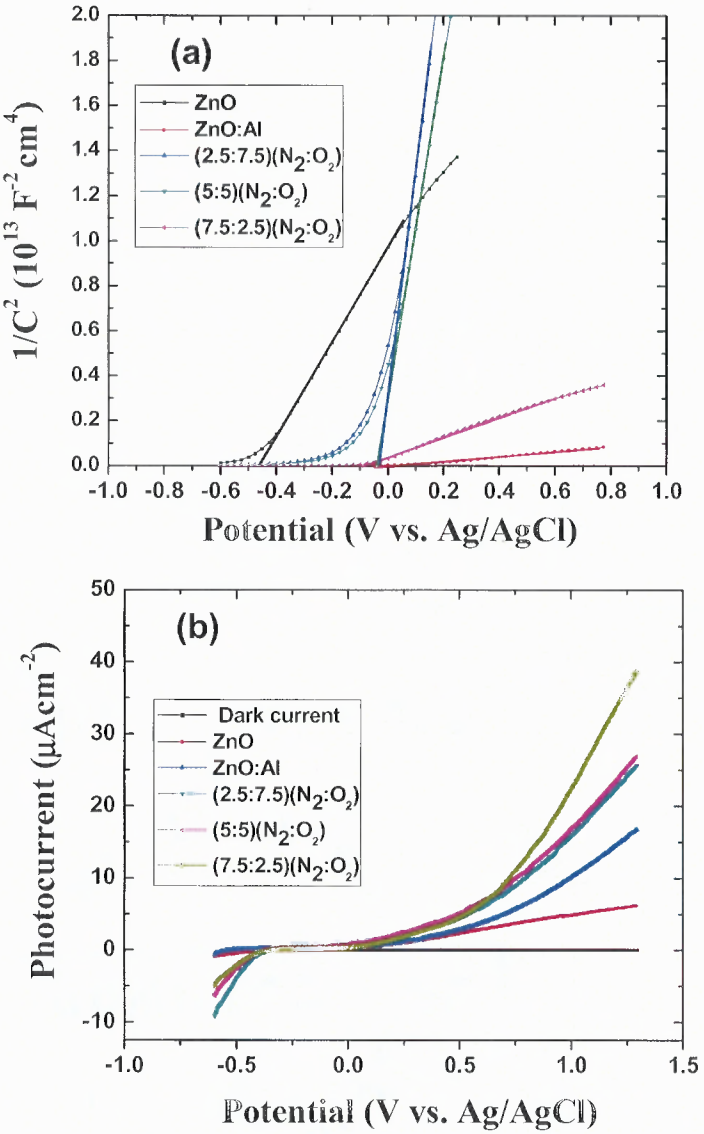

Figure 6.85 (a) Mott-Schottky plots of the ZnO, ZnO:Al, and ZnO:(Al,N)(O_2/N_2) films grown at 200 W in O_2 and mixed O_2 and N_2 gas ambient with N_2 mass flow rate of 25% to 75%. (b) Photocurrent-voltage curves of the ZnO, ZnO:Al, and ZnO:(Al,N)(O_2/N_2) films under the illumination with the UV/IR filter [224].

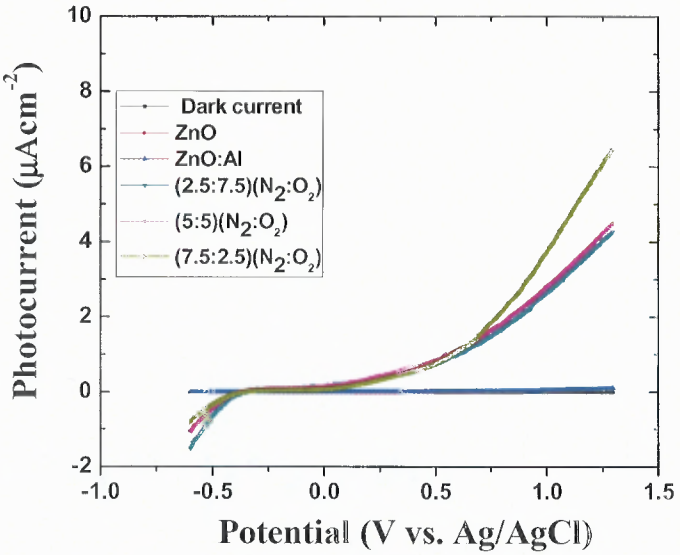

Figure 6.86 Photocurrent-voltage curves of the ZnO, ZnO:Al, and ZnO:(Al,N)(O_2/N_2) films under the illumination with the combined green and UV/IR filters [224].

The ZnO and ZnO:Al films exhibited no clear photoresponse because of their wide bandgap. The co-doped ZnO:(Al,N)(O_2/N_2) films exhibited photocurrents. The results clearly demonstrate that significantly reduced bandgap and enhanced photocurrents can be obtained with mixed O_2 and N_2 gas ambient with varying N_2 mass flow rate and the charge-compensated donor-acceptor co-doping approach [224].

6.14 Synthesis and Characterization of ZnO and GaN Solid-Solution Films

Synthesis and characterization of ZnO and GaN solid-solution films (ZnO:GaN) are reported in this part of the research work. ZnO:GaN solid-solution thin films with significantly reduced bandgaps were synthesized by using ZnO and GaN targets at 100°C, followed by post-deposition annealing at 500°C in ammonia for 4 hours.

Figure 6.87 shows the XRD curves of ZnO, and solid solution of ZnO:GaN thin films grown in Ar and mixed N_2 and O_2 ambient with N_2 mass flow rate of 25% to 75%,

respectively. The ZnO film exhibits poor crystallinity due to the low-temperature sputtering process. The ZnO:GaN solid-solution thin films grown at different N_2 mass flow rates showed better crystallinity than the pure ZnO film, despite faster deposition rate. Lack of significantly enhanced crystallnity for ZnO:GaN solid-solution thin films may be due to high RF power for ZnO target, resulting in faster deposition rate. It is known that a faster deposition rate sometimes deteriorates the crystal structure. As the mass flow rate of N_2 is increased from 25% to 75%, the (002) and (100) peaks are enhanced. Crystallite sizes were about 21, 22, 20, and 26 nm for the ZnO, 25%, 50%, and 75% N_2 mass flow rate for ZnO:GaN solid-solution thin films, respectively, which were estimated by applying the Debye-Scherrer equation to our XRD data. Figures 6.88(a-d) show AFM images from the ZnO, 25%, 50%, and 75% N_2 flow rate for ZnO:GaN solid-solution films. AFM images also confirmed that ZnO, and ZnO:GaN solid-solution films have similar morphology, and average crystal size is increased for ZnO:GaN films compared to ZnO films [225].

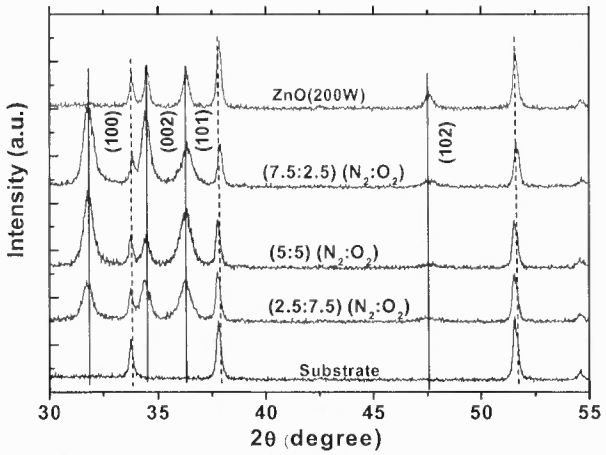

Figure 6.87 The X-ray diffraction curves of ZnO, and solid solution of ZnO:GaN thin films grown in Ar and mixed N_2 and O_2 ambient with N_2 mass flow rate of 25% to 75%, respectively [225].

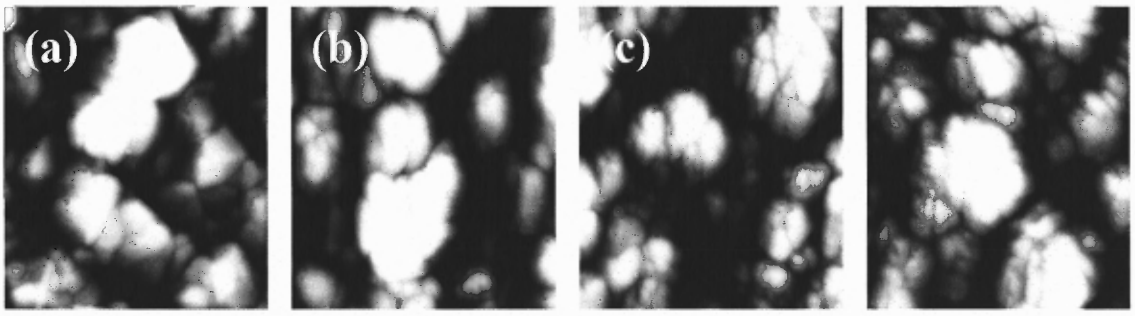

Figure 6.88 AFM images taken from (a) ZnO, (b) 25%, (c) 50%, and (d) 75%, ZnO:GaN solid-solution thin films [225].

Figure 6.89(a) shows the optical absorption spectra of the ZnO, and the solid solution of ZnO:GaN thin films grown in Ar and mixed N_2 and O_2 ambient with N_2 mass flow rate of 25% to 75%, respectively. The ZnO films showed optical absorption spectra and could only absorb light with wavelengths below 550 nm, due to their wide bandgap. However, the ZnO:GaN solid-solution thin films could absorb lower-energy photons, up to 1000 nm, indicating that the solid solution of ZnO and GaN (ZnO:GaN) can be used to shift the optical absorption into the visible region. Figure 6.91(b) shows the optical

absorption coefficients of the ZnO, and the solid solution of ZnO:GaN thin films. The direct electron transition from valence to conduction bands was assumed for the absorption coefficient curves, because ZnO and GaN films are known as direct-bandgap materials. The optical bandgaps of the films were determined by extrapolating the linear portion of each curve. The bandgap of the ZnO film is 3.25 eV. The direct optical bandgaps measured for ZnO:GaN solid-solution thin films deposited at varying N_2 mass flow rate from 25% to 75% gradually decreased from 3.15 to 2.9 eV. This reduction in bandgap is due to N-induced upshifting of the valance band. It is shown theoretically that the bottom of the conduction band for ZnO:GaN is mainly composed of 4s and 4p orbitals of Ga, whereas N2p orbitals are followed by Zn3d orbitals situated on the top of the valence band. The presence of Zn3d and N2p electrons in the upper valence band provides p-d repulsion for the VBM, which results in narrowing of the bandgap. The absorption from this impurity band cannot be characterized by direct band transitions and typically results in an absorption tail in the measured optical absorption curve. Such an absorption tail is clearly evident in Figure 6.89(b) for the ZnO:GaN solid-solution thin films. This tail can be considered further bandgap reduction, which enables light-harvesting in the much longer-wavelength regions compared to the ZnO film [225].

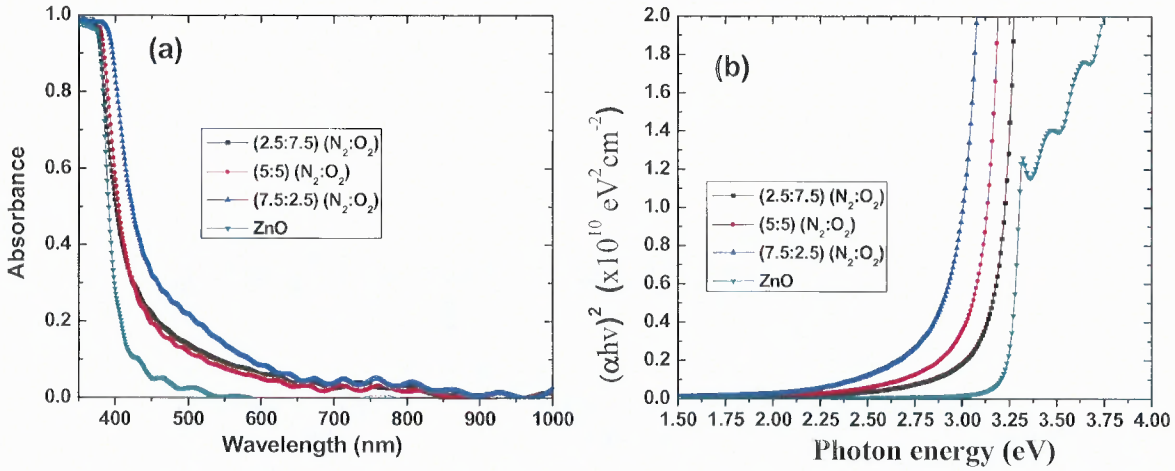

Figure 6.89 (a) The optical absorption spectra of the ZnO, and solid solution of ZnO:GaN thin films grown in Ar and mixed N_2 and O_2 ambient with N_2 mass flow rate of 25% to 75%, respectively. (b) Optical absorption coefficients of the ZnO, and solid solution of ZnO:GaN thin films [225].

Figure 6.90 shows Mott-Schottky plots of ZnO, and solid solution of ZnO:GaN thin films grown in Ar and mixed N_2 and O_2 ambient with N_2 mass flow rate of 25% to 75%, respectively. All the samples exhibited positive slopes, indicating n-type semiconductors [225].

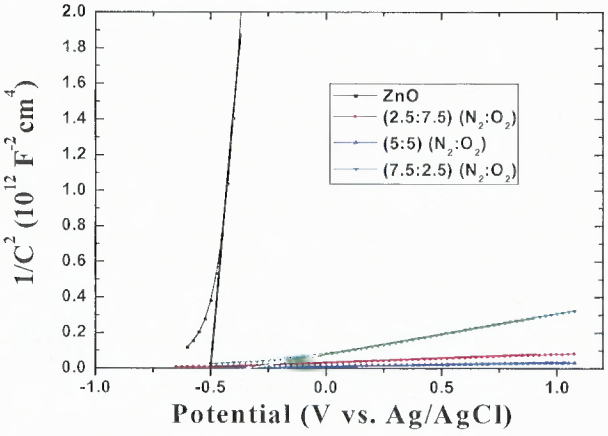

Figure 6.90 The Mott-Schottky plots of ZnO, and solid solution of ZnO:GaN thin films grown in Ar and mixed N_2 and O_2 ambient with N_2 mass flow rate of 25% to 75%, respectively [225].

Figures 6.91(a) and 6.91(b) show the photocurrent-voltage curves of ZnO and the solid solution of ZnO:GaN thin films grown in Ar and mixed N_2 and O_2 ambient with N_2 mass flow rate of 75%, respectively, under light-on/light-off illumination with the UV/IR filter. It showed clearly that the solid solution of ZnO:GaN thin film exhibited significantly increased photocurrents compared to the ZnO film. ZnO:GaN solid-solution thin films deposited with N_2 mass flow rate of 25% and 50%; it also showed enhanced photocurrents (not shown here) compared to ZnO thin film [225].

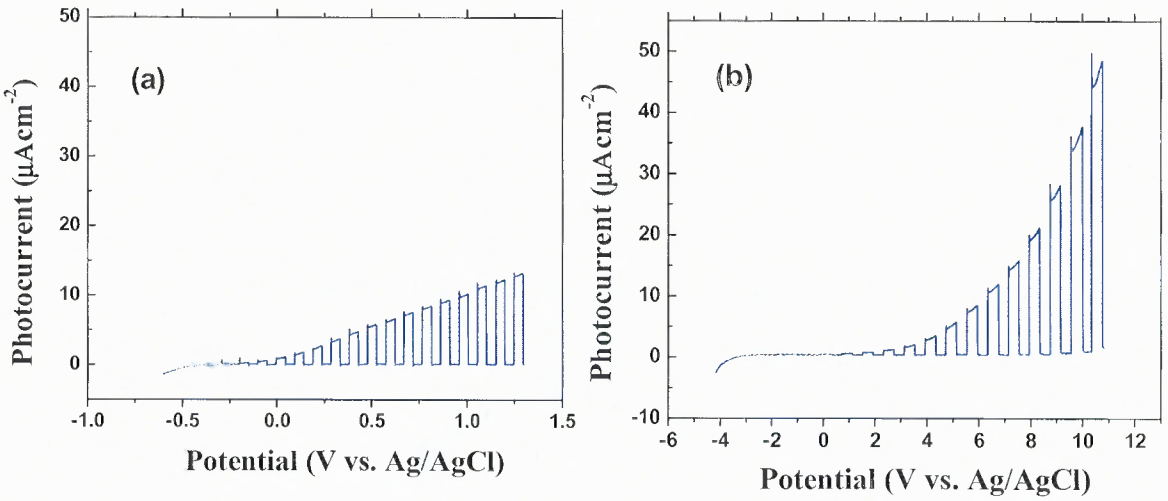

Figure 6.91 (a) Photocurrent-voltage curves of a ZnO film under light-on/light-off illumination with the UV/IR filter. (b) Photocurrent-voltage curves of a solid solution of ZnO:GaN thin films with N_2 mass flow rate of 75%, under light-on/light-off illumination with the UV/IR filter [225].

The photocurrent-voltage curves of ZnO, and solid solution of ZnO:GaN thin films grown in Ar and mixed N_2 and O_2 ambient with N_2 mass flow rate of 25% to 75%, respectively, under illumination with the UV/IR filter is shown in Figure 6.92. The ZnO film exhibited no clear photoresponse, due to its wide bandgap. The solid solution of ZnO:GaN thin films exhibited much higher photocurrent than the ZnO film, despite much

less light absorption. It indicates that a solid solution of ZnO:GaN thin films with significantly enhanced crystallinity using proper RF power and N_2 flow rate in the ambient can shift the optical absorption into the visible-light regions, thereby improving the PEC performance [225].

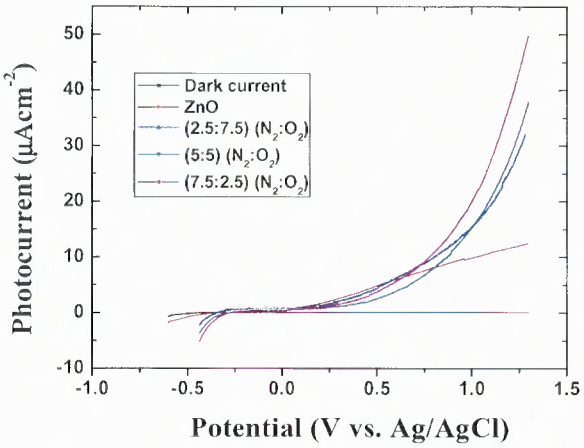

Figure 6.92 Photocurrent-voltage curves of a ZnO, and solid solution of ZnO:GaN thin films, respectively, under the illumination (a) with an UV/IR filter [225].

6.15 Effect of Gas Ambient and Varying RF Sputtering Power on ZnO and GaN Solid-Solution Films

In this part of the research work, effect of gas ambient and varying RF sputtering power for the synthesis of the solid solution of ZnO and GaN (ZnO:GaN) thin films are presented. The ZnO:GaN solid-solution thin films are synthesized by RF magnetron sputtering in Ar and mixed O_2 and N_2 gas ambient at 100°C, followed by post-annealing at 500°C in ammonia for 4 hours.

Figure 6.93 shows the XRD curves of ZnO, and solid solution of ZnO:GaN(Ar) thin films grown in Ar gas ambient. The ZnO film exhibits poor crystallinity. The ZnO:GaN(Ar) films deposited at ZnO(200W)GaN(70W) showed reduced crystallinity

compared to the ZnO film. This may be because of GaN-rich film. As the RF power of ZnO is increased to 300 W, ZnO:GaN(Ar) film showed improved crystallinity. The best crystallinity is observed for ZnO:GaN(Ar) film deposited at ZnO(400W)GaN(70W) RF power. When the RF power is increased to 500 W for ZnO, the crystallinity again becomes poor. It is known that a faster deposition rate can deteriorate the crystal structure. Therefore, poor crystallinity of the ZnO:GaN(Ar) thin films deposited at ZnO(500W)GaN(70W) RF power may be caused by high deposition rate. Crystallite sizes were 21, 6, 18, 28, and 16 nm for the ZnO, 200-W, 300-W, 400-W, and 500-W RF power of ZnO target for ZnO:GaN solid-solution thin films, respectively, which were estimated by applying the Debye-Scherrer equation to our XRD data [226].

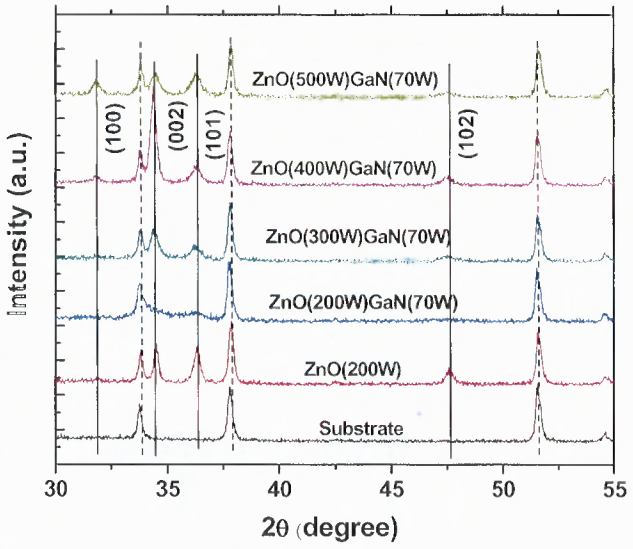

Figure 6.93 The X-ray diffraction curves of ZnO, and solid solution of ZnO:GaN(Ar) thin films grown in Ar gas ambient [226].

Figure 6.94 shows the optical absorption coefficients of the ZnO, and solid solution of ZnO:GaN(Ar) thin films grown in Ar gas ambient. The optical bandgaps of the films were determined by extrapolating the linear portion of each curve. The bandgap

of the ZnO film is 3.25 eV. The direct optical bandgaps measured for solid solution of ZnO:GaN(Ar) thin films for 200-W, 300-W, 400-W, and 500-W RF power of the ZnO target were 3.52, 3.48, 3.46, and 3.38 eV, respectively. It is clear that as the RF power of the ZnO target is increased from 200 to 500 W, the bandgap is decreased from 3.52 to 3.38 eV. These results indicates that the solid solution of ZnO:GaN(Ar) thin films grown in Ar gas ambient failed to shift the optical absorption into the long-wavelength region [226].

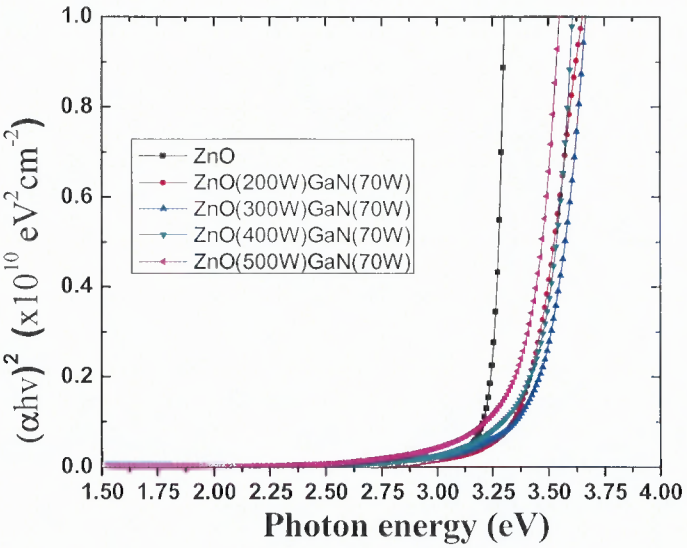

Figure 6.94 The optical absorption coefficients of the ZnO, and solid solution of ZnO:GaN(Ar) thin films grown in Ar gas ambient [226].

The photocurrent-voltage curves of the ZnO and solid solution of ZnO:GaN(Ar) thin films, under illumination with the UV/IR filter, are shown in Figure 6.95. It clearly shows that the solid solution of ZnO:GaN(Ar) thin film deposited at ZnO(400W)GaN(70W) RF power exhibited the best photocurrents, compared to any other films. The enhanced photocurrent may be due to the increased crystallinity of the

film grown at ZnO(400W)GaN(70W) RF power. At a potential of 1.2 V, the photocurrents were 6.5, 7.9, 8.2, 12.5, and 8.1 μAcm^{-2} for the ZnO, 200-W, 300-W, 400-W, and 500-W RF power of ZnO for the solid solution of ZnO:GaN(Ar) thin films, respectively. To investigate the photoresponses in the long-wavelength region, a green-color filter (wavelength: 538.33 nm; FWHM: 77.478 nm) was used with the UV/IR filter. The ZnO and solid solution of ZnO:GaN(Ar) thin films exhibited no clear photoresponse, due to its wide bandgap nature. The modest photocurrents achieved in ZnO and solid solution of ZnO:GaN(Ar) thin film grown in Ar ambient is because of its wide bandgap, which limits absorption to UV light. Therefore, it is necessary to reduce the bandgap of ZnO:GaN solid solution by reducing the bandgap to make absorption in the visible region possible and to use sunlight more efficiently. Using a proper gas mixture in the chamber ambient may play a significant role in narrowing the bandgap for ZnO:GaN solid-solution thin films [226].

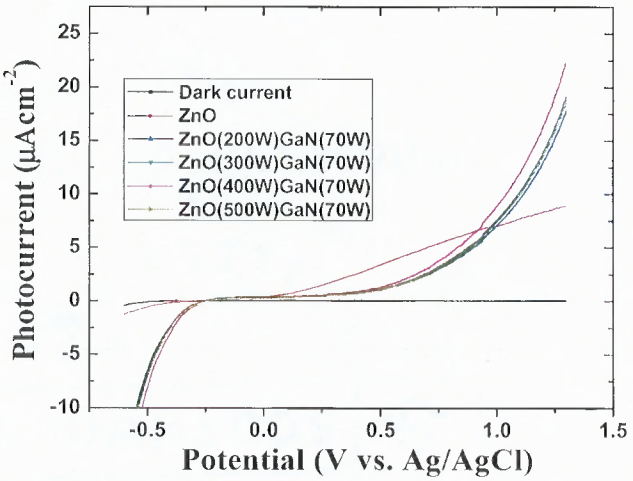

Figure 6.95 Photocurrent-voltage curves of the ZnO, and solid solution of ZnO:GaN(Ar) thin films grown in Ar gas ambient, under illumination with the UV/IR filter [226].

Figure 6.96 shows the XRD curves of ZnO, and ZnO:GaN(N_2/O_2) solid-solution films grown at fixed RF power of GaN target and varied RF power of ZnO target in mixed N_2 and O_2 gas ambient with N_2 mass flow rate of 75%. It is seen that the ZnO film exhibits poor crystallinity. The ZnO:GaN(N_2/O_2) films grown in mixed N_2 and O_2 gas ambient with N_2 mass flow rate of 75% shows better crystallinity. The enhancement in crystallinity is attributed to the use of mixed N_2 and O_2 gas ambient. The (002), (100), and (101) peaks are enhanced as the RF power of the ZnO target is increased with the fixed RF power (35 W) of the GaN target [226].

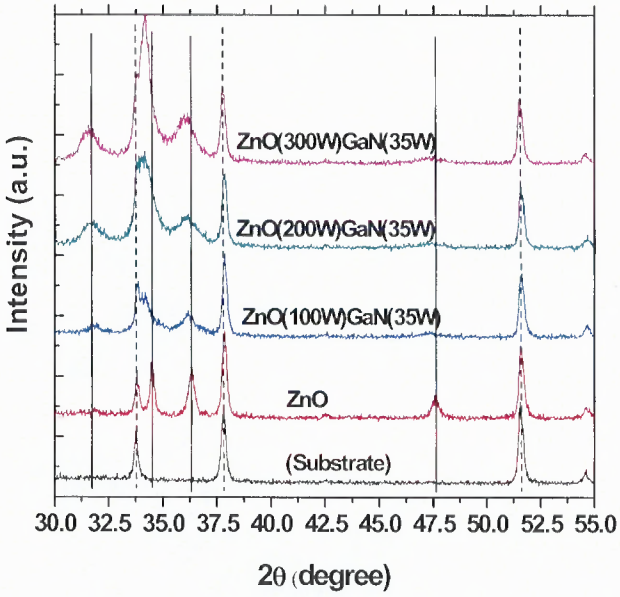

Figure 6.96 X-ray diffraction curves of the ZnO, and solid solution of ZnO:GaN(N_2/O_2) thin films grown in mixed N_2 and O_2 gas ambient [226].

Figure 6.97(a) shows the optical absorption coefficients of the ZnO, and ZnO:GaN(N_2/O_2) solid-solution films grown at fixed RF power of the GaN target and varied RF power of the ZnO target in mixed N_2 and O_2 gas ambient with N_2 mass flow rate of 75%. The direct optical bandgaps measured for ZnO:GaN(N_2/O_2) solid-solution films at N_2 mass flow rate from 75% for an increase in RF power of the ZnO target,

gradually decreased from 3.13 to 3.09 eV. The Mott-Schottky plots of the ZnO and ZnO:GaN(N_2/O_2) solid-solution films grown in mixed N_2 and O_2 gas ambient with N_2 mass flow rate of 75% is shown in Figure 6.97(b). All the samples exhibited positive slopes, indicating n-type semiconductors [226].

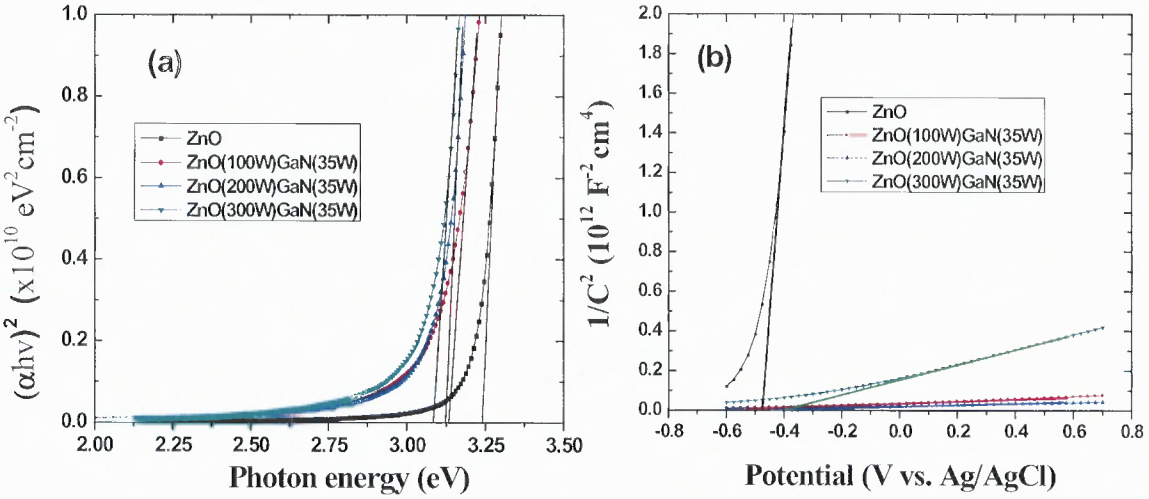

Figure 6.97 (a) The optical absorption coefficients of the ZnO, and solid solution of ZnO:GaN(N_2/O_2) thin films grown in mixed N_2 and O_2 gas ambient. (b) The Mott-Schottky plots of the ZnO, and solid solution of ZnO:GaN(N_2/O_2) thin films grown in mixed N_2 and O_2 gas ambient [226].

The photocurrent-voltage curves of the ZnO, and ZnO:GaN(N_2/O_2) solid-solution films grown in mixed N_2 and O_2 gas ambient with N_2 mass flow rate of 75%, under illumination with the UV/IR filter, is shown in Figure 6.98. It clearly shows that the ZnO:GaN(N_2/O_2) solid-solution films exhibit enhanced photocurrents, compared to the ZnO film. The enhanced photocurrent may be due to the increased crystallinity and bandgap reduction. At a potential of 1.2 V, the photocurrents were 6.5, 14, 17.5, and 26 μAcm^{-2} for the ZnO, 100-W, 200-W, and 300-W RF power of the ZnO target for ZnO:GaN(N_2/O_2) solid-solution films, respectively. The results clearly demonstrate that

significantly reduced bandgap with enhanced photocurrents can be obtained in solid solution of ZnO and GaN, (ZnO:GaN) films with mixed N_2 and O_2 gas ambient with varying the RF power approach [226].

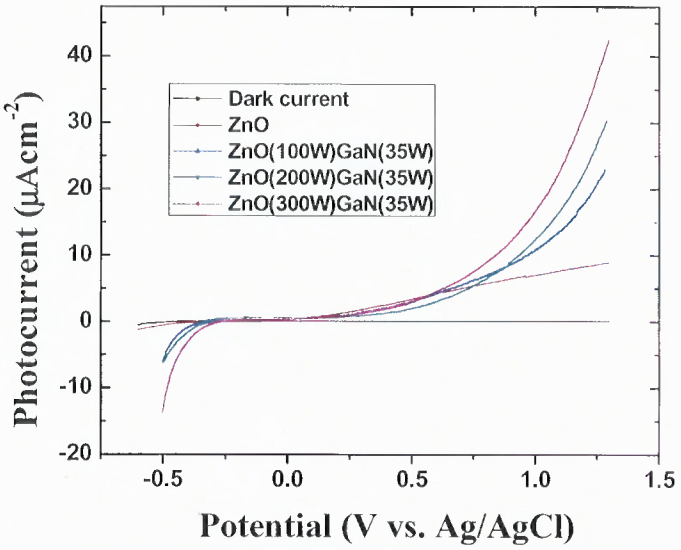

Figure 6.98 (a) Photocurrent-voltage curves of the ZnO, and solid solution of ZnO:GaN(N_2/O_2) thin films grown in mixed N_2 and O_2 gas ambient, under illumination with the UV/IR filter [226].

6.16 Synthesis and Characterization of Ternary Cobalt Spinel Oxides

Synthesis and characterization of ternary cobalt spinel are reported in this part of the research work.

$Co_{1+}X_{2-}O_4$ (X = Al, Ga, In) thin films were grown on Ag-coated stainless-steel plates (Ag/SS) and quartz glasses for PEC measurement and optical characterization, respectively, using an RF magnetron reactive co-sputtering system. Here, Ag/SS was required as the substrate because of the high-temperature oxide growth (800°C). Two sputter guns were used for the Co–Al–O and Co–In– O syntheses, where the Co_3O_4 target was fixed and the secondary target was changed to Al and In_2O_3 for $CoAl_2O_4$ and

$CoIn_2O_4$, respectively. The Co–Ga–O films were deposited using different amounts of Ga_2O_3 powder on the Co_3O_4 target. The distance between the sputter guns and substrate was fixed at 11 cm. The substrates were rotated during deposition for enhanced uniformity and the working pressure was 1.22 Pa. The sputtering ambient environment was mixed Ar and O_2 (O_2:Ar = 5:1) and the RF power of each sputter gun was varied to obtain appropriate chemical stoichiometry. All of the samples were controlled to exhibit similar film thicknesses on the order of 500 nm, as measured by stylus profilometry.

The representative experimental optical data for each ternary cobalt oxide material, synthesized under a range of sputtering conditions, are shown in Figure 6.99. From both the measured optical absorption coefficient and a fit to the Tauc relation for direct transitions, tailoring of the optical bandgap from 1.5 to 2.25 eV can be observed. Taking into account that the separation between the H_2/H_2O reduction and O_2/H_2O oxidation potentials is 1.23 eV, and that due to the presence of unavoidable losses (e.g., component resistance, electron-hole recombination) an additional overpotential is required (raising the optimal voltage to 1.7 eV), this optical bandgap range appears quite promising for PEC water-splitting application [113].

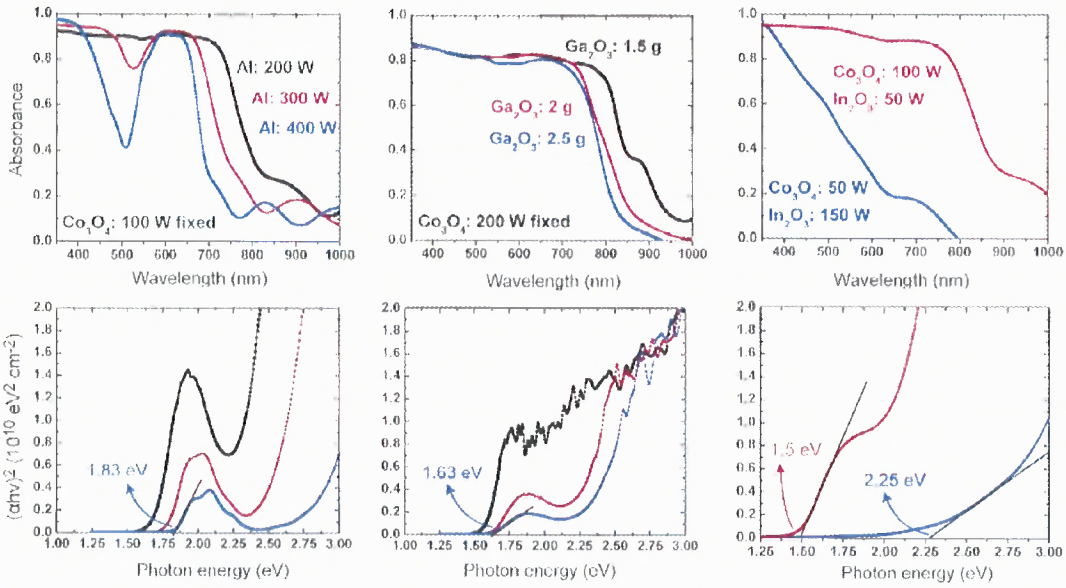

Figure 6.99 Measured optical absorption spectra (upper) and direct-bandgap fits (lower) of $Co_{1+}X_{2-}O_4$ compounds as a function of sputtering conditions: (left) X = Al, (centre) X = Ga and (right) X = In [113].

For $CoAl_2O_4$, the measured absorption features are consistent with previous reports [227,228]. The low-energy absorption peak for $CoAl_2O_4$ originates from the spin-allowed, parity-forbidden Co $^4A_2$ $^4T_1$ transitions, whereas the drop in absorption coefficient at higher energies results from a range of low-intensity spin-forbidden transitions. The shift to longer wavelengths with lower Al sputtering power can be understood as a transition toward the inverse Co_2AlO_4 spinel, which is known to possess a lower bandgap [229]. For $CoGa_2O_4$, the strong absorption profile is red-shifted to around 2.25 eV and begins to overlap with the low-energy absorption feature; this overlap is even more pronounced for $CoIn_2O_4$ at high Co_3O_4 sputtering power. At high In_2O_3 sputtering power, the Co–In–O samples exhibit the high levels of visible transmission expected from mixed-phase Co-substituted In_2O_3, i.e., the ternary composite is not fully formed. The time-dependent PEC response of each material was investigated under chopped-light illumination at a constant applied bias potential (*vs.* Ag/AgCl). The

cathodic currents of $CoAl_2O_4$ and $CoGa_2O_4$ were found to increase on illumination, as in Figure 6.100.

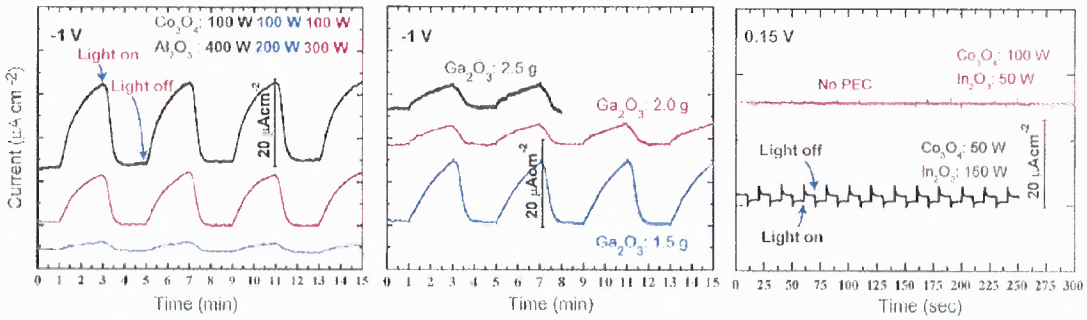

Figure 6.100 Time-dependent PEC response under light-on/light-off illumination at constant applied voltage for (left) Al, (center) Ga, and (right) In ternary cobalt oxides. For the Al and Ga spinels, illumination induces an increase in the background cathodic current (p-type response), whereas for In a small increase in the anodic current is observed (n-type response) [113].

This p-type PEC response suggests the presence of intrinsic hole carriers, which prior calculations have identified as cation vacancies [230]. However, poor photocurrents on the order of 20 μA cm^{-2} are observed in both cases (currents on the order of 10 mA cm^{-2} will be required from commercially viable materials). It is worth noting that the PEC response of $CoAl_2O_4$ is better than that of $CoGa_2O_4$, which will be discussed in more detail below. Unfortunately, all synthesized $CoIn_2O_4$ films failed to exhibit any significant PEC response. Indeed, the weak PEC response varied from p-type to n-type with different samples, but no significant photocurrent was observed in either case [113]. In addition to the low generated photocurrents, the second discouraging trend emerging from Figure 6.100 is the long relaxation times between sample illuminations. For the majority of PEC materials, the recovery time on the removal of light is on the order of seconds or less; however, for these materials, it is on the order of minutes. This implies poor carrier transport kinetics, originating from confined electrical carriers (i.e., heavy hole effective masses). A more-detailed comparison between the relaxation times of

$CoAl_2O_4$ and $CoGa_2O_4$ is shown in Figure 6.101. Ideally, the photocurrent decay for the chopped-light PEC system will closely follow a square wave; however, the response deviates greatly here [113].

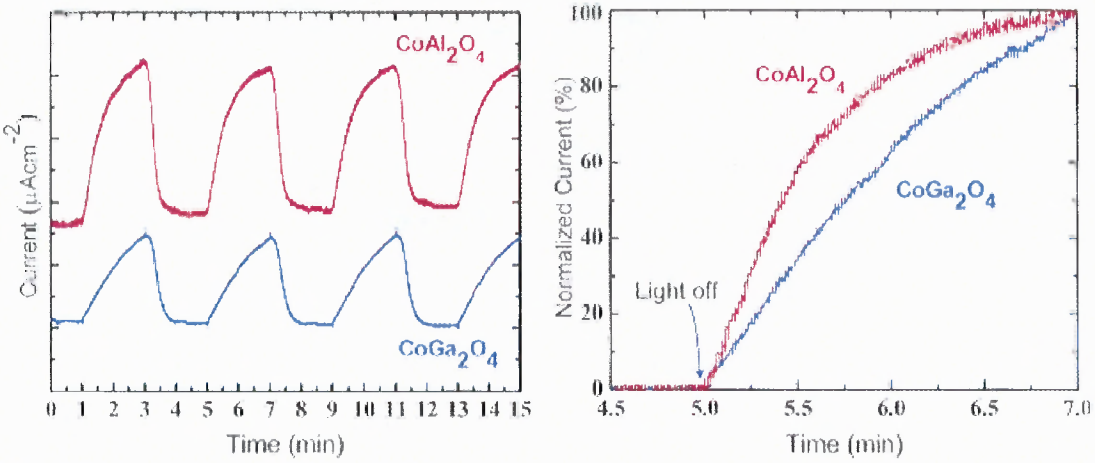

Figure 6.101 Photocurrent decay comparison between the $CoAl_2O_4$ and $CoGa_2O_4$ samples with the same bias voltage (−1 V) [113].

Direct comparison of the normalized current of the Al and Ga ternaries in Figure 6.101 shows much faster decay in the former, indicating better carrier transport kinetics; hence, $CoAl_2O_4$ exhibits marginally improved PEC response. One encouraging outcome is that both materials exhibited no evidence of corrosion in solution for sustained PEC testing periods.

Based on the initial electronic structure analyses, it was anticipated that the Co–In spinel may possess both the lowest bandgap and highest n-type conductivity (through the presence of the In 5s conduction states). However, although the synthesized In-based ternary oxides did not exhibit any significant photocurrent on illumination, the n-type PEC response time was much shorter, indicating the beneficial influence of the delocalized In 5s orbitals in the lower conduction band. To explore the origin of the performance failure in more detail, we first measured the dark currents without

illumination, as shown in Figure 6.102. Even for small applied potentials, the dark current is large, indicating that the film is not an intrinsic semiconductor; in fact, it is closer to a semimetallic state [113].

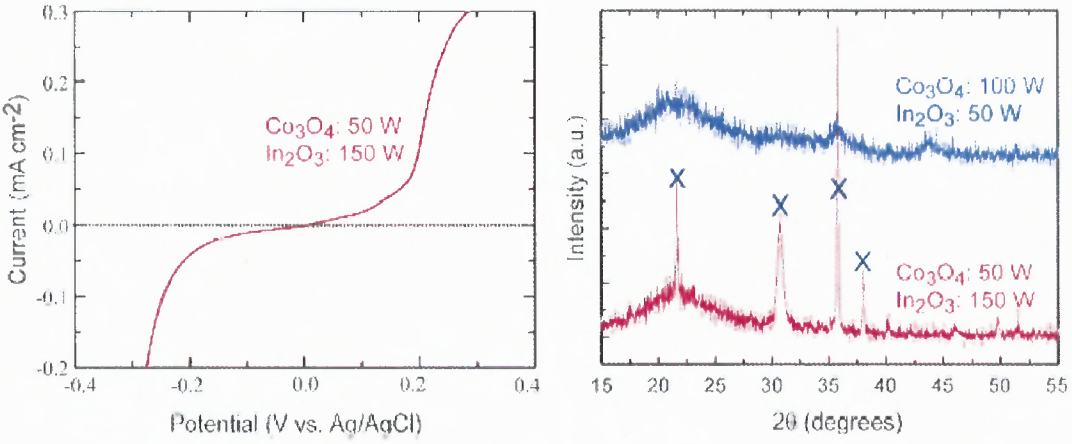

Figure 6.102 Measured dark current–voltage curve and powder XRD data for synthesized Co–In systems. The crosses in the XRD spectrum correspond to reflections associated with bixbyite In_2O_3 [113].

The XRD curves are also shown in Figure 6.102. The measurements clearly show that the deposited films are not pure $CoIn_2O_4$, but that they undergo significant phase segregation into Co_3O_4 and In_2O_3 (this has been confirmed by TEM analysis). Taking into account that In_2O_3 itself exhibits degenerate electron conduction behavior as an n-type transparent conducting oxide [75-77], the presence of In_2O_3 in the film will contribute to both the inferior PEC response and high dark-current levels. Within the limitations of our co-sputtering system, we could not succeed in synthesizing a homogeneous $CoIn_2O_4$ film [113].

6.17 Synthesis and Characterization of $CoAl_2O_4$–Fe_2O_3 *p-n* Nanocomposite Electrodes

Synthesis and characterization of $CoAl_2O_4$–Fe_2O_3 *p-n* nanocomposite electrodes are reported in this part of the research work.

The preparation of $CoAl_2O_4$–Fe_2O_3 *p-n* nanocomposite film electrodes starts from dispersing $CoAl_2O_4$ and Fe_2O_3 nanoparticles (size <50 nm, Sigma-Aldrich Co.) in ethanol by paint shaking for 2 hour. Mixed nanoparticles with Fe_2O_3 concentrations from 5 to 20 wt% were prepared. These colloids were thoroughly dispersed using a conditioning mixer by adding ethyl cellulose as the binder and -terpineol as a solvent for the pastes, followed by concentration using an evaporator. The pastes were doctor-bladed on Ag-coated stainless-steel substrates (Ag/SS), followed by calcination at 800°C for 4 hours in air to remove the binder. All samples have a similar film thickness of about 6 μm as measured by stylus profilometry [234].

When *p*-type and *n*-type nanoparticles are mixed together well with good nanoparticle interconnection, a three-dimensional *p-n* junction can be formed. To ensure quality nanoparticle interconnection, the mixed nanoparticle films need to be annealed at high temperature—here, 800°C, below the solid reaction temperature. The widely used fluorine-doped tin oxide-coated glass substrate is not suitable for this application because it is thermally unstable at this annealing temperature. Therefore used Ag/SS as an alternative substrate because the solubility of Ag in Fe is extremely small and the melting point of Ag is 960°C. Figure 6.103(a) shows XRD patterns for SS and Ag/SS before and after annealing at 800°C in air.

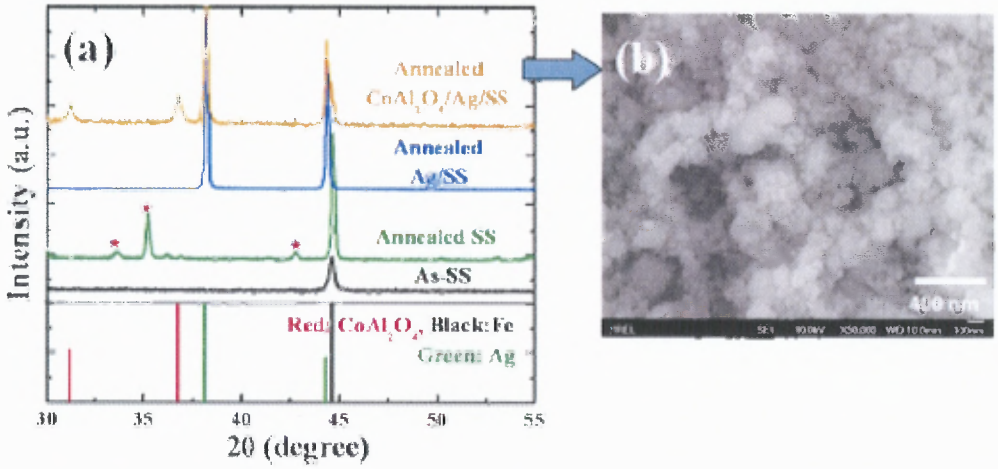

Figure 6.103 (a) XRD curve of unannealed and annealed SS substrates, annealed Ag/SS substrate, and $CoAl_2O_4$/Ag/SS. (b) SEM image of annealed $CoAl_2O_4$/Ag/SS [234].

The SS shows the formation of iron oxide (* peaks) on the surface after the annealing, indicating that SS is not appropriate as the substrate for $CoAl_2O_4$ electrodes. This is because iron oxide has very poor electrical conductivity, making it difficult to collect current from the $CoAl_2O_4$ to the SS. On the other hand, Ag/SS exhibited no evidence of formation of oxides after the annealing at 800°C in air. Therefore, $CoAl_2O_4$–Fe_2O_3 nanocomposite films could be coated on Ag/SS and annealed at 800°C without substrate deterioration (see the XRD curve of the annealed $CoAl_2O_4$/Ag/SS sample in Figure 6.103 (a)). The SEM image shown in Figure 6.103(b) indicates that the annealed nanocomposite electrode is nanoporous, and its particle size corresponds well to the crystallite size (33 nm) calculated from the XRD peak around 36.8°. The particle size is also the same as the unannealed particles, indicating that no obvious solid reaction occurred during the annealing [234].

Figure 6.104(a) shows the PEC response for a pure $CoAl_2O_4$ nanoparticle electrode under light-on/light-off conditions at −1 V. When the light was on, *cathodic* photocurrents were registered, indicating that $CoAl_2O_4$ is a *p*-type semiconductor. The

photocurrent as a function of applied potential (from 0.0 to −1.0 V) is shown in Figure 6.104(b). It shows that the onset potential of the photocurrent occurs at −0.2 V and the photocurrent saturates from −0.6 V. The inset in Figure 6.104(b) shows the stability of the electrode against photocorrosion when operated at −1 V. It is seen that $CoAl_2O_4$ is very stable in the basic solution, a property not typically seen for *p*-type materials [234].

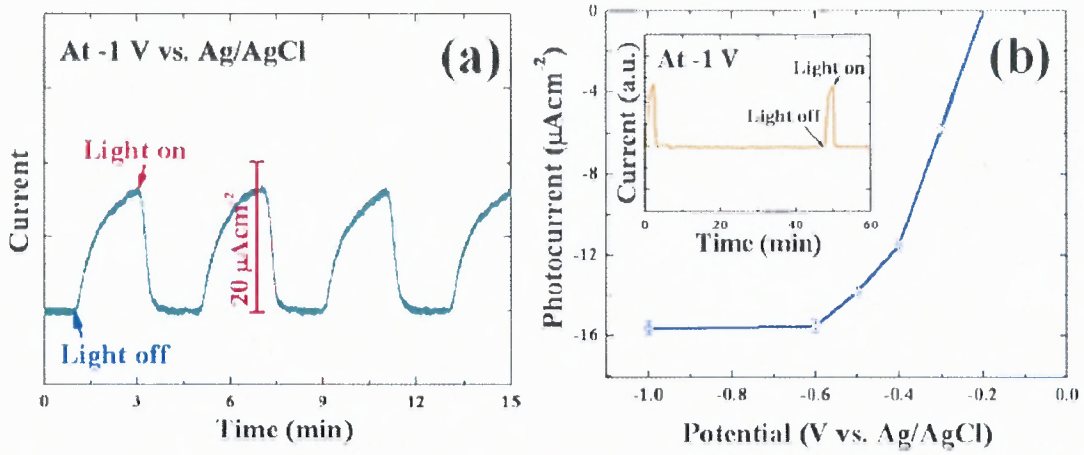

Figure 6.104. (a) PEC response measured for pure $CoAl_2O_4$ nanoparticle electrode with a time under the light-on/light-off conditions at constant −1 V. (d) Measured I-V curve for pure $CoAl_2O_4$ nanoparticle electrode [234].

Figure 6.105(a) shows the comparison of PEC responses of a nanocomposite film with 5 wt% Fe_2O_3 and a reference $CoAl_2O_4$ nanoparticle film. Again, the photocurrent is cathodic, meaning that the overall electrode behaves as *p*-type. The saturated photocurrents are lined up for comparison. It clearly shows that the photocurrent with the nanocomposite film is much larger than that with *p*-type $CoAl_2O_4$ nanoparticle film only. Figure 6.105(b) shows the photocurrents at −1 V for nanocomposite films with different amounts of Fe_2O_3. It is seen that all $CoAl_2O_4$–Fe_2O_3 *p-n* nanocomposite films exhibit much-improved PEC responses over the $CoAl_2O_4$ nanoparticle film. However, the enhancement does not increase linearly with the amount of Fe_2O_3 nanoparticles, because too much Fe_2O_3 would lead to a lower amount of *p*-type $CoAl_2O_4$ and less contact area

with electrolyte. The highest photocurrent is seen with an Fe_2O_3 content of 5 wt%. Figure 6.105(c) shows photocurrent measured at −1 V as a function as wavelength for the $CoAl_2O_4$ with 10 wt% Fe_2O_3. It clearly shows that the photoresponse of the nanocomposite film only occurs at the wavelengths less than ~532 nm (2.33 eV), which corresponds to the bandgap of $CoAl_2O_4$, rather than that of Fe_2O_3. This result further indicates that the enhanced photoresponses of nanocomposite films are not due to the contribution from Fe_2O_3, but to the reduced carrier recombination or carrier separation promoted by the three-dimensional *p-n* junction. Also note the very slow response time for these electrodes that is due to the mechanism of charge transport in these materials. Both the pure $CoAl_2O_4$ and the nanocomposite electrodes exhibit slow carrier-transport kinetics due to the large effective masses for both electrons and holes in $CoAl_2O_4$. The *p-n* nanocomposite structure does not address this problem.

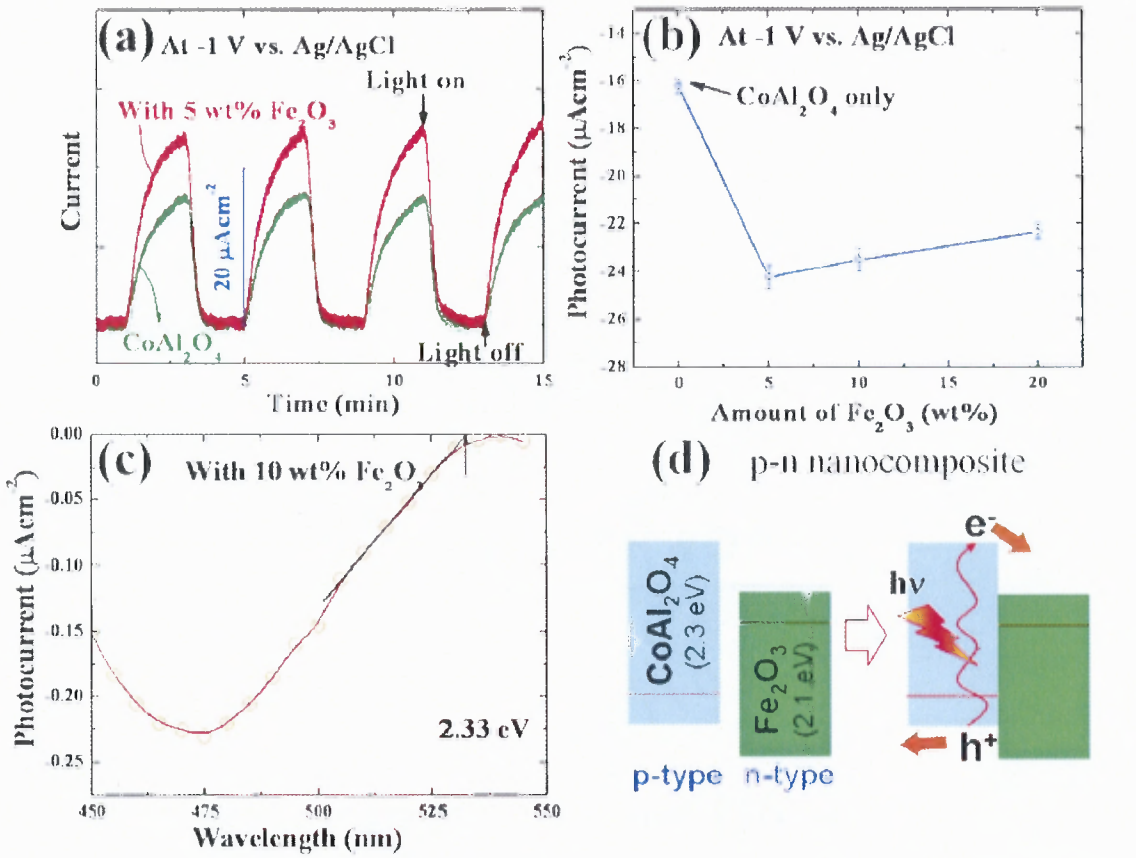

Figure 6.105 (a) Comparison of PEC responses for pure $CoAl_2O_4$ nanoparticle and *p-n* nanocomposite electrodes under the light-on/light-off conditions at −1 V. (b) Photocurrents at −1 V for nanocomposite films with different amount of Fe_2O_3. (c) Photocurrent at −1 V as a function as incident monochromatic light wavelength for the $CoAl_2O_4$ nanocomposite with 10 wt% Fe_2O_3. (d) Band diagram for *p*-type $CoAl_2O_4$ and *n*-type Fe_2O_3 nanocomposite [234].

The hypothesis as to why the $CoAl_2O_4$–Fe_2O_3 *p-n* nanocomposite electrodes exhibit enhanced PEC performance over the $CoAl_2O_4$ nanoparticle films is as follows: when *p*-type $CoAl_2O_4$ and *n*-type Fe_2O_3 nanoparticles are interconnected, a three-dimensional *p-n* junction can form with their valance bands and conduction bands (CBs) offset, as shown in Figure 6.105(d). Unlike conventional *p-n* junctions, no traditional depletion region—and thus, no built-in electrical field—is expected at the $CoAl_2O_4/Fe_2O_3$ and electrode/electrolyte interfaces due to the nanoparticle structure. This built-in electrical field in conventional *p-n* junction usually promotes holes to the *p*-side and

electrons to the *n*-side of the junction, which, in this case, is not desirable for water splitting. However, in this case, upon illumination, photogenerated electron-hole pairs will be separated due to the band offset, leading to reduced carrier recombination. Electrons will be injected into Fe_2O_3 and holes will remain in $CoAl_2O_4$. The electron injection will be much faster kinetically than the hydrogen reaction at the $CoAl_2O_4$ surface. Thus, hydrogen will be preferentially evolved at the Fe_2O_3 sites. We speculate that the enhancement on PEC performance is due to the formation of a three-dimensional *p-n* junction, which promotes photogenerated carrier separation and reduces their recombination. However, when an excessively large number of Fe_2O_3 nanoparticles is added in the film, Fe_2O_3 nanoparticles could shadow the $CoAl_2O_4$ and/or block interparticle hole-transport through nanoporous $CoAl_2O_4$ and thus limit the enhancement of photocurrent [234].

6.18 Synthesis and Characterization of Cu-W-Oxide Films

Synthesis and characterization of Cu-W-oxide films are reported in this part of the research work.

Figure 6.106 shows XRD curves for Cu-W-oxide films grown in O_2/Ar gas ambient. The RF power for the Cu target is fixed at 100 W and the W target RF power is changed from 100 to 150 W. It is seen that Cu-W-oxide films exhibited amorphous characteristics and there is no phase separation. This is due to the low-temperature deposition.

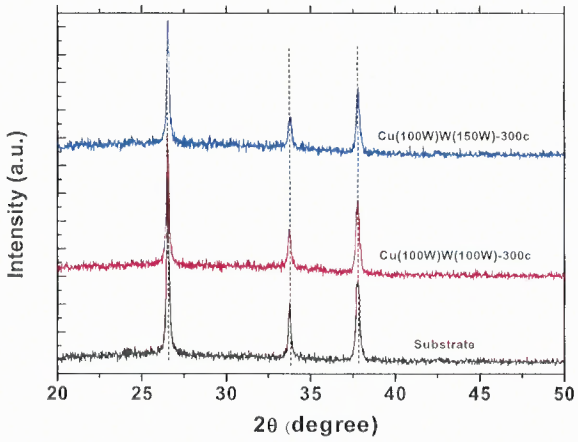

Figure 6.106 The X-ray diffraction curves of Cu-W-oxide films.

Figures 6.107 (a) and 6.107(b) show the optical absorption and optical absorption coefficients of the Cu-W-oxide films. The optical bandgaps of the films were determined by extrapolating the linear portion of each curve. The bandgap of the Cu-W-oxide film is about 2.1 eV.

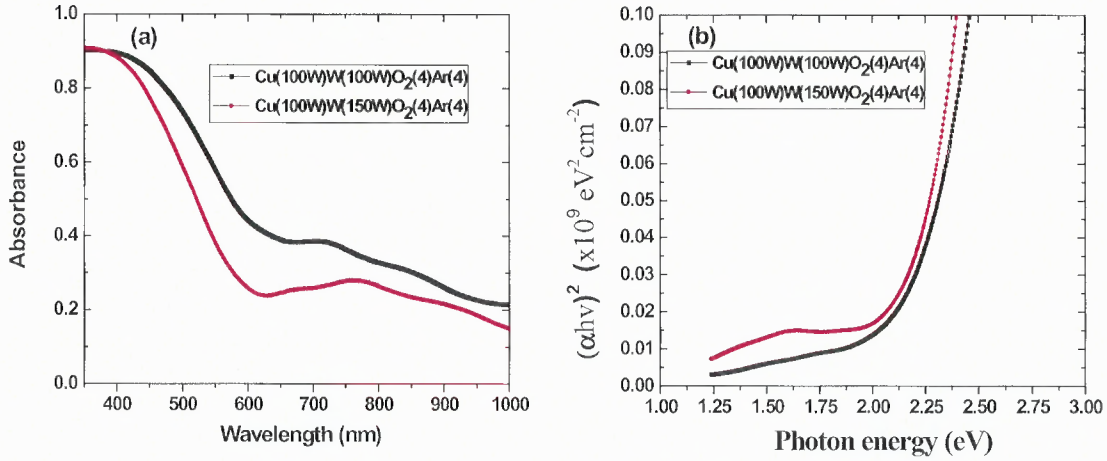

Figure 6.107 (a) The optical absorption spectra (b) Optical absorption coefficients of the Cu-W-Oxide films.

Figure 6.108 shows the photocurrent-voltage curves of Cu(100W)W(150W) film under light-on/light-off illumination with the UV/IR filter. It clearly showed that Cu-W-oxide film showed *p*-type behavior and exhibited photoresponse.

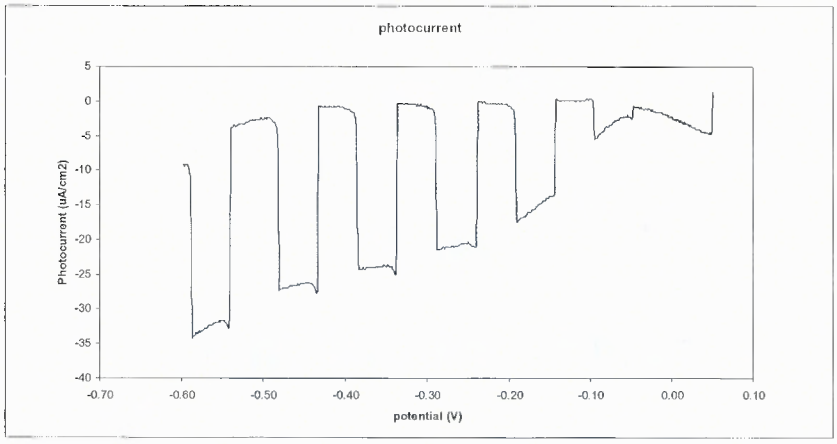

Figure 6.108 Photocurrent-voltage curves of a Cu(100W)W(150W) film under light-on/light-off illumination with the UV/IR filter in 1 M NaOH solution.

The Cu(100W)W(100W) film is annealed in air at 500°C for 2 hour. Figure 6.109 shows the photocurrent-time curves of Cu(100W)W(100W) film at applied potential of constant -0.3 V, before and after annealing. After annealing, the photoresponse increased to 12 μA/cm^2 from 9 μA/cm^2 (before annealing). The photoresponse decreased when the measurement is taken for a longer time.

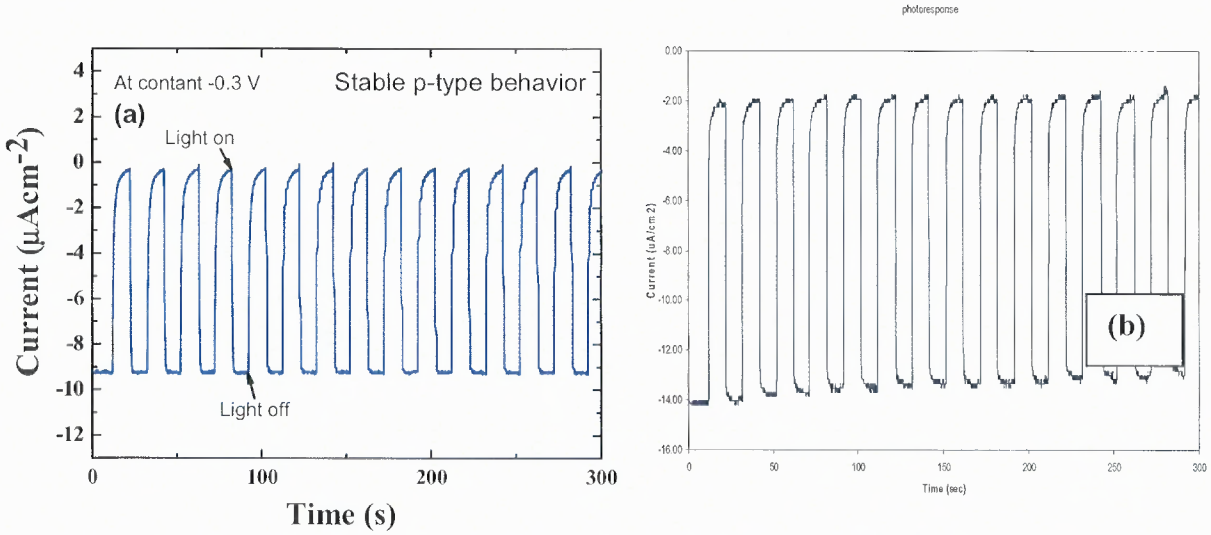

Figure 6.109 Photocurrent-time curves of a Cu(100W)W(100W) film at an applied potential of -0.3 V under light-on/light-off illumination with the UV/IR filter (a) before annealing and (b) after annealing.

6.19 Synthesis and Characterization of Cu-Ti-Oxide Films

Synthesis and characterization of Cu-Ti-oxide films are reported in this part of the research work.

Table 6.1 shows the sputtering conditions for Cu-W-oxide samples. Figure 6.110 shows XRD curves for Cu-Ti-oxide films grown in O_2/Ar gas ambient. The RF power for the Cu target and the Ti target RF power are varied. The Cu-Ti-oxide films also exhibited amorphous character and there is no phase separation, due to the low-temperature deposition.

Table 6.1 The Sputtering Conditions for Cu-Ti-Oxide Samples

Sample ID	Substrate Temp.	Oxygen (sccm)	Argon (sccm)	Cu (RF power, W)	Ti (RF power, W)
485	150	5	5	80	200
486	150	5	5	60	200
487	150	8	2	60	200
488	150	3	7	60	200
489	150	8	2	60	250
490	400	8	2	60	250
491	150	5	5	100	200
492	150	5	5	40	200
493	150	5	5	40	250
494	150	8	2	40	250

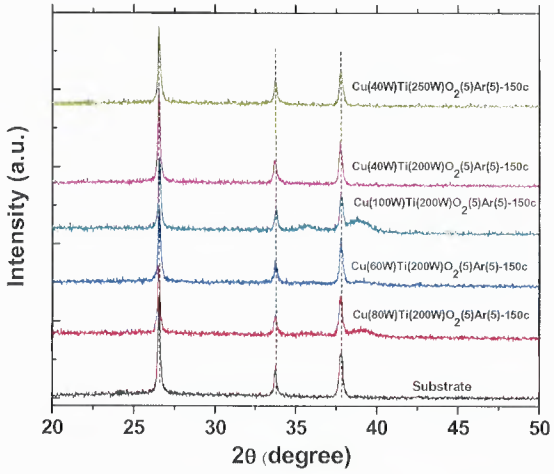

Figure 6.110 The X-ray diffraction curves of Cu-Ti-oxide films.

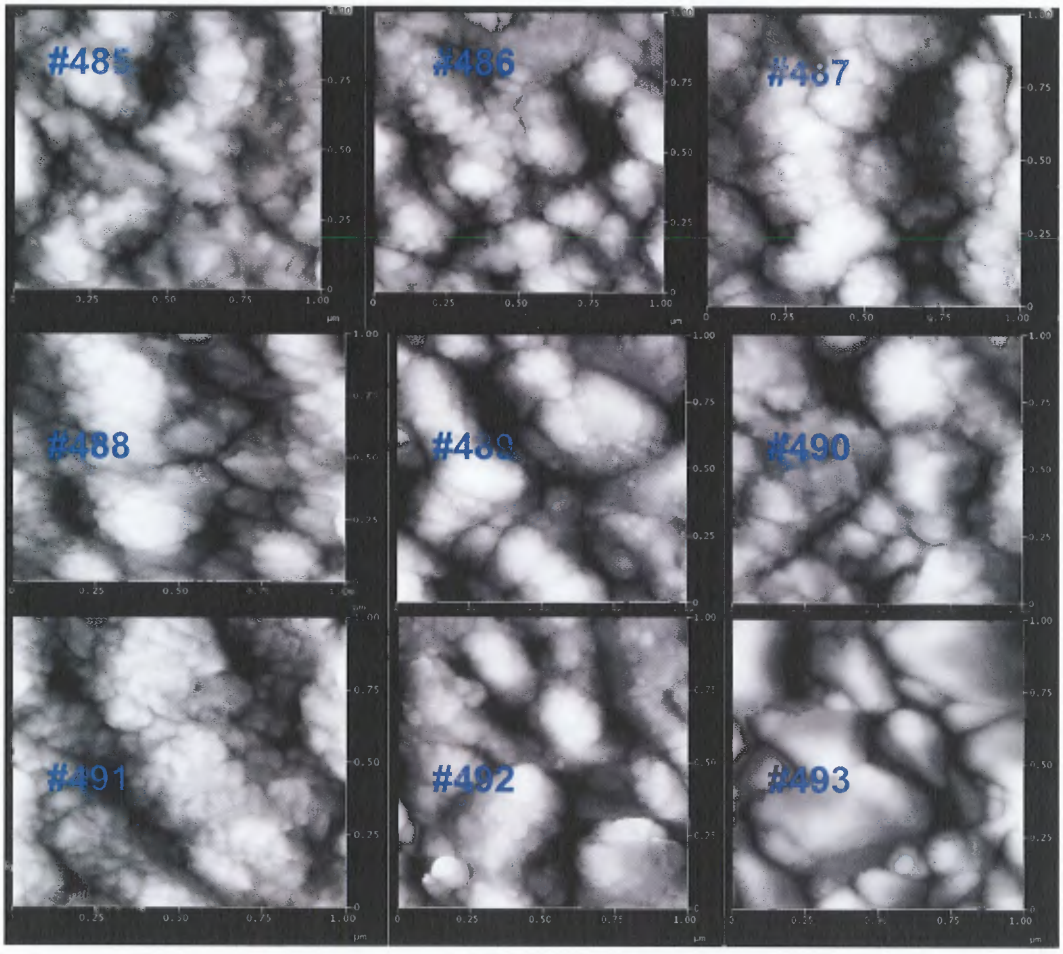

Figure 6.111 AFM images taken from Cu-Ti-oxide samples numbered #485 to # 493.

Figure 6.111 shows AFM surface morphologies of the Cu-Ti-oxide samples numbered #485 to # 493. It clearly shows that the Cu-Ti-oxide films are amorphous with porous character. Figure 6.112 shows FE-SEM top-views from Cu-Ti-oxide samples numbered #486, #487, #489, #490, #491, and # 493 at different magnification.

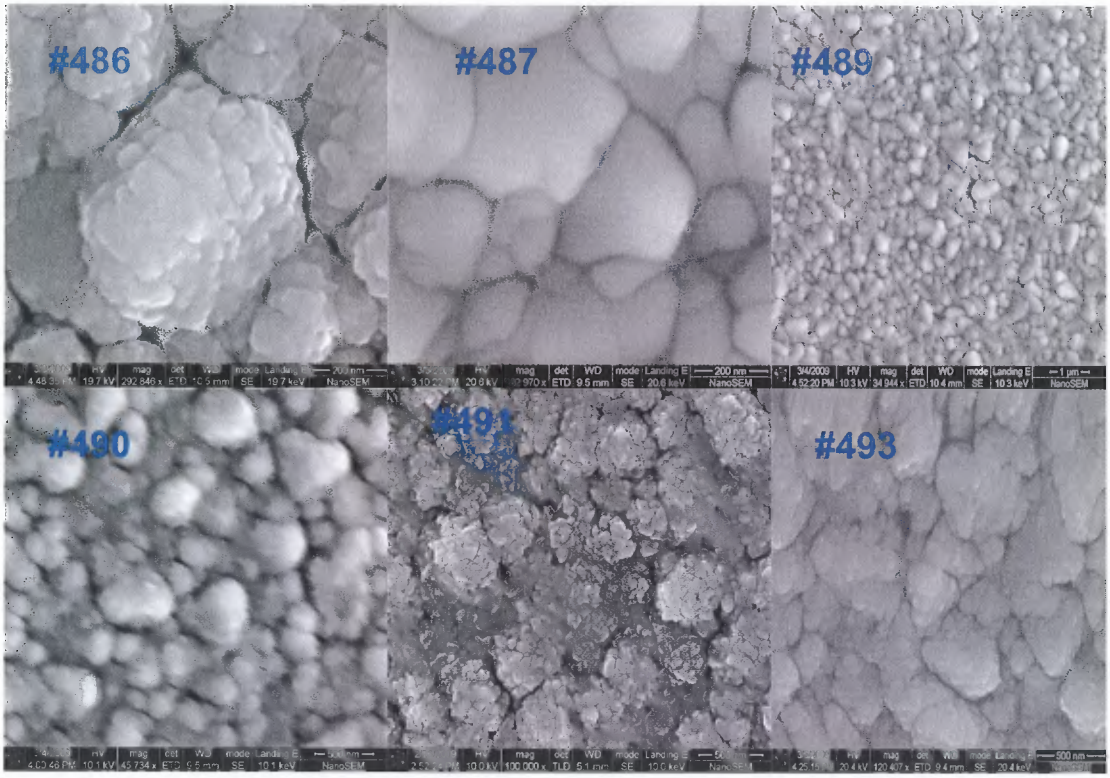

Figure 6.112 FE-SEM top-views from Cu-Ti-oxide samples numbered #486, #487, #489, #490, #491, and # 493.

Figures 6.113(a) and 6.13(b) show the optical absorption and optical absorption coefficients of the Cu-Ti-oxide films. The optical bandgaps of the films were determined by extrapolating the linear portion of each curve. The bandgap of the Cu-Ti-oxide film is varied from about 1.4 eV to about 2.1 eV.

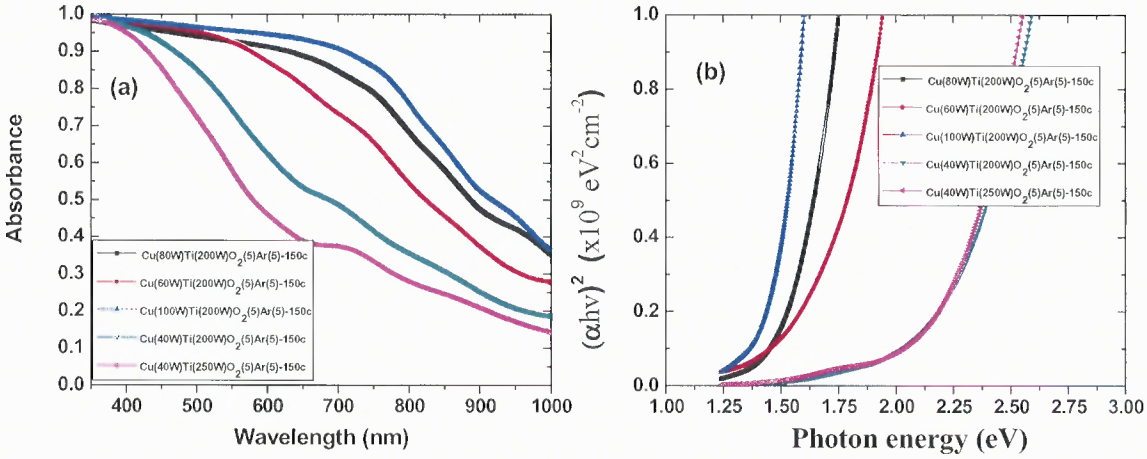

Figure 6.113 (a) The optical absorption spectra; (b) Optical absorption coefficients of the Cu-Ti-oxide films.

The Mott-Schottky plots of the Cu-Ti-oxide films are shown in Figure 6.114. All the samples exhibited negative slopes, indicating *p*-type semiconductors.

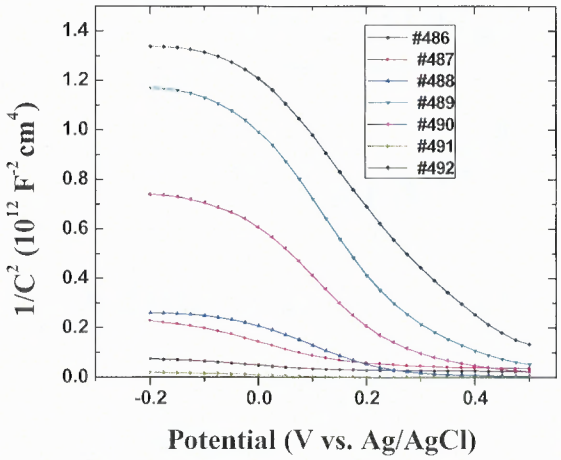

Figure 6.114 The Mott-Schottky plots of the Cu-Ti-oxide films.

Figure 6.115(a) shows the photocurrent-time curves of Cu(100W)Ti(200W) film under light-on/light-off illumination with the UV/IR filter in 1M NaOH solution. The Cu-Ti-oxide film showed *p*-type behavior and exhibited photoresponse. Figure 6.115(b)

shows the photocurrent-time curves of Cu(60W)Ti(200W) film at an applied potential of a constant -0.3 V. It can be seen that the Cu-Ti-oxide films are very stable.

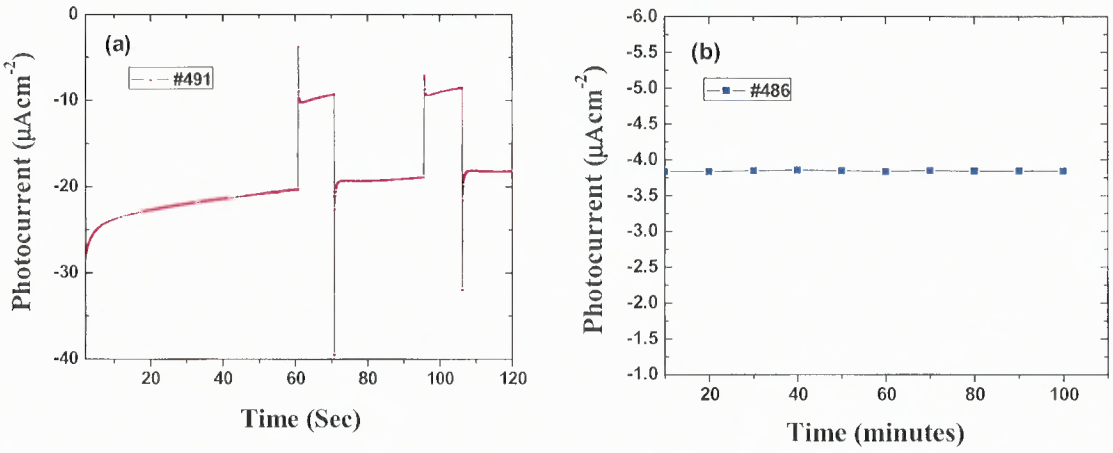

Figure 6.115 (a) Photocurrent-voltage curves of a Cu(100W)Ti(200W) film under light-on/light-off illumination with the UV/IR filter in 1 M NaOH solution. (b) Photocurrent-time curves of a Cu(60W)Ti(200W) film at an applied potential of -0.3 V under light-on/light-off illumination with the UV/IR filter.

6.20 Synthesis and Characterization of Cu-Sn-Oxide Films

Synthesis and characterization of Cu-Sn-oxide films are reported in this part of the research work.

Table 6.2 shows the sputtering conditions for Cu-Sn-oxide samples. Figure 6.116 shows XRD curves for Cu-Sn-oxide films grown in O_2/Ar gas ambient. The RF power for the Cu target is fixed at 120 W, and tin oxide powder of varying amount is dispersed on the Cu target. It is seen that Cu-W-oxide films exhibited amorphous character and phase separation. It should be noted that is was difficult to place the tin oxide powder uniformly on the slanted target.

Table 6.2 The Sputtering Conditions for Cu-Sn-Oxide Samples.

Sample ID	Substrate Temp	Oxygen (sccm)	Argon (sccm)	Cu (RF power, W)	SnO_2 powder (g)
495	150	5	5	120	0.36
496	150	5	5	120	0.11
497	150	5	5	120	0.04
498	425	5	5	120	0.32
499	150	8	2	120	0.32
500	400	3	7	120	0.32
501	150	5	5	120	0.72

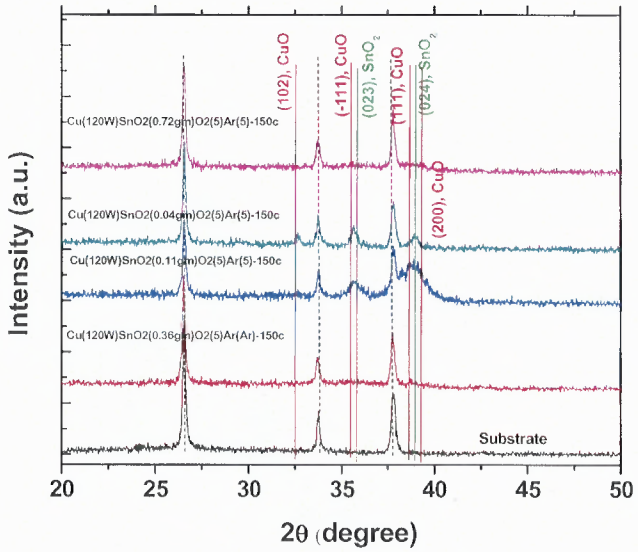

Figure 6.116 The X-ray diffraction curves of Cu-Sn-oxide films.

Figures 6.117 (a) and 6.117(b) show the optical absorption spectra and optical absorption coefficients of the Cu-Sn-oxide films. The optical bandgaps of the films were determined by extrapolating the linear portion of each curve. The bandgap of the Cu-Sn-oxide film is varied from about 1.6 to about 1.9 eV.

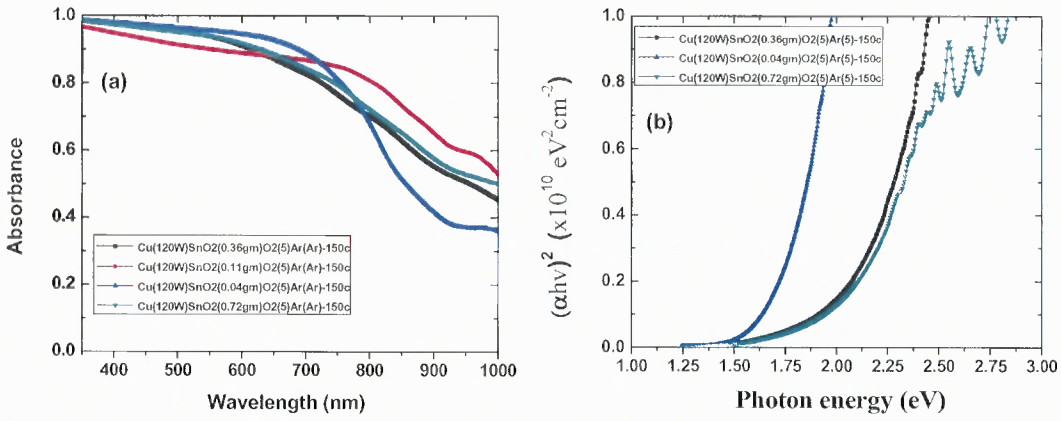

Figure 6.117 (a) The optical absorption spectra (b) Optical absorption coefficients of the Cu-Sn-oxide films.

Figure 6.118 shows the (a) XRD curves, (b) optical absorption spectra, and (c) optical absorption coefficients of the Cu-Sn-oxide films deposited at different O_2-to-Ar ratio. Figure 6.119 shows AFM surface morphologies of the Cu-Ti-oxide samples numbered #495, # 498, and # 499.

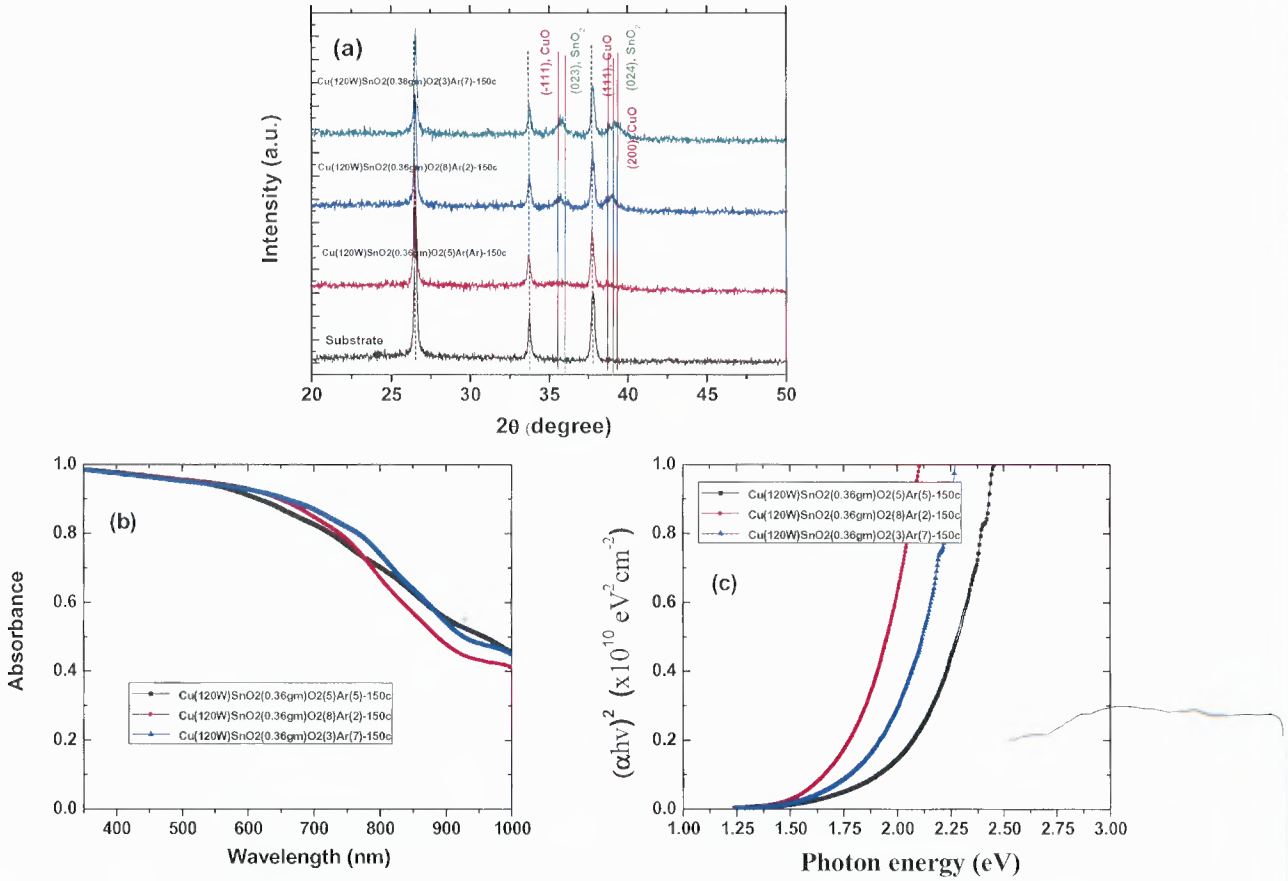

Figure 6.118 (a) X-ray diffraction curves of Cu-Sn-oxide films. (b) Optical absorption spectra and (c) optical absorption coefficients of the Cu-Sn-oxide films deposited at different O_2–to-Ar ratios.

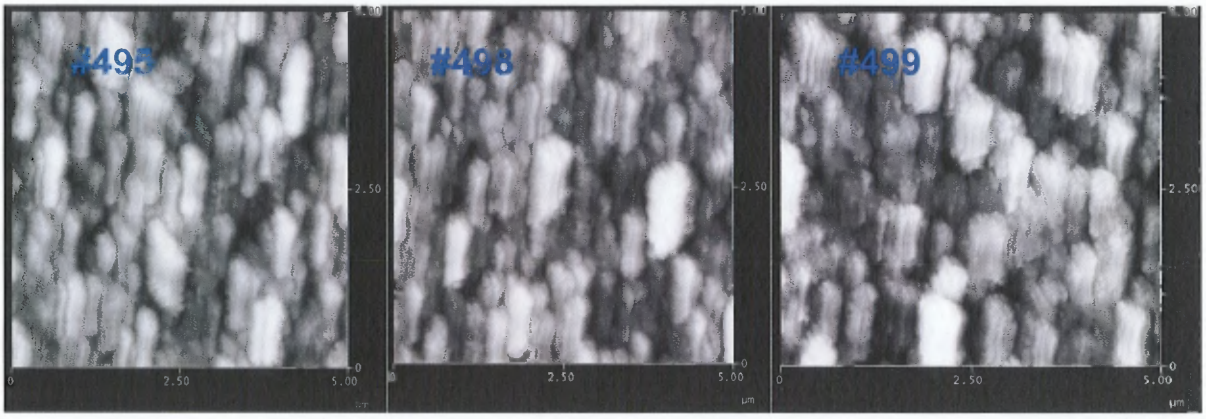

Figure 6.119 AFM images taken from Cu-Sn-oxide samples numbered #495, #498, and #499.

The Mott-Schottky plots and photocurrent-voltage curves of Cu-Sn-oxide films exhibited *p*-type behavior. However, the photocurrent was low and stability decreased after the photoelectrode was exposed for long-time measurements in 1M NaOH solution.

6.21 Synthesis and Characterization of Doped Cu-Ti-Oxide Films

Synthesis and characterization of doped Cu-Ti-oxide films are reported in this part of the research work.

Table 6.3 shows the sputtering conditions for doped Cu-Ti-oxide samples. Figure 6.120 shows the (a) XRD curves, (b) optical absorption spectra, and (c) optical absorption coefficients of the Al-doped Cu-Ti-oxide films deposited in O_2/Ar gas ambient. It is seen that Al-doped Cu-Ti-oxide films exhibited an amorphous character and phase separation. It should be noted that it was difficult to place tin oxide powder uniformly on the slanted target.

Table 6.3 The Sputtering Conditions for Doped Cu-Ti-Oxide Samples

Sample ID	Substrate Temp.	Oxygen (sccm)	Argon (sccm)	Cu (RF Power, W)	Ti (RF Power, W)
506 (Al_2O_3 = 0.1 gm)	150	5	5	100	200
507 (Al_2O_3 = 0.3 gm)	150	5	5	100	200
508 (WO_3 = 0.6 gm)	150	5	5	100	200
509 (WO_3 = 1 gm)	150	5	5	100	200
510 (SnO_2 = 0.3 gm)	150	5	5	100	200
511 (SnO_2 = 0.6 gm)	150	5	5	100	200

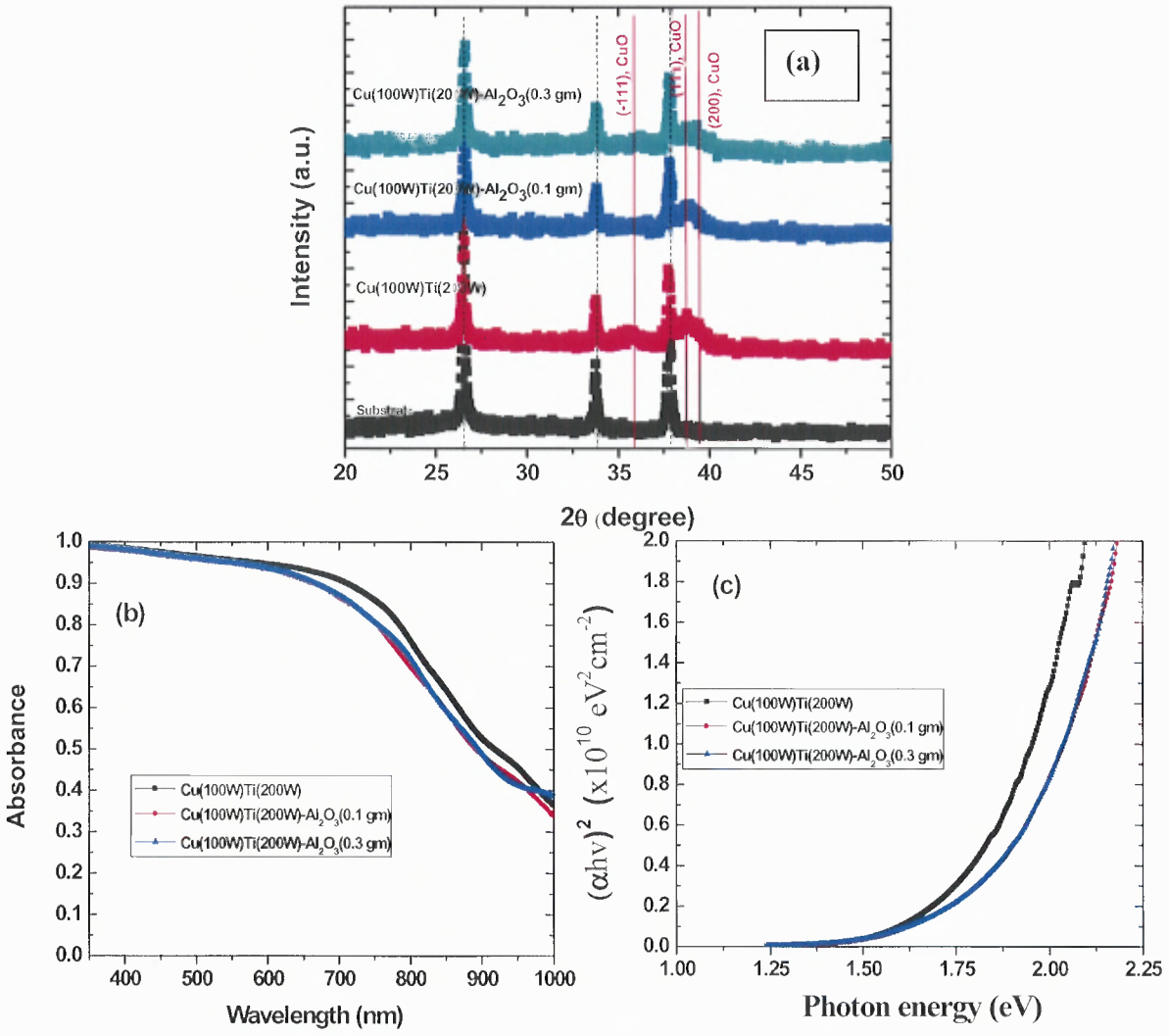

Figure 6.120 (a) X-ray diffraction curves, (b) optical absorption spectra, and (c) optical absorption coefficients of the Al-doped Cu-Ti-oxide films.

Figure 6.121 shows the (a) XRD curves, (b) optical absorption spectra, and (c) optical absorption coefficients of the W-doped Cu-Ti-oxide films deposited in O_2/Ar gas ambient. It is seen that W-doped Cu-Ti-oxide films exhibited amorphous character and phase separation. It should be noted that it was difficult to place tin oxide powder uniformly on the slanted target.

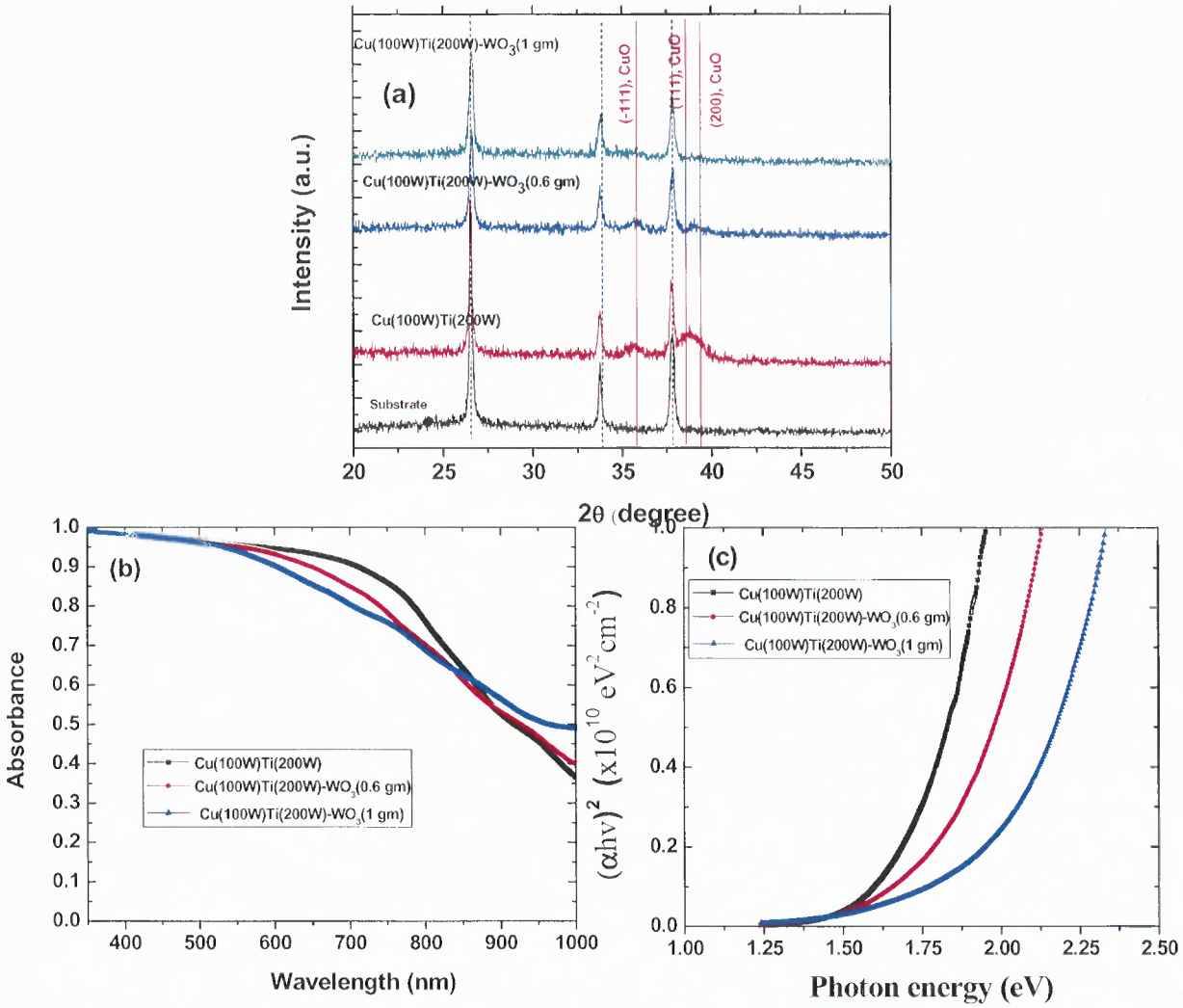

Figure 6.121 (a) X-ray diffraction curves, (b) optical absorption spectra, and (c) optical absorption coefficients of the W-doped Cu-Ti-oxide films.

Figure 6.122 shows the (a) XRD curves, (b) optical absorption spectra, and (c) optical absorption coefficients of the Sn-doped Cu-Ti-oxide films deposited in O_2/Ar gas ambient. It is seen that W-doped Cu-Ti-oxide films exhibited amorphous character and phase separation. It should be noted that it was difficult to place tin oxide powder uniformly on the slanted target.

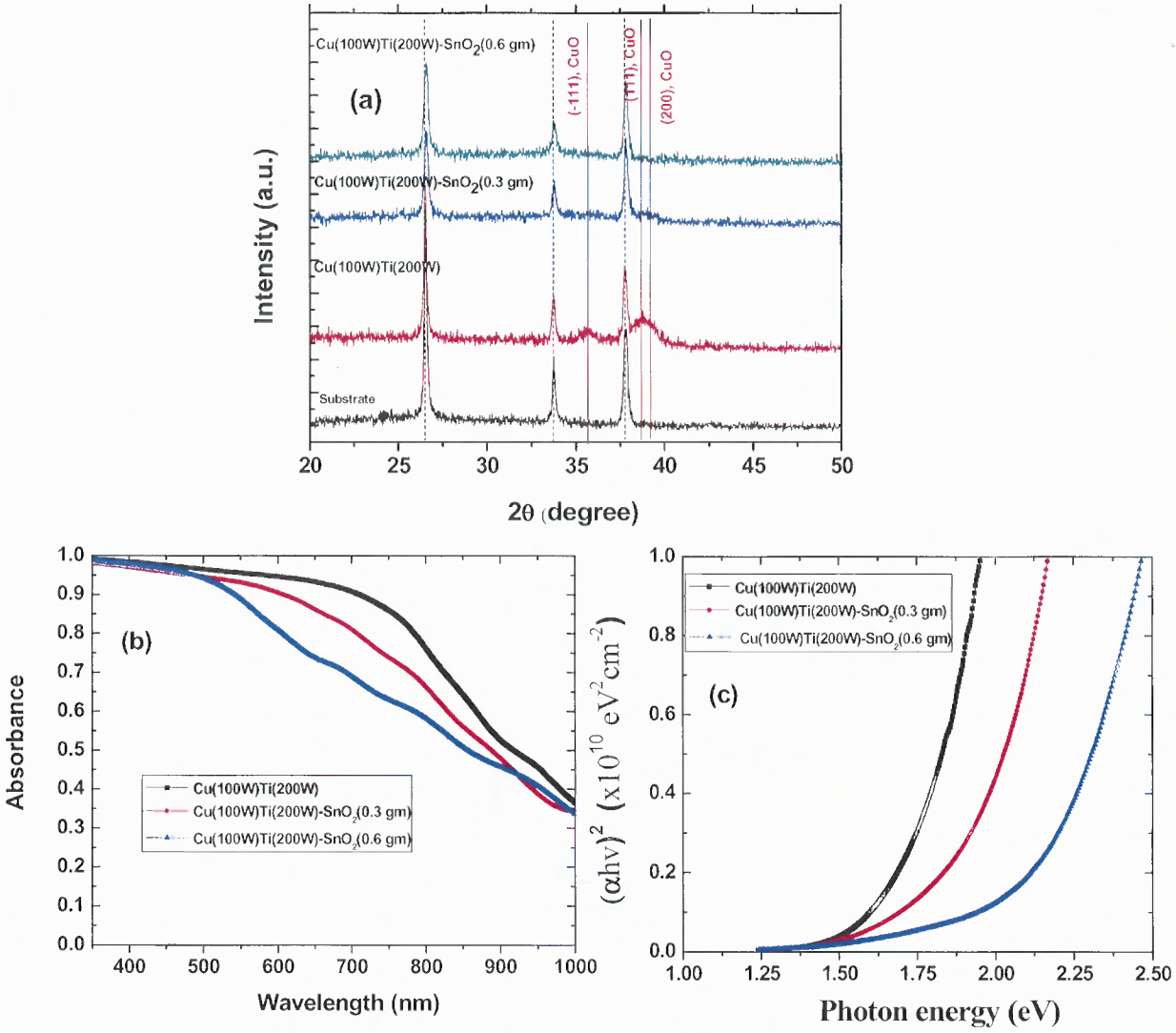

Figure 6.122 (a) X-ray diffraction curves, (b) optical absorption spectrum, and (c) optical absorption coefficients of the Sn-doped Cu-Ti-oxide films.

Figure 6.123 shows AFM surface morphologies of the Al-doped (#506), W-doped (#508), and Sn-doped (#510) Cu-Ti-oxide samples. The Mott-Schottky plots of the Cu-Ti-oxide films are shown in Figure 6.124. All the samples exhibited negative slopes, indicating *p*-type semiconductors.

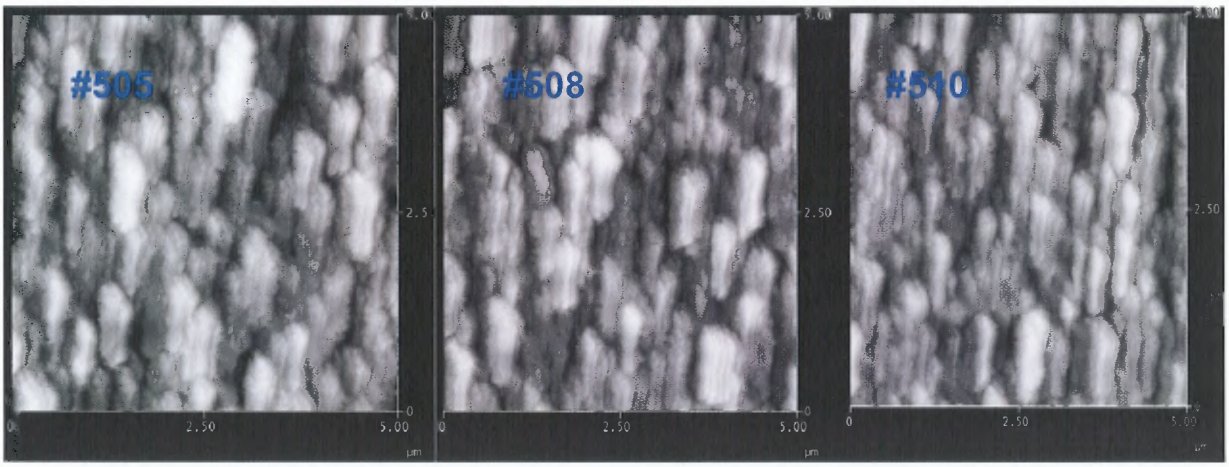

Figure 6.123 AFM images taken from Al-doped (#506), W-doped (#508), and Sn-doped (#510) Cu-Ti-oxide samples.

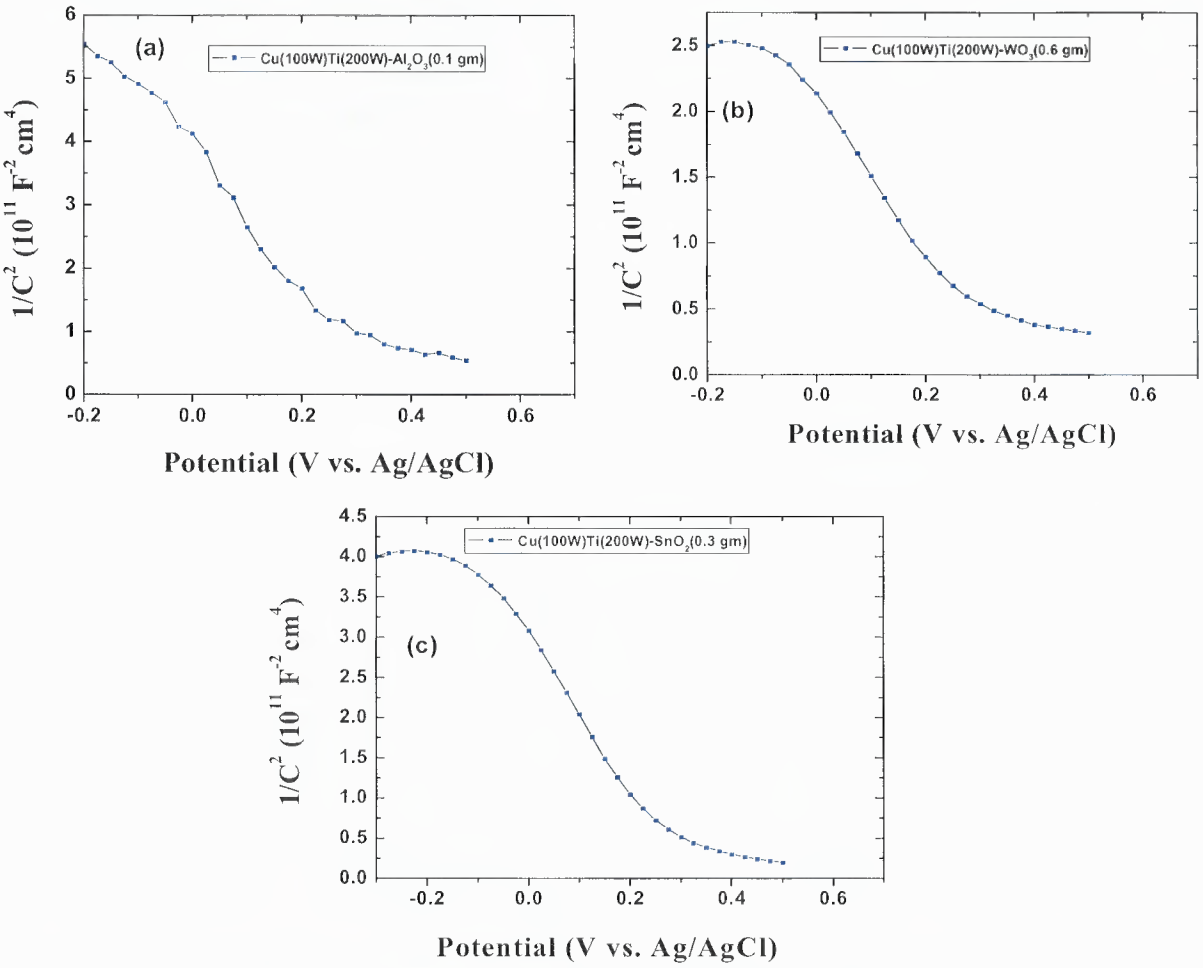

Figure 6.124 The Mott-Schottky plots of the Al-doped (#506), W-doped (#508), and Sn-doped (#510) Cu-Ti-oxide samples.

Figure 6.125 shows the photocurrent-voltage curves of (a) Al-doped, (b) W-doped, and (c) Sn-doped Cu-Ti-oxide films under continuous-light illumination with the UV/IR filter in 1 M NaOH solution. It showed clearly that doped Cu-Ti-oxide film has *p*-type behavior. However, there is not much improvement in exhibited photoresponse.

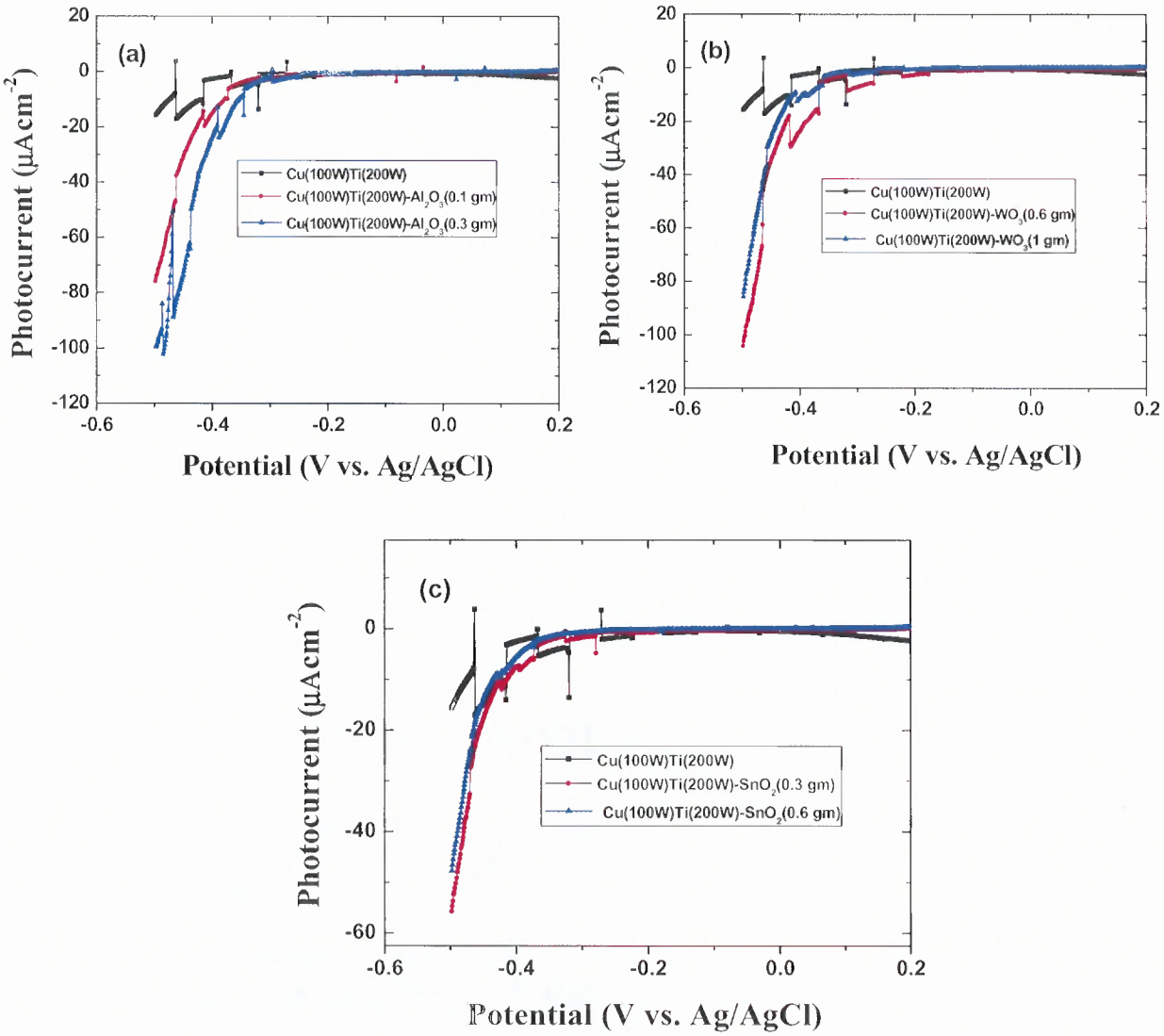

Figure 6.125 Photocurrent-voltage curves of (a) Al-doped, (b) W- doped, and (c) Sn-doped Cu-Ti-oxide films under continuous-light illumination with the UV/IR filter in 1 M NaOH solution.

6.22 Synthesis and Characterization of Doped Cu-W-Oxide Films

Synthesis and characterization of doped Cu-W-oxide films are reported in this part of the research work.

Table 6.4 shows the sputtering conditions for doped Cu-W-oxide samples. Figure 6.126 shows the (a) XRD curves, (b) optical absorption spectra, and (c) optical absorption coefficients of the Al-, Ti-, and Sn-doped Cu-W-oxide films deposited in O_2/Ar gas ambient. It is seen that Al-, Ti-, and Sn-doped Cu-W-oxide films exhibited amorphous character and no phase separation.

Table 6.4 The Sputtering Conditions for Doped Cu-W-Oxide Samples

Sample ID	Substrate Temp.	Oxygen (sccm)	Argon (sccm)	Cu (RF Power, W)	Ti (RF Power, W)
512 (SnO_2 = 0.5 gm)	150	5	5	80	120
513 (TiO_2 = 0.4 gm)	150	5	5	80	120
514 (Al_2O_3 = 0.1 gm)	150	5	5	80	120

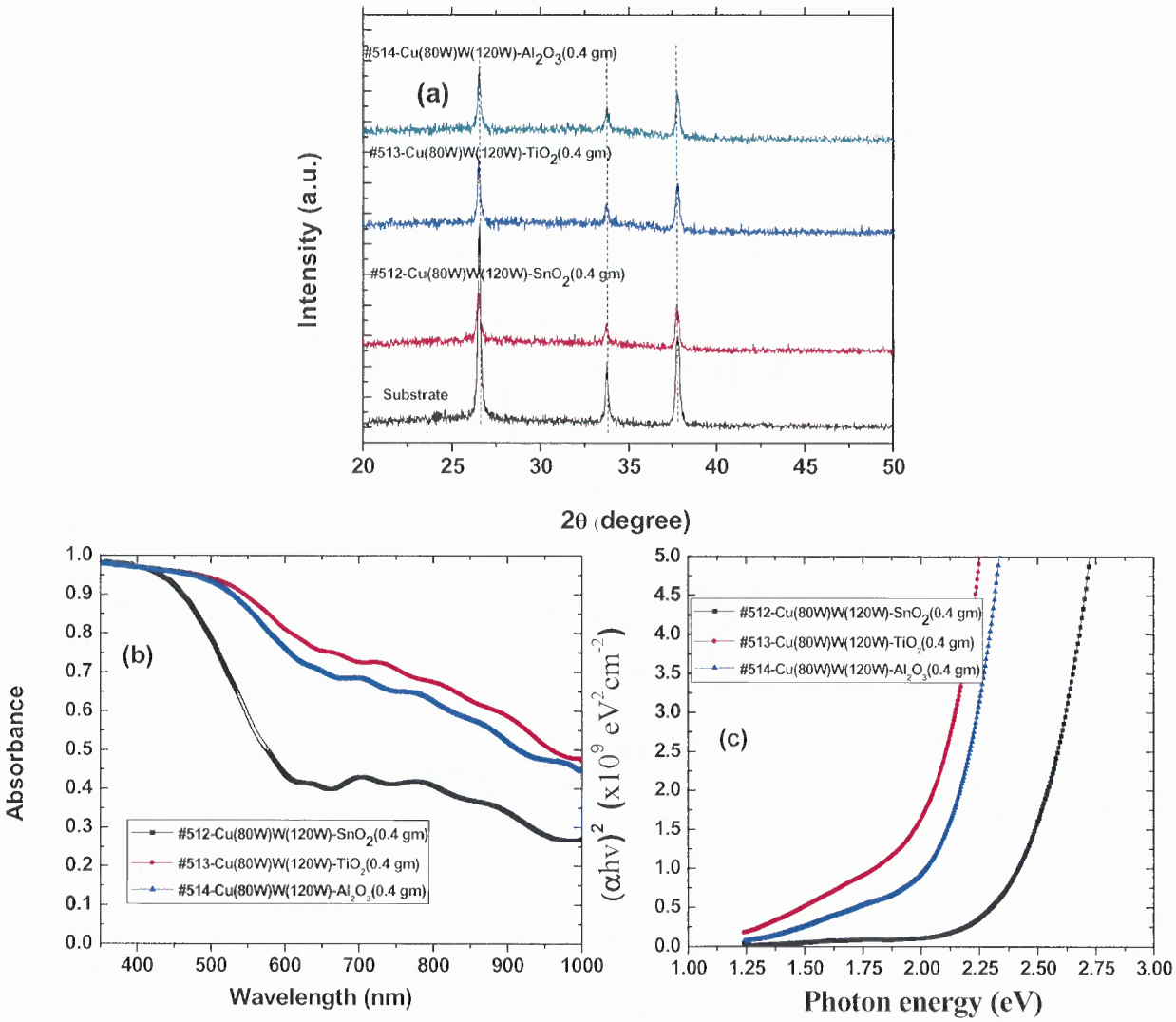

Figure 6.126 (a) X-ray diffraction curves, (b) optical absorption spectra, and (c) optical absorption coefficients of the Al-, Ti-, and Sn-doped Cu-W-oxide films.

Figure 6.127 shows AFM surface morphologies of the Sn-doped (#512), Ti-doped (#513), and Al-doped (#514) Cu-W-oxide samples.

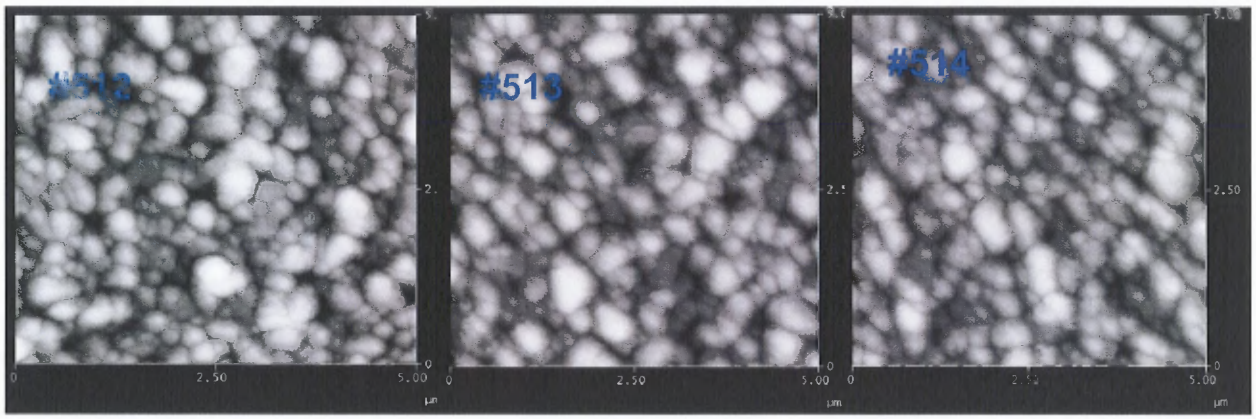

Figure 6.127 AFM images taken from Sn-doped (#512), Ti-doped (#513), and Al-doped (#514) Cu-W-oxide samples.

The Mott-Schottky plots and photocurrent-voltage curves of Sn-, Ti-, and Al-doped Cu-W-oxide films exhibited *p*-type behavior. However, the photocurrent was low and stability decreased after the photoelectrode was exposed for long-time measurements in 1M NaOH solution.

CHAPTER 7

SUMMARY AND CONCLUSIONS

In this work, deposition of metal-oxide thin films on fluorine-doped tin oxide (FTO)-coated glass substrates by RF reactive magnetron sputtering was studied with the objectives of obtaining high-quality metal-oxide thin films and understanding the process conditions and their feasibility as a photoelectrode for photoelectrochemical systems for hydrogen production in an aqueous solution by solar energy. The following conclusions can be drawn from the results of these experiments:

• Bandgap narrowing of N-incorporated ZnO (ZnO:N) was achieved by reactive RF magnetron sputtering in O_2/N_2 mixture ambient. ZnO:N films with various bandgaps were realized by varying N concentration, which was successfully controlled by varying the RF powers. When RF power was increased to 200 W, the ZnO:N films exhibited optical bandgaps similar to that of Zn_3N_2 films.

• The photoelectrochemical properties of N-incorporated ZnO (ZnO:N) films prepared by reactive RF magnetron sputtering were measured and compared with those of pure ZnO films. Nitrogen incorporation narrows the bandgap of ZnO and shifts the optical absorption into the visible-light regions. It was further found that the ZnO:N films provide considerable photoresponse in the long-wavelength regions up to above 600 nm. As a result, the ZnO:N films exhibit higher photocurrents than pure ZnO films under visible-light illumination.

• *p*-type ZnO thin films with significantly reduced bandgaps were synthesized by high Cu incorporation at room temperature and followed by post-deposition annealing at 500°C in air for 2 hours. The p-type conductivity was confirmed by Mott-Schottky plots and illuminated I-V analysis. The Cu^{+1} acceptor states at substitutional sites and their bandgap reduction were demonstrated by UV-visible absorption and X-ray excited valence-band measurements.

• *p*-type ZnO films with similar bandgaps but varying carrier concentrations through co-doping of Cu and Ga are synthesized. The ZnO:(Cu,Ga) films are synthesized by RF magnetron sputtering in O_2 gas ambient at room temperature, followed by post-deposition annealing at 500°C in air for 2 hours. The bandgap reduction and p-type conductivity are caused by the incorporation of Cu. The tuning of carrier concentration is realized by varying the Ga concentration. The carrier-concentration tuning does not significantly change the bandgap and crystallinity. However, it can optimize the carrier concentration to significantly enhance the PEC response for bandgap-reduced p-type ZnO thin films.

• The ZnO thin films co-doped by Ga and N, (ZnO:(Ga,N)) thin films were deposited by co-sputtering at room temperature and followed by post-annealing at 500°C in air for 2 hours. The ZnO:(Ga,N) thin films exhibited significantly enhanced crystallinity compared to ZnO doped solely with N at the same growth conditions. Furthermore, ZnO:(Ga,N) thin films exhibited enhanced N incorporation over ZnO doped solely with N at high temperatures. As a result, ZnO:(Ga,N) thin films achieved dramatically improved PEC response, compared to ZnO thin films doped solely with N at any conditions.

• Ga and N co-incorporated ZnO thin films [ZnO:(Ga:N)] with reduced bandgaps were deposited by co-sputtering at various N_2 gas flow rates in mixed N_2 and O_2 ambient at room temperature followed by post-annealing at 500°C in air for 2 hours. It was found that all of the ZnO:(Ga:N) films exhibited enhanced crystallinity, which can suppress the recombination rate between the photogenerated electrons and holes. However, phase segregation of Zn_3N_2 occurred in ZnO:(Ga:N) thin films in N-rich sputtering ambient. It was also found that ZnO:(Ga:N) thin films without phase separation of Zn_3N_2 exhibited much better PEC response due to the reduced bandgap and better crystallinity. Results suggest that the growth conditions must be controlled carefully to avoid phase separation in Ga and N co-incorporated ZnO thin films to improve PEC response.

• Ga-N co-doped ZnO thin films with reduced bandgaps were deposited on F-doped tin-oxide-coated glass substrates by RF magnetron sputtering at various substrate temperatures in mixed N_2 and O_2 gas ambient. It was found that Ga-N co-doped ZnO films exhibited enhanced crystallinity compared to undoped ZnO films grown under the same conditions. Furthermore, Ga-N co-doping ensured enhanced N-incorporation in ZnO thin films as the substrate temperature is increased. As a result, Ga-N co-doped ZnO thin films exhibited much improved PEC response, compared to ZnO thin films. Therefore, results suggest that the passive co-doping approach could be a means to improve PEC response for bandgap-reduced wide-bandgap oxides through impurity incorporation.

• ZnO thin films are deposited in pure Ar and mixed Ar and N_2 gas ambient at various substrate temperatures by RF sputtering ZnO targets. It was found that deposition in pure

Ar ambient leads to polycrystalline ZnO thin films. However, the presence of N_2 in the deposition ambient promotes the formation of aligned nanorods at temperatures above 300°C. ZnO thin films with aligned nanorods deposited at 500°C exhibit significantly enhanced PEC response, compared to polycrystalline ZnO thin films grown at the same temperature.

• Effects of substrate temperature and RF power on the formation of aligned nanorods in ZnO thin films were studied. ZnO thin films were sputter-deposited in mixed Ar and N_2 gas ambient at various substrate temperatures and RF powers. It was found that substrate temperature plays a more important role than RF power in the formation of ZnO nanorods. At low substrate temperatures (below 300°C), ZnO nanorods do not form regardless of RF powers. High RF power helps to promote the formation of aligned ZnO nanorods. However, lower RF powers usually lead to ZnO films with better crystallinity at the same substrate temperatures in mixed Ar and N_2 gas ambient, and therefore, better PEC response.

• ZnO thin films are deposited in pure Ar and mixed Ar and N_2 gas ambient at a substrate temperature of 500°C by RF sputtering of ZnO targets. All the films were deposited on fluorine-doped tin-oxide-coated glass substrates. It was found that the presence of an optimum N_2–to-Ar ratio in the deposition ambient promotes the formation of well-aligned ZnO nanorods. ZnO thin films grown at 25% N_2 gas flow rate promoted aligned nanorods along the c-axis that exhibit significantly enhanced PEC response, as compared to ZnO thin films grown at other N_2-to-Ar gas flow ratios. Results suggest that the chamber ambient is very important for forming aligned nanostructures, which offers

potential advantages for improving the efficiency of PEC water splitting for H_2 production.

• Uniform and large areas of a new form of ZnO nanocorals are synthesized. These nanostructures can provide suitable electrical pathways for efficient carrier collection, as well as large surface areas for the PEC cells. PEC devices made from these ZnO nanocoral structures demonstrate significantly enhanced photoresponse as compared to ZnO compact and nanorod films.

• Al and N co-doped ZnO thin films, ZnO:(Al,N), are synthesized by RF magnetron sputtering in mixed Ar and N_2 and mixed O_2 and N_2 gas ambient at 100°C. The ZnO:(Al,N) films deposited in mixed Ar and N_2 gas ambient did not incorporate N, whereas ZnO:(Al,N) films grown in mixed O_2 and N_2 gas ambient showed enhanced N incorporation and crystallinity as compared to ZnO:N thin films grown in the same gas ambient. As a result, ZnO:(Al,N) films grown in mixed O_2 and N_2 gas ambient showed higher photocurrents than the ZnO:(Al,N) thin films deposited in mixed Ar and N_2 gas ambient. Results indicate that the gas ambient plays an important role in N incorporation and crystallinity control in Al and N co-doped ZnO thin films.

• ZnO thin films with significantly reduced bandgaps were synthesized by doping N and co-doping Al and N at 100°C. All the films were synthesized by RF magnetron sputtering on F-doped tin-oxide-coated glass. It was found that co-doped ZnO:(Al,N) thin films exhibited significantly enhanced crystallinity as compared to ZnO films doped solely with N, ZnO:N, at the same growth conditions. Furthermore, annealed ZnO:(Al,N) thin films exhibited enhanced N incorporation over ZnO:N films. As a result, ZnO:(Al,N)

films exhibited improved photocurrents compared to ZnO:N films grown with pure N doping; this suggests that charge-compensated donor-acceptor co-doping could be a potential method for bandgap reduction of wide-bandgap oxide materials to improve their PEC performance.

• ZnO:GaN solid-solution thin films with significantly reduced bandgaps were synthesized by using ZnO and GaN targets at 100°C, followed by post-deposition annealing at 500°C in ammonia for 4 hours. All the films were synthesized by RF magnetron sputtering on F-doped tin-oxide-coated glass substrates. It was found that ZnO:GaN solid-solution thin films exhibited significantly reduced bandgap, and, as a result, showed improved PEC response compared to ZnO thin films. Furthermore, ZnO:GaN solid-solution thin films with various bandgaps were realized by varying the N_2 mass flow rate in mixed N_2 and O_2 chamber ambient.

• The ZnO:GaN solid-solution thin films are synthesized by RF magnetron sputtering in Ar and mixed O_2 and N_2 gas ambient at 100°C, followed by post-annealing at 500°C in ammonia for 4 hours. The ZnO:GaN solid-solution films deposited in Ar gas ambient failed to reduce the bandgap, whereas solid-solution ZnO:GaN films grown in mixed O_2 and N_2 gas ambient showed bandgap reduction. The solid-solution ZnO:GaN films deposited in mixed O_2 and N_2 gas exhibited enhanced crystallinity, shifting the optical absorption into the visible-light regions. The bandgap reduction in ZnO:GaN solid-solution films is realized by varying the RF powers; as a result, ZnO:GaN solid-solution films grown in mixed O_2 and N_2 showed higher photocurrents than the solid-solution ZnO:GaN thin films deposited in Ar gas ambient. Results indicate that reduced bandgap

with enhanced PEC response can be attained using the appropriate gas ambient and by varying the RF power.

• $Co_{1+\delta}X_{2-\delta}O_4$ (X = Al, Ga, In) thin films were grown on Ag-coated stainless-steel plates (Ag/SS) and quartz glass substrates using an RF magnetron reactive co-sputtering system. Ternary cobalt-based spinel oxides show excellent stability in solution and good visible-light absorption properties; their performance as PEC catalysts is limited by the poor transport properties induced by small polaron mobility.

• $CoAl_2O_4$–Fe_2O_3 *p-n* nanocomposite electrodes were deposited on Ag-coated stainless steel substrates and annealed at 800°C. It was found that the nanocomposite electrodes exhibited much improved photoresponses as compared to *p*-type $CoAl_2O_4$ only. The improvement in photoresponse to the band offset is at the three-dimensional *p-n* junction interface, which promotes photogenerated carrier separation and reduces carrier recombination.

• Cu-W-oxide films are deposited in mixed Ar and O_2 gas ambient by co-sputtering Cu and W targets at a substrate temperature of 300°C by using an RF magnetron sputtering system. All the films were deposited on fluorine-doped tin-oxide-coated glass substrates. It was found that films exhibited an amorphous structure with no phase separation. Optical bandgaps of the films can be tuned using an appropriate composition of Cu and W in the Cu-W-oxide films. All the films showed p-type behavior. After annealing the films at 500°C for 2 hours in air, the photoresponse increased. However, the stability of the film is decreased after PEC measurements are taken for a longer period of time.

• Cu-Ti-oxide films are deposited in mixed Ar and O_2 gas ambient by co-sputtering Cu and Ti targets at substrate temperatures of 150° and 400°C by using an RF magnetron sputtering system. All the films were deposited on fluorine-doped tin-oxide-coated glass substrates. It was found that films exhibited an amorphous structure with no phase separation. Optical bandgaps of the films can be tuned using an appropriate composition of Cu and Ti in the Cu-Ti-oxide films. All the films showed p-type behavior and exhibited good stability. However, the photoresponse was low.

• Cu-Sn-oxide films are deposited in mixed Ar and O_2 gas ambient at substrate temperatures of 150°, 400°, and 425°C by using an RF magnetron sputtering system. All the films were deposited on fluorine-doped tin-oxide-coated glass substrates. It was found that the films resulted in phase segregation. Optical bandgaps of the films can be tuned using appropriate compositions of the Cu and Sn in the Cu-Sn-oxide films. All the films showed p-type behavior. However, the photoresponse was low, and films exhibited poor stability.

• Al, W, and Sn doped Cu-Ti-oxide films are deposited in mixed Ar and O_2 gas ambient at a substrate temperature of 150°C by using an RF magnetron sputtering system. All the films were deposited on fluorine-doped tin-oxide-coated glass substrates. It was found that the films resulted in phase separation. All the films showed p-type behavior. However, the photoresponse was decreased further compared to Cu-Ti-oxide films, and films exhibited poor stability.

• Sn-, Ti-, and Al-doped Cu-W-oxide films are deposited in mixed Ar and O_2 gas ambient at a substrate temperature of 150°C by using an RF magnetron sputtering system. All the

films were deposited on fluorine-doped tin-oxide-coated glass substrates. It was found that the films resulted in phase separation. All the films showed p-type behavior and exhibited good stability. However, the photoresponse was decreased further compared to Cu-W-oxide films, and films exhibited poor stability.

REFERENCES

[1] T. Bak, J. Nowotny, M. Rekas, C.C. Sorell, *International Journal of Solar Energy*, 27, p. 991, 2002.

[2] D. Morgan, F. Sissine, Congressional Research Service, Report for Congress, The Committee for the National Institute for the Environment, Washington, DC 20006-1401, 28 April 1995.

[3] T. Nejat Veziroglu, *International Journal of Hydrogen Energy*, volume 23, p. 1077, 998.

[4] A. Szyszka, *International Journal of Hydrogen Energy*, volume 23, p. 849, 1998.

[5] C. Mitsugi, A. Harumi, F. Kenzo, *International Journal of Hydrogen Energy*, volume 23, p. 159, 1998.

[6] The Economist Technology, Quarterly, p. 29, March 25, 2001.

[7] US Department of Energy, National Renewable Energy Laboratory. Hydrogen the fuel for the future, DOE/GO-1- 95-099 DE95004024, March 1995.

[8] http://cobweb.ecn.purdue.edu/~vurade/; Internet; accessed 7 June 2008.

[9] A. Fujishima, K. Honda, *Nature*, 238, p. 37, 1972.

[10] T. Watanabe, A. Fujishima, K. Honda, *Chemistry Letters*, 897, 1974.

[11] A. Fujishima, K. Kohayakawa, K. Honda, *Journal of the Electrochemical Society*, 12, p. 1487, 1975.

[12] K. Honda, T. Ohta, editor. *Solar Hydrogen Energy Systems*, Oxford: Pergamon Press, p. 137, 1979.

[13] H. Yoneyama, H. Sakamoto, H. Tamura, *Electrochimica Acta*, 20, p. 341, 1975.

[14] T. Ohnishi, Y. Nakato, H. Tsubomura, *Ber Bunsen Ges*, 79, p. 523, 1975.

[15] J. G. Mavroides, D. I. Tchernev, J. A. Kafalas, D. F. Kolesar, *Materials Research Bulletin*, 10, p. 1023, 1975.

[16] A. J. Nozik, *Nature*, 257, p. 383, 1975.

[17] G. Hodes, D. Cahen, J. Manessen, *Nature*, 260, p. 312, 1976.

[18] M. S. Wrighton, A. B. Ellis, P. T. Wolczanski, D. L. Morse, H. B. Abrahamson, D. S. Ginley, *Journal of the American Chemical Society*, 98, p. 2774, 1976.

[19] H. Morisaki, T. Watanabe, M. Iwase, K. Yazawa, *Applied Physics Letters*, 29, p. 338, 1976.

[20] T. Watanabe, A. Fujishima, K. Honda, *Bulletin of the Chemical Society of Japan*, 49, p. 355, 1976.

[21] M. A. Butler, R. D. Nasby, R. K. Quinn, *Solid State Communication*, 19, p. 1011, 1976.

[22] J. M. Bolts, M. S. Wrighton, *Journal of Physical Chemistry*, 80, p. 2641, 1976.

[23] J. H. Carey, B. G. Oliver, *Nature*, 259, p. 554, 1976.

[24] B. O. Seraphin, In: B. O. Seraphin, editor, *Solar Energy Conversion,* Berlin: Springer, p. 5–56, 1979.

[25] A. J. Nozik, *Applied Physics Letters*, 29, p. 150, 1976.

[26] E. C. Dutoit, F. Cardon, W. P. Gomes, *Ber Bunsenges Ges*, 80, p. 475, 1976.

[27] J. G. Mavroides, J. A. Kafalas, D. F. Kolesar, *Applied Physics Letters*, 28, p. 241, 1976.

[28] P. D. Fleischauer, J. K. Allen, *Journal of Physical Chemistry*, 82, p. 432, 1978.

[29] R. Memming, *Electrochimica Acta*, 25, p. 77, 1980.

[30] M. A. Butler, M. Abramovich, F. Decker, J. F. Juliao, *Journal of the Electrochemical Society*, 128, p. 200, 1981.

[31] A. A. Soliman, Seguin HJJ, *Solar Energy Materials and solar cells*, 5, p. 95, 1981.

[32] J. Kiwi, K. GrXatzel, *Journal of Physical Chemistry*, 90, p. 637, 1986.

[33] G. Prasad, N. N. Rao, O. N. Srivastava, *International Journal of Hydrogen Energy*, 13, p. 399, 1988.

[34] B. O. Regan, O. GrXatzel, *Nature*, 353, p. 737, 1991.

[35] R. N. Pandey, K. S. Babu, D. Singh, O. N. Srivastava, *Bulletin of the Chemical Society of Japan*, 65, p. 1072, 1992.

[36] J. Augustynski, *Electrochimica Acta*, 38, p. 43, 1993.

[37] J. P. H. Sukampto, C. S. McMillan, W. Smyrl, *Electrochimica Acta*, 38, p. 15, 1993.

[38] L. D. Harvey, *International Journal of Hydrogen Energy*, 21, p. 583, 1996.

[39] J. R. Bolton, *Solar Energy*, 57, p. 37, 1996.

[40] R. N. Pandey, K. S. Chandra-Babu, O. N. Srivastava, *Progress in Surface Science*, 52, p. 125, 1996.

[41] G. Zhao, H. Kozuka, T. Yoko, *Solar Energy Materials and solar cells*, 46, p. 219, 1997.

[42] G. Zhao, S. Utsumi, H. Kozuka, T. Yoko, *Journal of Materials Science*, 33, p. 3655, 1998.

[43] Y. Hao, M. Yang, C. Hu, S. Cai, M. Liu, L. Fan, Y. Li, *Solar Energy Materials and solar cells*, 56, p. 75, 1998.

[44] M. Y. El Zayat, A. O. Saed, M. S. El-Dessouki, *International Journal of Hydrogen Energy*, 23, p. 259, 1998.

[45] Y. Liu, A. Hagfeldt, X. R. Xiao, S. E. Lindquist, *Solar Energy Materials and solar cells*, 55, p. 267, 1998.

[46] A. Stanley, B. Verity, D. Matthews, *Solar Energy Materials and solar cells*, 52, p. 141, 1998.

[47] R. N. Pandey, M. Misra, O. N. Srivastava, *International Journal of Hydrogen Energy*, 23, p. 861, 1998.

[48] M. Gomez, J. Rodriguez, S. Tingary, A. Hagfeldt, S. E. Lindquist, C. G. Granquist, *Solar Energy Materials and solar cells*, 59, p. 277, 1999.

[49] G. Zhao, H. Kozuka, H. Lin, T. Yoko, *Thin Solid Films*, 339, p. 123, 1999.

[50] G. Zhao, H. Kozuka, H. Lin, M. Takahashi, T. Yoko, *Thin Solid Films*, 340, p. 125, 1999.

[51] H. Kozuka, Y. Takahashi, G. Zhao, T. Yoko, *Thin Solid Films*, 358, p. 172, 2000.

[52] V. Aranyos, H. Grennberg, S. Tingry, S. E. Lindquist, A. Hagfeldt, *Solar Energy Materials and solar cells*, 64, p. 97, 2000.

[53] S. Chandra, Photoelectrochemical solar cells, NewYork: Gordon and Breach, 1985.

[54] S. R. Morrison, Electrochemistry at Semiconductor and Oxidized Metal Electrodes, New York: Plenum Press, p. 1, 1980.

[55] A. J. Nozik, In: Heller A, editor, Semiconductor liquid-junction solar cells, Proceedings of the Conference on the Electrochemistry and Physics of Semiconductor Liquid Interfaces under Illumination, Virginia: Airlie, p. 272, 1977.

[56] H. O. Finklea, In: H. O. Finklea, editor, *Semiconductor Electrodes*, Amsterdam: Elsevier, p. 1, 1988.

[57] J. Gerischer, In: B. O. Seraphin, editor, *Solar Energy Conversion*, Berlin: Springer, p. 115, 1979.

[58] O. Khaselev, J. A. Turner, *Science*, 280, p. 425, 1998.

[59] S. Licht, B. Wang, S. Mukerji, T. Soga, M. Umeno, H. Tributsch H, *Journal of Physical Chemistry B*, 104, p. 8920, 2000.

[60] Oriel-Instruments, Book of Photon Tools, p. 1, 1999.

[61] A. K. Ghosh, H. P. Muruska, *Journal of the Electrochemical Society*, 124, p.1516, 1977.

[62] J. F. Houlihan, D. B. Armitage, T. Hoovler, D. Bonaquist, D. P. Madacsi, L. N. Mulay, *Materials Research Bulletin*, 13, p. 1205, 1978.

[63] J. Akikusa, S. U. M. Khan, *International Journal of Hydrogen Energy*, 22, p. 875, 1997.

[64] B. O'Regan, M. Gratzel, *Nature*, 353, p. 737, 1991.

[65] B. A. Parkinson, A. M. Spitler, *Electrochimica Acta*, 37, p. 943, 1992.

[66] T. E. Philips, K. Moorijani, J. C. Murphy, T. O. Poehler, *Journal of the Electrochemical Society*, 129, p. 1210, 1982.

[67] C. P. Jagdish, *Zinc Oxide Bulk, thin films and Nanostructures*, (Elsevier, Oxford, 2006).

[68] C. W. Bunn, Proceedings of the Physical Society, London 47, p. 835, 1935.

[69] F. C. M. Van de Pol, *Ceramic Bulletin*, 69, p. 1959, 1990.

[70] D. R. Lide (Ed.), *CRC Handbook of Chemistry and Physics*, 73rd Edition, CRC Press, New York, 1992.

[71] D. C. Look, B. Clafin, Y. I. Alivov, S. J. Park, *Physica Status Solid, (a),* 201, p. 2203, 2004.

[72] S. J. Pearton, D. P. Norton, K. Ip, Y. W. Heo, T. Steiner, *Progress in Materials Science*, 50, p. 293, 2005.

[73] H. Hartman, R. Mach, B. Selle, Wide gap II-VI compounds as electronic materials, Current topics of Materials Science (E. Kaldis, Ed.), (North Holland, Amsterdam), vol. 9, p. 1, 1982.

[74] V. Srikant, D. R. Clarke, *Journal of Applied Physics*, 83, p. 5447, 1998.

[75] T. Minami, H. Nanto, S. Takata, *Japanese Journal of Applied Physics*, 24, p. L605, 1985.

[76] K. H. Kim, K. C. Park, D. Y. Ma, *Journal of Applied Physics*, 81, p. 7764, 1997.

[77] K. J. Kim, Y. R. Park, *Applied Physics Letters*, 78, p.75, 2001.

[78] W. W. Wenas, A. Yamada, K. Takahashi, *Journal of Applied Physics*, 70, p. 7119, 1991.

[79] D. C. Look, K. W. Hemsky, J. R. Sizelove, *Physical Review Letters*, 82, p. 2552, 1999.

[80] D. C. Look, C. Coskun, B. Clafin, G. C. Farlow, *Physica* B340-342, p. 32, 2003.

[81] F. Tuomisto, V. Ranki, K. Saarinen, D. C. Look, *Physical Review Letters*, 91, 205502, 2004.

[82] F. Leiter, H. alves, D. Pfisterer, N. G. Romanov, D. M. Hoffman, B. K. Meyer, *Physica* B340-342, p. 201, 2003.

[83] F. Oba, S. R. Nishitani, S. Isotani, H. Adachi, I. Tanaka, *Journal of Applied Physics*, 90, p. 824, 2001.

[84] C. G. Van de Walle, *Physical Review Letters*, 85, p. 1012, 2000.

[85] S. F. J. Cox, E. A. Davis, S. P. Cottrel, P. J. C. King, J. S. Lord, J. M. Gil, H. V. Alberto, R. C. Vilao, J. P. Duarte, N. Ayres de Campos, A. Weidinger, R. L. Lichti, S. J. C. Irvine, *Physical Review Letters*, 86, p. 2601, 2001.

[86] D. M. Hofmann, A. Hofstaetter, F. Leiter, H. Znou, F. Henecker, B. K. Meyer, S. B. Orlinskii, J. Schmidt, P. G. Baranov, *Physical Review Letters*, 88, p. 45504, 2002.

[87] D. Vogel, P. Kruger, J. Pollmann, *Physical Review B* 52, p. R14316, 1995.

[88] S. O. Kucheyev, J. E. Bradby, J. S. Williams, C. Jagadish, M. V. Swain, *Applied Physics Letters*, 80, p. 956, 2002.

[89] V. A. Coleman, J. E. Bradby, C. Jagdish, P. Munroe, Y. M. Heo, S. J. Pearton, D. P. Norton, M. Inoue, M. Yano, *Journal of Applied Physics*, 86, p. 203105, 2005.

[90] V. A. Coleman, J. E. Bradby, C. Jagadish, P. Munroe, M. R. Philips (unpublished).

[91] S. Adachi, Properties of Group-IV, III-V and II-VI Semiconductors, John Wiley and Sons, Ltd, West Sussex, England, 2005.

[92] D. I. Florescu, L. G. Mourokh, F. H. Pollak, D. C. Look, G. Cantwell, X. Li, *Journal of Applied Physics*, 91, p. 890, 2002.

[93] U. Ozgur, Y. I. Alivov, C. Liu, A. Teke, M. A. Reshchikov, S. Douan, V. Avrutin, S. J. Cho, H. Morkoc, *Journal of Applied Physics*, 98, p. 041301, 2005.

[94] H. Ibach, *Physica Status Solidi*, (b), 33, 257 (1969).

[95] W. N. Lawless and T. K. Gupta, *Journal of Applied Physics*, 60, 607 (1986).

[96] K. Ellmer, *Journal of Physics D: Applied Physics*, 34, p. 3097, 2001.

[97] S. B. Zhang, S. H. Wei, A. Zunger, *Physical Review B*, 63, p. 75205, 2001.

[98] M. S. Tokumoto, A. Smith, C. V. Santilli, S. H. Pulcinelli, A. F. Craievich, E.Elkaim, A. Traverse, V. Briois, *Thin Solid Films*, 416, p. 284, 2002.

[99] Z. F. Liu, F. K. Shan, Y. X. Li, B. C. Shin, Y. S. Yu, *Journal of Crystal Growth*, 259, p. 130, 2003.

[100] A. Sanchez-Juarez, A. Triburcio-Silver, A. Ortiz, E. P. Zironi, J. Rickards, *Thin Solid Films*, 333, p. 196, 1998.

[101] A. Bougrine, A. El Hichou, M. Addou, J. Ebothe, A. Kachouane, M. Troyon, *Materials Chemistry and Physics*, 80, p. 438, 2003.

[102] G. K. Paul, S. Bandyopadhyay, S. K. Sen, S. Sen, *Materials Chemistry and Physics*, 79, p. 71, 2003.

[103] Y. M. Lu, C. M. Chang, S. I. Ti, T. S. Wey, *Thin Solid Films*, 447-448, p. 56, 2004.

[104] Z. Znou, K. Kato, T. Komaki, M. Yoshino, H. Yushino, H. Yukawa, M. Morinaga, *International Journal of Hydrogen Energy*, 29, p. 323, 2004.

[105] S. K. kim, S. A. Kim, C. H. Lee, *Applied Physics Letters*, 85, p. 419, 2004.
[106] H. T. Cao, Z. l. Pei, J. Gong, C. Sun, R. F. Huang, L. S. Wen, *Surface & Coatings Technology*, 184, p. 84, 2004.

[107] J. B. Lee, H. J. Lee, S. h. Seo, J. S. Park, *Thin Solid Films*, 398-399, p. 641, 2001.

[108] G. A. Mohamed, E. M. Mohamed, A. A. EI-Fadl, *Physica*, B308-310, p. 949, 2001.

[109] M. Aven, II-VI Semiconducting Compounds (D. G. Thomas, Ed.), (Benjamin, New York 1967), p. 1232.

[110] C. H. Park, S. B. Zhang, S. H. Wei, *Physical Review* B66, p. 73202, 2002.

[111] A. Kobayashi, O. F. Sankey, and J. D. Dow, *Physical Review* B28, p. 946, 1983.

[112] L. G. Wang and A. Zunger, *Physical Review Letters*, 90, p. 256401, 2003.

[113] A. Walsh, K.-S. Ahn, S. Shet, M. N. Huda, T. Deutsch, H. Wang, J. A. Turner, S. H. Wei, Y. Yan and M. Al-Jassim, *Energy & Environmental Science*, DOI: 10. 1039/b822903a, 2009.

[114] M. Woodhouse, G. S. Herman and B. A. Parkinson, *Chemistry of Materials*, 17, p. 4318, 2005.

[115] M. Woodhouse and B. A. Parkinson, *Chemistry of Materials*, 20, 2495, 2008.

[116] A. Walsh, S. -H. Wei, Y. Yan, M. M. Al-Jassim, J. A. Turner, M. Woodhouse and B. A. Parkinson, *Physical Review* B, 76, 165119, 2007.

[117] K. M. E. Miedzinska, B. R. Hollebone and J. G. Cook, *Journal of Physics and Chemistry of Solids*, 48, p. 649, 1987.

[118] Y. Jugnet and T. M. Duc, *Journal of Physics and Chemistry of Solids*, 40, p. 29, 1979.

[119] J. Alacron, P. Escribano, R. M. Br. Martin, *Ceramic Transaction*, J 84, p. 170, 1985.

[120] L. Ji, S. Tang, H. C. Zeng, J. Lin, K. L. Tan, *Applied Catalysis A*, 207, p. 247 2001.

[121] N. El Habra, L. Crociani, C. Sada, P. Zanella, M. Casarin, G. Rossetto, G. Carta, G. Paolucci, *Chemistry of Materials,* 19, p. 3381, 2007.

[122] N. G. Matveeva, A. I. Shelykh, *Physica Status Solidi B*, 50, p. 83, 1972.

[123] B.J. Lokhande, M.D.Uplane, *Applied Surface Science*, 167, p. 243, 2000.
[124] A.E. hichou, A. Bougrine, J.L. Bubendorff, J. Ebothe, M. Addou, M. Troyon, *Semiconductor Science and Technology*, 17, p. 607, 2002.

[125] J. Ebothe, A. EI Hicho, P. Vautrot, M. Addou, *Journal of Applied Physics*, 93, p. 632, 2003.

[126] Y. Natsume, H. Sakata, *Thin Solid Films*, 372, p. 30, 2000.

[127] W. W. Wenas, A. Yamada, K. Takahashi, *Journal of Applied Physics*, 70, p. 7119, 1991.

[128] Y. Natsume, H. Sakata, T. Hirayama, *Journal of Applied Physics*, 72, p. 4203, 1992.

[129] T. Ohgaki, N. Ohashi, H. Kakemoto, S. Wada, Y. Adachi, H. Haneda, T. Tsurumi, *Journal of Applied Physics*, 93, p. 1961, 2003.

[130] K. L. Narasimhan, S. P. Pai, V.R. Palkar, R. Pinto, *Thin Solid Films*, 295, p. 104, 1997.

[131] A. V. Singh, R. M. Mehra, N. Buthrath, A. Wakahara, A. Yoshida, *Journal of Applied Physics*, 90, p. 5661, 2001.

[132] K. H. Kim, K. C. Park, d. Y. Ma, *Journal of Applied Physics*, 81, p. 7764, 1997.

[133] V. Assuncao, E. Fortunato, A. Marques, H. Aguas, I. Ferreira, M.E.V. Costa, R. Martins, *Thin Solid Films*, 427, p. 401, 2003.

[134] Klaus K. Schuegraf, *Handbook of thin film deposition processes and techniques*, Noyes Publication, Park Ridge, NJ, 1998.

[135] R. B. Marcus and S. Quigley, *Thin Solid Films*, Vol. 2, p. 467, 1968.

[136] S. Wolf and R. N. Tauber, *Silicon Processing for the VLSI Era*, Vol. 1-Process Technology, Lattice Press, Sunset Beach, CA, 2000.

[137] Brian Chapman, *Glow Discharge Processes, Sputtering and Plasma Etching*, Wiley-Interscience publication, 1980.

[138] http://home.earthlink.net/~hzeng/thinfilm.htm; internet; accessed 7 June 2008.

[139] http:///www.ccm.ecn.purdue.edu/dd/deposition_methods/ Internet; accessed 7 June 2008.

[140] M. Ohring, *The Materials Science of Thin Films*, Academic Press, 1990.

[141] Penning F.M, Die glimmenladung bci niedrrigen: *Physica*, vol. III, No. 9, p. 873, 1935.

[142] S. K. Gandhi, *VLSI Fabrication Principles: Silicon and Gallium Arsenide*, second edition, Wiley-Interscience Publication, 1994.

[143] http://www.pse.umass.edu/nano/e5.html; Internet; accessed 7 June 2008.

[144] M. Ohring, The materials science of thin films, Academic Press, 1990.

[145] J. I. Goldstein, D.E. Newbury, P. Echlin, D. C. Joy, A. D. Romig, Jr., C. E. Lyman, C. Fiori and E. Lifshin, *Scanning Electron Microscopy and X-ray Microanalysis*, A text for biologist, Materials Scientists, and Geologists, second edition, Plenum Press, 1994.

[146] D. M. Mattox, *Handbook of Physical Vapor Deposition*, Noyes Publications, Park Ridge, NJ, 1998.

[147] http://www.di.com; Internet: accessed 7 June 2008.

[148] K. Dieter, Schroder, *Semiconductor Material and Device Characterization*, Wiley Interscience Publication, 1998.

[149] R. G. Wilson, F.A. Stevie and C. W. Magee, *Secondary Ion Mass Spectroscopy*, John Wiley and Sons, New York, 1989.

[150] http://www.siliconfareast.com/SIMS.htm; Internet: accessed 7 June, 2008.

[151] http://www.answers.com/topic/system2-gif-1; Internet: accessed 7 June, 2008.

[152] http://www.eaglabs.com/techniques/analytical_techniques/xps_esca.php; Internet: accessed 7 June, 2008.

[153] http://nobelprize.org/educational_games/physics/microscopes/ Internet; accessed 7 June 2008.

[154] http://www.directindustry.com/prod/; Internet: accessed 7 June, 2008.

[155] www.ati.surrey.ac.uk/facilities/optical_suite; Internet: accessed 7 June, 2008.

[156] www.ndl.org.tw/ndl2006/department/cfteam/docs/modules/n&k: Internet accessed 7 June, 2008.

[157] http://findarticles.com/p/articles/: Internet accessed 7 June, 2008.

[158] B. S. Li, *Journal of Materials Research*, 18, p. 8, 2003.
[159] M. Futsuhara, K. Yoshioka, and O. Takai, *Thin Solid Films*, 322, p. 274, 1998.

[160] K.-S. Ahn, Y. Yan, and M. Al-Jassim, *Journal of Vacuum Science and Technology*, B 25(4), p. L23, 2007.

[161] K.-S. Ahn, S. Shet, T. Deutsch, Y. Yan, N. M. Ravindra, J. Turner, M. Al-Jassim *Materials Science &Technology* 2008 Conference and Exhibition, p 952, Pittsburgh, PA, USA, October 5-9, 2008,.

[162] Y. Yan, K.-S. Ahn, S. Shet, T. Deutsch, M. Huda, S. H. Wei, J. Turner, M. Al-Jassim, Solar hydrogen and nanotechnology II, *Proceedings of the SPIE*, Vol. 6650, p.66500H, 2007.

[163] S. Shet, K.-S. Ahn, T. Deutsch, Y. Yan, N. M. Ravindra, J. Turner, M. Al-Jassim, *Materials Science & Technology* 2008 Conference and Exhibition, Pittsburgh, PA, USA, October 5-9, 2008.

[164] F. K. Shan, B. I. Kim, G. X. Liu, Z. F. Liu, J. Y. Sohn, W. J. Lee, B. C. Shin, and Y. S. Yu, *Journal of Applied Physics*, 95, p. 4772, 2004.

[165] M. Gratzel, *Nature*, 414, p. 338, 2001.

[166] K. Keis, L. Vayssieres, H. Rensmo, S. E. Lindquist, and A. Hagfeldt, *Journal of Electrochemical Society*, 148, p. A149, 2001.

[167] G. Kresse and J. Furthmuller, *Computational Materials Science*, 6, p. 15, 1996.

[168] D. Vanderbilt, *Physical Review B*, 41, p. 7892, 1990.

[169] K.-S. Ahn, Y. Yan, S.-H. Lee, T. Deutsch, J. Turner, C. E. Tracy, C. L. Perkins, and M. Al-Jassim, *Journal of The Electrochemical Society*, 154 (9), p. B956-B959, 2007.

[170] M. Joseph, H. Tabata, and T. Kawai, *Japanese Journal of Applied Physics*, Part 2, 38, p. L1205, 1999.

[171] K. K. Kim, H. S. Kim, D. K. Hwang, J. H. Lim, and S. J. Park, *Applied Physics Letters*, 83, p. 63, 2003.

[172] A. Kobiayashi, O. F. Sankey, and J. D. Dow, *Physical Review B*, 28, p. 946, 1983.

[173] C. l. Perkins, S. H. Lee, X. Li, S. E. Asher, and T. J. Coutts, *Journal of applied Physics*, 97, p. 034907, 2005.

[174] Y. Yan, S. B. Zhang, and S. T. Pantelides, *Physical Review Letters*, 86, p. 5753, 2001.

[175] M. Gleria and R. Memming, *Journal of. Electroanalytical. Chemistry, Interfacial Electrochemistry*, 65, p.163, 1975.

[176] L. Bahadur, T. N. Rao, and J. P. Pandey, *Semiconductor Science and Technology*, 9, p. 275, 1994.

[177] K. Fujii and K. Ohkawa, *Journal of The Electrochemical Society*, 153, p. A468, 2006.

[178] J. Li and L. M. Peter, *Journal of Electroanalytical Chemistry, Interfacial Electrochemistry*, 193, p. 27, 1985.

[179] R. Beranek, H. Tsuchiya, T. Sugishima, J. M. Macak, L. Taviera, S. Fujimoto, H. Kisch, and P. Schmuki, *Applied Physics Letters*, 87, p. 243114, 2005.

[180] W. Schottky, *Z. Phys*, 118, p. 539, 1942.

[181] Y. Yan, M.M. Al-Jassim, and S.H. Wei, *Applied Physics Letters*, 89, p. 181912, 2006.

[182] K.-S. Ahn, T. Deutsch, Y. Yan, C.-S. Jiang, C. L. Perkins, J. Turner, and M. Al-Jassim, *Journal of Applied Physics*, 102, p. 023517, 2007.

[183] K.-S. Ahn, S. Shet, T. Deutsch, Y. Yan, N. M. Ravindra, J. Turner, M. Al-Jassim, *Materials Science & Technology* 2008 Conference and Exhibition, p. 901, Pittsburgh, PA, USA, October 5-9, 2008.

[184] S. Shet, K.-S. Ahn, T. Deutsch, Y. Yan, N. M. Ravindra, J. Turner, M. Al-Jassim, *Materials Science & Technology* 2008 Conference and Exhibition, Pittsburgh, PA, USA, October 5-9, 2008.

[185] *CRC Handbook of Chemistry and Physics,* edited by D. R. Lide (CRC, Boca Raton, FL, 2002), p.9, 2002.

[186] *Handbook of X-Ray Photoelectron Spectroscopy,* edited by John F. Moulder (PHI, 1992), 1992.

[187] C. X. Xu, X. W. Sun, X. H. Zhang, L. Ke, and S. J. Chua, *Nanotechnology*, 15, p. 856, 2004.

[188] S. U. M. Khan and J. Akikusa, *Journal of Physical Chemistry*, B, 103, p. 7184, 1999.

[189] W. P. Gomes and D. Vanmaekelbergh, *Electrochimica Acta*, 41, p. 967, 1996.

[190] S. Shet, K.-S. Ahn, Y. Yan, T. Deutsch, K. M. Chrustowski, J. Turner, M. Al-Jassim, *Journal of Applied Physics,* 103, p. 073504, 2008.

[191] C. Santato, M. Ulmann, and J. Augustynski, *Advanced. Materials*, 13, p. 511, 2001.

[192] N. Gopalakrishnan, B. C. Shin, H. S. Lim, T. Balasubramanian, and Y. S. Yu, *Journal of Crystal Growth*, 294, p. 273, 2006.

[193] R. A. Asmar, S. Juillaguet, M. Ramonda, A. Giani, P. Combette, A. Khoury, and A. Foucaran, *Journal of Crystal Growth*, 275, p. 512, 2005.

[194] K.-S. Ahn, Y. Yan, S. Shet, T. Deutsch, J. Turner, M. Al-Jassim, *Applied Physics Letters*, Vol. 91, issue 23, p. 231909, 2007.

[195] S. Shet, K.-S. Ahn, Y. Yan, T. Deutsch, M. Huda, N. M. Ravindra, M. Al-Jassim, J. Turner, 2008 TMS Annual Meeting & Exhibition, New Orleans, Louisiana, USA. USA, March 9-13, 2008.

[196] X. Li, Y. Yan, T.A. Gessert, C.L. Perkins, D. Young, C. DeHart, M. Young, and T.J. Coutts, *Journal of Vacuum Science and Technology*, A 21, p.1342, 2003.

[197] C. Jagadish and S. J. Pearton, *Zinc Oxide Bulk, Thin Films and Nanostructures*, Elsevier, Amsterdam, 2006.

[198] D. Paluselli, B. Marsen, E. L. Miller, and R. E. Rocheleau, *Electrochemical and Solid-State Letters*, 8, p. G301, 2005.

[199] S. Shet, K.-S. Ahn, H. Wang, R. Nuggehalli, Y. Yan, J. Turner, and M. Al-Jassim, Submitted to *Journal of Electronic Materials*, 2008.

[200] S.–H. Kang, J.–Y. Kim, Y. Kim, H.–S. Kim, and Y.–E. Sung, *Journal of Physical Chemistry* C, 111, p. 9614, 2007.

[201] S. Shet, K.-S. Ahn, Y. Yan, N. M. Ravindra, T. Deutsch, J. Turner, M. Al-Jassim, *Journal of Electronic Materials*, submitted, 2009.

[202] S. Shet, K.-S. Ahn, Y. Yan, N. M. Ravindra, T. Deutsch, J. Turner, M. Al-Jassim, *Journal of Electronic Materials*, 2008.

[203] K.-S. Ahn, S. Shet, T. Deutsch, C.-S. Jiang, Y. Yan, M. Al-Jassim, J. Turner, *Journal of Power Sources*, 176, p. 387, 2008.

[204] S. Shet, K.-S. Ahn, T. Deutsch, Y. Yan, J. Turner, M. Al-Jassim, N. M. Ravindra Materials Science & Technology 2008 Conference and Exhibition, p. 920, Pittsburgh, PA, USA, October 5-9, 2008.

[205] Y. Li, X. Li, C. Yang, and Y. Li, *Journal of Materials Chemistry*, 13, p. 2641, 2003.

[206] X. Liu, X. Wu, H. Cao, and R. P. H. Chang, *Journal of Applied Physics*, 95, p. 3141, 2004.

[207] W. I. Park, D. H. Kim, S.–W. Jung, and G.–C. Yi, *Applied Physics Letters*, 80, p. 4232, 2002.

[208] S. Choopun, H. Tabata, and T. Kawai, *Journal of Crystal Growth*, 274, p. 167, 2005.

[209] F. Xu, Z.–Y. Yuan, G.–H. Du, T.–Z. Ren, C. Bouvy, M. Halasa, and B.–L. Su, *Nanotechnology*, 17, p. 588, 2006.

[210] C. M. López and K.–S. Choi, *Chemical Communications*, p. 3328, 2005.

[211] M. Law, L. E. Greene, J. C. Johnson, R. Saykally, and P. Yang, *Nature Materials*, 4, p. 455, 2005.

[212] R. Asahi, T. Morikawa, T. Ohwaki, K. Aoki, and Y. Taga, *Science,* 293, p. 269, 2001.

[213] S. Dutta, S. Chattopadhyay, D. Jana, A. Banerjee, S. Manik, S. K. Pradhan, M. Sutradhar, and A. Sarkar, *Journal of Applied Physics*, 100, p. 114328, 2006.

[214] S. Shet, K.-S. Ahn, Y. Yan, N. M. Ravindra, T. Deutsch, J. Turner, and M. Al-Jassim, *(manuscript under preparation)*, 2009.

[215] S. Shet, K.-S. Ahn, N. M. Ravindra, Y. Yan, T. Deutsch, J. Turner, M. Al-Jassim, Materials Science & technology 2009 conference and exhibition, Pittsburgh, Pennsylvania, USA, manuscript *submitted* to *Ceramic Transactions*, October 25-29, 2009.

[216] Y. C. Choi, Y. M. Shin, Y. H. Lee, B. S. Lee, G. S. Park, W. B. Choi, N. S. Lee, and J. M. Kim, *Applied Physics Letters*, 76, p. 2367, 2000.

[217] K.-S. Ahn, Y. Yan, S. Shet, K. Jones, T. Deutsch, J. Turner, M. Al-Jassim, *Applied Physics Letters,* Vol. 93, issue 16, p. 163117, 2008.

[218] T. F. Jaramillo, S. H. Baeck, A. Kleiman-Shwarsctein, and E. W. McFarland, *Macromolecular Rapid Communications*, 25, p. 297, 2004.

[219] K. Vinodgopal, S. Hotchandani, and P. V. Kamat, *Journal of Physical Chemistry*, 97, p. 9040, 1993.

[220] A. Ghicov, H. Tsuchiya, J. M. Macak, & P. Schmuki, *Physica Status Solidi* A, 203, p. R28, 2006.

[221] S. Nakade, T. Kanzaki, Y. Wada, & S. Yanagida, and Stepped, *Langmuir*, 21, p. 10803, 2005.

[222] K.-S. Ahn, M. S. Kang, J. K. Lee, B. C. Shin, & J. W. Lee, *Applied Physics Letters*, 89, p. 013103, 2006.

[223] S. Shet, K.-S. Ahn, T. Deutsch, H. Wang, N. M. Ravindra, Y. Yan, J. Turner, M. Al-Jassim, *Journal of Materials Research, (accepted)*, 2009.

[224] S. Shet, K.-S. Ahn, T. Deutsch, H. Wang, N. M. Ravindra, Y. Yan, J. Turner, M. Al-Jassim, submitted to *Journal of Electronic Materials*, 2009.

[225] S. Shet, K.-S. Ahn, T. Deutsch, H. Wang, N. M. Ravindra, Y. Yan, J. Turner, M. Al-Jassim, *(manuscript under preparation)*, 2009.

[226] S. Shet, K.-S. Ahn, T. Deutsch, H. Wang, N. M. Ravindra, Y. Yan, J. Turner, M. Al-Jassim, *(manuscript under preparation)*, 2009.

[227] U. L. Stangar, B. Orel and M. Krajnc, *Journal of Sol-Gel Science and. Technology*, 26, p. 771, 2003.

[228] M. Zayat and D. Levy, *Chemistry of Materials*, 12, p. 2763, 2000.

[229] A. Walsh, S. -H. Wei, Y. Yan, M. M. Al-Jassim, J. A. Turner, M. Woodhouse and B. A. Parkinson, *Physical Review B*, 76, p. 165119, 2007.

[230] A. Walsh, Y. Yan, M. M. Al-Jassim and S.–H. Wei, *Journal of Physical Chemistry*, C, 112, p. 12044, 2008.

[231] A. Walsh, J. L. F. Da Silva, and S.–H. Wei, *Physical Review B*, 78, p. 075211, 2008.

[232] C. G. Granqvist and A. Hultaker, *Thin Solid Films*, 411, p. 1, 2002.

[233] P. D. C. King, T. D. Veal, D. J. Payne, A. Bourlange, R. G. Egdell and C. F. McConville, *Physical Review Letters*, 101, p. 116808, 2008.

[234] K.-S. Ahn, Y. Yan, M.-S. Kang, J.-Y. Kim, S. Shet, H. Wang, J. Turner, and M. Al-Jassim, *Applied Physics Letters*, 95, p. 022116, 2009.